



UNIVERSIDADE D  
COIMBRA

David Gomes Andrade

ANALYSIS OF THE THERMO-MECHANICAL  
CONDITIONS IN FRICTION STIR BASED  
TECHNOLOGIES

Doctoral Thesis in Steel and Composite Construction, supervised by  
Professor Dulce Maria Esteves Rodrigues and Professor Carlos Miguel  
Almeida Leitão, submitted to the Department of Civil Engineering, Faculty of  
Sciences and Technology of the University of Coimbra.

April 2021



Faculty of Sciences and Technology of the University of Coimbra

# ANALYSIS OF THE THERMO-MECHANICAL CONDITIONS IN FRICTION STIR BASED TECHNOLOGIES

David Gomes Andrade

*Doctoral Thesis in Steel and Composite Construction, supervised by  
Professor Dulce Maria Esteves Rodrigues and Professor Carlos Miguel  
Almeida Leitão, submitted to the Department of Civil Engineering, Faculty of  
Sciences and Technology of the University of Coimbra.*

April 2021



UNIVERSIDADE D  
COIMBRA





The work underlying the present thesis was supported by Foundation for Science and Technology (FCT, Portugal) through the PhD fellowship reference number SFRH/BD/130196/2017. This research was also sponsored by FEDER funds through Portugal 2020 (PT2020), by the Competitiveness and Internationalization Operational Program (COMPETE 2020) and national funds through the Portuguese Foundation for Science and Technology, under the R&D Unit Institute for Sustainability and Innovation in Structural Engineering (ISISE), under reference UIDB/04029/2020; Centre for Mechanical Engineering, Materials and Processes (CEMMPRE), under reference UIDB/00285/2020; and by the project Friction 4.0 (POCI-01-0145-FEDER-032089).





# Acknowledgements

---

This thesis would not have been possible without the corporation and support of many people, who directly or indirectly contributed to the success of this work:

Foremost, I would like to express my sincere gratitude to my advisors Professor Dulce Rodrigues and Professor Carlos Leitão for the continuous support, guidance, dedication, patience, encouragement provided during my PhD research, and for helping me in my personal and academic development.

I gratefully acknowledge the host institutions, ISISE (Institute for Sustainability and Innovation in Structural Engineering) and CEMMPRE (Centre for Mechanical Engineering, Materials and Processes) which welcomed me, giving me the conditions to perform my research. Thanks for the financial, academic and technical support provided. I would also like to extend my sincere thanks to all professors, researchers, students and collaborators of these research groups.

My sincere gratitude to the International Centre for Numerical Methods in Engineering (CIMNE), particularly to Professor Michele Chiumenti and Professor Narges Dialami for supplying the software used in the investigation.

A special thanks to my friends and research colleagues, from the Group of Technology of the Department of Mechanical Engineering, for their friendship and companionship throughout this journey.

To the publishers, the copyright holders and the scientific journals, my acknowledgement for providing the licenses allowing the printing and electronic reuse of the papers published under the scope of this research.

To my close friends for their support and camaraderie.

Finally, my deep appreciation goes to my family, to my mother, Olga, to my father, Bernardino, to my sister, Ângela, to my dog Jonas, for the patience and support. Last but not least, I would like to express my profound appreciation to Susana, for your daily personal support.

## Acknowledgements

# Abstract

---

Friction stir based technologies (FSBT), such as friction stir welding (FSW) and friction stir processing (FSP), are assumed as environment-friendly techniques for the joining/mechanical enhancement of several materials. However, in spite FSW and FSP have already been explored in important sectors of the transportation industry and in research, an exact knowledge of the thermo-mechanical conditions developed during welding/processing is still missing. There is no systematic information on the contact conditions between the FSW/P tool and the materials being processed and its relationship with process parameters and base materials mechanical, microstructural and surface properties, which difficult the control of the heat generation and plastic deformation during welding/processing.

FSBT are widely used for welding/processing heat treatable and non-heat-treatable aluminium alloys. On the other hand, although steels are the most widely used materials for engineering applications, due to its high melting temperature, the challenges related to the tool design and wear, still limits the welding/processing of these materials by FSBT. In this work, the main stir-based mechanisms, occurring during the FSW and friction stir spot welding (FSSW) processes, of heat treatable (AA2017-T451, AA6082-T651 and AA7075-T651) and non-heat-treatable (AA5083-H111) aluminium alloys, a mild steel (DC01), a high strength steel (HC420 LA), a dual-phase steel (DP600) and three different galvanised steels (DC01-ZE25/25, DX51D-Z140 and DX51D-Z200), were analysed. A thermal and mechanical analysis, which aimed the understanding of the heat generation mechanisms and the tool/workpiece interaction, respectively, was conducted using experiments and numerical simulation.

The experimental welding tests were performed under a diversified range of welding conditions, which enabled to analyse the influence of the tool dimensions, rotational speed, traverse speed, and base material mechanical and surface properties, on the welding/processing mechanisms. In all the welding trials, tungsten carbide pinless tools were used to enable extending the analysis of the heat generation to the welding of ferrous and non-ferrous alloys, avoiding the pin failure, and studying the feasibility of using pinless tools for the joining of thin steel plates. The thermo-mechanical conditions

## Abstract

during welding were assessed by registering the evolution of the welding temperatures and the tool torque and by conducting the mechanical, morphological and microstructural characterization of the welds.

The welding/processing mechanisms were also investigated by creating a database, containing experimental results from the literature, and relating the processing parameters with the process outputs, such as the tool torque and temperature. Additionally, the experimental data was coupled with numerical simulation from a 3D thermo-mechanical model for the FSW/P processes. A parametric finite element analysis on the influence of the processing parameters, tool dimensions and base material plastic properties, on the evolution of the contact conditions, strain rate, material flow, temperature and tool torque was conducted.

The investigation enabled to conclude that the tool dimensions have a very important influence, not only on the heat generation but also on the volume of material being stirred during welding/processing. The tool rotational speed is an important parameter controlling the heat generation and the strain rates experienced in the stirred volume. The only exception was observed for the FSSW of aluminium alloys, where for a constant tool geometry, a threshold in the welding temperatures was registered, which is independent of the rotational speed used. The traverse speed and the base material thickness were also found to be important factors governing the heat dissipation during welding/processing. The data from the experiments and from the numerical simulation were used for developing and calibrating analytical models for the torque and temperature, which were validated by fitting welding/processing data available from previous research works.

The use of pinless tools was also proved to be effective for the lap welding of thin steel plates. When welding with pinless tools, no material stirring across the lap interface takes place, which enables producing lap welds with no hooking or cold lap defects, and in this way, good mechanical strength, even for very high traverse speeds, in linear welding, or using very short process cycle times, in spot welding.

**Keywords:** Friction Stir Based Technologies; Friction Stir Welding; Thermo-mechanical conditions; Modelling.

# Resumo

---

As técnicas *friction stir welding* (FSW) e *friction stir processing* (FSP), são técnicas amigas do ambiente utilizadas para a soldadura/processamento de diversos materiais. Neste sentido, apesar dos processos de FSW e FSP já terem sido analisados em setores da indústria de transportes e em diversos trabalhos científicos, ainda não há um conhecimento exato das condições termomecânicas desenvolvidas durante o processo de soldadura/processamento, uma vez que as condições de contacto entre a ferramenta e os materiais processados não são ainda totalmente compreendidas, nem a sua relação com os parâmetros de processo e com as transformações mecânicas, microestruturais e superficiais dos materiais de base, o que dificulta o controlo da geração de calor e da deformação plástica durante o processo de soldadura/processamento.

As referidas técnicas são amplamente utilizadas para soldar/processar ligas de alumínio tratáveis termicamente e não tratáveis termicamente. Por outro lado, embora os aços sejam muito utilizados em aplicações de engenharia, o desgaste da ferramenta é uma importante limitação para a soldadura/processamento desses materiais. Nesse sentido, neste trabalho os principais mecanismos térmicos e mecânicos, que ocorrem durante a soldadura/processamento em ligas de alumínio tratáveis (AA2017-T451, AA6082-T651 e AA7075-T651) e não tratáveis (AA5083-H111) termicamente, aço macio (DC01), aço de elevada resistência (HC420 LA), aço bifásico (DP600) e em três aços galvanizados (DC01-ZE25/25, DX51D-Z140 e DX51D-Z200) foram analisados através da realização de diversos ensaios experimentais e simulação numérica.

Foi testada uma gama alargada de condições de soldadura o que permitiu analisar a influência das dimensões da ferramenta, da velocidade de rotação e avanço e das propriedades do material de base nas condições termomecânicas do processo. Em todos os ensaios realizados, foram utilizadas ferramentas sem pino de forma a permitir alargar a análise da geração de calor em ligas ferrosas e não ferrosas, evitando o colapso do pino, e estudar a viabilidade de utilizar ferramentas sem pino para produzir soldaduras em aço. Para avaliar as condições termomecânicas durante o processo de soldadura foi registada a evolução das temperaturas e do binário da ferramenta e realizada a caracterização mecânica, morfológica e microestrutural das soldaduras produzidas.

## Resumo

Os mecanismos de soldadura/processamento foram também investigados através da criação de uma base de dados com resultados experimentais da literatura, relacionando os parâmetros operatórios com o binário e a temperatura. Adicionalmente, os dados experimentais foram complementados através da análise numérica de um modelo termomecânico 3D dos processos FSW/P. Foi realizada uma análise paramétrica sobre a influência dos parâmetros de processo, dimensões da ferramenta e propriedades plásticas do material de base na evolução das condições de contacto, taxa de deformação plástica, transporte de material, temperatura e binário da ferramenta.

A investigação realizada permitiu concluir que as dimensões da ferramenta têm uma influência muito importante, não só na geração de calor, mas também no volume de material processado, enquanto que a velocidade de rotação governa a geração de calor e a taxa de deformação plástica. A única exceção foi observada para as soldaduras por pontos de ligas de alumínio, onde para uma ferramenta com geometria constante, atingiu-se um limite na geração de calor, independente da velocidade de rotação utilizada. A velocidade de avanço e a espessura do material de base são também fatores importantes que governam a dissipação de calor durante o processo de soldadura/processamento.

Os dados experimentais e numéricos foram também utilizados para o desenvolvimento e a calibração de modelos analíticos, capazes de prever a evolução do binário e da temperatura com os diversos parâmetros operatórios do processo.

Por fim, o estudo efetuado permitiu concluir que é possível utilizar ferramentas sem pino para produzir soldaduras em aço em junta sobreposta com excelente qualidade. Para ferramentas sem pino, não ocorre mistura do material ao longo da espessura das chapas a soldar, o que permitiu a produção de soldaduras sem a formação de defeitos e com boa resistência mecânica, mesmo para velocidades de avanço muito elevadas ou tempos de ciclo de soldadura curtos para soldadura por pontos.

**Palavras-chave:** *Friction Stir Based Technologies; Friction Stir Welding; Condições termomecânicas; Modelação.*



# Contents

---

Contents.....	vii
List of Figures.....	ix
List of Tables.....	xv
Acronyms and Symbols .....	xvii
1. Introduction.....	1
1.1. Objectives .....	6
1.2. Reading guide .....	7
2. Materials and Methods .....	9
2.1. Base materials .....	9
2.2. Experimental procedures .....	11
2.3. Numerical modelling.....	16
2.3.1. Modelling of the contact conditions .....	20
3. Thermal Analysis .....	27
3.1. Literature review .....	27
3.2. Temperature measurements .....	34
3.2.1. Spot welding of aluminium alloys .....	35
3.2.2. Spot welding of steels .....	39
3.2.3. Linear welding of aluminium alloys .....	41
3.3. Modelling the welding temperature .....	44
3.3.1. Linear welding .....	44
3.3.2. Spot welding .....	47
4. Mechanical Analysis .....	51
4.1. Literature review .....	51
4.1.1. Transport of material.....	51
4.1.2. Contact conditions .....	55

## Contents

4.1.3.	Strain rates .....	57
4.1.4.	Welding torque .....	61
4.2.	Numerical analysis of the stir mechanisms .....	68
4.3.	Assessment of the welding torque .....	73
4.3.1.	Linear welding .....	73
4.3.2.	Spot welding .....	76
4.4.	Modelling the welding torque .....	79
4.4.1.	Linear welding .....	79
4.4.2.	Spot welding .....	82
5.	Process Assessment .....	85
5.1.	Literature review .....	85
5.1.	Linear welding .....	88
5.1.1.	Analysis of the bonding mechanisms .....	89
5.1.2.	Morphological analysis .....	91
5.1.3.	Mechanical characterisation .....	99
5.2.	Spot welding .....	101
5.2.1.	Analysis of the bonding mechanisms .....	102
5.2.2.	Mechanical characterisation .....	103
5.2.3.	Analysis of the thermo-mechanical conditions .....	105
6.	Conclusions and Future Work .....	109
6.1.	Conclusions .....	109
6.2.	Future work suggestions .....	111
7.	References .....	113
	Appendix A .....	131
	Appendix B .....	149
	Appendix C .....	165
	Appendix D .....	191
	Appendix E .....	221

# List of Figures

---

<b>Figure 1</b> - Schematic representation of the friction stir based process. ....	3
<b>Figure 2</b> - Tool geometry and different microstructural zones. ....	3
<b>Figure 3</b> - Aluminium alloys and their properties: yield strength ( $\sigma_y$ ), ultimate tensile strength (UTS), hardness ( $HV_{0.2}$ ) and thermal conductivity (k). ....	10
<b>Figure 4</b> - Steels and their properties: ultimate tensile strength (UTS), hardness ( $HV_{0.2}$ ), galvanised coating thickness (CTh), carbon content ( $C_{eq}$ ) and grain size (GS) (adapted from “Article E”). ....	11
<b>Figure 5</b> – Tool geometry and designation (adapted from “Article A”). ....	12
<b>Figure 6</b> – Schematic representation of the experimental work conducted. ....	14
<b>Figure 7</b> - Schematic representation of the shear tension sample (a), and of the advancing (b) and retreating (c) side lap shear specimens. ....	16
<b>Figure 8</b> - Finite element model and respective sub-domains: Eulerian workpiece (a), ALE stirring zone (b) and Lagrangian tool (c) (adapted from “Article D”). ....	18
<b>Figure 9</b> - Stress-strain rate curves at a constant temperature of 25 °C (a) and 550 °C (b), and stress-temperature curves at a constant strain rate of 100 s <sup>-1</sup> (c) (adapted from “Article D”). ....	20
<b>Figure 10</b> - Evolution of the base material velocity at the tool/workpiece interface (a and b) and of the sticking fraction (c and d) with the welding time (adapted from “Article D”). ....	22
<b>Figure 11</b> - Evolution of the average sticking fraction with a(T) (a) and the rotational speed (b) (adapted from “Article D”). ....	23
<b>Figure 12</b> - Comparison between the AA6082-T6 weld cross section, with the streamlines, temperature and strain rate fields obtained through numerical simulation (adapted from “Article D”). ....	24
<b>Figure 13</b> - Microstructure and grain size distribution in the weld nugget (adapted from “Article D”). ....	26

## List of Figures

<b>Figure 14</b> - Range of rotational speeds ( $\omega$ ), traverse speeds ( $v$ ), shoulder diameters ( $D_s$ ), pin diameters ( $D_p$ ), pin lengths ( $p_l$ ), geometry parameters ( $G$ ) and temperature ( $T$ ) values covered by the database.....	29
<b>Figure 15</b> - Evolution of the temperature with the rotational speed (a), traverse speed (b) and tool dimensions (c) for the experimental works considered in the database.....	31
<b>Figure 16</b> - Schematic representation of the thermal analysis performed in current work. ....	35
<b>Figure 17</b> – Weld thermal cycle, represented by a blue line, and instantaneous temperature derivative in order of time ( $dT/dt$ ), represented by a black line, for the weld produced in AA7075 aluminium alloy, with the PL16 tool and a rotational speed of 660 rpm. ....	36
<b>Figure 18</b> – Evolution of the stabilized temperature values with the rotational speed and geometry parameter, for the AA2017 (a), AA5083 (b), AA6082 (c) and AA7075 (d) aluminium alloys.....	37
<b>Figure 19</b> – Hardness profiles for the welds produced in the AA6082 aluminium alloy with a constant rotational speed of 870 rpm and varied tool diameters between 10 to 18 mm (a), with a constant tool diameter of 12 mm, and varied rotational speed between 660 to 1500 rpm and (c) with the WC uncoated tool and the WC tools coated with the CrAlN, CrAlAgN and CrAlN/TiAlN films.....	39
<b>Figure 20</b> – Evolution of temperature with the rotational speed and tool dimensions for the DC (a), HC (b) and DP (c) steels. ....	40
<b>Figure 21</b> – Numerical results concerning the evolution of the temperature with the rotational speed and geometry parameter (a) and with the traverse speed and plate thickness (b). The points marked in black correspond to the welding temperatures registered for the spot welds produced with the PL18 tool in the AA6082 aluminium alloy.....	42
<b>Figure 22</b> – Numerical results concerning the evolution of the temperature with the traverse speed multiplied by the plates thickness ( $vt$ ), when heat dissipative effects are minimized (red squares) and maximized (black circles) (adapted from “Article C”). ...	44
<b>Figure 23</b> – Evolution of the welding temperatures, obtained in the numerical simulation, with the temperature coefficient $C_T$ (adapted from “Article C”). ....	45
<b>Figure 24</b> – Comparison between the experimental temperature values, from the database, with the temperature values calculated with Eq. 18 (adapted from “Article C”)......	46

<b>Figure 25</b> –Evolution of welding temperature with the $C_{T,SW}$ coefficient for the AA2017, AA5083, AA6082 and AA7075 aluminium alloys. ....	48
<b>Figure 26</b> –Evolution of welding temperature with the $C_{T,SW}$ coefficient for the DC, HC and DP steels. ....	49
<b>Figure 27</b> - Material flow representation (adapted from [104,105,108])......	52
<b>Figure 28</b> – Shoulder and pin-driven flow zones (adapted from Shah et al. 2018 [111]). .....	53
<b>Figure 29</b> - Range of rotational speeds ( $\omega$ ), traverse speeds ( $v$ ), shoulder diameters ( $D_s$ ), pin diameters ( $p_d$ ), pin lengths ( $p_l$ ), geometry parameters ( $G$ ) and torque ( $M$ ) values covered by the database.....	62
<b>Figure 30</b> – Evolution of the torque experimental values, from the database, with the rotational speed (a), traverse speed (b) and geometry parameter (c) (adapted from “Article C”). ....	63
<b>Figure 31</b> – Evolution of torque with the geometry parameter multiplied by the rotational speed ( $G\omega$ ) (adapted from “Article C”).....	64
<b>Figure 32</b> – Evolution of the welding streamlines and logarithmic equivalent strain rate with the traverse speed (a and b), rotational speed (a, c and d) and tool dimensions (a and e) (adapted from “Article D”). ....	69
<b>Figure 33</b> – Evolution of contact conditions, stirred area and strain rate with the rotational speed and geometry parameter, for a traverse speed of 250 mm/min (a) and 1000 mm/min (b). ....	71
<b>Figure 34</b> – Numerical results concerning the evolution of the welding temperature, contact conditions, stirred area and strain rate with the rotational speed and geometry parameter. ....	71
<b>Figure 35</b> – Evolution of the welding streamlines and logarithmic equivalent strain rate with the base material plastic properties (adapted from “Article D”). ....	73
<b>Figure 36</b> – Numerical results concerning the evolution of the torque with the rotational speed and the geometry parameter (a) and with the traverse speed and plate thickness (b).....	75
<b>Figure 37</b> – Numerical results concerning the evolution of torque with the traverse speed multiplied by the plate thickness ( $vt$ ) when heat dissipative effects are minimized (red squares) and maximized (black circles) (adapted from “Article C”). ....	76
<b>Figure 38</b> – Evolution of torque with time for the weld produced in the AA7075 aluminium alloy, with a tool diameter of 16 mm and a rotational speed of 660 rpm.....	77

## List of Figures

<b>Figure 39</b> – Evolution of the torque values with the rotational speed and geometry parameter, for the AA2017 (a), AA5083 (b), AA6082 (c) and AA7075 (d) aluminium alloys. ....	78
<b>Figure 40</b> – Evolution of the torque values with the rotational speed and geometry parameter, for the DC (a), HC (b) and DP (c) steels.....	78
<b>Figure 41</b> – Evolution of the torque values, obtained in the numerical simulations, with the torque coefficient (adapted from “Article C”). ....	80
<b>Figure 42</b> – Comparison of the experimental torque results, from the database, with the torque values calculated with Eq. 43 (adapted from “Article C”). ....	81
<b>Figure 43</b> – Evolution of torque values with the $C_{M,SW}$ coefficient, for the spot welds produced in AA2017 (a), AA5083 (b), AA6082 (c) and AA7075 (d) aluminium alloys. ....	83
<b>Figure 44</b> – Evolution of torque values with the $C_{M,SW}$ coefficient, for the spot welds produced in DC (a), HC (b) and DP (c) steels.....	84
<b>Figure 45</b> - Experimental works that have reported temperatures measurements in FSW and FSSW of carbon steels (Adapted from “Article B”). ....	86
<b>Figure 46</b> - Schematic representation of the process assessment analysis performed in current work for the linear welds.....	89
<b>Figure 47</b> – Comparison of the cross section (a and b) and material flow (c and d), computed through numerical simulation, of welds produced by pin and pinless tools. .	90
<b>Figure 48</b> – Magnification of the weld microstructure at the top surface (a) and SEM/EDS analysis (b). ....	91
<b>Figure 49</b> – Magnification of the weld microstructure at the plates bonding interface.	91
<b>Figure 50</b> – Cross sections of the welds manufactured at a constant tool rotational and traverse speeds of 1000 rpm and 600 mm/min and varying tool diameters from 10 to 16 mm (adapted from “Article A”).....	93
<b>Figure 51</b> – Cross sections of the welds manufactured with the PL16 tool, at a constant rotational speed of 1000 rpm and varying traverse speeds (adapted from “Article A”).	93
<b>Figure 52</b> – Cross sections of the welds manufactured with the PL16 tool, at a constant traverse speed of 600 mm/min and varying rotational speeds (adapted from “Article A”).....	94
<b>Figure 53</b> – Details of the microstructure at the AS and RS of the weld in Figure 51c (adapted from “Article A”).....	95

<b>Figure 54</b> – Details of the microstructure at the AS and RS of the weld in Figure 51e (adapted from “Article A”).....	95
<b>Figure 55</b> – Details of the microstructure at the AS and RS of the weld in Figure 52d (adapted from “Article A”).....	96
<b>Figure 56</b> – Schematic view of the tool, showing the linear velocities of points in the outer radius of the shoulder, at the advancing (point A) and retreating (point B) sides (adapted from “Article A”).....	98
<b>Figure 57</b> – Evolution of $V_B$ with the traverse speed (a) and rotational speed (b) (adapted from “Article A”).....	98
<b>Figure 58</b> – Evolution of torque values with the weld pitch $v/\omega$ (adapted from “Article A”).....	98
<b>Figure 59</b> – Load-displacement curves (a), strain maps (b–c) and fractured sample (d) for the weld produced with the PL16 tool at 600 mm/min and 1000 rpm (adapted from “Article A”).....	100
<b>Figure 60</b> – Load-displacement curves (a) and fractured sample (b) for the weld produced with the PL16 tool at 1000 mm/min and 1000 rpm (adapted from “Article A”).....	101
<b>Figure 61</b> – Load-displacement curves (a), strain maps (b–c) and fractured sample (d) for the weld produced with the PL16 tool at 600 mm/min and 1400 rpm (adapted from “Article A”).....	101
<b>Figure 62</b> - Schematic representation of the process assessment analysis performed in current work for spot welds.....	102
<b>Figure 63</b> – Comparison of the weld cross section (a) and strain rate map (b) for the spot weld produced in the DC steel with a rotational speed of 1140 rpm and with a tool diameter of 12 mm (adapted from “Article E”).....	103
<b>Figure 64</b> – Magnification of the weld microstructure at the plates bonding interface (adapted from “Article E”).....	103
<b>Figure 65</b> – Influence of the rotational speed, shoulder diameter, welding time and galvanised coating thickness on the shear tensile load of the welded joints (adapted from “Article E”).....	105
<b>Figure 66</b> – Thermal cycles for the welds produced in the steels DC, DCR2.5, DXR10 and DXR14, with the PL12 tool and a rotational speed of 870 rpm (a) and 1500rpm (b) (adapted from “Article B”).....	106

## List of Figures

**Figure 67** – Comparison between the welding temperatures, obtained through numerical simulation, for different levels of friction (a), with the welding thermal cycles for the DC and DXR14 welds (b), produced with the PL12 tool at 870 rpm. Velocity profiles, along the weld cross section, for different levels of friction (c–e) (adapted from “Article E”)..... 108



# List of Tables

---

<b>Table 1</b> – Friction stir based technologies. ....	1
<b>Table 2</b> – Published articles in the scope of the current work. ....	8
<b>Table 3</b> – Chemical composition, mechanical properties and thickness of the coatings. .....	12
<b>Table 4</b> – Welding parameters used in the experimental trial number 1: sensitivity analysis of the base materials characteristics, tool geometry and rotational speed on the welding thermo-mechanical conditions. ....	15
<b>Table 5</b> – Welding parameters used in the experimental trial number 2: sensitivity analysis of the tool material on the welding thermo-mechanical conditions. ....	15
<b>Table 6</b> – Welding parameters used in the experimental trial number 3: sensitivity analysis on the suitability of using of pinless tools to produce steel spot welds.....	15
<b>Table 7</b> – Welding parameters used in the experimental trial number 4: sensitivity analysis on the suitability of using pinless tools to produce linear lap welds of galvanised steels. ....	16
<b>Table 8</b> – Evolution of the $\mu$ and $m$ values with temperature, for the AA6063-T6 aluminium alloy [48] and AISI 1018 mild steel [49].....	18
<b>Table 9</b> – Thermo-mechanical formulation of the numerical model (adapted from [48]). .....	19
<b>Table 10</b> – Experimental works that analyse the influence of the processing parameters on the welding thermal cycles registered during the FSSW and FSW processes of aluminium alloys.....	28
<b>Table 11</b> – Range of strain rates reported in the literature (adapted from “Article D”).	60
<b>Table 12</b> – Experimental works that analyse the influence of the processing parameters on torque during FSW of aluminium alloys (Adapted from “Article C”). ....	62
<b>Table 13</b> – Base material thicknesses, shoulder diameters, pin diameters and geometry parameters used in the numerical simulations.....	69
<b>Table 14</b> – Constants for the torque models, calculated using the experimental results from the database. ....	82

## List of Tables

# Acronyms and Symbols

---

$\dot{\epsilon}$	– Strain rate
$A$	– Base material constitutive constant
$a$	– Torque model constant
$a(T)$	– Consistency parameter
ALE	– Arbitrary Lagrangian-Eulerian
$A_M$	– Torque model constant
APR	– Advance per revolution
As	– Advancing side
$A_{sh}$	– Cross sectional area of the shoulder
$a_z$	– Base material constant
$b$	– Torque model constant
$b_b$	– Body forces vector per unit of mass
BM	– Base material
$b_z$	– Base material constant
$c$	– Specific heat
$C_{eq}$	– Carbon content
$C_M$	– Torque coefficient for linear welding
$C_{M,SW}$	– Torque coefficient for spot welding
$C_T$	– Temperature coefficient for linear welding
$C_{T,CR}$	– Critical Temperature coefficient for linear welding
$C_{T,SW}$	– Temperature coefficient for spot welding
$C_{T,SW,CR}$	– Critical Temperature coefficient for spot welding
$CTh$	– Galvanised coating thickness
$d_g$	– Recrystallized grain size
DIC	– Digital Image Correlation
$D_{mesh}$	– Viscoplastic dissipation
$D_p$	– Pin diameter
$D_s$	– Shoulder diameter
$d_z$	– Plunge depth

## Acronyms and Symbols

FMB – Friction melt bonding

FSB – Friction stir brazing

FSBT – Friction stir based technologies

FSLW – Friction stir lap welding

FSP – Friction stir processing

FSW – Friction stir welding

FW – Friction welding

$F_x$  – Tool longitudinal force

$F_z$  – Axial force

$G$  – Geometry parameter

$GS$  – Grain size

HAZ – Heated affected zone

$h_{cond}$  – Heat transfer coefficient by conduction

$h_{conv}$  – Heat transfer coefficient by convection

$h_d$  – Depth of the dynamically recrystallised zone

HSHSRS – High strength materials with high strain rate sensitivity

HLSRS – High strength materials with low strain rate sensitivity

$HV_{0.2}$  – Hardness

JIF – Journal impact factor

$k$  – Thermal conductivity

$K(T)$  – Temperature dependent material consistency

$K_0$  – Modified Bessel function of the second kind and zero order

$K_M$  – Torque model constant for linear welding

$K_{M,SW}$  – Torque model constant for spot welding

$K_T$  – Temperature model constant for linear welding

$K_{T,SW}$  – Temperature model constant for spot welding

LSHSRS – Low strength materials, with high strain rate sensitivity

LSRS – Low strength materials, with low strain rate sensitivity

$m$  – Strain rate sensitivity parameter

$M$  – Torque

$M_0$  – Minimum torque value

$M_f$  – Torque pre-exponential parameter

$M_{slipping}$  – Torque for full slipping contact conditions

$M_{sticking}$  – Torque for full sticking contact conditions

- $n$  – Base material constitutive constant
- $n_M$  – Torque decay parameter
- $P$  – Contact axial pressure
- $p$  – Pressure field
- PAZ – Process affected zone
- $p_l$  – Pin length
- $Q$  – Power
- $q$  – Sensitivity parameter to the sliding velocity
- $Q^*$  – Non-dimensional heat input
- $q_{cond}$  – Heat through conduction
- $q_{conv}$  – Heat through convection
- $Q_E$  – Activation energy
- $Q_{eff}$  – Power transfer efficiency coefficient
- $r$  – Radial distance from the centre of the tool
- $R$  – Universal gas constant
- $R^2$  – Pearson correlation coefficient
- $r_d$  – Radius of the dynamically recrystallised zone
- $r_m$  – Average of the pin and shoulder radius
- $r_p$  – Tool pin radius
- $R_s$  – Retreating side
- $r_s$  – Tool shoulder radius
- $s$  – Stress deviator
- SEM/EDS – Scanning electron microscopy/energy-dispersive spectroscopy
- $t$  – Plate thickness
- $T$  – Temperature
- $T^*$  – Non-dimensional temperature
- $T_0$  – Temperature at the interface between the shear layer and the base material
- TAFW – Tool Assisted Friction Welding
- $T_{CT}$  – Temperature threshold
- $T_{env}$  – Environmental temperature
- $t_i$  – Time
- $T_{in}$  – Initial temperature
- $T_{max}$  – Maximum temperature
- TMAZ – Thermomechanically Affected Zone

## Acronyms and Symbols

$T_s$  – Solidus temperature

$T_{st}$  – Temperature in the stirring zone

$T_{tool}$  – Tool temperature

UTS – Ultimate tensile strength

$V$  – difference between the linear advancing and the rotational speeds ( $v_v - v_\omega$ )

$v$  – Traverse speed

$v_{BM}$  – Base material velocity at the tool/workpiece interface

$v_f$  – Velocity field

$v_{mesh}$  – Velocity of the mesh

$v_{tool}$  – Tool velocity

$v_v$  – linear velocities associated with the tool advancing movement

$v_\omega$  – linear velocities associated with the tool rotational movement

$w$  – Shear layer width

$x$  – Perpendicular distance to the welding direction from the tool retreating side

$Z$  – Zener-Hollomon parameter

$\alpha_f$  – Friction coefficient used in the Norton's friction law

$\alpha_M$  – Torque model constant

$\alpha_T$  – Temperature model constant

$\alpha_t$  – Tilt angle

$\alpha_{TT}$  – Temperature model constant

$\beta_M$  – Torque model constant

$\beta_s$  – Shoulder cone angle

$\beta_{sh}$  – Base material constitutive constant

$\beta_T$  – Temperature model constant

$\beta_{TT}$  – Temperature model constant

$\delta$  – Sticking fraction

$\delta_0$  – Slipping constant

$\delta_{avg}$  – Average sticking fraction along the tool/workpiece interface

$\delta_s$  – Slipping fraction

$\Delta v_s$  - Relative sliding velocity

$\varepsilon$  – Strain

$\eta$  – Process efficiency

$\theta$  – Fraction of plastic dissipation

$\lambda_M$  – Torque model constant

$\lambda_T$  – Temperature model constant

$\mu$  – Viscosity parameter

$\mu_f$  – Friction coefficient

$\rho$  – Material Density

$\sigma_8$  – Yield stress of the material at 80% of  $T_s$

$\sigma_{eq}$  – Equivalent stress

$\sigma_y$  – Material yield strength

$\tau$  – Shear stress

$\tau_f$  – Shear stress due to the slipping contact condition

$\tau_p$  – Stress due to the sticking contact condition

$\phi$  – Ratio of heat transported between the tool and the workpiece

$\varphi$  – Temperature model constant for linear welding

$\varphi_{sw}$  – Temperature model constant for spot welding

$\omega$  – Rotational speed

$\omega_0$  – Reference tool rotational speed

$\omega_{crit}$  – Critical rotational speed

$\xi$  – Speed up factor

## Acronyms and Symbols



# 1. Introduction

---

The friction stir based technologies (FSBT) are a family of solid-state processing techniques used for the joining and/or mechanical enhancement of metallic materials. These techniques are labelled “stir based” since it were derived from the friction stir welding (FSW) and friction stir processing (FSP) technologies, envisaging diversified industrial applications. In Table 1 are listed some of the FSBT developed up to date. Since all the stir-based techniques are based in the same operating procedures of the FSW process and display similar thermo-mechanical conditions, in some parts of the document, instead of referring to FSBT, it will be only written FSW. However, it is important to enhance that all the conclusions and modelling assumptions, assumed in current work, are valid for all the welding and processing variants of the FSW technology.

**Table 1** – Friction stir based technologies.

<i>FSBT</i>	<i>Application</i>		<i>Variants</i>
<i>Friction stir welding</i> [1]	<i>Joining</i>	<i>linear</i>	<i>Friction melt bonding process</i> [2] <i>Pulsed friction stir welding</i> [3] <i>Tool assisted friction stir welding</i> [4] <i>Friction stir soldering</i> [5]
		<i>spot</i>	<i>Friction stir spot welding</i> [6] <i>Friction stir riveting</i> [7] <i>Friction bit joining</i> [8] <i>Friction stir spot brazing</i> [9]
<i>Friction stir processing</i> [10]	<i>Mechanical enhancement</i>		<i>Friction stir surfacing</i> [11] <i>Friction stir channelling</i> [12] <i>Friction stir texturing</i> [13] <i>Friction stir consolidation</i> [14]

As schematised in Figure 1, the stir-based technologies make use of a rotating non-consumable tool, which is subjected to an axial force and linear motion, during materials processing [15]. The tool rotation and translation motions promote, not only, the heating by friction of the materials to be joined/processed, but also its plastic deformation under complex loading conditions and very high strain rates. The material stirring is so complex that the flow of the material is usually described as a combination of forging and extrusion [16]. In Figure 2 is shown the standard geometry of a tool, which typically consists of a

## Introduction

round shoulder and a pin [17]. The pin is usually classified according to the geometry, such as cylindrical, conical or faceted, and may also be threaded, flat or grooved [17]. Like the pin, the shoulder may also have diversified configurations. Some of the most common are the conical, concave, convex and flat, with or without concentric rings. According to Threadgill et al. 2009 [18], the shoulder is the tool component responsible for the heat generation, due to the friction with the surface of the workpiece. The primary function of the pin, on the other hand, is to promote the material flow throughout the thickness of the workpiece, due to the combined action of its rotational and translational movements [15]. The axial force and the tool plunge depth are the process parameters responsible for ensuring the contact between the tool and the base material. The tool tilt angle, which corresponds to the angle between the axis of rotation and the welding perpendicular direction, also contributes in controlling the tool forging action and, consequently, the material flow around the tool.

Typically, the stir-based technologies can be operated in position control or force control. Position control consists in plunging the tool in the material to be welded/processed, to a predetermined depth, while force control consists in plunging the tool until a predetermined axial force is reached. As shown in Figure 1, in FSW, the main process parameters are the tool geometry, the rotational speed ( $\omega$ ), the traverse speed ( $v$ ), the tilt angle ( $\alpha_t$ ) and the tool axial force ( $F_z$ ), in force control, or the tool plunge depth ( $d_z$ ), in position control. According to the literature, the tool rotational and traverse speeds are important process parameters since they control the heat input and the material flow during welding, and consequently, the final properties of the processed materials. Also, due to the simultaneous rotation and linear motions of the tool, the material flow is not symmetrical around the tool axis, being possible to identify two opposite sides in each stir welded/processed operation: the advancing (AS) and the retreating (RS) sides. The advancing side is the side of the tool where the rotational direction is the same as the traverse direction, while the retreating side corresponds to the side of the tool where the tool rotation is opposite to the tool travel direction.

A complementary process, to FSW, is the friction stir spot welding (FSSW) technology, whose main difference, relative to the linear FSW, is that the advancing displacement of the tool does not exist. In FSSW, the tool is plunged into the base material, until a desired plunging depth is reached. A dwell stage begins after the plunge depth is achieved, during which the tool remains in contact with the upper plate surface, heating and stirring the base materials, until the tool removal. Usually, since the weld

processing time only lasts a few seconds, FSSW can be considered a transient process because of the short thermal cycles.

The materials stirred by any of the FSBT are composed of several regions, with different microstructures, as schematized in Figure 2. In the figure, the region identified as Base Material (BM), represents the portion of material which is not affected by the heat or plastic deformation induced by the process. The Heat Affected Zone (HAZ) represents the portion of material which did not undergo any plastic deformation during welding, but it was subjected to thermal cycles which induced microstructural changes on it. The Thermomechanical Affected Zone (TMAZ) represents the portion of material which, simultaneously, experienced plastic deformation and high temperatures, during processing. Inside this region, the Nugget, represents the part of the TMAZ which underwent the highest temperatures and the most intense plastic deformation, gathering optimum conditions for the occurrence of dynamic recrystallisation.

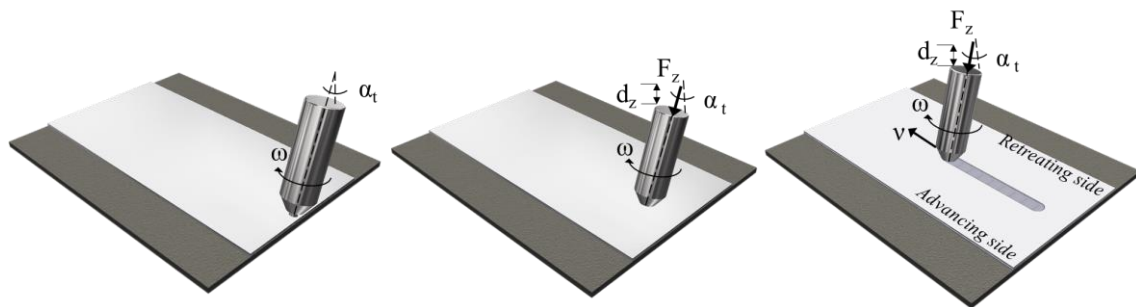


**Figure 1** - Schematic representation of the friction stir based process.

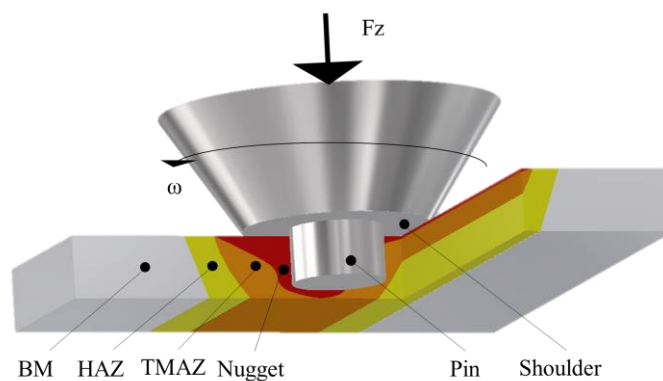


**Figure 2** - Tool geometry and different microstructural zones.

In stir-based technologies, both the heat generation and the material flow, are determined by the process parameters, the tool geometry and the base material properties,

## Introduction

which in turn, determine the thermo-mechanical conditions developed during welding. The suitability of the FSW technology to weld materials such as aluminium alloys [18–20], steels [21,22], magnesium alloys [23,24], titanium alloys [25], polymers [26–28], among others, was already proved. However, despite the large number of practical applications and research studies on FSW and other stir-based technologies, there is still an important gap in which concerns to the knowledge of the fundamental mechanisms taking place during welding. Due to the absence of accurate models of the FSW thermo-mechanisms, any new process development is planned based on trial-and-error experiments.

The uncertainties relative to the thermo-mechanisms governing the friction stir based processes include the characterization of the contact conditions, between the tool and the workpiece, the understanding of the mechanisms governing the heat generation and the characterization of the material flow and the way it is determined by the mechanical properties of the base materials. The analysis of this former aspect is especially complex, since information on the mechanical behaviour of metallic materials, at the temperatures and strain rates imposed by the stir-based technologies, is almost inexistent in the literature. The lack of data results from the difficulty in reproducing the complex loading conditions imposed by the welding tool on the base materials, using current laboratory apparatus.

In addition to the above-described problems, it is also important to enhance that the analytical models available in the literature for predicting the temperature and torque, which are process outputs related to the thermal and mechanical energies associated with the process, were developed considering a very narrow ranges of process parameters and most of it lack experimental validation. Also, most of the models formulations are complex, requiring difficult to determine variables, such as the contact conditions, the friction coefficient and/or base material properties under the thermo-mechanical conditions imposed by the FSW process [29]. So, developing reliable and efficient models, enabling to determine the torque and temperature, based on process parameters, is still required. Such models would enable predicting and controlling the welding temperature, which is useful for avoiding the formation of defects due to inadequate material flow, for optimizing welds properties, such as microstructure and strength, as well for limiting the heat input in the structure, allowing to minimize residual stresses and distortions. Predicting the torque and temperature, according to the base material and

process parameters, is also useful for developing real time process control strategies, a main requirement of Industry 4.0 [30–33].

In the investigation performed under this dissertation, a thermal and mechanical analysis of two stir-based technologies, the FSW and FSSW processes, was performed. The thermal and mechanical analysis, which aimed the understanding of the heat generation mechanisms and the tool/workpiece interaction, respectively, was developed by performing a coupled experimental and numerical investigation, for two base material families: ferrous and aluminium alloys.

The experimental plan considered the execution of a large number of bead-on-plate spot welds in aluminium alloys, as well as performing spot and linear lap welding of several steels. The aluminium alloys used in the investigation were the AA2017-T451, AA5083-H111, AA6082-T651 and AA7075-T651 alloys. The steels tested were the DC01, HC420 LA and DP600 non-galvanised steels and the DC01-ZE25/25, DX51D-Z140, DX51D-Z200 galvanised steels. A wide range of welding conditions were tested for all the base materials and, for all the welding trials, tungsten carbide pinless tools, with different diameters, were used. The use of these type of tools enabled, not only, performing an analysis of the heat generation and torque evolution, with process parameters, for the ferrous and non-ferrous alloys, but also, to study the suitability of the pinless tools to be used for the joining of thin steel plates, which is an almost unexplored subject in the literature. To accomplish this last objective, a deep morphological and mechanical characterization of spot and linear lap steel welds, produced under a very diversified range of tool diameters and rotational and traverse speeds, was also performed. In this analysis, special attention was put in characterizing the influence of the galvanised coating on the thermo-mechanical conditions developed during welding, and in this way, on the welds properties.

In addition to the experimental tests, to enable a clear understanding of the phenomena governing the evolution of the welding temperature and torque during the FSW and FSSW of aluminium alloys, a database with a broad range of experimental results, from the literature, was generated. The experimental results, obtained under the scope of current dissertation, and the literature data, were coupled with the results of a numerical simulation analysis, performed using COMET, a FSW dedicated software, developed by CIMNE. Analytical models, which enable calculating the torque and the temperature in the spot and linear welding of ferrous and non/ferrous alloys, were

developed and validated. The numerical analysis was also used for explaining some aspects of the heat generation in the spot welding of galvanised steel plates.

### *1.1. Objectives*

The objectives of current work were, in first, to understand the thermo-mechanical phenomena governing the heat generation and the torque evolution in stir-based techniques, in second, to establish analytical models that can be used to optimise and guide the industrial implementation of these techniques, and in third, to assess the suitability of using pinless tools in the spot and linear welding of very thin steel plates. In order to reach these objectives, the following tasks were performed:

- **Thermal Analysis**

Temperature measurements were carried out when performing bead-on-plate spot welding of aluminium alloys, and linear and spot welding of steels, under a very diversified range of processing conditions. A database with temperature and process parameters, collected from the literature, was generated. The information of the database was used for establishing the process parameters window to be tested in the numerical simulation analysis, performed with COMET software, as well as for validating the models developed under the scope of the dissertation. The models developed, using the coupled experimental-numerical analysis, enable determining the temperature, from process parameters, in FSW and FSSW of aluminium alloys and steels.

- **Mechanical analysis**

Torque measurements were performed in the same tests carried out for assessing the thermal cycles and data on the torque evolution with process parameters was collected from the literature. The evolution of the contact conditions, between the tool and the workpiece, with process parameters, was analysed using numerical simulation. In the same way, the strain rates experienced by the base materials were assessed using numerical simulation and the main processing parameters governing it were determined. As for the temperature, relationships between the processing parameters, the tool geometry and the tool torque were established and validated.

- **Process assessment**

The phenomena that govern the material flow and the heat generation, as well as the bonding mechanisms, in the spot and linear lap welding of galvanised and non-galvanised steels, with pinless tools, were analysed using experiments and numerical simulation. Microstructural and mechanical characterization of the welds was performed in order to assess the strength and properties of the joints. Process parameters windows were established for the linear and spot lap welding of steels with pinless tools.

## *1.2. Reading guide*

The text of this dissertation was organised to provide a comprehensive synopsis of the overall investigation. In the next chapters, results already published in the form of articles will be complemented with some unpublished data. In Table 2 are listed the articles in which most of the results of the thesis were published. The ID provided in the table, for each article, will be used throughout the text for identifying the published results, whenever they are provided in the form of figures and tables. The thesis is divided into seven chapters, that will be described in the next (except the current Chapter 1, *Introduction*).

In Chapter 2, labelled *Materials and Methods*, are introduced the base materials tested in this work, as well as the testing plan developed with the aim of performing a sensitivity analysis on the thermo-mechanical conditions in stir-based technologies. Details of the fully coupled thermo-mechanical model, implemented in COMET, the software which was used to simulate the FSW and FSSW processes, are also provided.

In Chapter 3, labelled *Thermal Analysis*, the heat generation and dissipation in FSBT is discussed. This chapter includes a state-of-the-art on the subject under analysis, as well as the results obtained in current investigation. Those results are discussed and its original contribution in relation to the current knowledge on FSBT will be highlighted. In this chapter, the results already published in the articles listed in Table 2 are complemented with data still unpublished.

In Chapter 4, labelled *Mechanical Analysis*, it is addressed the mechanical interaction between the tool and the workpiece. The mechanisms governing the transport of material and the contact conditions, in FSBT, are discussed. The strain rates and tool torque are also assessed. As in Chapter 3, first, it is provided a state-of-the-art on the

## Introduction

subject, and then, the results obtained are discussed. Again, the published data is complemented with some unpublished results.

In Chapter 5, labelled *Process Assessment*, are presented the results of the mechanical and microstructural characterization of steel welds, produced using pinless tools. In addition to the analysis of the welds produced, the thermo-mechanical conditions developed during the welding of galvanised and non-galvanised steels will be compared and the bonding mechanism will be identified. Based on this analysis, process parameters windows, for the lap joining of thin steel plates, with pinless tools, will be provided. As in the previous chapters, a state-of-the-art on the subject under analysis will be presented before the discussion of results.

In Chapter 6, labelled *Conclusions and Future Work*, are presented the main conclusions of the thesis and some suggestions for future work.

In Chapter 7, labelled *References*, are listed all the references cited in this work.

Finally, in Appendices A to E, are presented the papers produced within the scope of the dissertation.

**Table 2** – Published articles in the scope of the current work.

<b>Article ID</b>	<b>Title</b>	<b>Journal</b>	<b>Year</b>	<b>JIF (2019)</b>
A	<i>Properties of lap welds in low carbon galvanised steel produced by tool assisted friction welding [34]</i>	<i>Journal of Materials Processing Technology</i>	2018	4.799
B	<i>Influence of base material characteristics and process parameters on frictional heat generation during Friction Stir Spot Welding of steels [35]</i>	<i>Journal of Manufacturing Processes</i>	2019	4.229
C	<i>Modelling torque and temperature in friction stir welding of aluminium alloys [36]</i>	<i>International Journal of Mechanical Sciences</i>	2020	4.456
D	<i>Analysis of contact conditions and its influence on strain rate and temperature in Friction Stir Welding [37]</i>	<i>International Journal of Mechanical Sciences</i>	2021	4.456
E	<i>Influence of the galvanized coating thickness and process parameters on heat generation and strength of steel spot welds [38]</i>	<i>Thin-Walled Structures</i>	2021	4.108



## 2. Materials and Methods

---

This chapter, in which are introduced the base materials and methodologies used in the current investigation, is divided in three different parts. In the first part, the base materials used in the investigation are identified and their main properties are described. In the second part, the processing parameters and the tool geometries tested, for the characterization of the thermo-mechanical conditions developed during welding, as well as the laboratory techniques applied for the mechanical and microstructural characterization of the welds, are described. In the third part, the fully coupled thermo-mechanical model used to simulate the FSW and FSSW processes is introduced. The assumptions made for modelling the contact conditions in FSW are also explained and validated in this chapter.

### *2.1. Base materials*

To date, the most common base materials welded/processed using FSBT were the aluminium alloys. So, due to the huge quantity of results and information available, a database collecting experimental results from the literature, regarding the torque and temperature measurements in FSW and FSSW of AA2xxx, AA5xxx, AA6xxx and AA7xxx aluminium alloys, was constructed. An experimental campaign was also conducted, envisaging the analysis of the heat generation in stir-based processes. In that analysis, the heat treatable AA2017-T451, AA6082-T651 and AA7075-T651 aluminium alloys and the non-heat treatable AA5083-H111 aluminium alloy, provided in 10 mm thick plates, were used. By using thick aluminium alloy plates it was intended to fully capture the entire size and morphology of all the process affected zones, which was useful for comparing the thermal and mechanical response of the different alloys.

The aluminium alloys yield strength ( $\sigma_y$ ), ultimate tensile strength (UTS), hardness ( $HV_{0.2}$ ) and thermal conductivity ( $k$ ), at room temperature, are compared in Figure 3. As it is possible to conclude from the figure, all the alloys tested displayed important differences in yield and tensile strength. The thermal conductivity was also similar for the heat-treatable alloys, but 30% lower for the non-heat treatable alloy.

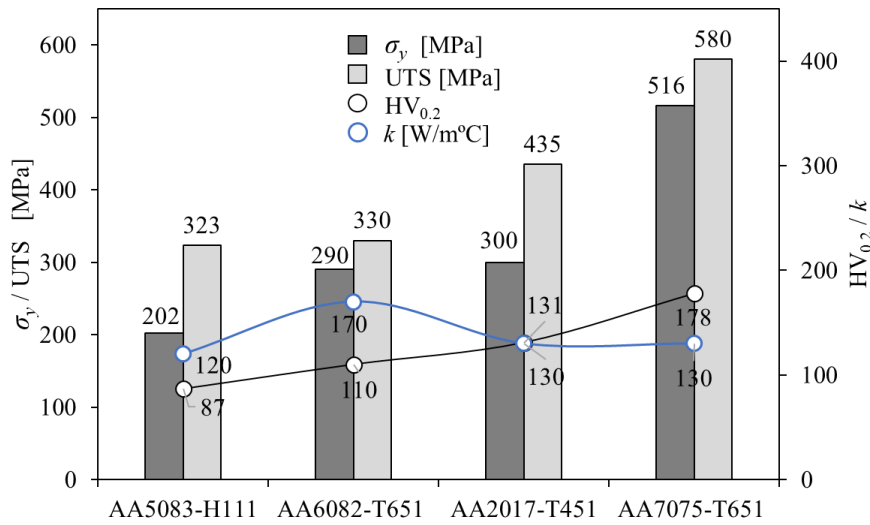


**Figure 3** - Aluminium alloys and their properties: yield strength ( $\sigma_y$ ), ultimate tensile strength (UTS), hardness ( $HV_{0.2}$ ) and thermal conductivity ( $k$ ).

Steels were the other family of base materials considered in this study, due to its enormous potential to be used in the analysis of the thermo-mechanical phenomena in FSW. This potential results from the huge amount of information on the metallurgical and mechanical behaviour of steels at very high temperatures and strain rates. In this work, a dual-phase steel (DP600), a high strength steel (HC420), a mild steel (DC01) and three galvanised steels (DC01-ZE25/25, DX51D-Z140 and DX51D-Z200), all provided in 1 mm thick plates, were used. The ultimate tensile strength, hardness, equivalent carbon content ( $C_{eq}$ ), grain size ( $GS$ ) and galvanised coating thickness ( $CTh$ ) of the different steels tested in the investigation are compared in Figure 4. As it shown in the figure, the DC01, DC01-ZE25/25, DX51D-Z140 and DX51D-Z200 steels had similar chemical composition and mechanical properties, while having different galvanised coating thicknesses. These steels were properly selected to enable the analysis of the galvanised coating thickness on the heat generation during welding. The DP600 and HC420 steels were selected to display important differences in strength and equivalent carbon content, relative to the DC01 steel. Throughout the text, the steels DP600, HC420, DC01, DC01-ZE25/25, DX51D-Z140 and DX51D-Z200 will be labelled as DP, HC, DC, DCR2.5, DXR10 and DXR14, respectively.

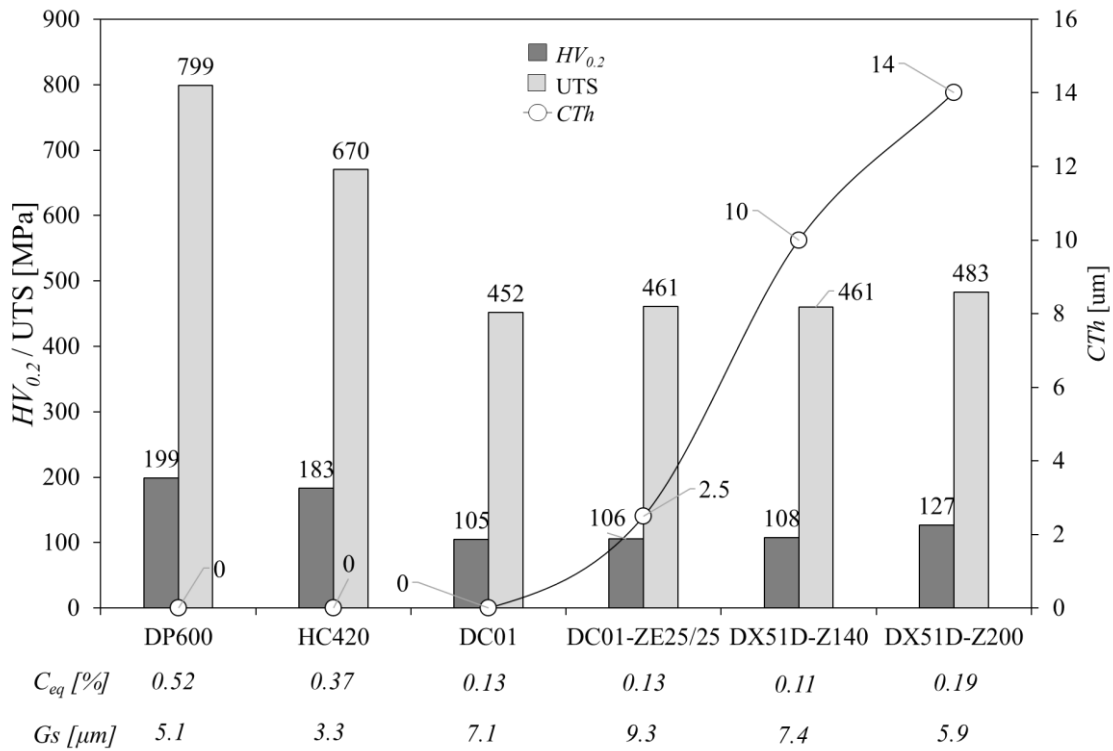
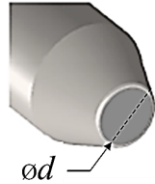


**Figure 4** - Steels and their properties: ultimate tensile strength (UTS), hardness ( $HV_{0.2}$ ), galvanised coating thickness ( $CTh$ ), carbon content ( $C_{eq}$ ) and grain size ( $G_s$ ) (adapted from “Article E”).

## 2.2. Experimental procedures

The welding tests carried out under the scope of this thesis were performed using tungsten carbide (WC) pinless tools, with a flat shoulder, as that schematised in Figure 5. Pinless tools were chosen in order to enable producing aluminium and steel welds, under a varied range of welding conditions, without pin collapse. By excluding the pin from the tool geometry, no important influence on the temperature results was expected, relative to conventional FSW tools, since it was already established, by previous authors, that the tool shoulder has the prominent role on the heat generation during welding. To analyse the influence of the tool dimensions on the heat generation, tools with shoulder diameters of 10, 12, 14, 16 and 18 mm were tested. In the text, the different tools will be labelled according to the tool diameter as PL10, PL12, PL14, PL16 and PL18, respectively.

To analyse the influence of the tool material on the thermo-mechanical conditions developed during welding, uncoated and coated WC tools were tested. Monolithic CrAlN and CrAlAgN coatings, and a multi-layered CrAlN/TiAlN film, were tested for the coated tools. The chemical composition, the mechanical properties and the thickness of the different coatings are displayed in Table 3.



$\varnothing d$	Designation
10 mm	PL10
12 mm	PL12
14 mm	PL14
16 mm	PL16
18mm	PL18

**Figure 5** – Tool geometry and designation (adapted from “Article A”).

**Table 3** – Chemical composition, mechanical properties and thickness of the coatings.

	<i>CrAlN</i>	<i>CrAlAgN</i>	<i>CrAlN/TiAlN</i>
<b>Chemical composition (at.%)</b>	Cr – 36.2 Al – 14.2 N – 49.6	Cr – 30.3 Al – 9.8 Ag – 10.3 N – 49.7	Cr – 24.3 Al – 14.8 Ti – 13.3 N - 47.5
<b>Hardness (GPa)</b>	18	20	20
<b>Young’s Modulus (GPa)</b>	280	251	469
<b>Elastic strain to failure (H/E) parameter</b>	0.064	0.080	0.043
<b>Coating thickness (<math>\mu\text{m}</math>)</b>	2.6	3.1	3.5

To assess the influence of the tool dimensions, of the rotational and the traverse speeds, of the contact conditions and of the base material properties, on the thermo-mechanical conditions developed during welding and on the joints characteristics, in spot and linear welding of the ferrous and non-ferrous alloys, different experiments were conducted, using the apparatus displayed in Figure 6. As shown in the figure, all the welding tests were performed in a *MTS I-STIR PDS* machine, in position control. In the experiments performed, the thermal analysis was conducted by recording the welding temperature fields with a *FLIR A655sc* thermographic camera and analysing it by using the procedures developed under the scope of this thesis, which are described in “Article B”. To perform the mechanical analysis, the instantaneous evolution of the spindle torque was also recorded and analysed. Several welding trials were performed using the parameters represented in Table 4 to Table 7. The different welding trials were conducted with the following objectives:

1. To perform a sensitivity analysis on the influence of base materials characteristics, tool dimensions and rotational speed, on the thermo-mechanical conditions occurring during spot welding. With this objective, spot welds in DC, HC and DP steels and bead-on-plate spot welds in

AA2017, AA5083, AA6082 and AA7075 aluminium alloys, were produced. This analysis was performed by varying the tool diameter and the rotational speed between 10 to 18 mm and 660 to 1500 rpm, respectively. In all the spot welding experiments, a long dwelling period of 60 s was used, to ensure that steady-state conditions were reached until the end of the welding process (Table 4).

2. To analyse the influence of the tool material on the heat generation. This analysis was performed by testing monolithic (CrAlN and CrAlAgN) coatings and a multi-layered coating (CrAlN/TiAlN). The coatings were produced in 12 mm diameter tools and tested in the spot welding of the AA6082 aluminium alloy, using a rotational speed of 660 rpm. The selection of the base material for testing the coated tools was based on previous works from the workgroup [39,40], which showed that this alloy experience intense flow softening during welding, a characteristic favourable for ensuring that the coating was not destroyed/removed during the welding (Table 5).
3. To test the use of pinless tools in the spot welding of steels. Uncoated steel plates and galvanised steel plates, with different coating thicknesses, were used in this study. The influence of the galvanised coating on the heat generation was analysed by producing spot welds in DC, DCR2.5, DXR10 and DXR14 steels with rotational speeds between 870 to 1500 rpm and a constant tool diameter of 12 mm. The influence of the galvanised coating on the welding time was assessed by testing dwelling periods of 5, 15, 30 and 60 s, in the spot welding of the DC and DXR14 steels, i.e. in the uncoated steel and in the steel with the highest coating thickness. In these tests, the rotational speed and the tool diameter were varied between 870 to 1500 rpm and 10 to 16 mm (Table 6).
4. To test the use of pinless tools in the linear lap welding of galvanised steels. The influence of the advancing speed on the thermo-mechanical conditions developed during welding was analysed by performing linear welds in DXR14 steel, i.e. the steel with the highest coating thickness. The tests were

## Materials and Methods

carried out by varying the tool diameter, and the rotational and the traverse speed, from 10 to 16 mm, 600 to 1400 rpm and 200 to 1200 mm/min, respectively (Table 7).

After welding, for the microstructural analysis, metallographic samples were extracted from the welds, polished according to standard procedures, etched and observed/analysed using a *Leica DM 4000M LED* optical microscope and a *CARL ZEISS Merlin* field microscope, for the scanning electron microscopy and energy-dispersive X-ray spectroscopy (SEM/EDS) of the samples.

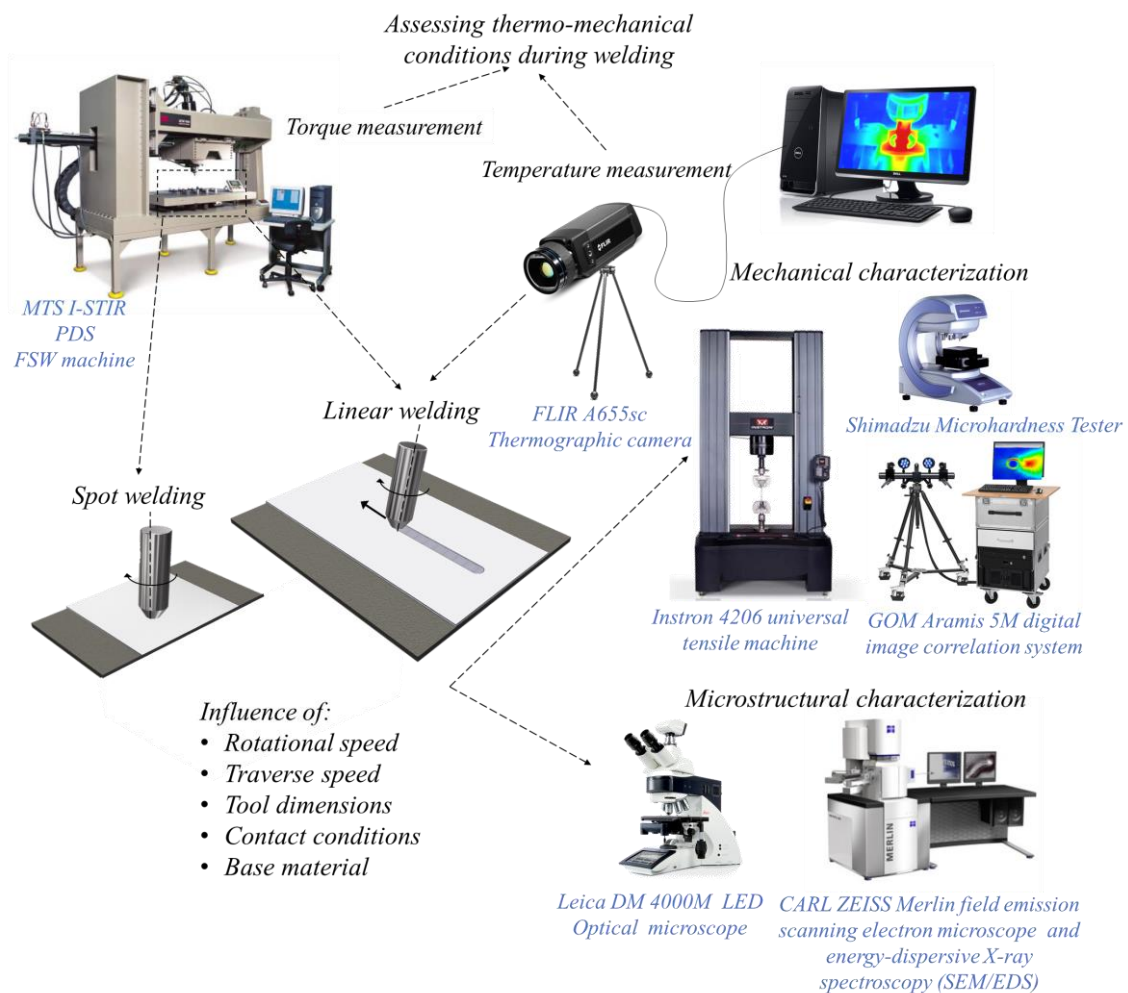


**Figure 6** – Schematic representation of the experimental work conducted.

The strength of the spot and linear steel welds was assessed by performing tensile-shear tests in an *Instron 4206* universal tensile testing machine, operating in quasi-static

loading conditions. For the spot welds, tensile-shear samples were prepared according to Figure 7a. For the linear welds, retreating and advancing side lap shear specimens were prepared as schematised in Figure 7b and c, respectively, and tested according to the procedures described in Costa et al. 2015 [41]. To prevent the bending of the samples during testing, plates with a thickness equal to that of the welded sheets were glued at each end of the shear tension samples. During testing, the *GOM Aramis 5M system* was used for strain data acquisition using Digital Image Correlation (DIC), following the procedures detailed in Leitão et al. [42,43]. Hardness measurements were performed, transverse to the cross section of the welds, using a *Shimadzu Microhardness Tester*, with 200 g load and 15 s holding time.

**Table 4** – Welding parameters used in the experimental trial number 1: sensitivity analysis of the base materials characteristics, tool geometry and rotational speed on the welding thermo-mechanical conditions.

<i>Material</i>	<i>Joint configuration</i>	<i>Plate thickness [mm]</i>	<i>Tool diameter [mm]</i>	<i>Rotational speed [rpm]</i>	<i>Tilt angle [°]</i>	<i>Plunge depth [mm]</i>	<i>Dwell time [s]</i>
DC HC DP	<i>lap joint</i>	1	10 - 16	870 – 1500	0	0.5	60
AA2017 AA5083 AA6082 AA7075	<i>Bead-on-plate</i>	10	10 - 18	660 - 1500	0	0.5	60

**Table 5** – Welding parameters used in the experimental trial number 2: sensitivity analysis of the tool material on the welding thermo-mechanical conditions.

<i>Material</i>	<i>Joint configuration</i>	<i>Plate thickness [mm]</i>	<i>Tool diameter [mm]</i>	<i>Tool material</i>	<i>Rotational speed [rpm]</i>	<i>Tilt angle [°]</i>	<i>Plunge depth [mm]</i>	<i>Dwell time [s]</i>
AA6082	<i>Bead-on-plate</i>	10	12	WC WC+ CrAlN WC+ CrAlAgN WC+ CrAlN/TiAlN	660	0	0.5	60

**Table 6** – Welding parameters used in the experimental trial number 3: sensitivity analysis on the suitability of using of pinless tools to produce steel spot welds.

<i>Material</i>	<i>Joint configuration</i>	<i>Plate thickness [mm]</i>	<i>Tool diameter [mm]</i>	<i>Rotational speed [rpm]</i>	<i>Tilt angle [°]</i>	<i>Plunge depth [mm]</i>	<i>Dwell time [s]</i>
DC DCR2.5 DXR10 DXR14	<i>lap joint</i>	1	10-16	870 - 1500	0	0.5	5-60

**Table 7** – Welding parameters used in the experimental trial number 4: sensitivity analysis on the suitability of using pinless tools to produce linear lap welds of galvanised steels.

<i>Material</i>	<i>Joint configuration</i>	<i>Plate thickness [mm]</i>	<i>Tool diameter [mm]</i>	<i>Rotational speed [rpm]</i>	<i>Tilt angle [°]</i>	<i>Plunge depth [mm]</i>	<i>Advancing speed [mm/min]</i>
<i>DXR14</i>	<i>lap joint</i>	<i>1</i>	<i>10 - 16</i>	<i>600 - 1400</i>	<i>2</i>	<i>0.5</i>	<i>200 – 1200</i>

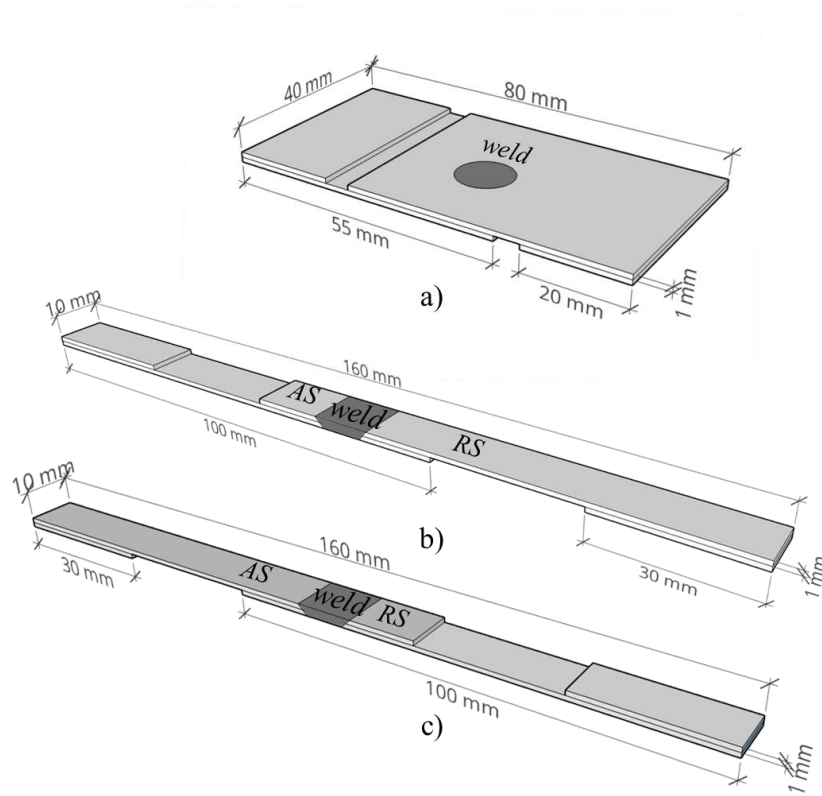


**Figure 7** - Schematic representation of the shear tension sample (a), and of the retreating (b) and advancing (c) side lap shear specimens.

### 2.3. Numerical modelling

The thermo-mechanical conditions in FSW were analysed using COMET software, a 3D thermo-mechanical model proposed by Chiumenti et al. 2013 [44] and Dialami et al. 2013 [45]. As shown in Figure 8, in this numerical model, three different domains, representing the tool, the stir zone and the workpiece, are considered. A Lagrangian formulation is used for modelling the rotating tool, while ALE and Eulerian formulations are used for modelling the stir zone and the rest of the workpiece, respectively.

The Norton’s friction law is used to model the friction at the tool/workpiece interface [46,47]:



$$\tau_f = a(T) \|\Delta v_s\|^{q-1} \Delta v_s. \quad (1)$$

In the previous equation,  $\tau_f$  is the friction shear stress,  $\Delta v_s$  is the relative sliding velocity between the tool and the workpiece,  $q$  is the sensitivity to the sliding velocity and  $a(T)$  is the consistency parameter given by

$$a(T) = -\alpha_f K(T), \quad (2)$$

where  $\alpha_f$  is the friction coefficient and  $K(T)$  is the temperature dependent material consistency. In order to ensure that the mixed contact conditions characteristic of the FSW process were accurately captured by the numerical model,  $a(T)$  values ranging from 50 to 500 MPa, were tested. With this selection, several friction coefficients were assumed, since  $K(T)$  is a material related constant. The sensitivity to the sliding velocity parameter was assumed to be constant ( $q = 0.5$ ) [47].

In COMET, the base material plastic behaviour is modelled by using the Norton-Hoff constitutive model,

$$\sigma_{eq}(\dot{\epsilon}, T) = \sqrt{3} \mu (\sqrt{3} \dot{\epsilon})^m, \quad (3)$$

where  $\sigma_{eq}$  is the equivalent stress,  $\dot{\epsilon}$  is the equivalent strain rate and  $\mu$  and  $m$  are constants that determine the strength and the strain rate sensitivity, respectively, of the base material. The numerical simulations performed considered the base material constitutive properties of the AA6063-T6 aluminium alloy and AISI 1018 mild steel, taken from Dialami et al. 2017 [48] and Tello et al. 2010 [49], respectively. The evolution of  $\mu$  and  $m$ , with the temperature, is shown in Table 8 for the two base materials.

For the numerical simulations performed in aluminium and steel, a finite element mesh with 32000 nodes and 180000 tetrahedral elements was used. During the numerical simulation, the torque and forces acting on the tool are calculated by appropriate integration of the normal stresses at the tool/workpiece interface. The coupled thermo-mechanical model, as well as the numerical strategies used to solve the problem, are summarized in Table 9. For a more detailed explanation of the thermal and mechanical models, and of the computational framework, see Refs [44–48,50,51].

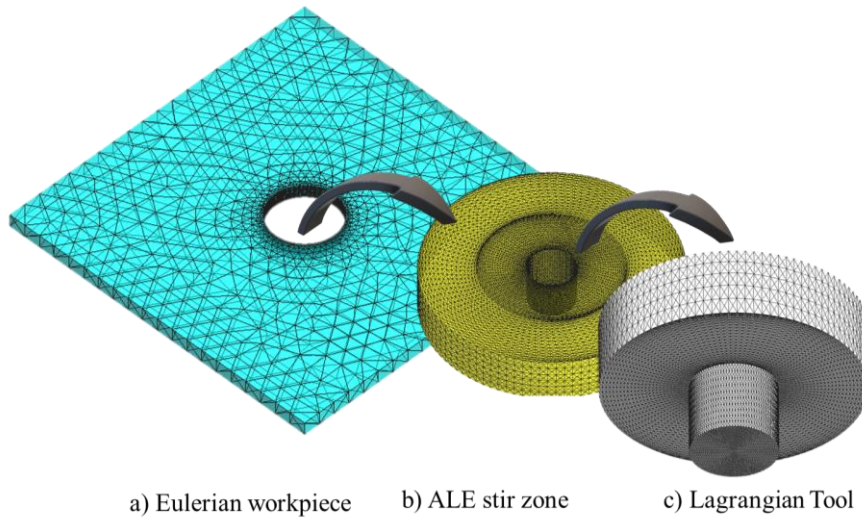


**Figure 8** - Finite element model and respective sub-domains: Eulerian workpiece (a), ALE stirring zone (b) and Lagrangian tool (c) (adapted from “Article D”).

**Table 8** – Evolution of the  $\mu$  and  $m$  values with temperature, for the AA6063-T6 aluminium alloy [48] and AISI 1018 mild steel [49].

$T$ [°C]	AA6063-T6		AISI 1018	
	$\mu$ [MPa]	$m$	$\mu$ [MPa]	$m$
50	105.9	0.025	480.8	0.009
150	79.36	0.035	359.3	0.013
250	56.87	0.049	259.6	0.017
350	38.48	0.068	190.4	0.022
450	24.02	0.094	146.3	0.028
550	13.69	0.131	113.1	0.035
650	0	0.182	87.0	0.044
750			66.2	0.055
850			49.3	0.069
950			35.8	0.085
1050			25.4	0.104
1150			17.8	0.123
1250			12.4	0.142
1350			8.2	0.162
1450			0	0.201

In order to have a better insight into the heat generation and bonding mechanisms in steel welding, the same testing procedures described in Table 6 and Table 7 were modelled and simulated. In addition, a parametric analysis, aimed at investigating the influence of the process parameters on the heat generation, heat dissipation, contact conditions and stirred volume, was conducted, considering the welding of aluminium alloys. Numerical simulations were performed, using the AA6063-T6 aluminium alloy

constitutive properties, rotational and traverse speeds between 300 and 1500 rpm and 250 to 2000 mm/min, respectively, and varied tool dimensions. The tool pin diameter ( $D_p$ ), the pin length ( $p_l$ ), the shoulder diameter ( $D_s$ ) and base material thickness ( $t$ ) were varied in the range of 4 to 10 mm, 1.8 to 8.5 mm, 12 to 30 mm and 2 to 10 mm, respectively. In addition, some conceptual materials were generated and used to analyse the influence of the plastic properties of the base materials on the thermo-mechanical conditions developed during welding. The base materials stress-strain rate curves, for a constant temperature of 25 °C and 550 °C, and the stress-temperature curves, for a constant strain rate of 100 s<sup>-1</sup>, are represented in Figure 9a to c. In the figure, the base material represented by the yellow line was modelled using the AA6063 constitutive properties from Table 8. The remaining base materials used in the analysis were conceptually developed by varying  $\mu$  and  $m$  values, taken from the AA6063 aluminium alloy, from -90 % to +100 %, as shown in Figure 9. The HSHSRS and the HSLSRS are high strength materials ( $\mu = +100$  %) but with high ( $\mu = +100$  %) and low ( $m = -90$  %) strain rate sensitivity, respectively. On the other hand, the LSHSRS and LSLSRS are low strength materials ( $\mu = -90$  %), but with high ( $m = +100$  %) and low ( $m = -90$  %) strain rate sensitivity, respectively.

**Table 9** – Thermo-mechanical formulation of the numerical model (adapted from [48]).

<b>Mechanical partition</b>	
$\nabla s + \nabla p + \rho b_b = 0$	Momentum balance equation
$\nabla \cdot \mathbf{v}_f = 0$	Continuity equation
$\dot{\epsilon} = \nabla^s \mathbf{v}_f$	Kinematic equation
$\sigma_{eq} = \sqrt{3/2} (s:s)^{1/2}$	Equivalent stress
<b>Thermal partition</b>	
$\rho c \left( \frac{1}{\xi} \frac{dT}{dt} + (\mathbf{v}_f - \mathbf{v}_{mesh}) \cdot \nabla T \right) - \nabla \cdot (k \nabla T) = D_{mesh}$	Energy balance equation
$D_{mesh} = \theta s: \dot{\epsilon}$	Viscoplastic dissipation
$q_{conv} = h_{conv}(T - T_{env})$	Heat convection
$q_{cond} = h_{cond}(T - T_{tool})$	Heat conduction

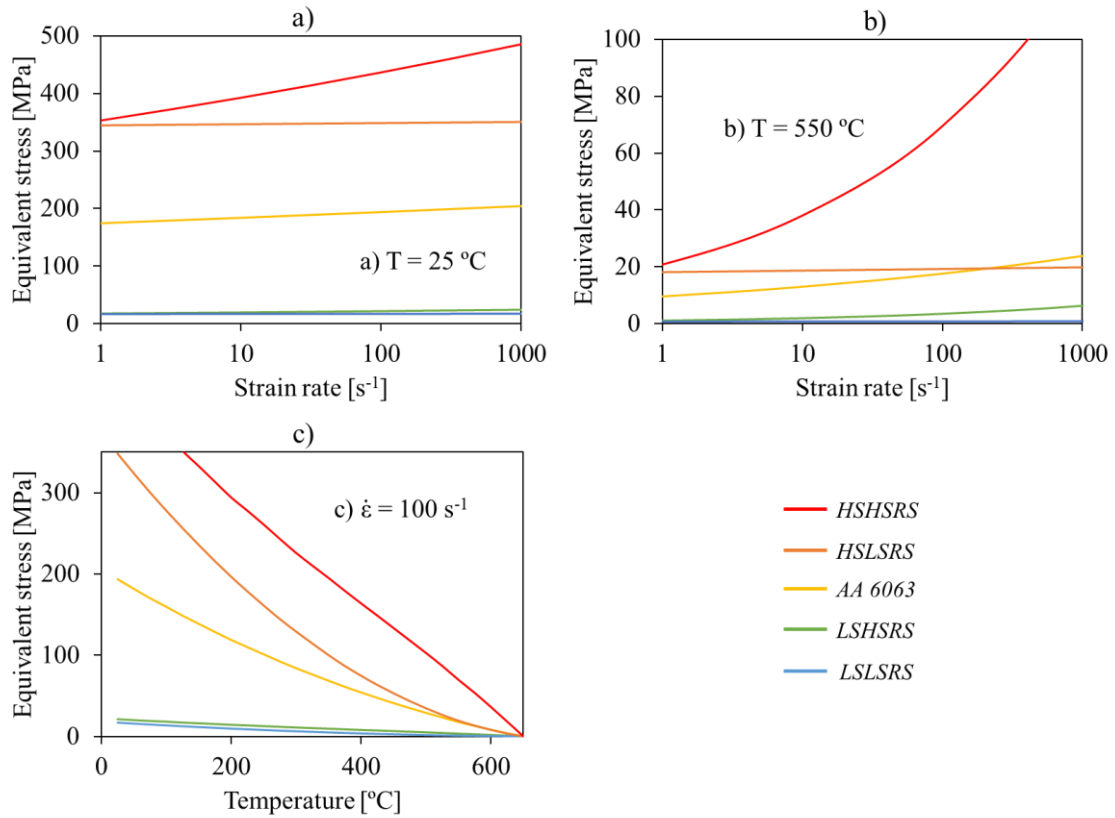


**Figure 9** - Stress-strain rate curves at a constant temperature of 25 °C (a) and 550 °C (b), and stress-temperature curves at a constant strain rate of 100 s<sup>-1</sup> (c) (adapted from “Article D”).

### 2.3.1. Modelling of the contact conditions

The suitability of the numerical model to reproduce the mixed contact conditions characteristic of the FSW process, and to accurately predict the strain rates and the welding temperatures developed during the welding, was tested in the current work, first, by performing a parametric analysis, and second, by comparing numerical and experimental results.

The results of the parametric analysis on the contact conditions, which was published in “Article D”, were obtained by ranging  $a(T)$ , in Eq. 1, from 50 to 500 MPa and using the AA6063 alloy constitutive properties for modelling the base material. A tool with a shoulder diameter of 18 mm and a pin length and diameter of 6 mm, was used. In the sensitivity analysis, constant tool rotational and traverse speeds of 600 rpm and 250 mm/min, respectively, were used. The contact conditions between the tool and the workpiece were assessed by measuring the sticking fraction  $\delta$ , as suggested by Schmidt et al. 2003 [52]:

$$\delta = \frac{v_{BM}}{v_{tool}}. \quad (4)$$

In the equation,  $v_{BM}$  represents the velocity of the base material, at the tool/workpiece interface, and  $v_{tool}$  is the tool velocity. According to Schmidt et al. 2003 [52], when the sticking fraction is equal to one, it means that the contact is 100 % sticking. When the sticking fraction is equal to zero, it means that the contact is 100 % slipping.

Figure 10a and b compare the evolution of the base material and tool velocities, at the tool/workpiece interface, in two different stages of the FSW process, i.e. at the beginning of the welding process ( $t = 0.04$  s) and after steady state conditions are reached ( $t = 5$  s). The figure refers to numerical simulations performed using  $a(T)$  equal to 90 and 500 MPa. In Figure 10c and d is compared the distribution of the sticking fraction, calculated using the velocity profiles of Figure 10a and b, respectively. In the next, to characterise the contact conditions, the average sticking fraction ( $\delta_{avg}$ ), which is the average of the sticking fraction values calculated for all the points along the tool/workpiece interface, will be used.

Analysing Figure 10 it is possible to conclude that, in both numerical simulations, the tool and the material velocities increase with the radial distance from the tool axis, and its maximum values are reached at the outer shoulder edge. The figure also enables to conclude that, irrespective of  $a(T)$ , the sticking fraction increased with the welding time, satisfactorily reproducing the evolution of the contact conditions during the dwelling period at the beginning of the FSW process. Although, meanwhile for the simulations performed with  $a(T) = 90$  MPa, slipping contact conditions ( $\delta_{avg} \approx 0$ ) prevailed at the initial stage of the welding process ( $t = 0.04$ s), for the simulations performed with  $a(T) = 500$  MPa, a large sticking fraction ( $\delta_{avg} \approx 0.8$ ) was registered since the beginning of the welding process. When using  $a(T) = 90$  MPa, once steady state conditions were reached ( $t = 5$  s), mixed slipping/sticking contact conditions ( $\delta_{avg} \approx 0.7$ ) were developed. On the other hand, when using  $a(T) = 500$  MPa, full sticking ( $\delta_{avg} \approx 1$ ) prevailed after steady state conditions were reached. Another important difference between the simulations performed with the different consistency parameter values is that, for the simulations ran with  $a(T) = 90$  MPa, the contact conditions were not symmetrical nor uniform along the tool diameter, since the beginning of the welding process, being registered higher sticking fractions at the retreating side than at the

advancing side of the tool. However, for the simulations ran with  $a(T) = 500$  MPa, contact conditions were almost symmetrical and became uniform, at the shoulder/workpiece interface, when steady state conditions were reached. For  $a(T) = 90$  MPa, the sticking fraction was also higher, at the inner shoulder diameter, where the tool velocity is lower and the weld nugget is formed due to the dragging of the material from the shoulder influence zone to the pin influence zone [53].

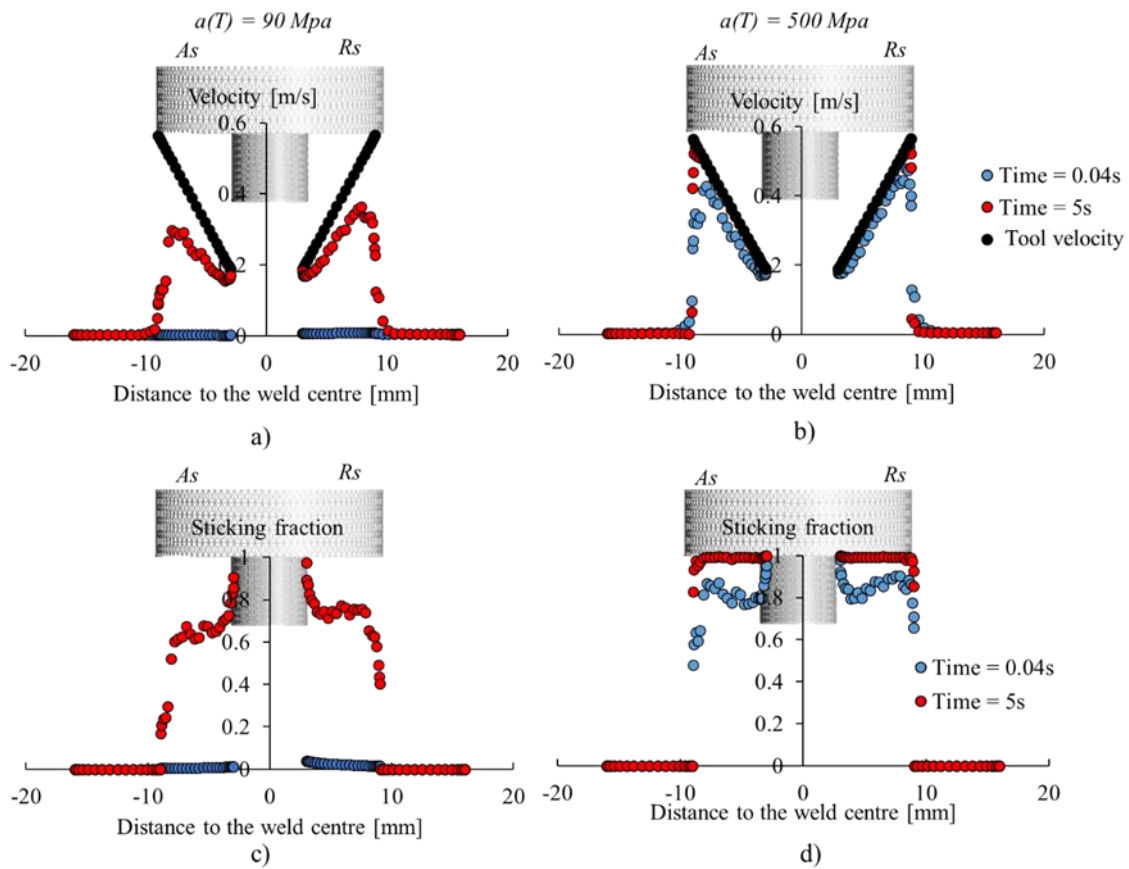


**Figure 10** - Evolution of the base material velocity at the tool/workpiece interface (a and b) and of the sticking fraction (c and d) with the welding time (adapted from “Article D”).

The analysis performed in the previous paragraph showed important differences in contact conditions at the tool/workpiece interface when different values were assumed for the consistency parameter in the Norton friction law. So, to better understand the evolution of the contact conditions with  $a(T)$ , and its influence on heat generation and material flow, numerical simulations were ran using a varied range of tool rotational speeds (300, 600, 900 and 1200 rpm). Figure 11a and b show the evolution of the average

sticking fraction with  $a(T)$  and with the rotational speed, respectively. In the figures, it is also plotted the evolution of the welding temperature for the range of welding conditions tested. The welding temperature was calculated by computing the average temperature in the stirring volume, i.e. considering only the amount of material with equivalent strain rate values higher than zero.

Analysing Figure 11a and b, it can be concluded that, independently of the rotational speed, the sticking fraction increases with  $a(T)$ . For  $a(T) < 200$  MPa, slipping contact and mixed slipping/sticking contact prevail, depending on the tool rotational speed. For  $a(T) > 200$  MPa, sticking contact prevails, mainly for rotational speeds higher than 600 rpm. Figure 11 also shows that the low temperatures associated with the very low rotation speed of 300 rpm, is only simulated for  $a(T) < 100$  MPa and that the transition between prevalent slipping, at low rotational speeds, to prevalent sticking, at high rotational speeds, is only simulated for  $a(T) = 90$  MPa. Based on these results,  $a(T) = 90$  MPa was selected to be used in the analysis of the evolution of the contact conditions and strain rate with process parameters. In the next, this option will be validated based on experimental results.

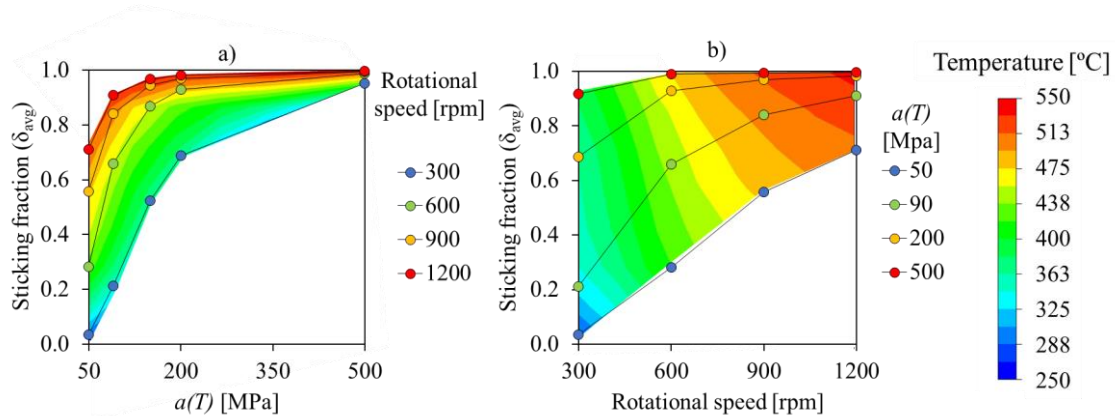


**Figure 11** - Evolution of the average sticking fraction with  $a(T)$  (a) and the rotational speed (b) (adapted from “Article D”).

In Figure 12 is now shown a cross-section of a weld performed in the AA6082-T6 aluminium alloy using a tool with shoulder and pin diameters of 21 mm and 7 mm, respectively, and rotational and traverse speeds of 500 rpm and 200 mm/min, respectively. In the figure are also displayed the streamlines representing the material flow around the tool, determined as in Dialami et al. 2014 [54], and the strain rate and temperature distributions, in the weld cross section, obtained when simulating the

experimental FSW test. Despite the room temperature properties of the AA6063-T6, to which refer the material constitutive properties used in the numerical simulations, and the AA6082-T6 alloys, used to fabricate the weld in the figure, are different, at the very high temperatures reached during FSW, it is expected that both alloys display similar properties and that the numerical and experimental results may be compared. Actually, analysing the streamlines in Figure 12, it is possible to conclude that, for the FSW conditions modelled, the numerical simulations preview that the material is stirred under the shoulder for more than one revolution. This prevision is corroborated by the cross-section of the weld, which displays a large shoulder influence zone. However, in order to better demonstrate the good agreement between the numerical and the experimental results, the grain size (GS) distribution in weld nugget, represented in Figure 13, was compared with the grain size distribution calculated using the temperature and strain rate distributions displayed in Figure 12.

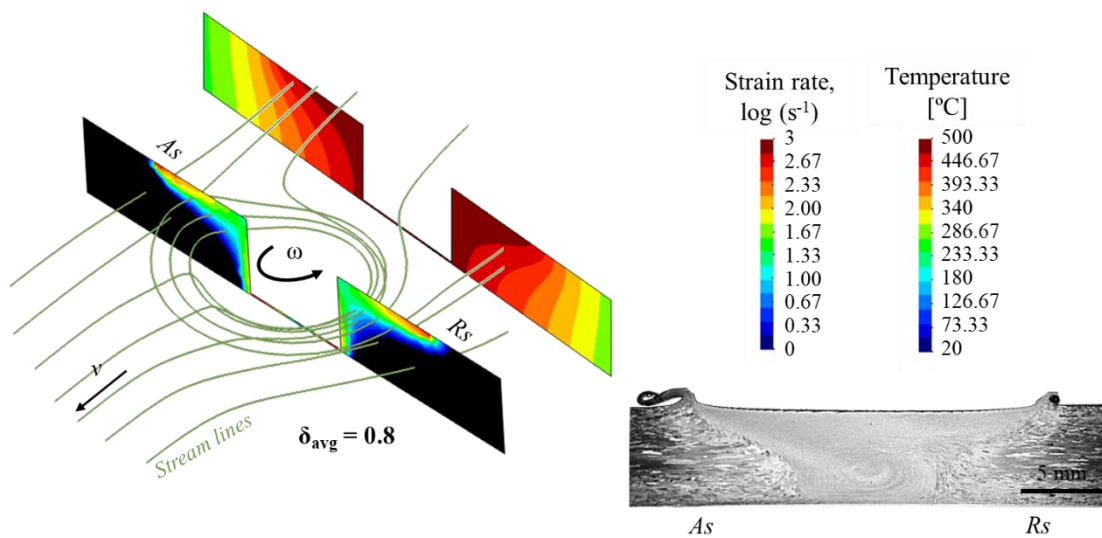


**Figure 12** - Comparison between the AA6082-T6 weld cross section, with the streamlines, temperature and strain rate fields obtained through numerical simulation (adapted from “Article D”).

Figure 13a and b clearly illustrate the large dispersion in GS inside the nugget of the weld in Figure 12. According to Leal et al. 2008 [53] the onion rings are composed by intercalated layers, which result from the incorporation of the plasticised material dragged under the shoulder into to the shear layer around the pin. Magnifications of the microstructure in different locations of the nugget, identified by numbers 1 to 5 in Figure 13a, as well as the grain size distribution in these different regions, are shown in Figure



13c to m. Analysing the figure, it is possible to observe zones with smaller grain size intercalated with zones with larger grain size. As it is known, in thermo-mechanical processes with severe plastic deformation, such as FSW, the dynamic recrystallisation phenomena contribute to the grain refinement in the weld nugget. According to Huang and Logé, 2016 [55], the recrystallisation kinetics and the recrystallised grain size increases with increasing temperatures and decreasing strain rates. The Zener-Hollomon parameter ( $Z$ )

$$Z = \dot{\epsilon} \left( \frac{Q_E}{RT} \right) \quad (5)$$

have been used to incorporate the strain rates ( $\dot{\epsilon}$ ) and the deformation temperature ( $T$ ) into a single parameter by several works in FSW [56–60]. In the equation,  $R$  is the gas constant and  $Q_E$  is the deformation activation energy. The relation between the Zener-Hollomon parameter and the recrystallised grain size ( $d_g$ ) is given by [59,60]

$$\ln(d) = a_z - b_z \times \ln(Z), \quad (6)$$

where  $a_z$  and  $b_z$  are material constants. For the AA6063 aluminium alloy, the activation energy is about 153 kJ/mol [61]. Fitting the experimental results in Figure 13, it was determined that  $a_z$  and  $b_z$  constants are equal to 15 and 0.44, respectively. In Figure 13b, the grain size distribution obtained from the microstructural analysis is compared with the grain size distribution obtained through the numerical simulation, using Eq. 5 and 6 and the constants determined using the experimental results. Analysing the figure, it is possible to conclude that the grain size distribution estimated using the numerical results satisfactorily reproduce the experimental ones, which validates the option taking in modelling the contact conditions.

## Materials and Methods

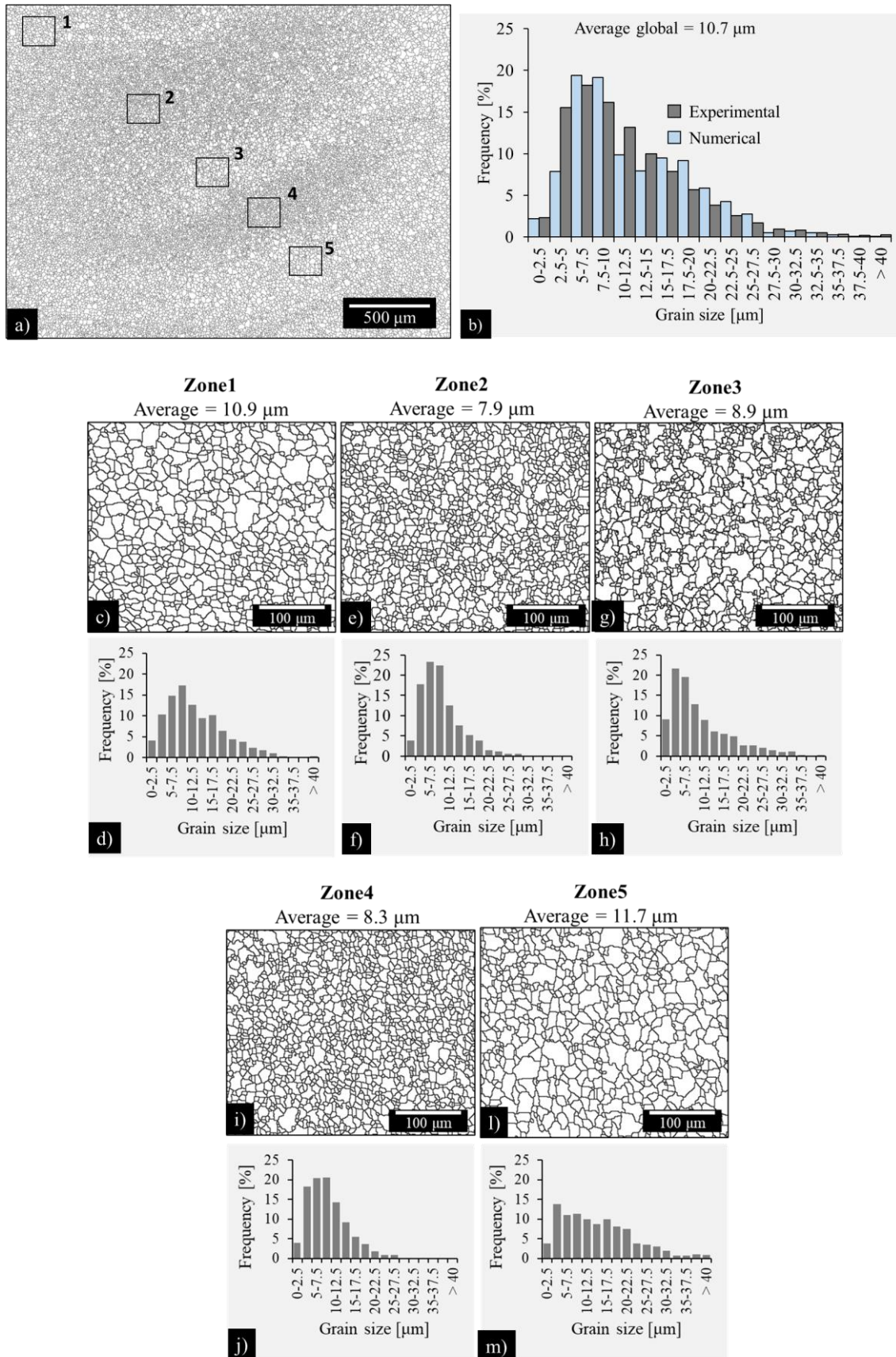


**Figure 13 - Microstructure and grain size distribution in the weld nugget (adapted from "Article D").**

## 3. Thermal Analysis

---

In this chapter, an analysis on the influence of the process parameters on the heat generation and dissipation during welding is presented. The chapter begins with a literature review of the works published on this subject, being given special focus to the description of the analytical models available in the literature to predict the heat generation and the welding temperatures. After this, the results obtained in the current work are presented. Those results enabled to understand the relationship between the processing parameters, the tool dimensions and the base material properties, with the welding temperatures. The welding conditions tested, in the numerical simulation analysis and in the experimental tests, enabled the development of analytical models for predicting the FSW and FSSW temperatures, based on process parameters, which are presented and validated at the end of the chapter.

### *3.1. Literature review*

The plastic deformation, associated with the material flow, and the friction, between the tool and the base material, are the main sources of heating and material softening in friction stir based processes. The heating and cooling conditions, associated with the thermal cycles, together with the plastic deformation, are also important phenomena that affect the final microstructure and the mechanical properties of the stirred material.

Since stir-based technologies are solid-state joining techniques, it is expectable that the welding thermal cycles may be fully controlled by a suitable selection of the tool characteristics and processing parameters. In this way, a database containing data from different FSW and FSSW tests, in AA2xxx, AA5xxx, AA6xxx and AA7xxx aluminium alloys, in lap and butt joint configurations, was created. The references used to collect the data are presented in Table 10. The database generated comprises not only the welding temperatures ( $T$ ) registered by the different authors, but also the rotational and traverse speeds, the pin diameter ( $D_p$ ), the pin length ( $p_l$ ) and the shoulder diameter ( $D_s$ ) used in each work. In order to take into account, the influence of the tool dimensions on the welding outputs, a geometry parameter ( $G$ ) was developed

$$G = \frac{\pi}{4} D_p^2 + \pi D_p p_l + \frac{\pi}{4} (D_s^2 - D_p^2), \quad (7)$$

which corresponds to the contact area between the tool and the workpiece. For complex pin or shoulder geometries,  $G$  was calculated assuming an equivalent cylindrical geometry. In Figure 14 is represented the range of temperatures, rotational and traverse speeds, pin diameters, pin lengths, shoulder diameters and geometry parameters covered in the database, for each aluminium alloy. Due to the large variety of process parameters and tool dimensions considered in the database, the values registered for the temperatures varied in the range of 155 to 590 °C. However, it should be noticed that the temperature measurement position and/or technique varied for the different works, which may have an important influence on the range of the results collected.

**Table 10** – Experimental works that analyse the influence of the processing parameters on the welding thermal cycles registered during the FSSW and FSW processes of aluminium alloys.

AA 2xxx	AA 5xxx	AA 6xxx	AA 7xxx
<ul style="list-style-type: none"> <li>• Gerlich et al. 2007 [58]</li> <li>• Xu et al. 2009 [64]</li> <li>• Arora et al. 2011 [67]</li> <li>• Ramanjaneyulu et al. 2014 [70]</li> <li>• Rao et al. 2015 [73]</li> </ul>	<ul style="list-style-type: none"> <li>• Peel et al. 2006 [62]</li> <li>• Tufaro et al. 2015 [65]</li> <li>• Costa et al. 2019 [68]</li> </ul>	<ul style="list-style-type: none"> <li>• Sato et al. 2002 [63]</li> <li>• Peel et al. 2006 [62]</li> <li>• Emam and Domiaty 2009 [66]</li> <li>• Bakavos and Prangnell 2009 [71]</li> <li>• Wade and Reynolds 2010 [74]</li> <li>• Upadhyay and Reynolds 2012 [76]</li> <li>• Reza-E-Rabby and Reynolds 2014 [78]</li> <li>• Su et al. 2016 [79]</li> <li>• Costa et al. 2019 [68]</li> <li>• Kalinenko et al. 2020 [80]</li> <li>• Salih et al. 2020 [81]</li> </ul>	<ul style="list-style-type: none"> <li>• Gerlich et al. 2006 [57]</li> <li>• Emam and Domiaty 2009 [66]</li> <li>• Upadhyay and Reynolds 2010 [69]</li> <li>• Mehta et al. 2011 [72]</li> <li>• Papahn et al. 2015 [75]</li> <li>• Giraud et al. 2016 [77]</li> </ul>

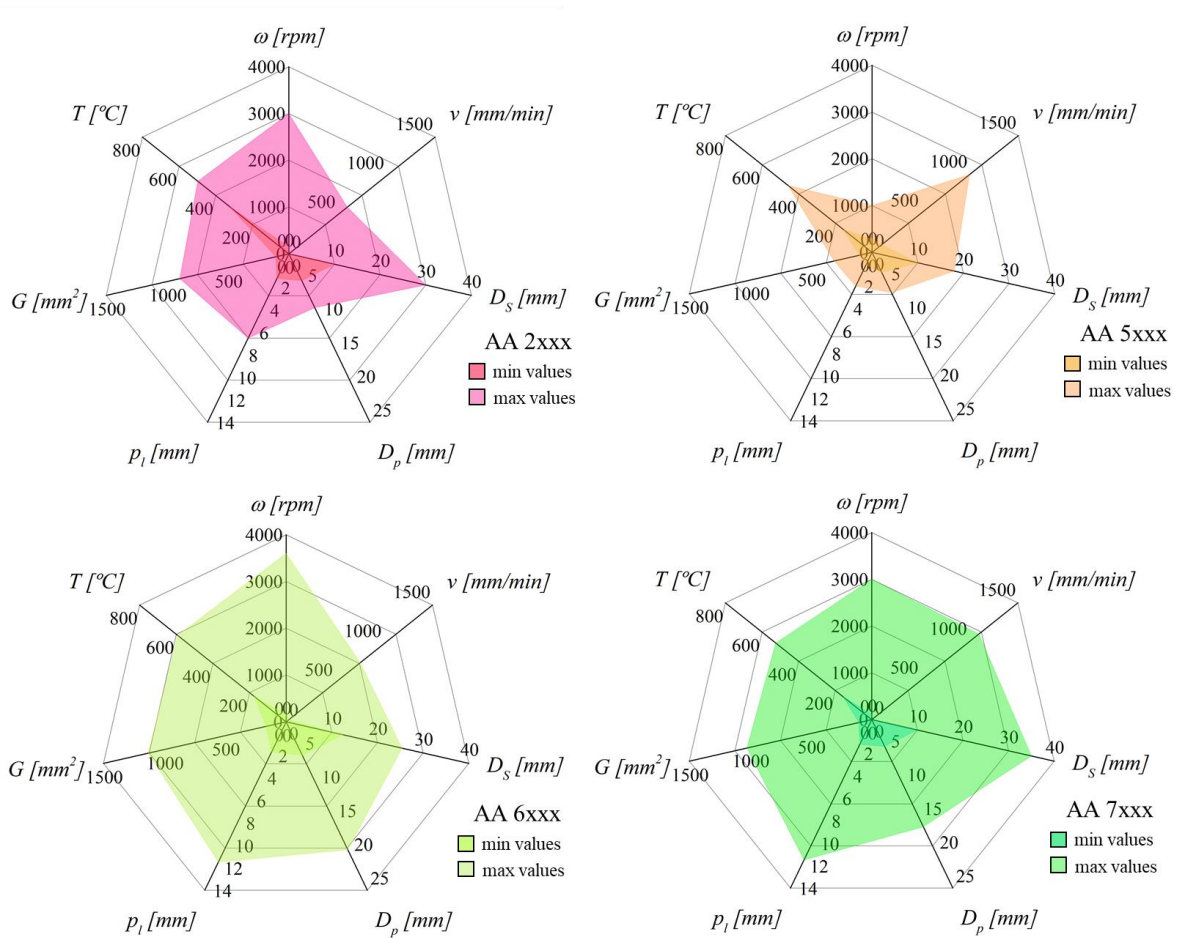


**Figure 14** - Range of rotational speeds ( $\omega$ ), traverse speeds ( $v$ ), shoulder diameters ( $D_s$ ), pin diameters ( $D_p$ ), pin lengths ( $p_l$ ), geometry parameters ( $G$ ) and temperature ( $T$ ) values covered by the database.

In Figure 15a to c is now shown the evolution of the welding temperatures registered for all the works considered in the database, as a function of the rotational speed, traverse speed and tool dimensions. As shown in Figure 15a, for all the works analysed, it is possible to observe that the welding temperature increased with the rotational speed. Although, some authors [57,58,63,69,78] also observed that the welding temperature increases non-linearly with the rotational speed, stabilising for temperatures close to the solidus temperature of the alloy being welded and never reaching the melting temperature of the base material. This was attributed, by Gerlich et al. 2006 [57] and Gerlich et al. 2007 [58], to the occurrence of incipient local melting, which induces slipping contact conditions at the tool-workpiece interface, reducing the heat generation. Upadhyay and Reynolds 2010 [69] also stated that with the increase of the welding

## Thermal Analysis

temperature, there is a decrease in the base material flow stress, which limits the power generation by plastic dissipation.

Analysing now Figure 15b, it is possible to conclude that increasing the traverse speed leads to a decrease of the temperatures registered during the process. Xu et al. 2009 [64] reported that increasing the traverse speed, while maintaining constant the rotational speed, affects the heat input but not the heat generation. According to several authors, the combination of the rotational and linear motions of the tool has an important influence on the heat distribution, creating an asymmetry in temperature between the advancing and retreating sides. However, meanwhile some authors reported higher temperatures at the advancing side of the tool [81–85], some other reported higher temperatures at the retreating side [86,87], which makes the temperature distribution analysis a subject under continuous discussion. Analysing now in Figure 15c the influence of the tool dimensions on the registered temperatures, it is possible to conclude that it is consensual that the FSW temperature increases with the tool dimensions. According to Mehta et al. 2011 [72] and Su et al. 2016 [79], the temperatures increase with the tool dimensions due to the higher frictional and mechanical work.

Despite in all the works analysed in the previous paragraphs it was depicted an evolution of the welding temperature with the tool dimensions, and the rotational and the traverse speeds, no global trend in the temperature evolution with those process parameters may be depicted when analysing the results plotted in Figure 15. This may be related to the fact that, nor the temperature measurement techniques were similar, nor the temperature measurement positions, which may had influence on the maximum temperatures registered by the different authors. Additionally, the heat dissipation conditions may also had been different among the different works. Likewise, no specific correlation between the welding temperatures registered and the aluminium alloy being welded can also be inferred from the analysis of the figures. Finally, it is important to enhance that, even though the results in Figure 15 refer to the FSW of aluminium alloys, a similar evolution in temperature with process parameters was also registered for other materials such as steels [21,22,88,89], magnesium [90,91] and titanium alloys [25].

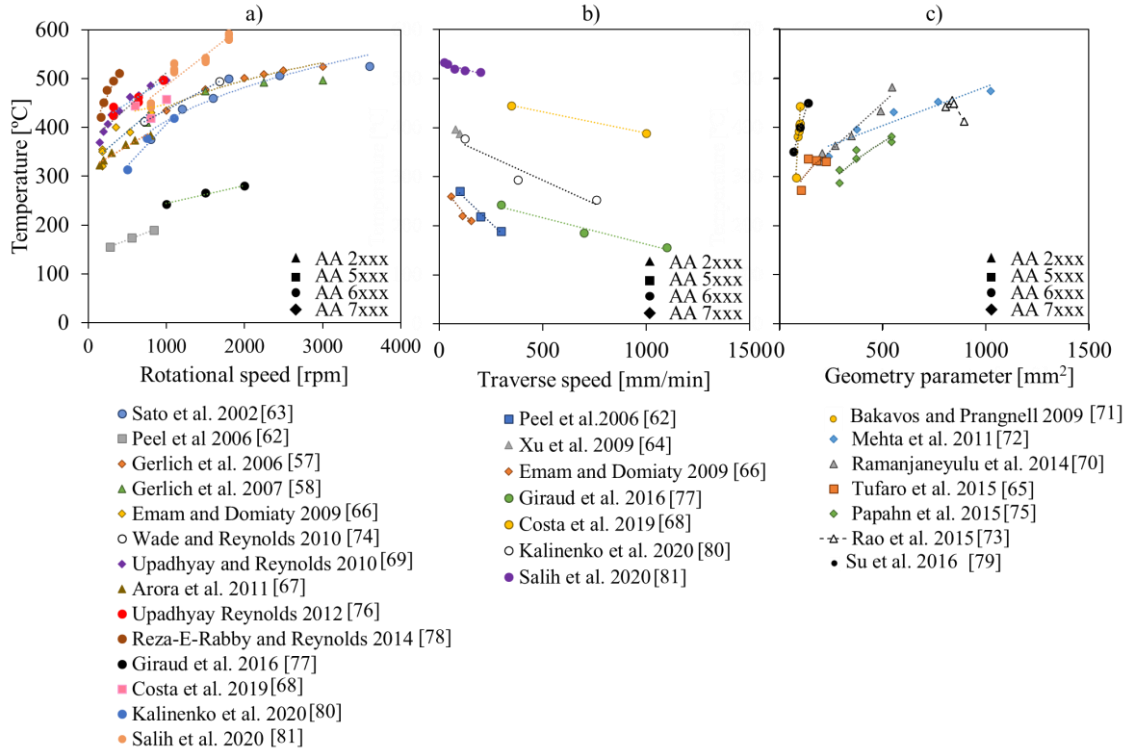


**Figure 15** - Evolution of the temperature with the rotational speed (a), traverse speed (b) and tool dimensions (c) for the experimental works considered in the database.

Up to date, several techniques have been used to quantify the heat input during welding. The most common technique makes use of the welding power to assess the heat input ( $Q$ ), as follows [92,93]:

$$Q = M\omega + F_x v \approx M\omega. \quad (8)$$

In the previous equation,  $M$  is the tool torque and  $F_x$  is the longitudinal force. The term associated with the longitudinal force ( $F_x v$ ) is usually neglected since it represents less than 1% of the total welding power [93]. According to Schmidt et al. 2003 [52] the previous equation may be reformulated as

$$Q = \frac{2}{3} \pi \tau \times \omega [(r_s^3 - r_p^3)(1 + \tan(\beta_s)) + r_p^3 + 3r_p^2 p_l], \quad (9)$$

where  $\tau$  is the shear stress,  $\beta_s$  is the shoulder cone angle,  $r_s$  is the radius of the tool shoulder and  $r_p$  is the radius of the tool pin. This equation is valid for a tool with a cylindrical pin,

## Thermal Analysis

without threads, and a circular shoulder with a cone angle  $\beta_s$ . For a tool with  $r_s = 9$  mm,  $r_p = 3$  mm,  $p_l = 4$  mm and  $\beta_s = 10^\circ$ , Schmidt et al. 2003 [52] calculated that the contribution of the tool shoulder, pin side and pin tip, for the total welding power are 86 %, 11 % and 3 %, respectively. These values shows that the shoulder is the main element of the tool in determining the heat generation.

According to Hamilton et al. [94,95], the effect of the tool penetration on heat input can be assessed by a transfer efficiency coefficient ( $Q_{eff}$ ), given by the ratio between the length of the pin and the thickness of the workpiece ( $t$ ):

$$Q_{eff} = \left(\frac{p_l}{t}\right) \times Q. \quad (10)$$

Although these equations are very useful for calculating the heat input, they do not provide any information regarding the temperatures attained during welding. In this way, Roy et al. 2006 [96] and Arora et al. 2011 [97] used the following mathematical formulation

$$T^* = \alpha_T \times \log_{10}(Q^*) + \beta_T, \quad (11)$$

based on a non-dimensional heat input parameter, to calculate the peak temperature in FSW. In the equation,  $\alpha_T$  and  $\beta_T$  are fitting constants. The non-dimensional temperature  $T^*$  is defined as

$$T^* = \frac{T_{max} - T_{in}}{T_s - T_{in}} \quad (12)$$

where  $T_{max}$  is the peak temperature,  $T_s$  is the solidus temperature of the base material and  $T_{in}$  is the initial temperature.  $Q^*$  is the non-dimensional heat input, given by

$$Q^* = \frac{\sigma_8 A_{sh} \omega c \phi}{k v^2} \quad (13)$$

where  $\sigma_8$  is the yield stress of the material at 80% of  $T_s$  and  $A_{sh}$  is the cross-sectional area of the shoulder. The parameter  $\phi$  represents the ratio of heat transferred between the tool and the workpiece, which can be calculated by



$$\phi = \left[ \frac{(k\rho c)_{workpiece}}{(k\rho c)_{Tool}} \right]^{1/2}. \quad (14)$$

where  $\rho$ ,  $c$  and  $k$  are the material density, specific heat and thermal conductivity, respectively. The material properties in the above equation are those taken at an average temperature between  $T_{in}$  and  $T_s$ . It should also be noticed that Eq. 12 is only valid when  $Q^*$  lies in the range  $4 \times 10^2 < Q^* < 3.7 \times 10^5$ . Arora et al. 2011 [97] determined the  $\alpha_T$  and  $\beta_T$  values, as 0.1508 and 0.0976, respectively, using results relative to the FSW of the AA2524, 304L SS and Ti-6Al-4V base materials.

An important difficulty in using the above models, for estimating the welding power and/or temperature, is that they require the knowledge of the mechanical behaviour of the material under the thermo-mechanical conditions imposed by the FSW process, which is very difficult to determine. Those uncertainties lead to the development of other analytical models, relating the welding temperatures with the process parameters. Qian et al. 2012 [98], Ramanjaneyulu et al. 2014 [70] and Xiong et al. 2014 [99] used the following relationship,

$$\frac{T_{max}}{T_s} = \beta_{TT} \left( \frac{\omega^2}{v \times 10^4} \right)^{\alpha_{TT}}, \quad (15)$$

which takes into account the influence of the traverse and rotational speeds on the heat input, to estimate the peak temperature in the stir zone. In the equation,  $\beta_{TT}$  and  $\alpha_{TT}$  are fitting parameters, ranging from 0.04 to 0.06 and 0.65 to 0.75, respectively. It is also important to notice that in Eq. 15, only the tool rotational and traverse speeds are considered, to calculate the welding peak temperature. The equation does not take into account the effect of the tool dimensions and plate thickness on the heat input.

As discussed in the previous paragraphs, the main limitations of the models available in the literature for determining the heat generation and the peak temperature in FSW are, for some of it, the inclusion in its formulation of difficult to determine variables, such as very high temperature material properties, or, in most of the cases, the exclusion from its formulation of process parameter related variables, such as tool dimensions, despite it is well known that this process parameter has a strong influence on the heat generation. It is also important to enhance that none of the models described was validated

for a large range of base materials or welding conditions. This implies that, most of that models constants, are not valid when applied to experimental conditions different from those used by the authors of the model.

In the current work, the heat generation in spot welding of aluminium and ferrous alloys and in the linear welding of aluminium alloys, was assessed by performing experiments and numerical simulation tests, respectively. The process parameters tested in the numerical simulations were planned to cover most of the process conditions identified in the literature review for aluminium alloys. By coupling the experimental and the numerical results, new models for determining the welding temperature in stir-based processes, such as FSW and FSSW, were developed. Contrary to the models described in the literature review, the models developed under the scope of this dissertation consider the influence of the tool dimensions and of the plate thickness, on the heat generation and dissipation during welding. The models developed were validated, not only for the experimental conditions tested in the current work, but also for the welding conditions tested in the literature for aluminium alloys.

### *3.2. Temperature measurements*

The work carried out to analyse the heat generation during the spot and linear welding of the steels and aluminium alloys is schematically represented in Figure 16. The temperature evolution during the spot welding, was assessed by performing welds in the alloys identified in the figure. More precisely, it was performed bead-on-plate spot welding of thick AA2017, AA5083, AA6082 and AA7075 aluminium alloys (Figure 3) and spot welding of thin DC, HC and DP steel plates (Figure 4), using a very diversified range of processing parameters (Table 4). Tungsten carbide pinless tools, with different diameters, were used in all the tests (Figure 5). The influence of the tool material, on the heat generation, was also assessed by testing coated and uncoated tools. As already explained in this dissertation, using tools without pin enabled extending the analysis of the heat generation to the welding of steels. In all the experiments, the dwelling time was set equal to 60 s, in order to enable capturing the stabilization of the welding temperature after the tool plunging.

In addition to the assessment of the temperature evolution during spot welding, the heat generation during the tool linear displacement was also analysed, for the aluminium alloys, but this time, using numerical simulation.

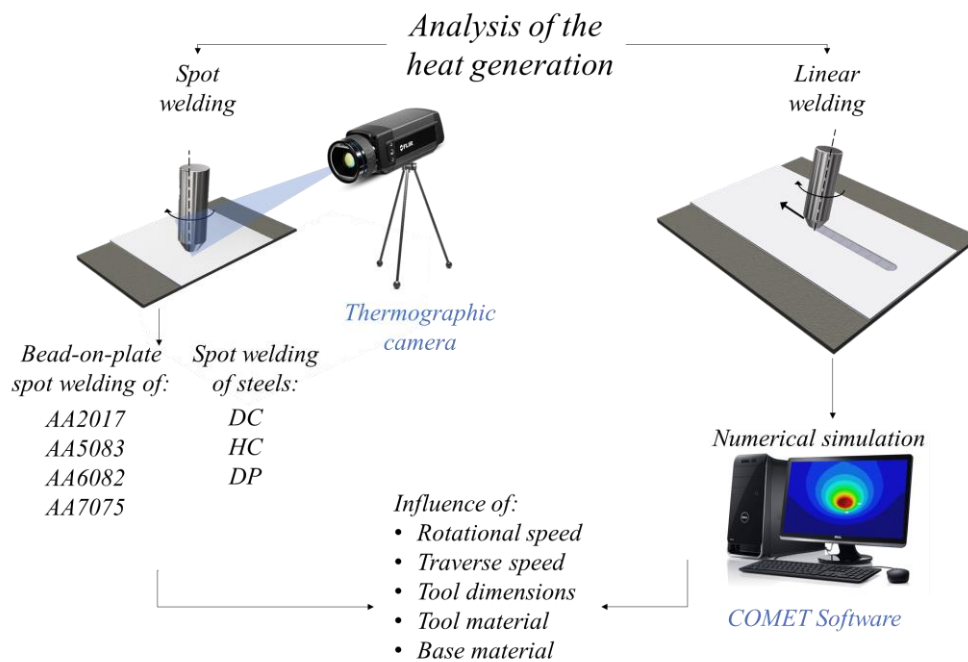


**Figure 16** - Schematic representation of the thermal analysis performed in current work.

### 3.2.1. Spot welding of aluminium alloys

In Figure 17 is shown the thermal cycle registered during the bead-on-plate spot welding of the AA7075 aluminium alloy, with the PL16 tool and a rotational speed of 660 rpm. The thermal cycle represented in the figure enables to identify three main stages: a heating period, which coincides with the tool plunging into the workpiece, during which the temperature rises, a steady state period, during which the temperature remains almost constant, and a cooling period, during which the temperature decreases, after welding.

In Figure 17 is also represented the instantaneous derivative of the temperature ( $dT/dt$ ), used in current work to determine the duration of the three different welding stages described above. The instantaneous derivative corresponds to the instantaneous heating rate, when it displays positive values, and to the instantaneous cooling rate, when reaching negative values. To determine the length of the steady state period, it was assumed that the heating period ends when  $0 \leq dT/dt \leq 4$  °C/s. Once the duration of the steady state period was set, the average temperature attained during this period, which also corresponds to the maximum temperature reached in the process, was determined by calculating the average of the temperatures recorded during that time interval.

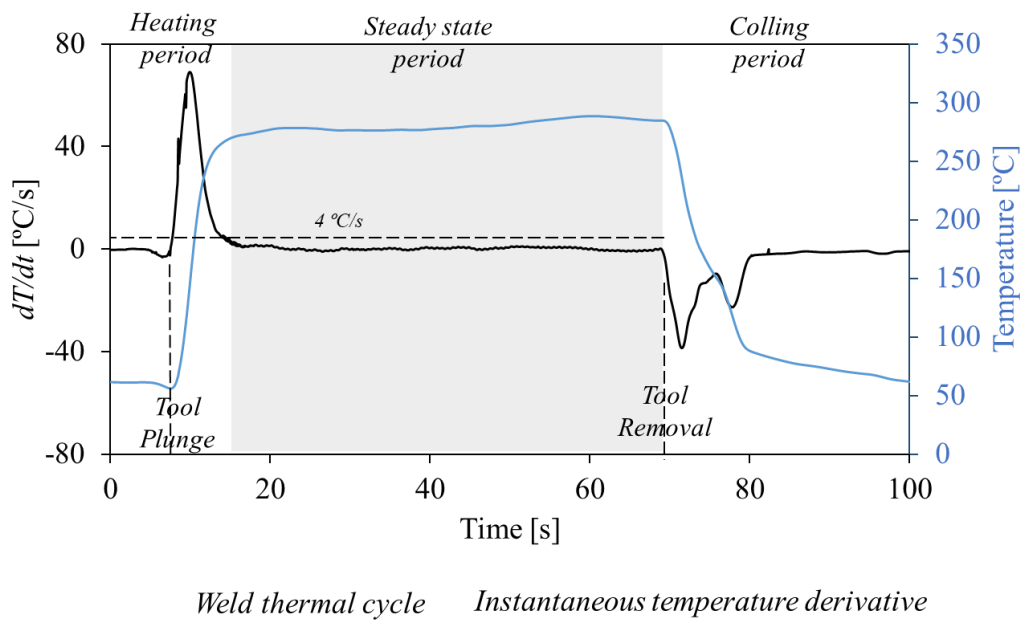


**Figure 17** – Weld thermal cycle, represented by a blue line, and instantaneous temperature derivative in order of time ( $dT/dt$ ), represented by a black line, for the weld produced in AA7075 aluminium alloy, with the PL16 tool and a rotational speed of 660 rpm.

In Figure 18 is plotted the evolution of the maximum temperature values, determined from the welding thermal cycles, with the rotational speed and the geometry parameter, for all the bead-on-plate spot welds produced in aluminium alloys. The results were obtained by varying the rotational speeds, between 660 to 1500 rpm and the shoulder diameters, between 10 to 18 mm. Analysing the figure, it is possible to conclude that, for each base material, the welding temperature increases with the tool diameter, irrespective of the rotational speed used. Increasing the tool diameter from 10 to 18 mm resulted in an increase of around 250 °C in the welding temperature, for all the aluminium alloys tested. The figure also shows that, for each tool diameter, independent of the aluminium alloy tested, the temperature almost did not vary with the rotational speed, which indicates that there is a shoulder diameter related temperature threshold. This shoulder diameter related temperature threshold is similar for all the aluminium alloys tested.

Another important conclusion that can be taken from Figure 18 is that for aluminium alloys, 600 rpm is the limit rotational speed for which the heat generation stabilizes to values independent of the rotational speed. However, the figure also shows that the temperature stabilization does not only occurs when the welding temperature approaches the melting temperature of the alloys being welded, as stated in some

literature. This shoulder diameter dependent temperature threshold was registered even when the temperatures measured were far below the melting temperature of the alloy being welded. So, the occurrence of incipient melting at the shoulder/workpiece interface cannot be applied for explaining the temperature stabilization in current work. However, the results also show that, independent of the aluminium alloy being welded, for rotational speeds higher than 600 rpm, the welding temperatures may be previewed/controlled by a proper choice of the tool diameter. To the current authors knowledge, no previous work reported the same type of conclusions.

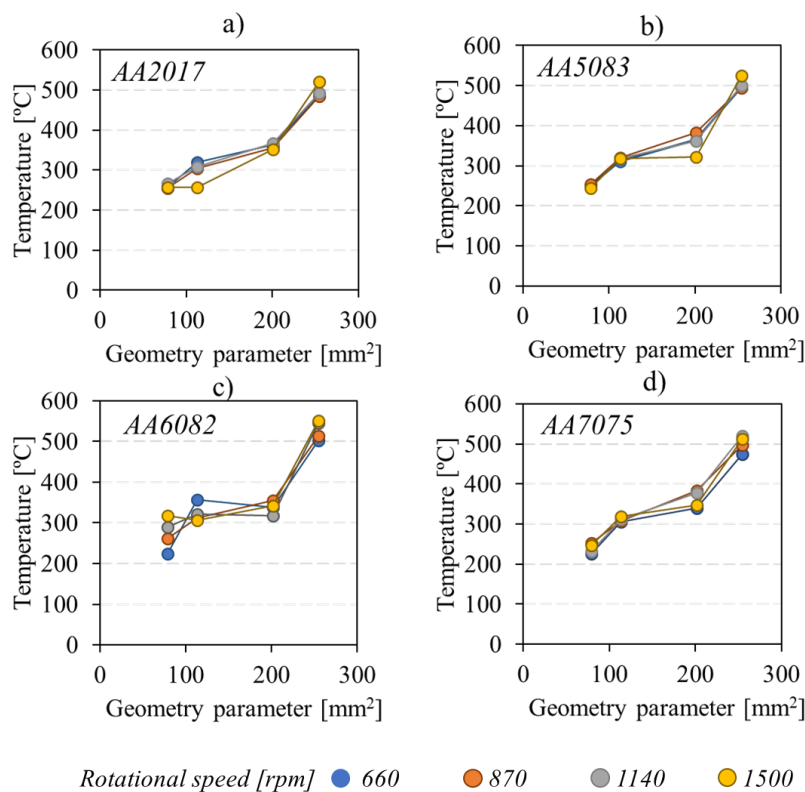


**Figure 18** – Evolution of the stabilized temperature values with the rotational speed and geometry parameter, for the AA2017 (a), AA5083 (b), AA6082 (c) and AA7075 (d) aluminium alloys.

In order to check if the reported trends on the temperature evolution, with the tool dimensions and the rotational speed, were not related with inaccuracies in the temperature acquisition during welding, hardness measurements were performed in the cross-section of the welds produced in the heat treatable AA6061-T651 aluminium alloy, which according to MacKenzie et al. 2016 [100], was the one with the lowest quenching sensitivity among all the alloys tested.

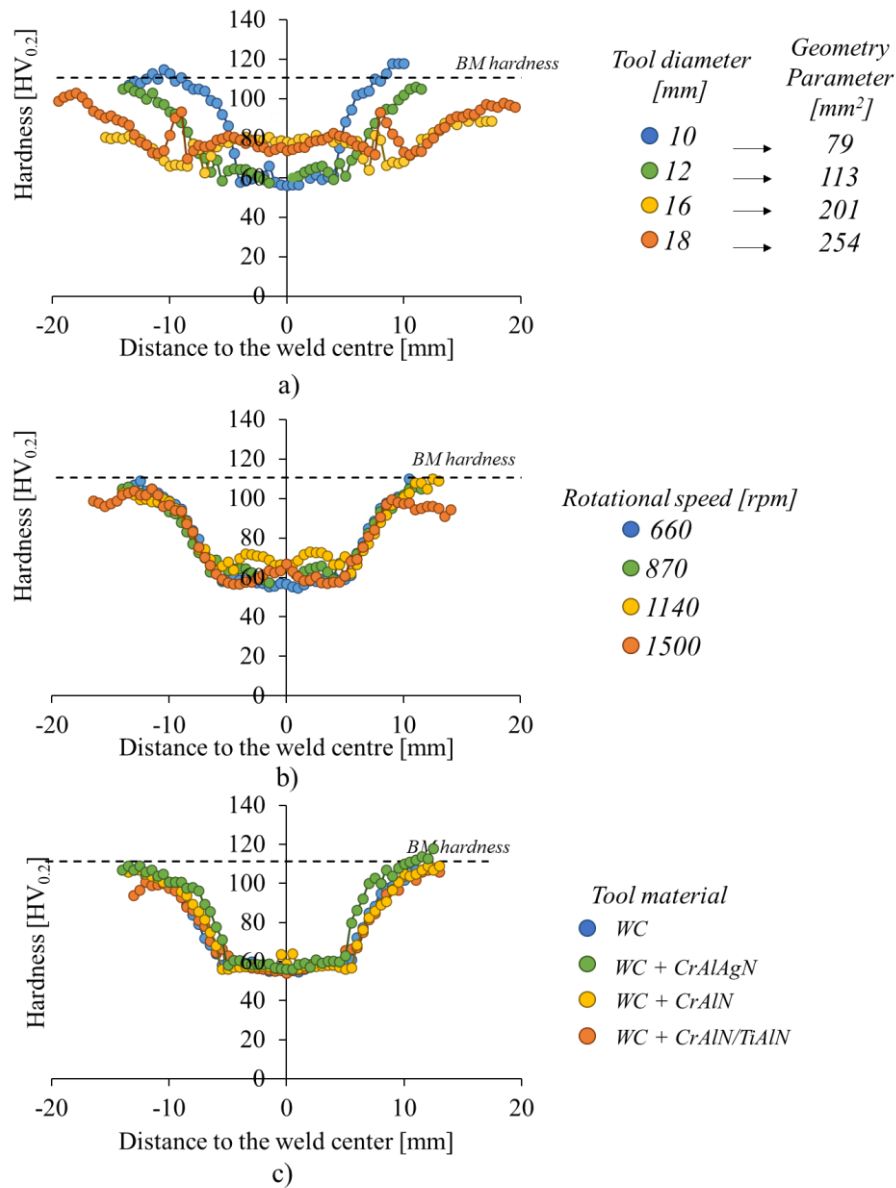
## Thermal Analysis

Figure 19 compares the hardness profiles for the welds produced in the AA6061-T651 aluminium alloy with varied tool diameters (Figure 19a), rotational speeds (Figure 19b) and tool coatings (Figure 19c). More precisely, in Figure 19a are shown the hardness profiles for the welds produced with a constant rotational speed of 870 rpm, and varied tool diameters between 10 to 18 mm. Analysing the figure, it is possible to conclude that the hardness profile/values varied according to the tool diameter used. As it is well-known, for the AA6061-T651 aluminium alloy, the hardness varies with temperature with respect to the precipitate evolution [18,19,63]. The thermal exposure of the alloy during welding lead to the overaging of the peak aged precipitates, which become coarse and incoherent, leading to the hardness decrease in the process affected zone shown in Figure 19a. On the other hand, the hardness recovery in the middle of the welds, which can be clearly observed for the welds produced with the PL16 and PL18 tools, results from the full solubilization of the strengthening precipitates, due to the high temperatures attained in this region and to the intense plastic deformation promoted by the tool, followed by reprecipitation during the cooling period subsequent to the welding [18]. It is also inferred that the hardness of the welds produced with the PL10 and PL12 tools was lower than that of the PL16 and PL18 tools welds. This is related to the lower temperatures and faster cooling rates experienced during the welding with the PL10 and PL12 tools, which were not sufficient to promote reprecipitation in the same conditions experienced during the welding with the PL16 and PL18 tools.

In Figure 19b is now shown the evolution of the hardness profiles with the rotational speed. The hardness profiles displayed in the figure correspond to the welds produced with the PL12 tool and rotational speeds between 660 to 1500 rpm. Analysing the figure, it is possible to conclude that, the evolution of the hardness with the distance to the weld centre is very similar to that shown in Figure 19a. However, in Figure 19b, no important differences in the hardness profiles shape and values may be observed for the welds produced with different rotational speeds. This is related to the small influence that the rotational speed had on the welding thermal cycles.

In Figure 19c are now compared the hardness profiles for the welds produced with the uncoated WC tool and with the CrAlN, CrAlAgN and CrAlN/TiAlN coated tools, with a constant rotational speed of 660 rpm, in the AA6082 aluminium alloy. The figure shows that all the hardness profiles are similar, indicating that the heat generation was similar for all the tools, irrespective of its characteristics. This result enables to conclude

that the shoulder diameter dependent temperature threshold is independent of the tool material and only varies with the tool dimensions.



**Figure 19** – Hardness profiles for the welds produced in the AA6082 aluminium alloy with a constant rotational speed of 870 rpm and varied tool diameters between 10 to 18 mm (a), with a constant tool diameter of 12 mm, and varied rotational speed between 660 to 1500 rpm and (c) with the WC uncoated tool and the WC tools coated with the CrAlN, CrAlAgN and CrAlN/TiAlN films.

### 3.2.2. Spot welding of steels

For the ferrous alloys, the heat generation was analysed by performing spot welds in DC, HC and DP steels. In Figure 20 it is plotted the evolution of the maximum temperature values with the rotational speed and the tool geometry parameter, for the different steels.

## Thermal Analysis

The results plotted in the figure, which were extracted from Articles B and E, were obtained by varying the rotational speed, between 870 to 1500 rpm, and the shoulder diameter, between 10 to 16 mm. The maximum temperature values were determined from the steel spot welds thermal cycles, using the same procedures already explained for the aluminium alloys.

Analysing Figure 20, it is possible to conclude that, contrary to that registered for the aluminium alloys, for the steels, the evolution of the maximum temperature with the process parameters varies according to the alloy composition. Another important difference relative to the aluminium alloys is that no shoulder diameter related temperature threshold can be depicted from the figure. However, the figure enables to depict a temperature threshold of 1100°C, which is common to all the alloys. Meanwhile for the DC and HC steels, the threshold temperature was only reached when welding at the highest rotational speed of 1500 rpm and with the larger tool diameters, for the DP steel, the temperature threshold was reached for almost all the welding conditions tested.

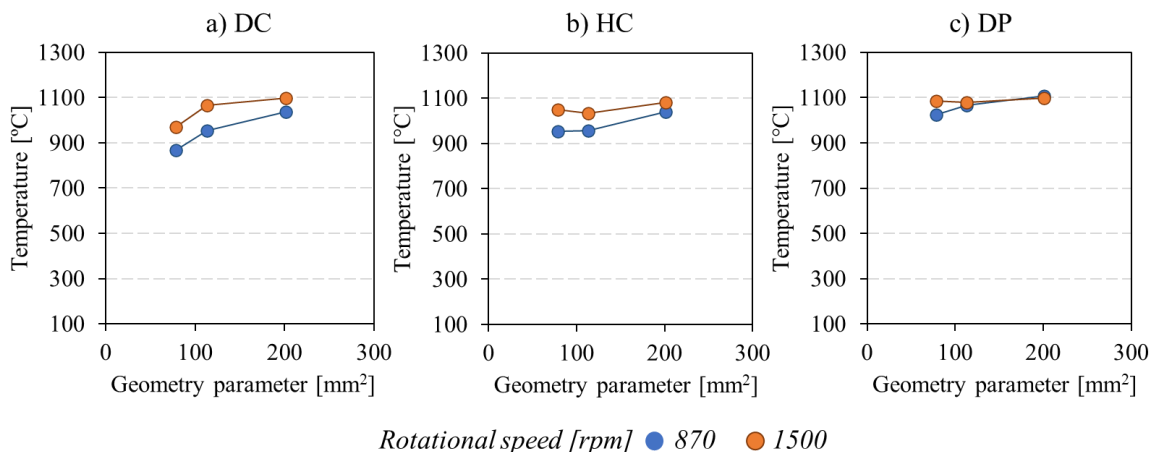


**Figure 20** – Evolution of temperature with the rotational speed and tool dimensions for the DC (a), HC (b) and DP (c) steels.

The results in Figure 20 indicate that, contrary to the aluminium alloys, the ferrous alloys display different sensitivity to the process parameters, according to its chemical composition. Meanwhile, for the DP steel, the welding temperature is of 1100 °C, independently of the process parameters, for the DC and HC steels, the temperature may be varied, between 900 and 1100 °C, by welding at rotational speeds lower than 1500 rpm and using small shoulder diameters.



### 3.2.3. *Linear welding of aluminium alloys*

As already explained in this dissertation, the heat generation and dissipation during the linear displacement of the tool was analysed through the numerical simulation of the FSW process, conducted using COMET software. The numerical simulations were performed considering the AA6063-T6 aluminium alloy constitutive properties (Table 8) and a very diversified range of process parameters. Namely, the tool dimensions, plate thicknesses and welding speeds assumed in the numerical simulation analysis were selected in order to cover the same range of parameters tested in the experimental works covered by the database (Figure 14). The numerical simulation results, extracted from “Article C”, are discussed in the next.

In Figure 21a is shown the evolution of the welding temperature, with the rotational speed and the geometry parameter, and in Figure 21b is shown the evolution of the welding temperature, with the traverse speed and the plate thickness. The welding temperatures displayed in the figure were calculated by computing the average of the temperatures in all the nodes inside the stirred material volume, i.e. considering only the amount of material with equivalent strain rate values higher than zero. For obtaining the results in Figure 21a, the rotational speed was varied between 300 to 1500 rpm and a constant welding speed of 250 mm/min was used. The tool dimensions were set assuming proportionality between the shoulder diameter ( $D_s$ ) and the thickness of the plates ( $t$ ), by using the equation proposed by Zhang et al. 2012 [101]:

$$D_s = 2.2t + 7.3. \quad (16)$$

The pin dimensions were established using a  $D_p/D_s$  ratio of 3 and a  $p/t$  ratio of 0.85 [102]. The thickness of the base material and the shoulder diameter were varied between 1 to 10 mm and 12 to 30 mm, respectively. For obtaining the results in Figure 21b, no proportionality between the shoulder diameter and the plates thickness was considered. Instead, a tool with a constant tool diameter of 18 mm and  $p/t$  ratio of 0.85 was used, while the plates thickness was varied from 1 to 9 mm. In the numerical simulations, the tool rotational and traverse speeds were varied between 300 to 1500 rpm and 250 to 1000 mm/min, respectively.

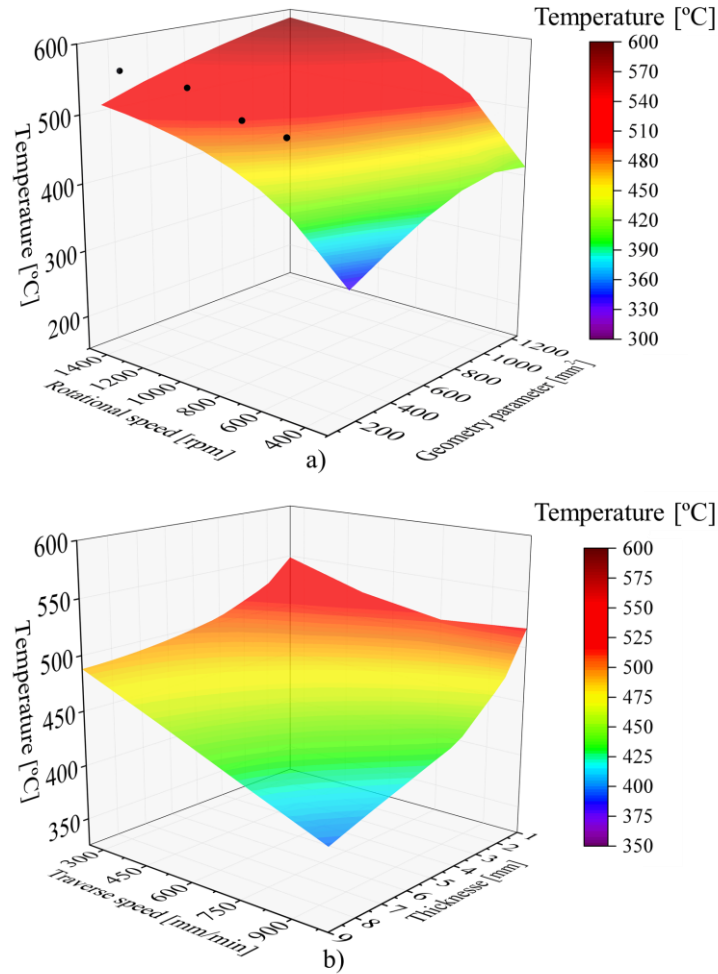


**Figure 21** – Numerical results concerning the evolution of the temperature with the rotational speed and geometry parameter (a) and with the traverse speed and plate thickness (b). The points marked in black correspond to the welding temperatures registered for the spot welds produced with the PL18 tool in the AA6082 aluminium alloy.

Analysing Figure 21a, it is possible to conclude that the welding temperatures increase with the rotational speed and the tool dimensions, stabilising in maximum values for large values of rotational speeds and/or tool dimensions. The stabilisation of the maximum temperature corresponds to the threshold in heat generation [1], which according to most of the published literature, prevent the welding temperature from reaching the base material melting temperature, ensuring solid-state welding, irrespective of the welding parameters. It is also possible to conclude that the influence of the tool dimensions on the welding temperatures is more significant for low than for high rotational speeds, and that the influence of the rotational speed on the welding temperature is more significant for small geometry parameter values.

In Figure 21a, it is also represented using black dots, the temperature values registered for the bead-on plate spot welds produced in the AA6082 aluminium alloy, with the 18 mm diameter tool. The geometry parameter of this tool is the only one, among all the tools tested in spot welding, which is in the same range of the geometry parameter of the tools tested in the numerical simulation work, and, in this way, in the same range of the tools tested in most of the published works on FSW of aluminium alloys. According to the figure, it is possible to conclude that the shoulder diameter related temperature threshold, registered in the spot welding tests, for rotational speeds higher than 600 rpm, is also coincident with the temperature stabilisation predicted by the numerical simulation. Since for the remaining tools tested in spot welding, the geometry parameter is outside the range of the tool geometry parameters tested in linear welding, the welding temperatures may not be compared. In spite of this, the figure enables to conclude that, contrary to what was registered for the spot welding of aluminium alloys, for the linear welding, no threshold in temperature with the rotational speed was observed for temperatures far below the melting point of the alloy being welded.

Analysing now Figure 21b, it is possible to depict an influence of both the traverse speed and the plate thickness on the welding temperature. However, the influence of these two parameters on the welding temperatures is less pronounced than that of the rotational speed and of the tool dimensions, since these two parameters do not have influence on the heat generation, but only affect the heat dissipation. This way, the figure shows that temperature always decreases when increasing the traverse speed and/or the plate thickness. However, these results also enhance that the influence of the traverse speed is higher for thicker plates, and the influence of the plate thickness is enhanced for higher traverse speeds.

In Figure 22 is now show the evolution of the temperature versus the product of the traverse speed by the plate thickness ( $vt$ ). In the figure, the results plotted with red squares correspond to the numerical simulations of Figure 21a, in which heat dissipative effects associated with the thickness and the traverse speed were minimised by assuming a constant value for  $v$  and setting the shoulder diameter proportional to the plates thickness. The results plotted with circles correspond to the numerical simulations of Figure 21b, in which the shoulder diameters, plate thicknesses and traverse speeds were selected in order to enhance the heat dissipative effects on the temperature fields. Analysing Figure 22, it is possible to conclude that the welding temperature increases with the tool dimensions

and rotational speed, which were found as the main factors in heat generation in the previous analysis, but decrease non-linearly with the  $vt$  product.

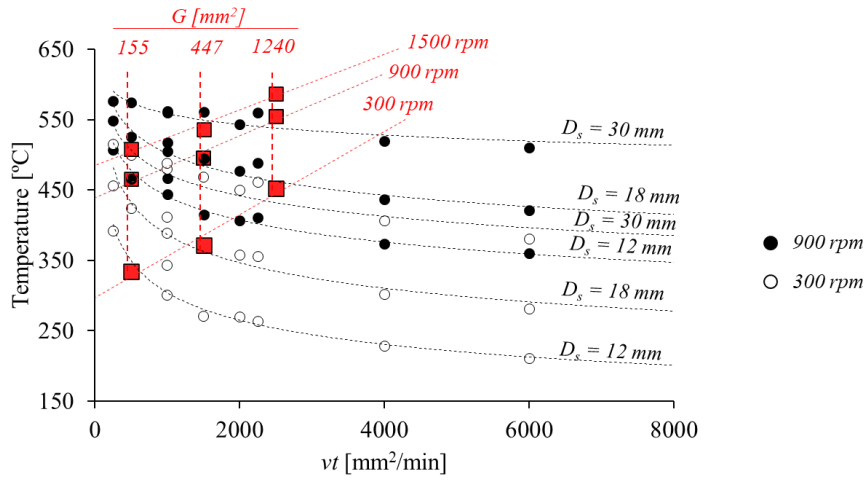


**Figure 22** – Numerical results concerning the evolution of the temperature with the traverse speed multiplied by the plates thickness ( $vt$ ), when heat dissipative effects are minimized (red squares) and maximized (black circles) (adapted from “Article C”).

### 3.3. Modelling the welding temperature

The data from the numerical and experimental tests was used for developing analytical models, that relate the process parameters with the welding temperature, in FSW and FSSW. Since the temperature evolution with process parameters, for the aluminium alloys, was found to be different between the FSW and FSSW, and in addition, the advancing movement of the tool does not exist in FSSW, different models were proposed for each process.

#### 3.3.1. Linear welding

The sensitivity analysis performed using numerical simulation enabled to understand the relation between the tool dimensions, the rotational speed, the traverse speed and the plate thickness with the welding temperatures. From the results in Figure 22, a temperature coefficient,  $C_T$ , was proposed to predict the temperature in linear welding:

$$C_T = \frac{G\omega}{\sqrt{vt}}. \quad (17)$$

In Figure 23 is represented the evolution of the welding temperatures, obtained in the numerical simulations for the AA6063-T6 aluminium alloy versus the temperature coefficient  $C_T$ . The figure shows that  $C_T$  satisfactorily reflects the evolution of the welding temperatures, until a threshold in the heat generation is reached, for  $C_T$  values higher than 20000, which is known to ensure solid-state welding conditions. According to the figure a model for quantifying the evolution of the welding temperature with the processing parameters was proposed:

$$\begin{cases} T = \lambda_T \times K_T \times C_T^\varphi, & \text{for } C_T < C_{T,cr} \\ T = \lambda_T \times T_{CT}, & \text{for } C_T \geq C_{T,cr} \end{cases} \quad (18)$$

In the previous equations,  $K_T$  and  $\varphi$ , are constants related to the base material being welded, and  $\lambda_T$  is a constant that takes in consideration the influence of the different experimental techniques used to measure the temperatures, such as differences in the position at which the temperature was measured and differences in the backing plate material, among others. The  $C_{T,CR}$  parameter represents the critical temperature coefficient value from which no increase in the welding temperature ( $T_{CT}$ ) occurs irrespective of the welding parameters used. From the numerical simulation results it was determined that, for aluminium alloys,  $K_T = 50$ ,  $\varphi = 0.25$ ,  $C_{T,cr} = 20000$  and  $T_{CT} = 560$  °C. The value of  $T_{CT}$  is also in agreement with the maximum temperature values registered by the experimental works covered by the database (Figure 14).

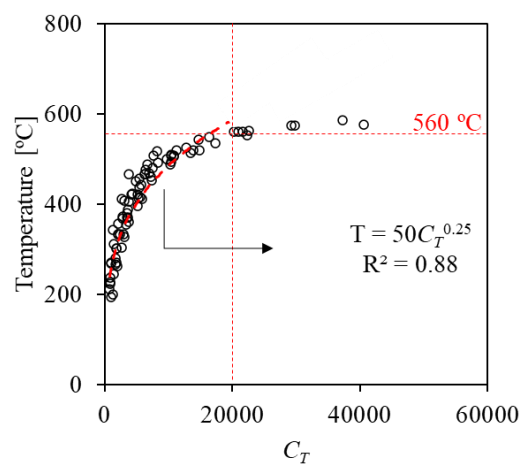


**Figure 23** – Evolution of the welding temperatures, obtained in the numerical simulation, with the temperature coefficient  $C_T$  (adapted from “Article C”).

## Thermal Analysis

The proposed model was validated by comparing the temperature values previewed by Eq. 18 with the experimental results from the database, as is shown in Figure 24. According to the figure, the temperature values computed through Eq. 18 always follow the temperature results obtained by the different authors and the different welding conditions, i.e. different shoulder diameters, traverse and rotational speeds. Also, no adjustment in  $K_T$  and  $\varphi$  parameters was necessary, indicating that these parameters are constant for all aluminium alloys. Although, the  $\lambda_T$  factors needed to be determined individually for each one of the experimental works, due to the strong dependence of the temperatures registered from the experimental apparatus used to assess it.

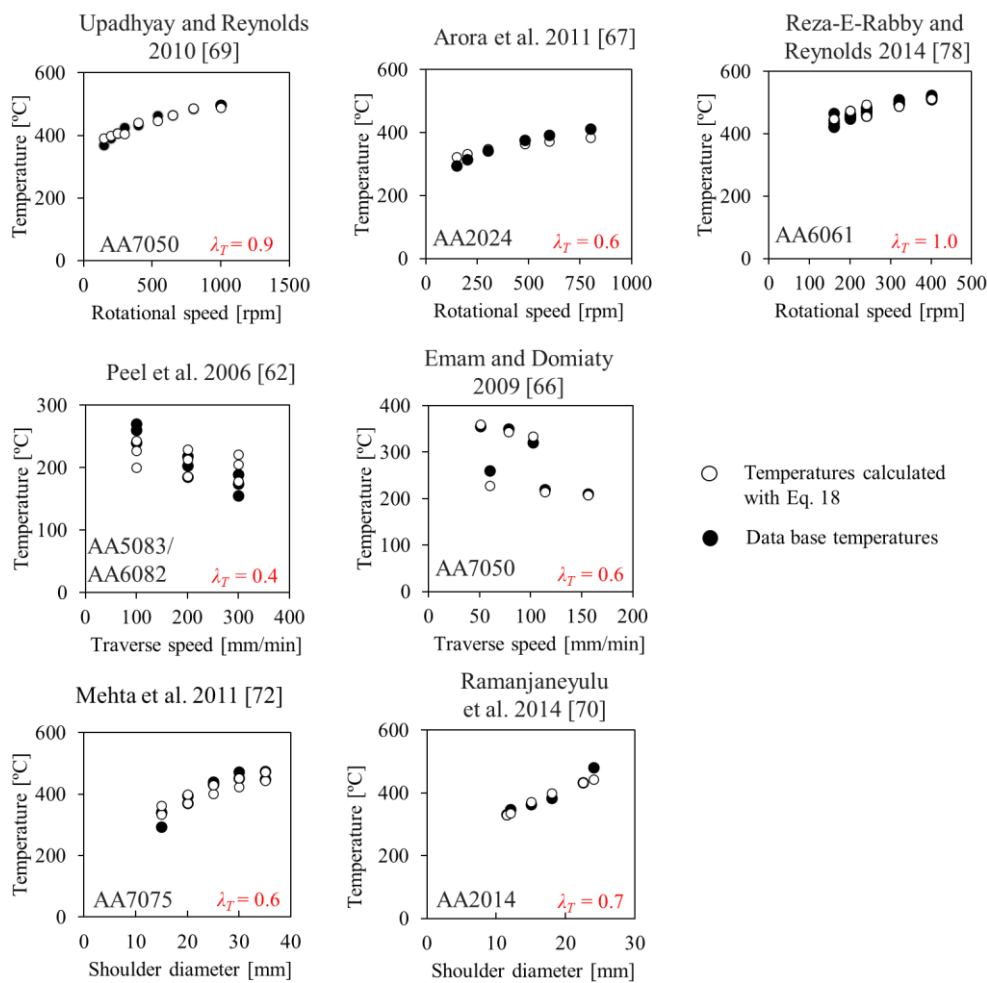


**Figure 24** – Comparison between the experimental temperature values, from the database, with the temperature values calculated with Eq. 18 (adapted from “Article C”).

### 3.3.2. Spot welding

#### 3.3.2.1. Aluminium alloys

The temperature measurements during the aluminium alloys spot welding tests enabled to conclude that the rotational speed was a secondary parameter governing the thermal cycles, contrary to that registered when analysing the heat generation in linear welding. Since for rotational speeds higher than 600 rpm, in spot welding, no variation of the welding temperature with the rotational speed was registered, the temperature model proposed for determining the temperatures in linear welding, had to be adapted in order to better fit the spot welding temperatures. In this way, for spot welding, the temperature coefficient  $C_T$  was adapted, by withdrawing the traverse speed from its formulation and by considering the important influence of the rotational speed on the heat generation threshold. So, a new coefficient,  $C_{T,SW}$ , is proposed,

$$\begin{cases} C_{T,SW} = \frac{G\omega}{\sqrt{t}}, \text{ for } \omega < \omega_{crit} \\ C_{T,SW} = \frac{G\omega_{crit}}{\sqrt{t}}, \text{ for } \omega \geq \omega_{crit}, \end{cases} \quad (19)$$

where  $\omega_{crit}$  is the critical rotational speed. According to current results,  $\omega_{crit}$  is equal to 600 rpm for aluminium alloys. The  $C_{T,SW}$  coefficient was tested using the experimental results for the AA2017, AA5083, AA6082 and AA7075 aluminium alloys. Figure 25 clearly shows that  $C_{T,SW}$  coefficient satisfactorily reproduces the evolution of the spot welding temperature, for the aluminium alloys, through the relationship

$$\begin{cases} T = \lambda_T \times K_{T,SW} \times C_{T,SW}^{\varphi_{SW}}, \text{ for } C_{T,SW} < C_{T,SW,cr} \\ T = \lambda_T \times T_{CT}, \text{ for } C_{T,SW} \geq C_{T,SW,cr}, \end{cases} \quad (20)$$

in which  $K_{T,SW}$  and  $\varphi_{SW}$  are constants and  $C_{T,SW,CR}$  represents the critical temperature coefficient value from which no further increase in the welding temperature occurs irrespective of the welding parameters used, i.e. irrespective of the tool diameter. Using the experimental results it was determined that  $K_{T,SW} = 1.34$  and  $\varphi_{SW} = 0.55$ . Once again, although the AA2017, AA5083, AA6082 and AA7075 aluminium alloys have different chemical compositions and mechanical strength, at room temperature (Figure 3), the evolution of the welding temperatures with  $C_{T,SW}$  was very similar for all the alloys. In

## Thermal Analysis

addition, although a very large range of experimental conditions was tested no threshold in the evolution of temperature with  $C_{T,SW}$  was observed in Figure 25, it is possible to admit that the value of  $T_{CT}$  is the same in the linear and spot welding, which was already determined to be 560 °C. This value of  $T_{CT}$  corresponds to a critical temperature coefficient value of  $C_{T,SW,cr} = 60000$ .

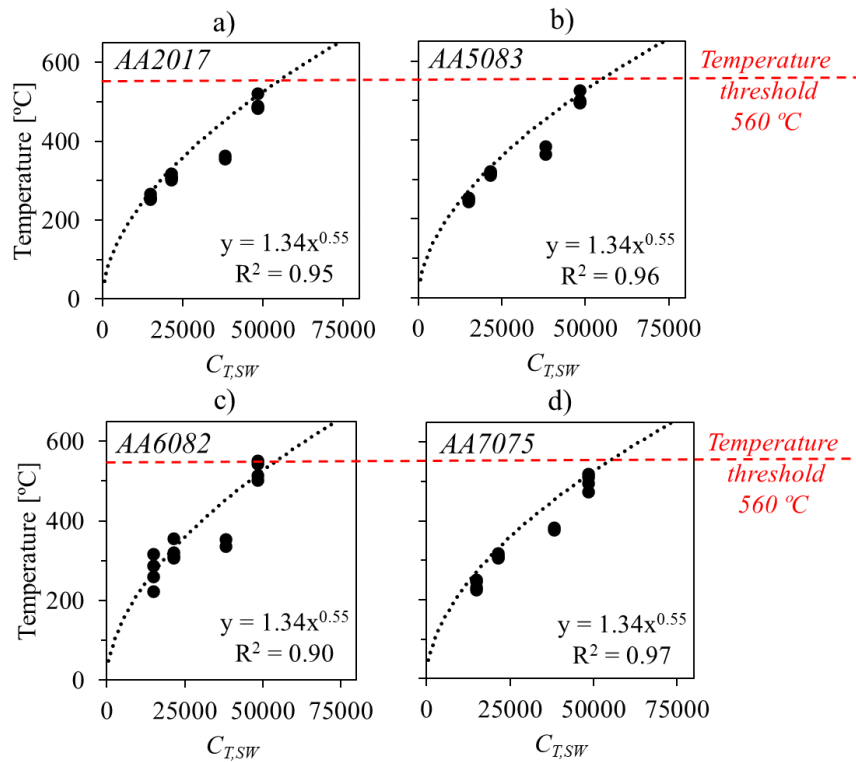


**Figure 25** –Evolution of welding temperature with the  $C_{T,SW}$  coefficient for the AA2017, AA5083, AA6082 and AA7075 aluminium alloys.

### 3.3.2.2. Ferrous alloys

In the spot welding of the steels no shoulder diameter related temperature threshold, as that registered for the aluminium alloys, was determined, being assumed that in the welding of the steels, the range of rotational speeds tested were below  $\omega_{crit}$ . In Figure 26 is shown the evolution of the welding temperature for the DC, HC and DP steels with  $C_{T,SW}$ . The figure shows that the  $C_{T,SW}$  coefficient satisfactorily reproduces the evolution of the spot welding temperature, with process parameters, for all the steels. Using Eq. 20 it was determined that  $K_{T,SW}$  is equal to 143, 359 and 582, while  $\varphi_{,SW}$  is equal to 0.17, 0.09 and 0.05, for the DC, HC and DP steels, respectively. Analysing the  $K_{T,SW}$  and  $\varphi_{,SW}$



coefficients values it is possible to conclude that, meanwhile  $K_{T,SW}$  increase as the strength of the steels increase,  $\varphi_{,SW}$  decreases as the strength of the steels increase, enabling to model the process parameter independent temperature threshold depicted in Figure 20, for the highest strength steel. That temperature threshold, which is common to all the steels, is in the range of 1100 °C, corresponding to a  $C_{T,SW,cr} = 200000$ .

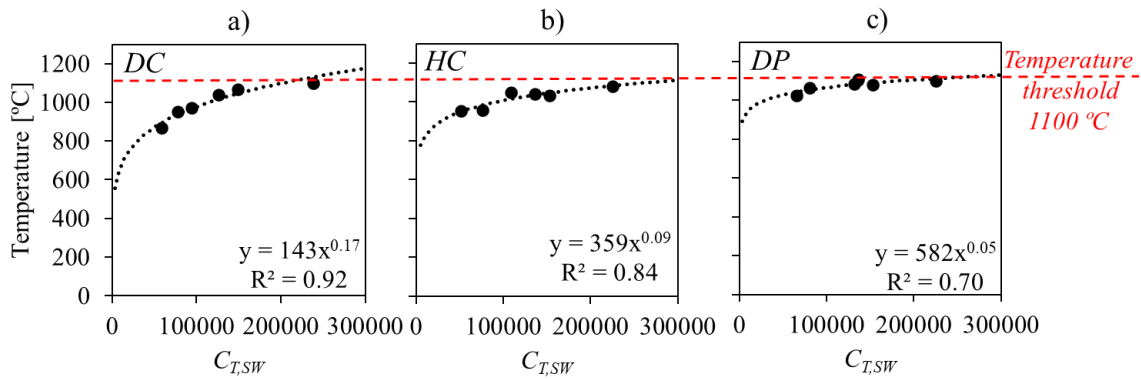


**Figure 26** –Evolution of welding temperature with the  $C_{T,SW}$  coefficient for the DC, HC and DP steels.

To conclude the chapter it is possible to say that the accurate prediction of the experimental results, for the very large range of welding conditions and base materials tested, proves that the proposed temperature coefficient is reliable for predicting the evolution of temperature, for spot and linear welding.



## 4. Mechanical Analysis

---

In this chapter, a mechanical analysis of the welding process, focusing on the interaction between the tool and the base material, is addressed. First, a literature review about the influence of the process parameters on the transport of material during welding, on the contact conditions at the tool/workpiece interface and on the strain rates in the stirred volume, is presented. The literature review also addresses the torque evolution with process parameters, since this machine output was already found to be, not only the most convenient parameter for evaluating the mechanical energy spent in the welding process, but also a machine output with important potential to be used in the real time control of the stir-based operations. After the literature review, the results obtained in the current work are discussed. The influence of the tool dimensions, rotational and traverse speeds and base material properties on the material flow, on the strain rates and on the contact conditions developed during welding is addressed, in first, using the results of the numerical analysis performed on this subject. In second, the evolution of the tool torque with processing parameters, for the spot and linear welding of aluminium alloys and steels, which was also assessed by performing a coupled experimental and numerical analysis, is discussed. The results of that analysis enabled the development of a new analytical model to predict the tool torque, from process parameters, which is presented and validated at the end of the chapter.

### *4.1. Literature review*

#### *4.1.1. Transport of material*

As stated before, in FSW, the material stirring is promoted by the rotational and translational movements of the tool. The tool/workpiece interaction is also responsible for the heating and softening of the stirred material, and the combination of these effects with the tool motion, promote a very complex material flow during processing.

One of the first works that aimed to analyse the transport of material in FSW, through the use of markers, was performed by Reynolds 2000 [103]. Based on the post-

welding visualisation of the trajectory of the markers, the author characterised the transport of material in FSW as an in-situ extrusion process, where the tool shoulder, the backing plate and the adjacent base material form an “extrusion chamber” moving with the tool. However, after the pioneer contribution from Reynolds 2000 [103], the characterization of the material flow mechanisms during FSW remained a subject of research. According to Liechty and Webb 2007 [104] and as is shown in Figure 27a, the material, from both the advancing and retreating sides, is transported one pin diameter backwards relative to the tool translation movement. Liu and Nelson 2016 [105] determined that the material intercepting the tool pin path is placed behind the tool approximately at the same transverse position as its initial location, as represented in Figure 27b. Although, Liu and Nelson 2016 [105] also stated that the material at the advancing side is transported forward, due to the pin movement and rotates to a position behind it, being disrupted in arc-shaped fragments, while the material at the retreating side is only transported backwards relative to the tool motion. The spacing between the arc-shaped fragments is typically the same as the distance travelled by the tool during a single rotation [106,107].

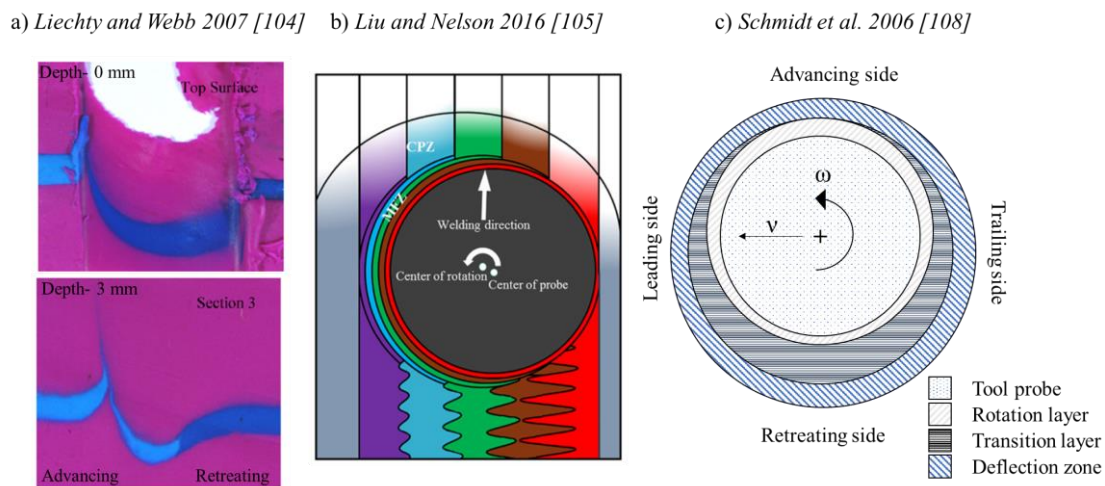


**Figure 27** - Material flow representation (adapted from [104,105,108]).

According to Schmidt et al. 2006 [108] the material flow promoted by the pin may be divided in three different layers: a rotation layer, a transition layer and a deflection layer, as shown in Figure 27c. The rotation layer is the one closest to the pin, where the material may stay for more than one rotation, while the transition layer is the one located between the rotation and the deflection layers. According to the authors, during welding,

the base material coming from the transition layer, enters the rotation layer and then returns to the transition layer, being finally deposited. The deflection layer, adjacent to the transition layer, consists of the TMAZ region. As shown in Figure 28, two additional flow partitions were also already related with the tool geometry, which are the shoulder driven flow and the pin-driven flow [109–111].

The tool pin is the main tool component responsible for the material stirring and mixing in the thickness direction, especially in thick plates [112]. Elangovan and Balasubramanian, 2007 [113] and Trimble et al. 2015 [114] used the volume displacement ratio, i.e. the volume occupied by the pin while rotating divided by the volume held by the pin while stationary, to characterise the transportation of material for different tool pin geometries. They found that cylindrical pins have a volume displacement ratio of 1, concluding that the transport of material from the leading to the trailing side of the tool results from the shearing action of the pin. They also found that the cylindrical pin produces less plastic deformation and stirring than square (with a volume displacement ratio of 1.42) or triflute (with a volume displacement ratio of 1.49) pin geometries. The flat faces of the square pin or the helical flutes of the triflute, create a pulsating stirring action due to the associated eccentricity. The pulsating stirring action offers resistance to the regular flow of plasticised material, which also generates additional frictional heat [114,115]. Threaded pins have also been used by several authors [17,116–118] to improve the material flow during welding. According to them, the use of threaded pins improves the vertical transport of material during welding due to the generation of an additional downforce.

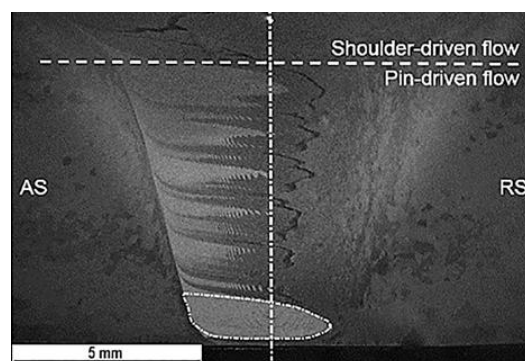


**Figure 28** – Shoulder and pin-driven flow zones (adapted from Shah et al. 2018 [111]).

## Mechanical Analysis

The shoulder is the main responsible for the heat generation, allowing the material softening and its transport by the tool during welding [17]. According to Leal et al. 2008 [53], the tool shoulder also has a very important role in the transport of material during welding, since the onion rings in the TMAZ, which are composed by intercalated material layers, result from the incorporation of the plasticised material dragged by the shoulder into the shear layer surrounding the pin. In the welding of thin plates, Galvão et al. 2013 [112] also concluded that in order to avoid defects formation, the shoulder geometry must be carefully selected, since this tool component should be able to drag material into the pin influence zone. The influence of the tool shoulder diameter on the plastic deformation was analysed by Ramanjaneyulu et al. 2014 [70]. According to the authors, increasing the shoulder diameter diminishes the volume of the shoulder driven-flow. However, in spite of this, the volume of material dragged around the tool increases, and consequently, the total TMAZ volume increases.

Although the tool geometry determines the characteristics of the material stirring, the material flow patterns also depend on the level of plasticization of the material under the tool, which in turn depends on the welding temperatures and on its physical and mechanical properties [112]. For instance, in FSW of dissimilar aluminium alloys, Li et al. 1999 [119] and Liechty and Webb 2007 [104], observed that when the softer aluminium alloy is placed at the advancing side of the tool, it is stirred into the harder alloy, placed at the retreating side, and a vortex flow is formed, which is more pronounced than when the alloys being joined have similar strength. When the harder alloy is placed at the advancing side of the tool, being stirred against the softer material, the vortex flow becomes minimal. Also, in the butt welding of AA6082 and AA5083 aluminium alloys, Leitão et al. 2012 [39], observed that under the same welding conditions, the heat-treatable alloy had better weldability than the non-heat-treatable alloy. According to the authors, the AA6082 alloy displays a more intense flow softening at high temperatures, than AA5083 alloy, which allows an easier dragging and mixing of this base material during welding. On the other hand, the AA5083 alloy, which is sensitive to hardening at high strain rates, is more difficult to be dragged and stirred by the tool, and because of that, has lower weldability than the AA6082 alloy. In dissimilar and similar friction stir lap welding (FSLW) of AA5754 and AA6082 aluminium alloys, Costa et al. [120,121] and Sabari et al. 2020 [40], observed that the upward material flow was much more significant when the AA6082 alloy was the lower plate in the lap joint configuration, conducting to the formation of severe hooking defects. In the same way, in similar

welding, the heat-treatable alloy was found to be more sensitive to defects formation, such as the hook defect, than the non-heat-treatable alloy.

Globally, the results discussed in this item show that, in FSW, the weldability of the alloys is closely related to the transport of material by the tool, which in turn is a mechanical process that is determined by the plastic properties of the base materials being welded, by the tool geometry and by the joint configuration.

#### 4.1.2. *Contact conditions*

As described in the previous section, in FSW, the interaction between the tool and the base material is very complex. This interaction is determined, not only, by the tool geometry, but also by the contact conditions between the tool and the material being welded/processed. Schmidt et al. 2003 [52] defined three possible contact conditions, between the tool and the workpiece: full sticking contact conditions, when the stirred material stick to the moving tool, full slipping contact conditions, when the material remains stationary relative to the movement of the tool, and partial sticking/slipping contact conditions, when the workpiece material accelerates to a velocity less than the tool surface velocity. To assess the contact conditions, Schmidt et al. 2003 [52] proposed the use of a contact state variable coefficient ( $\delta$ ) to quantify the sticking fraction, already defined in Eq. 4. As already explained, when the contact state variable coefficient is equal to 1, it means that the contact is 100% sticking. When the contact state variable coefficient is equal to zero, it means that the contact is 100% slipping. On the other hand, a slipping fraction ( $\delta_s$ ) can be calculated as

$$\delta_s = 1 - \delta. \quad (21)$$

Through a tracing particle analysis, several authors [105,108,122,123] reported that the ratio between the angular velocity of the material and the rotational speed of the tool is always lower than 1, which is an evidence that mixed slipping/sticking conditions prevail at the tool/workpiece interface during welding. Schmidt et al. 2006 [108] and Morisada et al. 2015 [123], for example, calculated that the average velocity in the transition zone is only a fraction of the rotational speed of the pin, varying approximately between 0.1 to 0.3, according to Schmidt et al. 2006 [108], and between 0.4 to 0.7, according to Morisada et al. 2015 [123].

Several authors [18,62,124] also observed that during FSW, the amount of material mixing increases when the tool rotational speed increases. This was related to the fact that sticking contact conditions prevail at the tool/workpiece interface, at high rotational speeds, allowing the material in contact with the pin to perform several revolutions around it [104]. However, contrary to these findings, Ramanjaneyulu et al. 2014 [70] and Morisada et al. 2015 [122,123], reported slipping contact conditions for very high rotational speeds, which they attributed to the high angular speed of the tool. For this condition, the authors observed surface defects and small voids in the stir zone.

In addition to the material flow analysis, using tracing particles, Arora et al. 2009 [125] used an empirical equation for estimating the slipping fraction during FSW:

$$\delta_s = 0.2 + 0.6 \times \left( 1 - \exp \left( -\delta_0 \frac{\omega r_m}{\omega_0 r_s} \right) \right). \quad (22)$$

In the equation,  $\delta_0$  is a constant for slip, which may be adjusted to fit the experimental results,  $\omega_0$  is a reference value for the tool rotational speed,  $r_s$  is the radius of the shoulder and  $r_m$  is the average of the pin and shoulder radius. Arora et al. 2011 [97] determined that, for the FSW of AA2524, 304L and Ti-6Al-4V,  $\delta_0$  was equal to 3, 2 and 2.5, respectively, and  $\omega_0$  was taken as 400 rpm for all materials.

For the FSW of the aluminium alloy AA7075-T6, Mehta et al. 2011 [72] used the following expression for estimating the spatial variation of the slipping fraction

$$\delta_s = 0.31 \times \exp \left( \frac{\omega r}{1.87} \right) - 0.026, \quad (23)$$

where  $r$  is the radius of the tool. According to the authors, the previous equation is only valid for values of  $\omega r$  from 0.1 to 1.6 m/s.

Contrary to the previous models (Eq. 22 and 23), which relate the contact conditions with the rotational speed and the tool diameter, Qian et al. 2012 [98] proposed the following equation,

$$\delta_s = 1 - A \times \exp \left[ - \left( \frac{Q_E}{RT_{st}} \right)^{\beta_{sh}} \right], \quad (24)$$



based on a modified Arrhenius equation, for relating the slipping fraction with the base material properties and the welding temperature. In the equation,  $A$  and  $\beta_{sh}$  are experimental constants,  $Q_E$  is the activation energy for deformation,  $R$  is the universal gas constant and  $T_{st}$  is the stir zone temperature. For the FSW of the AA 1100-H14 aluminium alloy, the authors determined that  $A$  and  $\beta_{sh}$  are equal to  $4.07 \times 10^7$  and 0.89, respectively.

The results discussed above show that contact conditions in FSW are determined by the tool geometry, the welding parameters and the base material properties [105]. However, although the friction is assumed as the primary physical phenomena governing FSW, the real contact conditions developed during welding are still not well understood. Since up to date, there is no experimental technique for measuring  $\delta$ , the characterization of the contact conditions remains a subject of research. The difficulty in determining it, forced the use of simplified contact conditions in most of the works published on the modelling of the FSW process, i.e. pure sticking [94,126–134] or pure slipping [47,94,131,134–136] contact conditions were assumed on most of the works performed on the numerical simulation of the FSW process. Mixed slipping-sticking contact conditions were modelled, by some authors, who prescribed specific velocity profiles at the tool/workpiece interface [94,131,137–140].

### 4.1.3. Strain rates

During FSW, the intense strain and strain rates induced by the tool on the base materials, and the very high temperatures, are the main responsible for the microstructural changes in the stirred volume, which are mainly determined by the plastic deformation and by the precipitation kinetics and/or the dynamic recrystallisation. The understanding of the mechanisms that promote the plastic deformation, and the development of models that can estimate the strain rates and the temperatures induced by the tool during welding, can help in predicting the final microstructure/strength of the welds, as well as the possibility of defects formation.

Several works attempted to analyse and measure the strain rates during FSW, by using different techniques, such as microstructural analysis, tracing materials, analytical models and numerical simulation. Masaki et al. 2008 [141] and Kumar et al. 2018 [142] determined that the strain rate values increased during FSW by increasing the tool rotational speed. Kumar et al. 2018 [142] also reported that the rotational speed presented higher influence on the strain rate than the traverse speed. Contrary to this, Gerlich et al.

2006 [57] and Gerlich et al. 2007 [58], reported a decrease of the strain rate with the increase of the rotational speed. The authors attributed this behaviour to the local melting of second phase particles at the tool/workpiece interface. Frigaard et al. 2001 [56] and Kumar et al. 2018 [142] also measured lower strain rate values in the stirring zone, than that previewed based on the analysis of the angular velocity of the tool. According to the authors, these results indicate the occurrence of slipping contact conditions between the tool and the workpiece.

Long et al. 2007 [143] and Reynolds 2008 [107] proposed a simplified model to calculate the strain of the material in the shear layer around the pin:

$$\varepsilon = \ln\left(\frac{l}{APR}\right) + \left| \ln\left(\frac{APR}{l}\right) \right|. \quad (25)$$

The previous equation considers the distance that the tool advances per revolution (APR), and calculate  $l$  using the equation

$$l = 2r_p \cos^{-1}\left(\frac{r_p - x}{r_p}\right) \quad (26)$$

where  $r_p$  is the tool pin radius, and  $x$  is the distance normal to the welding direction, at the retreating side of the tool. This model is supported by the assumption that to satisfy the mass balance, at each tool revolution, a volume of material, given by the product of the pin diameter by the pin height and the tool advance per rotation, has to be transported. This material volume is transported backwards, by approximately one tool diameter, being assumed that there is no vertical flow of the material. Due to the simplicity of the model, the material flow promoted by the shoulder and the bottom of the pin is not considered, which limits its application.

Based on Eq. 25, Ramanjaneyulu et al. 2014 [70] proposed that the strain rate can be calculated by

$$\dot{\varepsilon} = \frac{\varepsilon}{t_i} \quad (27)$$

where  $t_i$  is the time in seconds, which can be calculated by dividing APR by the traverse speed.

According to Chang et al. 2004 [59], because of the slipping/sticking contact conditions, the flow rate may be proportional to, or lower than, the rotational speed of the tool. Taking the assumption that the material flow velocity is about half of the rotational speed of the pin, the authors calculated the strain rate using the following equation

$$\dot{\epsilon} = \frac{\omega}{2} \times \frac{2\pi r_d}{h_d} \quad (28)$$

in which  $r_d$  and  $h_d$  are the effective radius and depth of the dynamically recrystallised zone.

For FSSW with a flat shoulder tool and a cylindrical pin, Roth et al. 2014 [136] proposed the following equation

$$\dot{\epsilon} = \frac{\omega}{8w} (3r_p + r_s), \quad (29)$$

to calculate the average strain rate in the shear layer. In the equation,  $w$  is the shear layer width, which according to Tello et al. 2009 [144] may be calculated by:

$$w = r_p \left[ \frac{2(T_{st}-T_0)}{\eta A} \left( \frac{\tau \times r_p^2}{k} \right)^n \left( \frac{\eta K_0 \omega}{(T_0-T_{in})} \right)^{n+1} \right]^{1/2}. \quad (30)$$

In the previous equation,  $A$  and  $n$  are the Sheppard and Wright constitutive material parameters,  $k$  is the base material thermal conductivity,  $\eta$  is the welding process efficiency, which considers mechanical energy converted into heat,  $K_0$  is the modified Bessel function of the second kind and zero order,  $\tau$  is the shear stress of the alloy,  $T_0$  is the temperature at the interface between the shear layer and the base material,  $T_{st}$  is the temperature at the interface between the shear layer and the base material,  $T_{st}$  is the temperature in the stirring zone and  $T_{in}$  is the initial temperature.

Table 11 summarises the strain rate values reported in the literature, determined using different techniques, for several base materials and process conditions. Analysing the table, it is possible to conclude that the estimated strain rate values widely vary, between 1 to 1600 s<sup>-1</sup>, in accordance with the different measurement techniques, process

## Mechanical Analysis

parameters and base materials. This indicates that it is still necessary to deepen the study of the plastic deformation during FSW and also to develop experimental methodologies to quantify it.

**Table 11** – Range of strain rates reported in the literature (adapted from “Article D”).

Technique	Author	Base Material	Rotation speed [rpm]	Traverse speed [mm/min]	Strain rate [s <sup>-1</sup> ]
<b>Microstructural</b>	Frigaard et al. 2001 [56]	AA6082 and AA7018	1500	720	1-20
	Gerlich et al. 2006 [57]	AA7075-T6	1000-3000	0	20-650
	Gerlich et al. 2007 [58]	AA2024 T351	750-3000	0	0.6-1600
	Masaki et al. 2008 [141]	AA1050	600-1200	100	1.7-2.7
<b>Tracers</b>	Chen and Cui, 2009 [145]	A356 (Al-7Si-0.3Mg)	740	168	3.5-85
	Morisada et al. 2015 [122]	A1050	1000	400	13.4-15
	Kumar et al. 2018 [142]	Visco-plastic fluid	75-425	50-110	8-44
	Liu et al. 2019 [146]	Copper C1100P	800	150	20.8
<b>Analytical model</b>	Chang et al. 2004 [59]	AZ31	180-1800	90	5-50
	Long et al. 2007 [143]	5083-O, 2219-T87 and 7050-T751	544-844	76.2	20-350
	Ramanjaneyulu et al. 2014 [70]	AA2014-T6	1000	600	123-160
<b>Numerical</b>	Nandan et al. 2006 [147]	304 Stainless Steel	300	101	130
	Nandan et al. 2006 [148]	AA6061	344	95	150
	Nandan et al. 2007 [149]	AISI 1018	450	25.2	40
	Mukherjee and Ghosh, 2010 [150]	AA5083	1500	50.8	87
	Ammouri et al. 2015 [151]	AZ31B alloy	600-2000	75-900	34-122
	Sharghi and Farzadi, 2018 [152]	AA6061/ Al-Mg2Si	1120	120	975
	Du et al. 2020 [153]	AA2219, AA5083 and AA6082	150-1302	100-1100	23-434

#### 4.1.4. *Welding torque*

The tool torque is a FSW process response that can be related to the heat input, material flow, process parameters and defect formation. Longhurst et al. 2010 [154] propose the use of the tool torque as a parameter to control the welding process, instead of the axial force. According to these authors, operating the FSW process in torque control would allow the process parameters to be adapted faster to any changes in the workpiece characteristics. Qian et al. 2012 [98], Galvão et al. 2012 [155] and Kumari et al. 2019 [156] also found that the tool torque signal could be related to the formation of surface defects and to the contact conditions, at the tool/workpiece interface, during welding. In the next, a review of the published works on the relationship between the tool torque with the thermo-mechanical conditions and with the FSW process parameters is presented.

In order to have a much broader analysis on the evolution of the tool torque with the processing parameters, a database containing data from more than 300 welds, in AA2xxx, AA5xxx, AA6xxx and AA7xxx aluminium alloys, in lap and butt joint configurations, was created. The references used to collect the data are presented in Table 12. The database generated comprises not only the tool torque ( $M$ ) registered by the different authors, but also the rotational and the traverse speeds, the pin diameter, the pin length, the shoulder diameter and the geometry parameter computed for the tools used in each work. In Figure 29 is represented the range of torque results, rotational and traverse speeds, pin diameters, pin lengths, shoulder diameters and geometry parameters covered in the database, for each aluminium alloy. Due to the large variety of process parameters and tool dimensions considered in the database, the values registered for the torque varied in the range of 6 to 320 Nm.

The evolution of all the torque values, considered in the database, with the rotational speed, traverse speed and geometry parameter is shown in Figure 30a to c. The effect of the different process parameters on torque was ranked based on the Pearson correlation coefficient ( $R^2$ ). From the figure, it is possible to conclude that both the tool dimensions and the tool rotational speed may be statistically related to the torque, while no important relation between the traverse speed with the torque may be inferred. Comparing the evolution of the torque with the rotational speed and the tool geometry, it is also possible to conclude that both have a comparable influence on the torque since the Pearson correlation coefficients are similar.

**Table 12** – Experimental works that analyse the influence of the processing parameters on torque during FSW of aluminium alloys (Adapted from “Article C”).

AA 2xxx	AA 5xxx	AA 6xxx	AA 7xxx
<ul style="list-style-type: none"> <li>• Yan et al. 2005 [157]</li> <li>• Long et al. 2007 [143]</li> <li>• Arora et al. 2011 [67]</li> <li>• Su et al. 2013 [159]</li> <li>• Ramanjaneyulu et al. 2014 [70]</li> </ul>	<ul style="list-style-type: none"> <li>• Peel et al. 2006 [62]</li> <li>• Long et al. 2007 [143]</li> <li>• Leitão et al. 2012 [158]</li> <li>• Quintana and Silveira 2017 [160]</li> <li>• Cuellar and Silveira 2017 [161]</li> <li>• Costa et al. 2019 [68]</li> </ul>	<ul style="list-style-type: none"> <li>• Peel et al. 2006 [62]</li> <li>• Emam and Domiaty 2009 [66]</li> <li>• Cui et al. 2010 [93]</li> <li>• Wade and Reynolds 2010 [74]</li> <li>• Leitão et al. 2012 [158]</li> <li>• Reza-E-Rabby and Reynolds 2014 [78]</li> <li>• Banik et al. 2018 [162]</li> <li>• Costa et al. 2019 [68]</li> </ul>	<ul style="list-style-type: none"> <li>• Long et al. 2007 [143]</li> <li>• Emam and Domiaty 2009 [66]</li> <li>• Upadhyay and Reynolds 2010 [69]</li> <li>• Mehta et al. 2011 [72]</li> </ul>

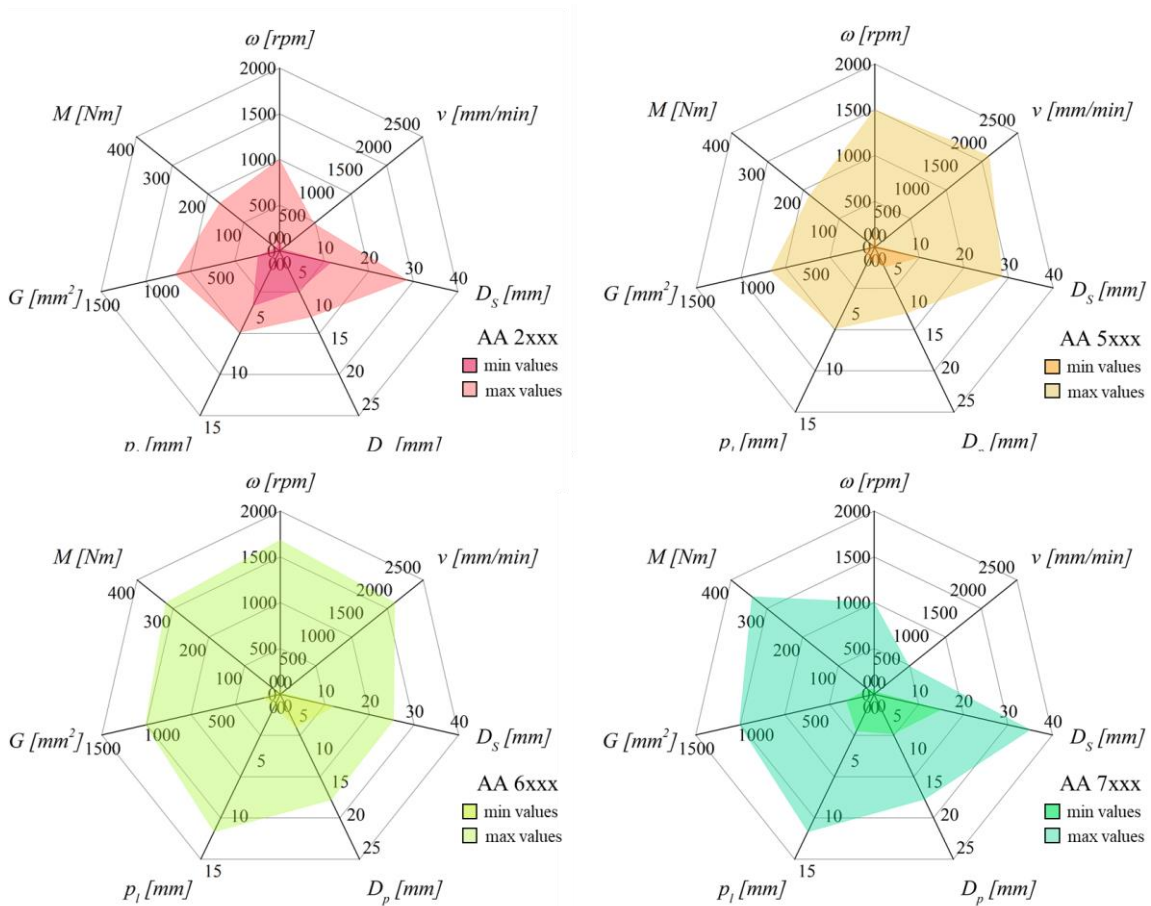


**Figure 29** - Range of rotational speeds ( $\omega$ ), traverse speeds ( $v$ ), shoulder diameters ( $D_s$ ), pin diameters ( $p_d$ ), pin lengths ( $p_l$ ), geometry parameters ( $G$ ) and torque ( $M$ ) values covered by the database.

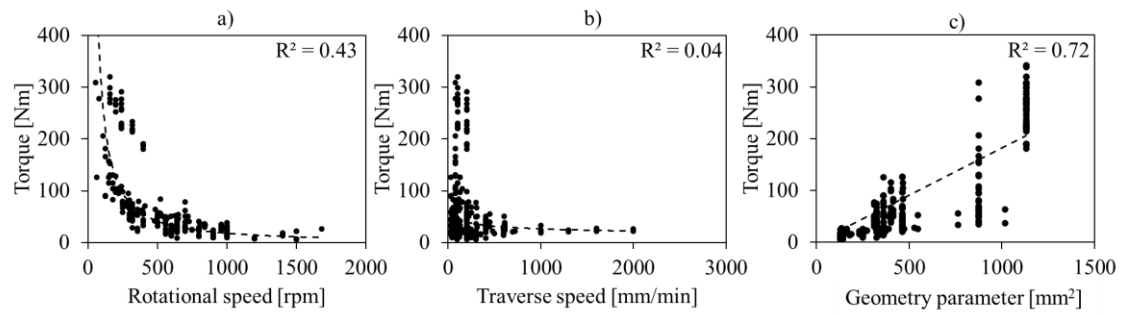


**Figure 30** – Evolution of the torque experimental values, from the database, with the rotational speed (a), traverse speed (b) and geometry parameter (c) (adapted from “Article C”).

Based on the previous analysis, the evolution of the torque versus the product  $G\omega$  was analysed and plotted, for each base material analysed in the database, as is shown in Figure 31a. In the figure, each colour identifies different levels of geometry parameters and each symbol identifies the different grade of aluminium alloys considered in the database. Analysing the results, it is possible to conclude that irrespective of the base material welded, the torque results may be divided in different curves/trends in accordance with the tool dimensions. The registered torque values are higher for the tools with larger dimensions. According to Arora et al. 2009 [67] and Quintana et al. 2017 [161] the increase of the torque with the tool shoulder diameter is justified with the increase of the contact area between the tool and the workpiece.

For each curve of Figure 31a, it is also possible to observe that the torque decreases exponentially with the increase of the rotational speed. This was justified by several works with the influence that the rotational speed has on the welding temperatures and, consequently, on the flow strength of the base materials during welding [62,93,158,160]. However, meanwhile for the lower geometry parameter values, a trend line may be plotted fitting almost accurately the decrease of the torque with the rotational speed, for all the materials, for the larger geometry parameter values (green symbols), an important dispersion of results may be observed. This dispersion is shown in more detail in Figure 31b, where the different traverse speeds used are identified. Analysing Figure 31a and b it is possible to conclude that the traverse speed only has an important influence on the torque values when tools with large dimensions are used.

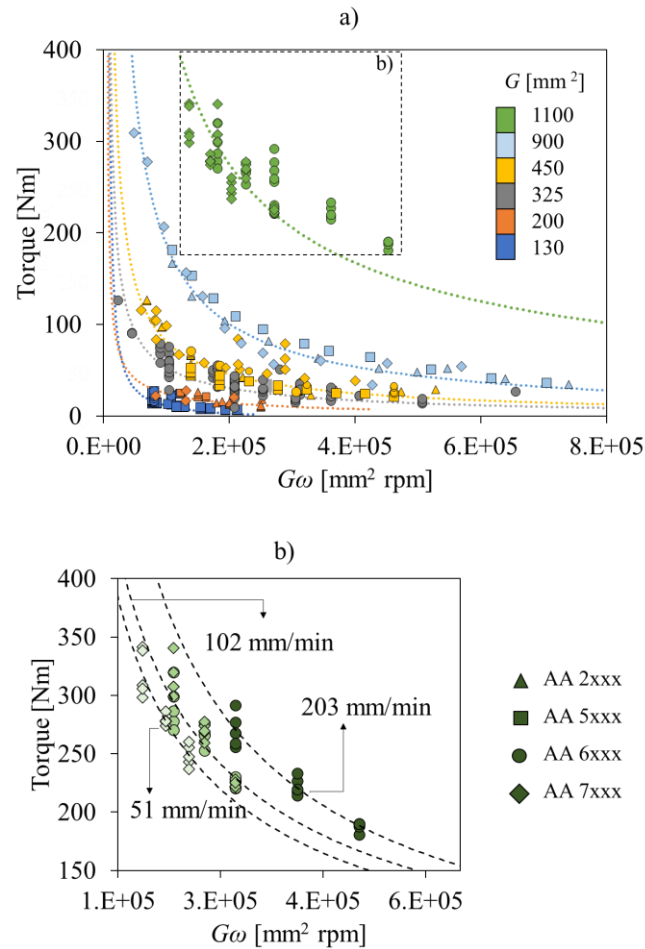


**Figure 31** – Evolution of torque with the geometry parameter multiplied by the rotational speed ( $G\omega$ ) (adapted from “Article C”).

In addition to the influence of the process parameters on torque, an important influence of the base material plastic properties, was observed by Galvão et al. 2012 [155] in similar and dissimilar butt welding of AA5083-H111 and copper-DHP, and by Sabari et al. 2020 [40], in similar and dissimilar FSLW of AA5754 and AA6082 aluminium alloys. Galvão et al. 2012 [155] found that the torque registered during welding depends on the base materials combinations. The highest and lower torque values were recorded in the similar welding of copper, and in the dissimilar welding of aluminium/copper, respectively. The lower torque values during the dissimilar welding were justified by the formation of intermetallic compounds, with low melting temperature, which induced tool slipping during welding. On the other hand, Sabari et al. 2020 [40] observed that the torque values were higher in AA5754-AA6082 dissimilar lap welding than in AA6082 similar lap welding. This torque evolution showed that the presence of the AA5754 alloy,



regardless of being located at the bottom or at the top of the lap joint, promoted an increase in the welding torque. The lower torque values, registered for the AA6082 alloy, were related to the thermal softening of the heat-treatable alloy during welding.

The influence of the base material thickness on torque was analysed by Leitão et al. 2012 [158]. According to the authors, for the same welding pitch ( $\omega/v$ ) the torque was always lower for the welds performed in thinner plates. The lower torque values were attributed, by the authors, to the lower amount of material being processed by the tool and to the more homogeneous temperature distribution throughout the thickness of the thinner plates.

As it was shown above, the torque evolution is also very sensitive to the welding parameters. Based on these findings, torque analysis is being used for establishing relationships between FSW process parameters and process outputs, such as welds quality. More precisely, modelling the relation between the process parameters and the tool torque is expected to enable, for example, developing digital tools to be used in the online control of the joints quality.

The tool torque can be modelled to take into account the individual contribution of the different tool components (shoulder and pin), to the welding torque, through the following equation [52,163]:

$$M = M_{shoulder} + M_{pin\ surface} + M_{pin\ bottom} \quad (31)$$

$$M = \int_{r_p}^{r_s} (r\tau)2\pi r dr + (r_p\tau)2\pi r_p h + \int_0^{r_p} (r\tau)2\pi r dr \quad (32)$$

where  $r$  is the radial distance from the centre of rotation and  $\tau$  is the shear stress due to the sticking/slipping contact condition. The shear stresses in the shear layer surrounding the pin may be estimated by [52,67,136]

$$\tau = \delta \times \tau_p + (1 - \delta)\tau_f \quad (33)$$

where  $\tau_p$  is the shear stress due to the sticking contact and  $\tau_f$  is the shear stress due to the slipping contact. The shear stress due to the sticking contact can be estimated based on the von Mises yield criterion as follows:

$$\tau_p = \frac{\sigma_y}{\sqrt{3}}. \quad (34)$$

In the equation,  $\sigma_y$  is the material yield strength. The shear stress due to the slipping contact condition can be estimated using the Coulomb's friction law

$$\tau_f = \mu_f P \quad (35)$$

where  $\mu_f$  is the friction coefficient between the tool and the workpiece and  $P$  is the contact pressure. For a tool with a cylindrical pin, without threads, and a circular shoulder, with a cone angle  $\beta_s$ , the following expression can be derived to determine the tool torque:

$$M = \frac{2}{3} \pi \tau [(r_s^3 - r_p^3)(1 + \tan\beta_s) + r_p^3 + 3r_p^2 p_l]. \quad (36)$$

Using Eqs. 33 to 36, the torque can be modelled by [52]

$$M = \frac{2}{3} \pi [\delta \tau_p + (1 - \delta) \mu_f P] \times [(r_s^3 - r_p^3)(1 + \tan\beta_s) + r_p^3 + 3r_p^2 p_l]. \quad (37)$$

With the above equation, it is possible to calculate the torque for full sticking conditions ( $M_{sticking}$  when  $\delta = 0$ ) and for full slipping conditions ( $M_{slipping}$  when  $\delta = 1$ ). Although, the previous model requires the knowledge of the base material mechanical properties, the slipping fraction and the friction coefficient, under the thermo-mechanical conditions imposed by the FSW process, which hinders its implementation in process control. A simpler model that relates the torque with the rotational and traverse speeds was proposed by Colegrove and Shercliff 2003 [164]:

$$M = A_M \frac{v^{\alpha_M}}{\omega^{\beta_M}}. \quad (38)$$

where  $\beta_M$ ,  $\alpha_M$  and  $A_M$  are constants. The previous model can only predict the evolution of torque if the values of  $\omega$  and  $v$  are kept inside a certain range. For instance, when the rotational speed is close to zero, the torque values become too high, and for very high

values of rotational speed, the torque values become zero. Based on this model limitations, Cui et al. 2010 [93] developed an alternative model:

$$M = M_0 + M_f e^{-n_M \omega}. \quad (39)$$

In the previous equation,  $M_0$  is the minimum torque value,  $n_M$  is the decay parameter, and  $M_f$  is the pre-exponential parameter. Also, according to Cui et al. 2010 [93], the maximum value of torque occurs when the rotational speed is close to zero, and can be calculated using Eq. 37, for a pure sticking condition, assuming that the mechanical strength of the material is equal to the ultimate tensile strength at room temperature.

Leitão et al. 2012 [158] proposed another fitting curve which relates the tool torque with the rotational speed:

$$M = a \times \omega^{-b}. \quad (40)$$

In this equation,  $a$  and  $b$  are constants. According to the authors, the constant  $a$  depends on the base material thickness, being independent of the base material properties, while the constant  $b$  was found to have a strong relationship with the welding speed used. Another equation, which relates the tool torque with the welding temperature, was proposed by Tello et al. 2009 [144]

$$M = \frac{2\pi k(T_0 - T_{in})}{\eta \omega K_0} \quad (41)$$

where  $k$  is the thermal conductivity of the base material,  $\eta$  is the efficiency of the process,  $K_0$  is the modified Bessel function of the second kind and 0 order and  $T_0$  and  $T_{in}$  are the temperature in the shear layer interface with the base material and the initial temperature of the base material, respectively.

In general, the torque models reported to date are focused on a limited range of processing parameters and were developed for a very specific material, tool geometry or plate thickness. This implies that most of the models constants are not valid when applied to other experimental conditions. Also, some of the mentioned models require difficult to determine variables, such as material properties, contact conditions or friction coefficient at the very high temperatures and strain rates imposed by the process. To overcome the

above-described limitations, in the current dissertation, a new model that estimates the torque values, in FSW and FSSW, by considering a very large range of process parameters, was developed and validated using the results from current work and the torque results covered by the database.

### *4.2. Numerical analysis of the stir mechanisms*

A parametric analysis on the influence of the tool dimensions, tool velocities and base material plastic properties on the stir mechanisms, i.e. on the material flow, stirred volume, contact conditions and strain rates, was conducted using numerical simulation. Based on the numerical simulation results published in “Article D”, the influence of the above-described processing parameters, on the material flow, may be summarised as shown in Figure 32, where the streamlines and the strain rate distribution maps, in the welds cross sections, for different welding conditions, are represented. The results in the figure were obtained for the AA6063-T6 aluminium alloy and by varying the rotational speed, between 300 to 1200 rpm, and the traverse speed, between 250 to 1000 mm/min. The tool dimensions values were set assuming proportionality between the shoulder diameter and the thickness of the plates, by using Eq. 16. The pin dimensions were established using a  $D_s/D_p$  ratio of 3, and a  $p/t$  ratio of 0.85 [102]. As summarised in Table 13, the thickness of the base material, shoulder diameter, pin diameter and respective geometry parameters were varied between 2 and 10 mm, 12 to 30 mm, 4 to 10 mm and 134 to 974 mm<sup>2</sup>, respectively.

The streamlines in Figure 32a show that, during welding, the material is stirred from the advancing to the retreating side of the tool, being deposited approximately one pin diameter backwards, relative to the tool translational movement. Comparing the streamlines in the different images, it is also possible to conclude that for a constant tool rotational speed, increasing the traverse speed, led to a reduction in the stirred volume. This result is related to the decrease in the weld pitch (rot/min), which reduced the volume of material stirred in each revolution (Figure 32b). A reduction of the stirred volume also occurs when reducing the rotational speed, for a constant tool traverse speed (Figure 32c). However, when decreasing the rotational speed, not only the stirred volume is decreased, but also the capability of the tool in extruding the material during a full revolution around the pin is reduced, which usually conducts to the formation of tunnel defects at the advancing side of the welds. Contrary to this, increasing the rotational speed, for a

constant traverse speed (Figure 32d), or increasing the tool dimensions(Figure 32e), while keeping the same process parameters, leads not only to an increase of the stirred volume, but also to a more intense stirring action. This last assumption may be inferred from the streamlines, which clearly indicate that the material is rotated for more than one revolution around the tool for these two conditions.

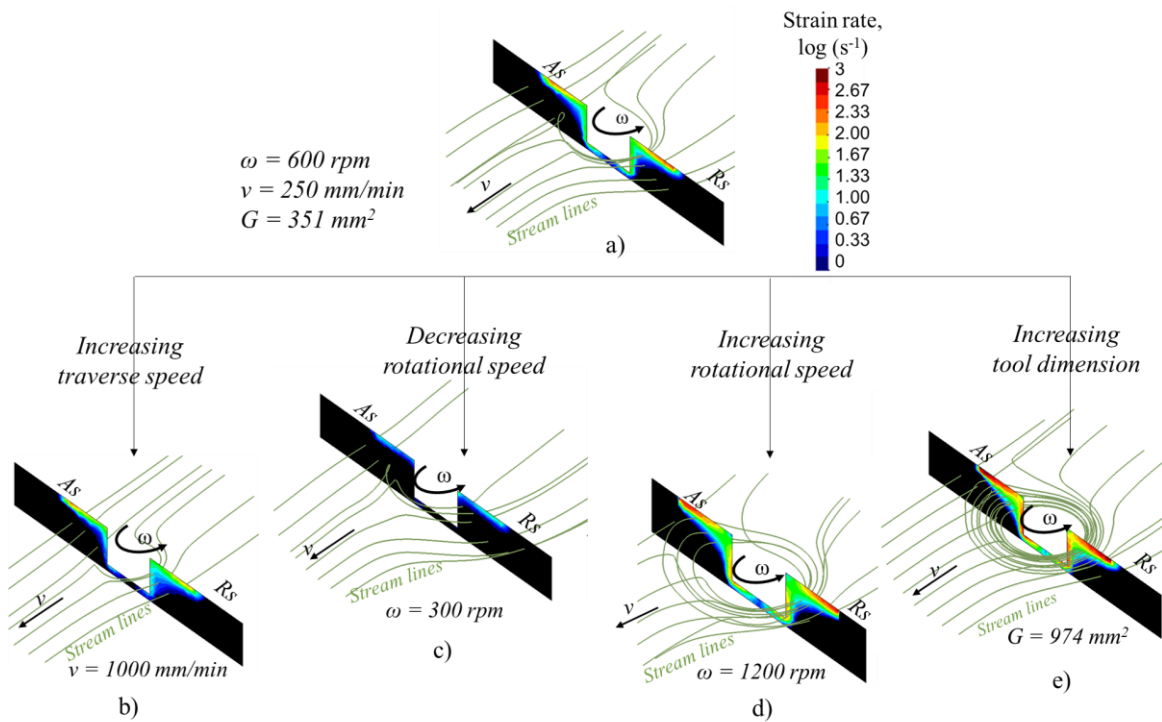


**Figure 32** – Evolution of the welding streamlines and logarithmic equivalent strain rate with the traverse speed (a and b), rotational speed (a, c and d) and tool dimensions (a and e) (adapted from “Article D”).

**Table 13** – Base material thicknesses, shoulder diameters, pin diameters and geometry parameters used in the numerical simulations.

$t$ [mm]	$D_s$ [mm]	$D_p$ [mm]	$G$ [mm <sup>2</sup> ]
2	12	4	134
6	18	6	351
10	30	10	974

The influence of the tool dimensions and of the rotational and traverse speeds on the contact conditions, is summarized in Figure 33. The results in the figure, which also illustrates the influence of the process parameters on the stirred material volume and on the average strain rate values, were obtained by varying the rotational speed from 300 to 1200 rpm, the geometry parameter from 134 to 974 mm<sup>2</sup> and using two different traverse

## Mechanical Analysis

speeds of 250 mm/min (Figure 33a) and 1000 mm/min (Figure 33b). The contact conditions were assessed by using the contact state variable  $\delta$ , defined in Eq. 4, and the amount of material stirred by the tool was evaluated by measuring the area, in the strain distribution maps, where the equivalent strain rate values were higher than zero. Analysing the figure, it is possible to conclude that the contact conditions developed during welding are determined by the processing parameters. For small tool dimensions, high traverse speeds and low rotational speeds, slipping contact conditions prevail. Decreasing the traverse speed, or increasing the rotational speed and/or the tool dimensions, leads to the increase of the sticking fraction, until full sticking contact conditions are reached. The evolution of the contact conditions observed in Figure 33 may be related to the material streamlines shown in Figure 32. The comparison shows that the material only rotates several times around the tool when the contact conditions are close to full sticking. On the other hand, the formation of weld defects, may also be associated with low values of sticking fraction, i.e. with prevalent slipping conditions.

Figure 33 also enables to conclude that the strain rates in the stirred volume are mainly determined by the tool rotational speed, varying from an average of 50 to 400 s<sup>-1</sup>, when the tool rotational speed is increased from 300 to 1200 rpm. The figure also shows that independently of the rotational or traverse speeds used, the stirred material volume always increases with the geometry parameter and that the rotational and traverse speed are secondary parameters governing it. However, using high or low values of rotational and traverse speeds, respectively, also conduct to an increase in the stirred volume.

In Figure 34 is now shown the relation between the stir mechanisms with the welding temperatures. In the figure is shown the evolution of the welding temperature, contact conditions, stirred area and strain rate for the numerical results of Figure 33a. Analysing the figure, is possible to conclude that in the lower temperatures domain, the sticking fraction evolves with the geometry parameter and rotational speed in the same way as the temperature, i.e. the dashed lines almost follow the contour of the isotherms. On the other hand, in the higher temperatures domain, corresponding to large values of geometry parameter and rotational speeds, meanwhile the sticking fraction becomes very high and almost constant, the temperature continues to increase with the geometry parameter and the rotational speeds. Since both the temperature and the strain rate deeply vary in the full sticking domain ( $\delta > 0.9$ ), it is possible to conclude that the increase in heat generation is due to an increase in the adiabatic heat generation associated with the plastic deformation of the stirred material at very high strain rates. On the other hand, the

increase of temperature with the tool dimensions may be attributed to the increase in the amount of material stirred by the tool.

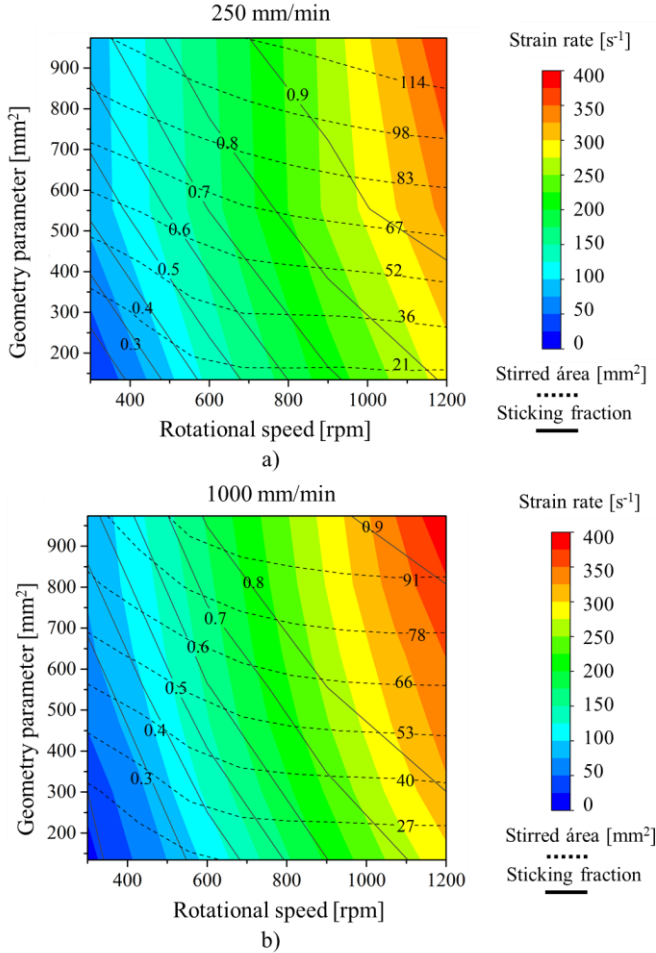


Figure 33 – Evolution of contact conditions, stirred area and strain rate with the rotational speed and geometry parameter, for a traverse speed of 250 mm/min (a) and 1000 mm/min (b).

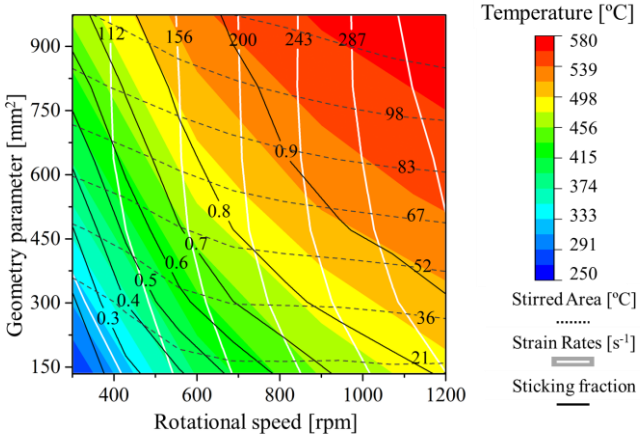
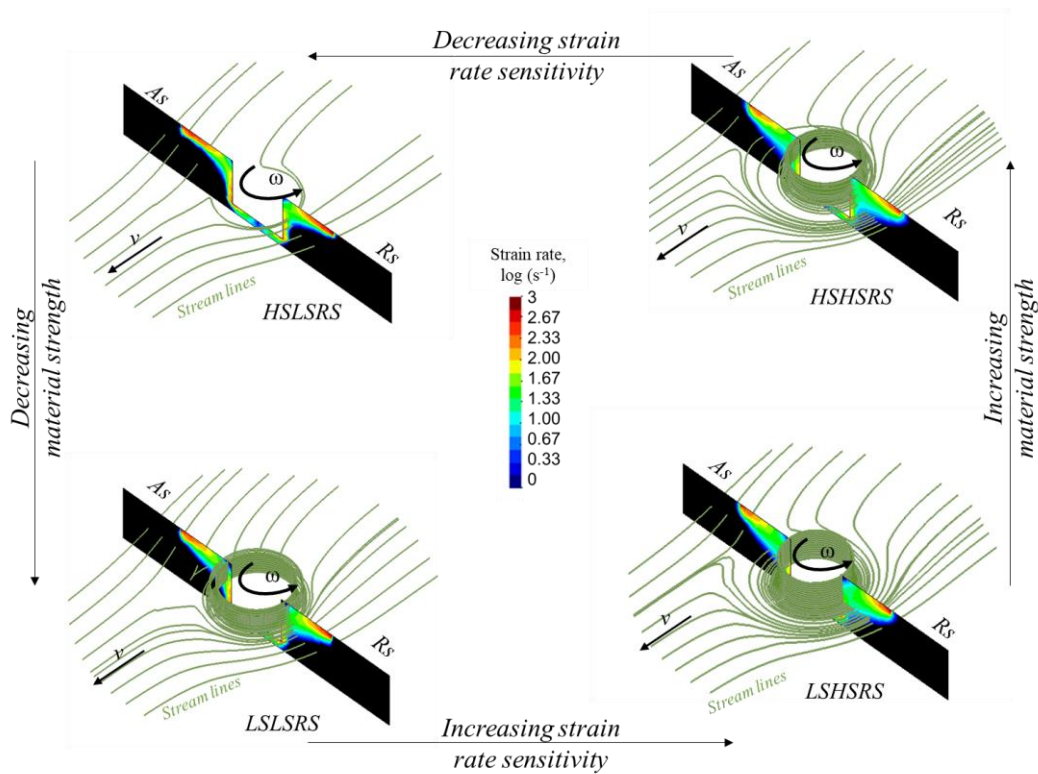


Figure 34 – Numerical results concerning the evolution of the welding temperature, contact conditions, stirred area and strain rate with the rotational speed and geometry parameter.

In addition to the influence of the process parameter on the stir mechanism during welding, the material flow around the tool also depends on the base material properties. Although, up to date, none of the works that addressed this subject were able to correlate the material flow with the base material mechanical properties such as mechanical strength or strain rate sensitivity. In this way, based on the results in “Article D”, the influence of the base material mechanical strength and strain rate sensitivity, on material flow, is shown in Figure 35. In the figure are represented material streamlines and strain rate distributions for four different base materials: the HSHSRS and HSLSRS materials, which are high strength materials with high and low strain rate sensitivity, respectively; the LSHSRS and LSLSRS materials which are low strength materials, but with high and low strain rate sensitivity, respectively. The results shown in the figure were obtained for constant rotational and traverse speeds of 600 rpm and 250 mm/min, respectively, and a tool with a geometry parameter of 351 mm<sup>2</sup>. Also, full sticking contact conditions were forced in the numerical simulations, in order to enhance the influence of the plastic properties of the base materials on the material flow. Analysing the streamlines, as well as the distribution of the logarithmic equivalent strain rate in the weld cross sections, it is possible to conclude that only for the HSLSRS material it was previewed that the material performed no more than one rotation around the tool. On the other hand, for materials with lower mechanical strength and/or higher strain rate sensitivity, it is possible to observe that the material completed several rotations around the tool. For materials with lower strength, the flow stress required to plastically deform the material is inferior, which improves the flowability of the material during the process. It is also important to notice that for the materials with lower strain rate sensitivity, the streamlines and the strain rate become constricted to a narrower region around the tool, when compared to the materials with higher strain rate sensitivity.





**Figure 35** – Evolution of the welding streamlines and logarithmic equivalent strain rate with the base material plastic properties (adapted from “Article D”).

### 4.3. Assessment of the welding torque

Similarly, to what was performed in the thermal analysis, the torque evolution with process parameters, in linear welding, was assessed by performing numerical simulations with COMET. The torque evolution with process parameters in spot welding was assessed by performing bead-on-plate spot welding of thick AA2017, AA5083, AA6082 and AA7075 aluminium alloys and spot welding of thin DC, HC and DP steel plates. In the next, the numerical and experimental results are discussed.

#### 4.3.1. Linear welding

According to the literature review, the tool torque is a suitable parameter to control the FSW process due to its close relationship with the process parameters, heat input and material flow. So, to analyse the influence of the full range of processing parameters tested in the literature, on the torque evolution, a sensitivity analysis was conducted in the current work. In Figure 36a is shown the evolution of the welding torque with the rotational speed and the geometry parameter, plotted using the results published in

“Article C”. The results in the figure were obtained by performing numerical simulations of the FSW process, for the AA6063-T6 aluminium alloy. In the simulations, the rotational speed was varied between 300 and 1500 rpm and a constant welding speed of 250 mm/min was used. The tool dimensions were set assuming proportionality between the shoulder diameter and the plates thickness, using Eq. 16, and assuming plate thicknesses varying between 2 and 10 mm. The pin dimensions were established using a  $D_s/D_p$  ratio of 3, and a  $p/t$  ratio of 0.85. The tool dimensions, plate thicknesses and welding speeds were selected in order to be in the same range of the experimental works covered by the database.

Analysing Figure 36a, it is possible to conclude that, for a constant rotational speed, the torque registered in the numerical simulations increased with the tool dimensions, and for a constant geometry parameter, the torque decreased by increasing the rotational speed. The figure also shows that the influence of the tool dimensions on the torque evolution is more significant for low than for high rotational speeds and, on the other hand, the influence of the rotational speed on the torque evolution is more significant for large than for low geometry parameter values. The decrease of the torque with the rotational speed may be attributed to the increase in the heat generation and consequent base material softening, as reported when analysing the heat generation mechanism during welding. On the other hand, the increase in the torque with the geometry parameter has to be related to the increase of the amount of material stirred by the tool, as observed when analysing the mechanism that govern the transport of material during welding (Figure 33).

In Figure 36b is shown the evolution of the torque with the traverse speed and the plate thicknesses, obtained for a constant rotational speed of 900 rpm. For the results shown in the figure no proportionality between the shoulder diameter and the plates thickness was considered, instead a tool with a constant diameter of 18 mm, a  $D_s/D_p$  ratio of 3 and a  $p/t$  ratio of 0.85 was used, while the plates thickness was varied from 1 to 9 mm. Analysing the results, it is possible to conclude that the torque registered in the numerical simulations increased with the traverse speed and plates thickness. The figure also shows that the influence of the traverse speed on the torque evolution is more significant for high than for low values of plate thickness and, on the other hand, the influence of the plates thickness on the torque evolution is more significant for higher than for lower traverse speeds.

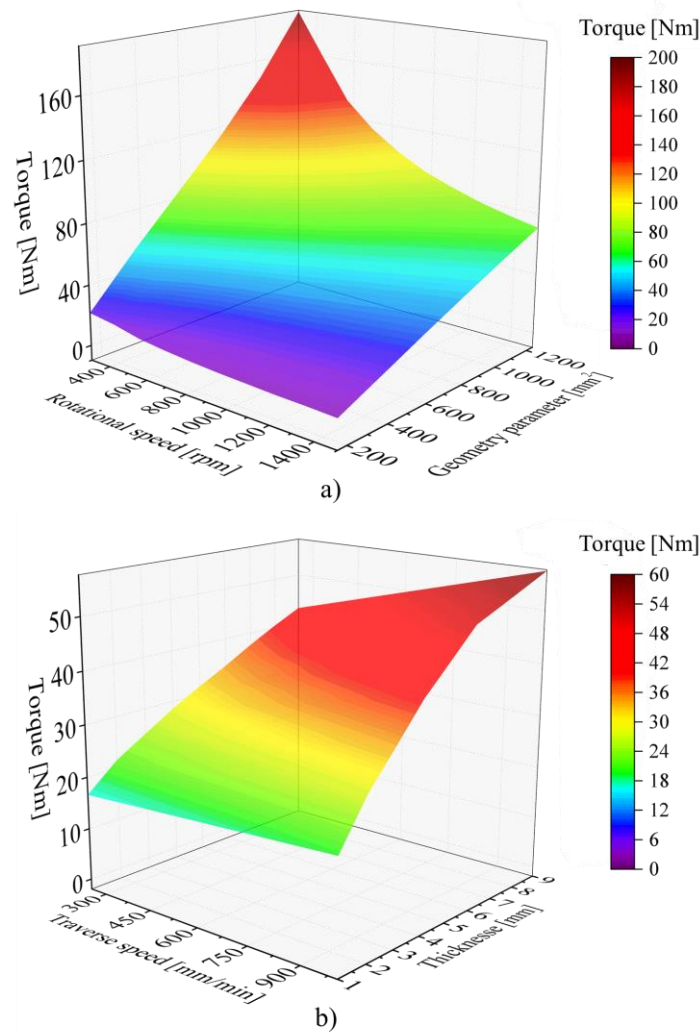


**Figure 36** – Numerical results concerning the evolution of the torque with the rotational speed and the geometry parameter (a) and with the traverse speed and plate thickness (b).

In Figure 37, is now shown the evolution of the welding torque with the product of the traverse speed by the plate thickness ( $v\tau$ ), the two parameters which were found to be important factors in determining the heat dissipation during welding. In the figure, the results plotted with red squares correspond to the numerical simulations of Figure 36a, in which heat dissipative effects associated with the thickness and the traverse speed were minimised by assuming a constant value for  $v$  and setting the shoulder diameter proportional to the plates thickness. The results plotted with circles correspond to the numerical simulations of Figure 36b, in which the shoulder diameters, plate thicknesses and traverse speeds were selected in order to enhance the heat dissipative effects on the temperature fields. Analysing the figure, it is possible to conclude that the torque decreases with the rotational speed, due to its important influence on the heat generation,

but increases with the geometry parameter, which is the main factor in determining the volume of material stirred by the tool. The torque also increases non-linearly with the product ( $vt$ ), due to the important influence of both parameters in the heat dissipation, i.e. in decreasing the welding temperature.

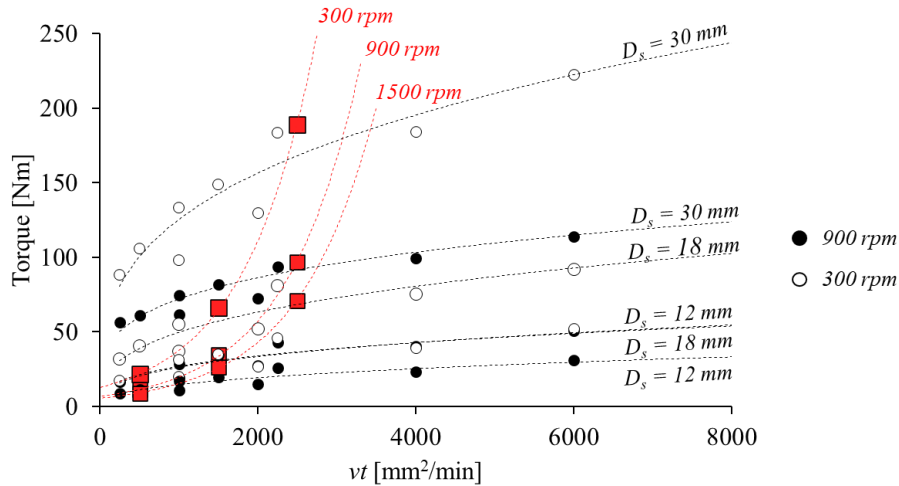


**Figure 37** – Numerical results concerning the evolution of torque with the traverse speed multiplied by the plate thickness ( $vt$ ) when heat dissipative effects are minimized (red squares) and maximized (black circles) (adapted from “Article C”).

### 4.3.2. Spot welding

Figure 38 shows the evolution of torque with time, registered for the weld produced in the AA7075 aluminium alloy, with a tool with 16 mm diameter and a rotational speed of 660 rpm. It is possible to observe that the torque rapidly increased at the beginning of the welding process, as the tool was plunged into the workpiece. At the end of the plunging phase, the torque reached its maximum value and then started to decrease, when the dwelling phase started, reaching steady-state values after a certain time. After the tool removal, the torque instantaneously started to decrease. The torque evolution with time was identical in all the welding tests, independently of the processing parameters and/or base material tested.

Figure 39 and Figure 40 show the evolution of the torque values with the rotational speed and the tool dimensions, in the spot welding of the aluminium alloys and steels, respectively. To be able to correlate the torque with the temperature, the torque values were calculated considering the same time interval used to determine the welding temperatures (Figure 17). The results in Figure 39 correspond to the welds produced in the AA2017, AA5083, AA6082 and AA7075 aluminium alloys by varying the rotational

speeds, between 660 to 1500 rpm, and the shoulder diameters, between 10 to 18 mm. The results in Figure 40 correspond to the welds produced in the DC, HC and DP steels by varying the rotational speeds, between 870 to 1500 rpm, and the shoulder diameters, between 10 to 16 mm. Analysing both figures, it is possible to conclude that the evolution of the torque with the process parameters is equal to the one already reported for the linear welding, i.e. the tool torque decreases with the increase of the rotational speed and decrease with the decrease of the tool dimensions. The figures also show that the evolution of the torque with the process parameters was identical for the ferrous and non-ferrous alloys.

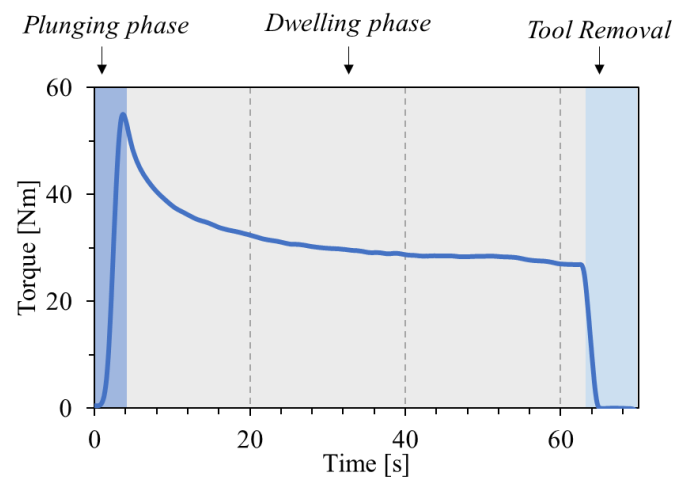


**Figure 38** – Evolution of torque with time for the weld produced in the AA7075 aluminium alloy, with a tool diameter of 16 mm and a rotational speed of 660 rpm.

However, by relating the torque evolution in Figure 39 and Figure 40, with the results of the thermal analysis carried out in section 3.2, for spot welding, it is possible to conclude that the torque is not directly related to the welding temperatures. For instance, for the welds produced in the aluminium alloys, a shoulder diameter related temperature threshold was registered for rotational speeds higher than 600 rpm. However, according to Figure 39, no stabilisation in the torque evolution with the rotational speed may be observed. In the same way, for the spot welds produced in the DP steel, with the larger tool diameters, no variation in the temperature with the rotational speed was registered, although according to Figure 40, for the same welding conditions, a decrease in torque may be observed. These results suggests that for the welding conditions for which a threshold in the welding temperatures is observed, the mechanical interaction between the tool and the workpiece, and in this way, the heat generation mechanism, have to be different for the different rotational speeds.

## Mechanical Analysis

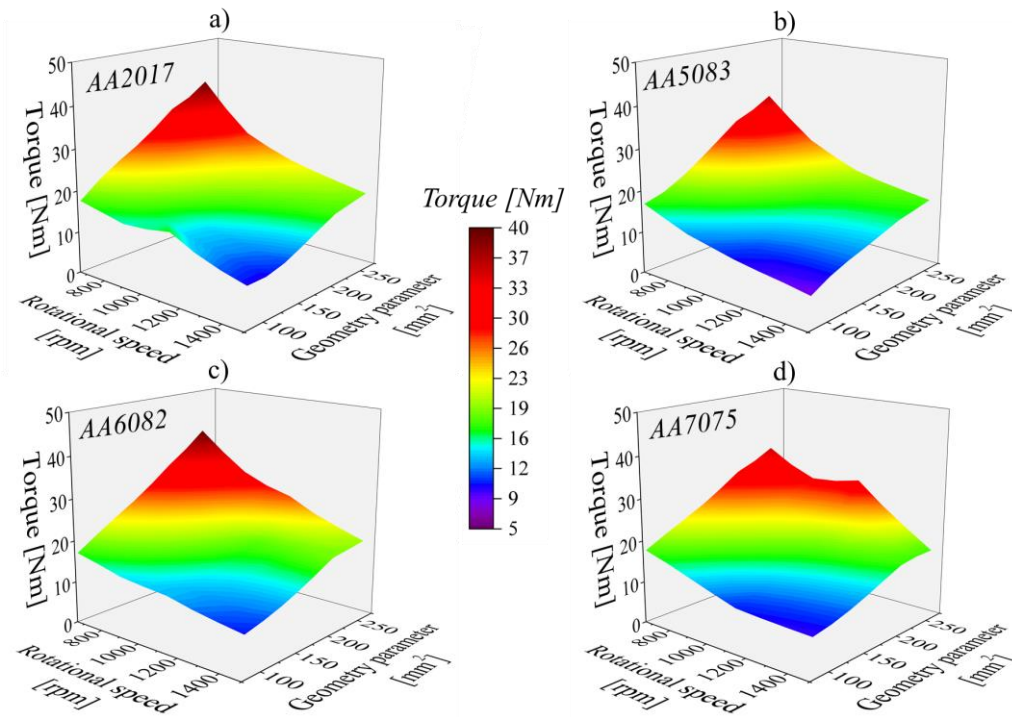


**Figure 39** – Evolution of the torque values with the rotational speed and geometry parameter, for the AA2017 (a), AA5083 (b), AA6082 (c) and AA7075 (d) aluminium alloys.

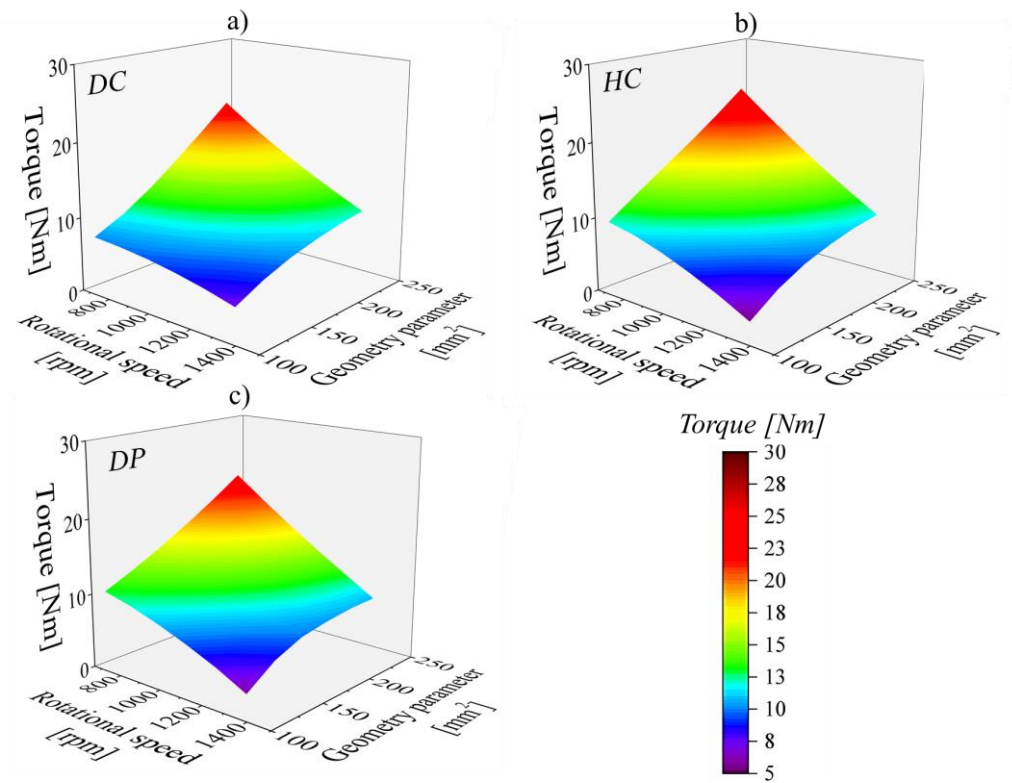


**Figure 40** – Evolution of the torque values with the rotational speed and geometry parameter, for the DC (a), HC (b) and DP (c) steels.

#### 4.4. Modelling the welding torque

The data from the numerical and experimental tests was used for developing analytical models, that relate the process parameters with torque, in FSW and FSSW. Since the traverse displacement of the tool does not exist in FSSW, different models were proposed for the FSW and FSSW processes.

##### 4.4.1. Linear welding

The parametric analysis performed in the previous sections allowed to understand and to assess the evolution of the welding torque with the process parameters. Considering the results from Figure 37, obtained in the numerical simulation of the linear welding, a torque coefficient,  $C_M$ , is proposed to quantify the evolution of the tool torque with the processing parameters:

$$C_M = \frac{G}{\omega} \sqrt[4]{v \times t}. \quad (42)$$

In Figure 41 are plotted the torque values obtained in the numerical simulations performed in current work versus the torque coefficient. According to the figure, it is possible to establish a linear relationship between the torque and  $C_M$  as follows:

$$M = K_M C_M \quad (43)$$

In the previous equation,  $K_M$  is a constant related to the base material being welded. Fitting the numerical results it was determined that  $K_M = 6$ .

As it was done in the thermal analysis, the torque model was also validated by comparing of the model previsions with the torque data from the literature. The results obtained are shown in Figure 42. In order to fit accurately the experimental results, the torque values computed using Eq. 43 had to be multiplied by a  $\lambda_M$  constant. The need for this constant may be associated with different welding setups or different procedures in acquiring the torque results and or computing the average torque values. According to the figure, by adjusting  $\lambda_M$  for the different references, it is possible to conclude that the proposed model is able to predict with accuracy the torque results obtained by the

different authors, which shows that the  $C_M$  coefficient is able to reproduce satisfactorily the torque evolution for the welding conditions covered by the database.

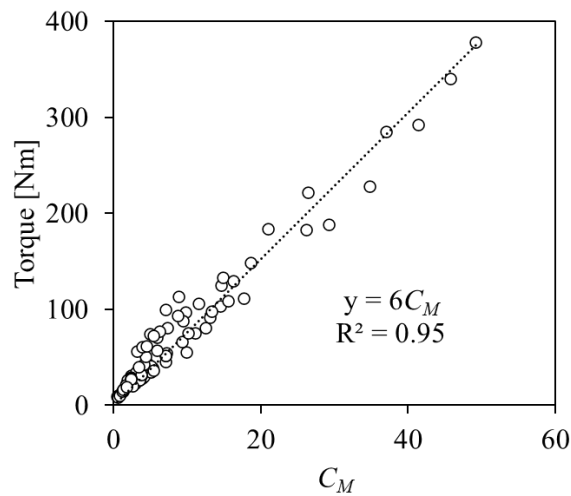


**Figure 41** – Evolution of the torque values, obtained in the numerical simulations, with the torque coefficient (adapted from “Article C”).

In Table 14 are now shown the fitting constants for several of the torque models referred in the literature review, obtained using the experimental results of the database. To assess the quality of the correlation between the experimental values with the ones predicted by the models available in the literature, the Pearson correlation coefficient was calculated individually for each model. Analysing the table, it is possible to conclude that the proposed model provides better predictions on the torque evolution with process parameters than the other models. This improvement is related to the fact that a larger number of process variables are considered in the model proposed in this dissertation. It is also assumed that a good assessment of the evolution of the thermal and mechanical conditions developed during welding, with the process parameters and plate thickness, was achieved in the current work, due to the extended parametric analysis performed.



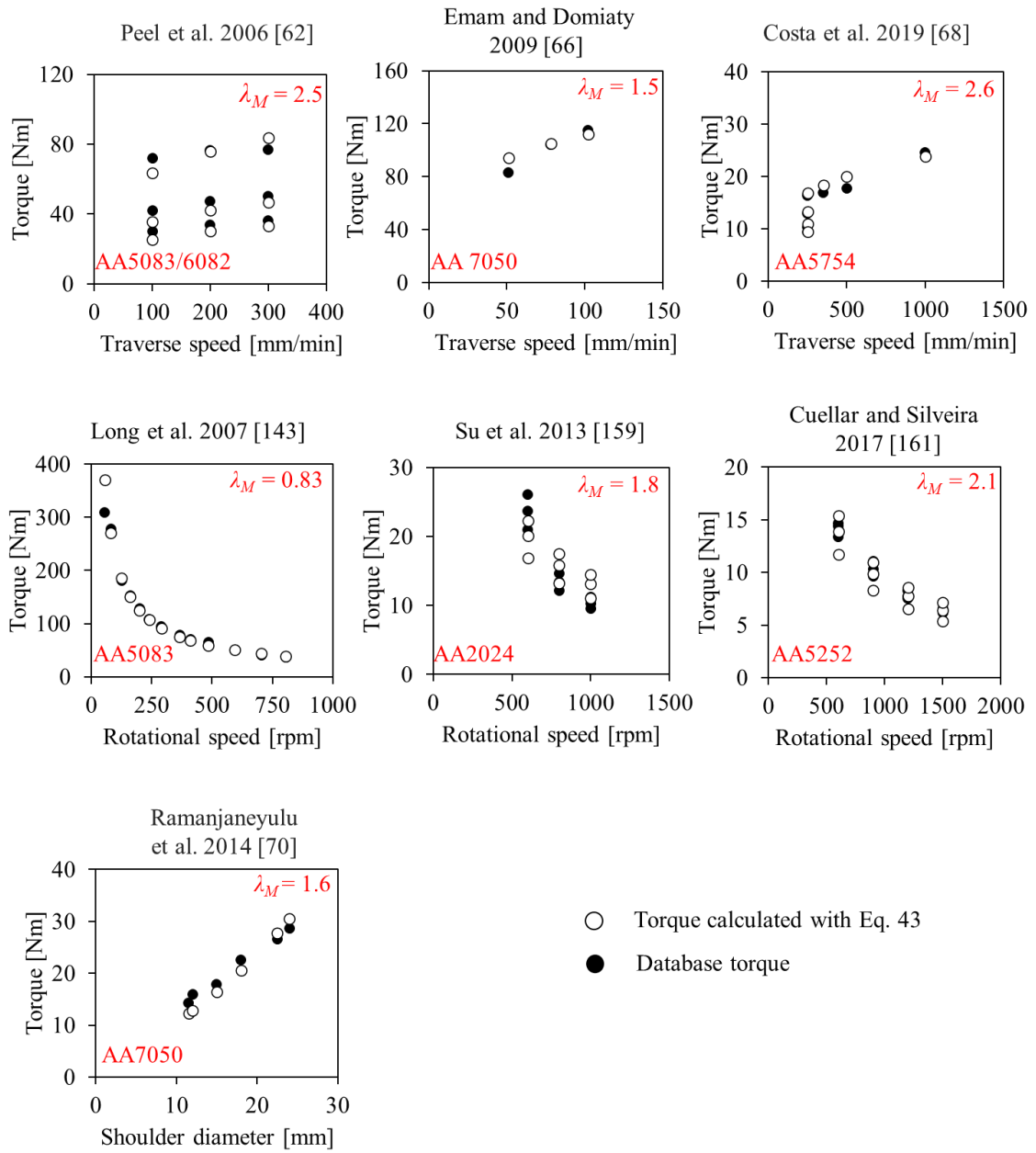


**Figure 42** – Comparison of the experimental torque results, from the database, with the torque values calculated with Eq. 43 (adapted from “Article C”).

**Table 14** – Constants for the torque models, calculated using the experimental results from the database.

Model	Constants	
<i>Colegrove and Shercliff</i> 2003 [164]	$A_M$	10700
	$\alpha_M$	0.20
	$\beta_M$	0.97
	$R^2$	<b>0.77</b>
<i>Cui et al. 2010</i> [93]	$M_0$	7
	$M_f$	414
	$n_M$	4.17e-3
	$R^2$	<b>0.69</b>
<i>Leitão et al. 2012</i> [158]	$a$	15438
	$b$	0.87
	$R^2$	<b>0.59</b>
<i>Proposed Model</i>	$K_M$	6
	$R^2$	<b>0.96</b>

#### 4.4.2. Spot welding

As shown in the previous sections, the evolution of the welding torque with the rotational speed and the tool dimensions is identical in spot and in linear welding. Although, since in spot welding the linear displacement of the tool does not exist, the  $C_M$  coefficient was rearranged by withdrawing the traverse speed from Eq. 42. So, the  $C_{M,SW}$  coefficient, is proposed for modelling the torque evolution with process parameters in spot welding:

$$C_{M,SW} = \frac{G}{\omega} \sqrt[4]{t}. \quad (44)$$

In Figure 43 and Figure 44 is plotted the evolution of the torque values obtained in the spot welding of the AA2017, AA5083, AA6082 and AA7075 aluminium alloys and of the DC, HC and DP steels, respectively, with the  $C_{M,SW}$  coefficient. The figures enable to conclude that the proposed coefficient fits satisfactorily the experimental results. It is also possible to depict a linear relationship between the torque values and  $C_{M,SW}$ , which can be expressed through the relationship,

$$M = K_{M,SW} \times C_{M,SW}, \quad (45)$$

in which  $K_{M,SW}$  is a constant. Fitting the experimental results in Figure 43 and Figure 44 it was determined that for the aluminium alloys and for the steels tested in current work,  $K_{M,SW}$  is equal to 62 and 80, respectively. It is also interesting to notice that although the base materials tested have different chemical compositions and mechanical strength, at room temperature (Figure 3 and Figure 4), the evolution of the torque with  $K_{M,SW}$  was similar for the different ferrous and non-ferrous alloys.

Finally, it is also important to conclude the accurate prediction of the experimental results, for the very large range of welding conditions and base materials tested, proves that the torque coefficient is reliable for predicting the evolution of torque.

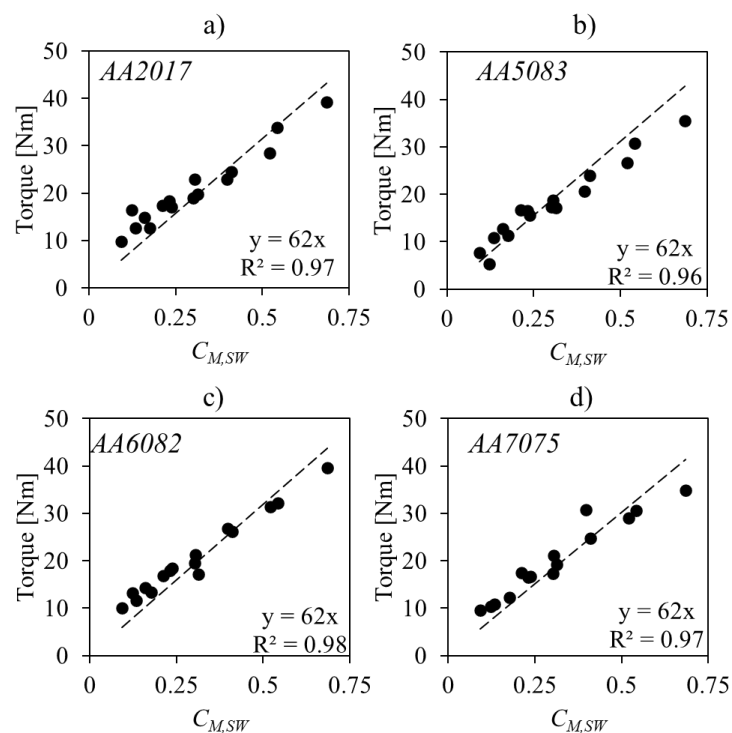


**Figure 43** – Evolution of torque values with the  $C_{M,SW}$  coefficient, for the spot welds produced in AA2017 (a), AA5083 (b), AA6082 (c) and AA7075 (d) aluminium alloys.

## Mechanical Analysis

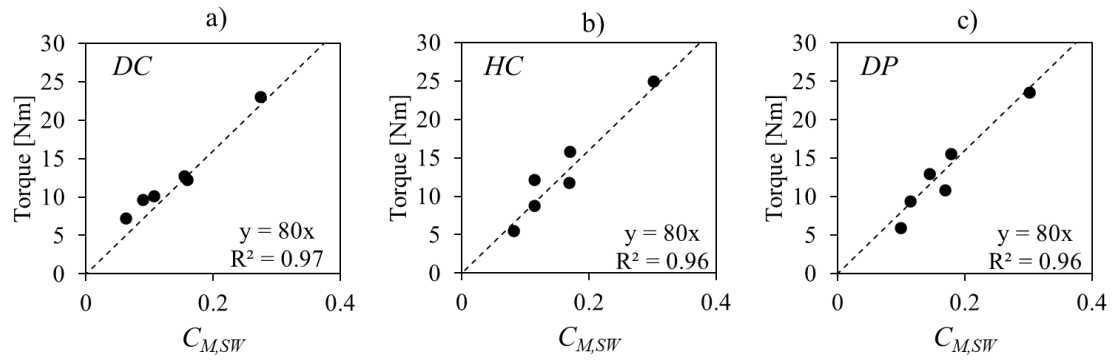


**Figure 44** – Evolution of torque values with the  $C_{M,SW}$  coefficient, for the spot welds produced in DC (a), HC (b) and DP (c) steels.

## 5. Process Assessment

---

The feasibility of using pinless tools to produce spot and linear lap welds in very thin steel plates is analysed in this chapter. First, a literature review on the similar and dissimilar joining of steels using pinless tools is presented. After this, the results of the current work are shown. The bonding mechanisms in linear lap welding of steels, with pin and pinless tools, are compared and the main differences between them are highlighted. The quality of the linear welds is discussed based on the morphological and mechanical characterization of the joints, produced under a varied range of tool diameters, traverse and rotational speeds. The influence of the rotational speed, tool diameter and dwell time on the quality of the spot welds produced in galvanised and non-galvanised steels, is also analysed. To better assess the influence of the galvanised coating on the thermo-mechanical conditions developed during spot welding, steels with different coating thicknesses were tested.

### *5.1. Literature review*

Steels are the most commonly used material for engineering applications due to its high strength and low cost. Since the development of FSW, there has been a growing number of studies investigating the feasibility of using this welding process in the joining of steels. Several authors pointed out that the main advantage of using FSW, instead of the conventional fusion welding methods, in the joining of steels, is the possibility of producing welds with low heat input. The range of temperatures attained in the FSW of steels is shown in Figure 45, where are listed some experimental works reporting temperature measurements in linear and spot joining of carbon steels [21,88,89,165–169]. The figure shows that the welding of steels may be successfully performed in a temperature range between 400 to 1300 °C. According to the authors cited in the figure, this temperature range is suitable for obtaining welds with favourable microstructure, avoiding the formation of brittle phases, and with good mechanical properties.

## Process Assessment

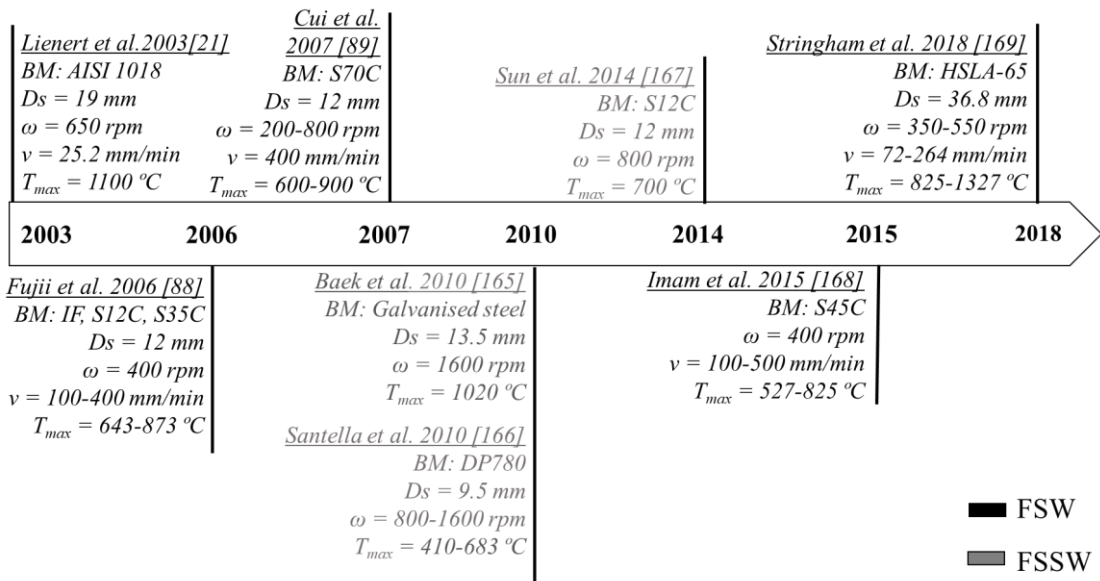


**Figure 45** - Experimental works that have reported temperatures measurements in FSW and FSSW of carbon steels (Adapted from “Article B”).

However, even though FSW may be used to produce steel welds with good quality, its application at an industrial level is still very limited, when compared with the number of existing applications for aluminium alloys [22]. According to Çam 2011 [170] and Rai et al. 2011 [17], this is related to the fact that for steels, the wear and/or rupture of the pin represents a huge drawback, in FSW, since durable and economic tool materials, capable of welding high melting point alloys, have not yet been developed. For the lap welding of very thin steel plates, one possible solution for this problem was proposed by Mira-Aguiar et al. 2016 [4], who suggested the use of pinless tools.

Mira-Aguiar et al. 2016 [4] used a tungsten carbide pinless tool, with a diameter of 12 mm, in the linear lap welding of 1 mm thick DX51D and DC01 steel plates, with rotational and traverse speeds of 1000 rpm and 600 mm/min, respectively. According to the authors, due to the absence of the pin, no material stirring takes place across the lap plates interface during the welding with pinless tools, as in the lap welding using conventional FSW tools. So, the joining of the plates results from the plastic deformation of the interface, at the very high pressure and the very high temperature promoted by the pinless tool, following mechanism very similar to that operating in Friction Welding (FW). Since the welding mechanisms were reported to be different from the ones in FSW, but similar to that governing FW, the authors labelled the process as Tool Assisted Friction Welding (TAFW).

Andrade et al. 2018 [171] compared the material flow in the dissimilar lap welding of aluminium and copper by TAFW and FSW. These authors also reported different joining mechanisms, when comparing the welds fabricated by the two processes. For the welds produced by FSW, an intercalated lamellae structure composed of aluminium and copper was registered at the lap interface, which promoted the joining of the base materials by mechanical interlocking. When TAFW was used, no plastic deformation was registered during welding, except that associated with the axial compression of the tool. The authors observed an intermetallic layer, at the interface, which they associated to the diffusion between both base materials.

Kim et al. 2017 [172] also tested a WC-Co pinless tool in the butt welding of 1 mm thick 430M2 ferritic stainless steel. Welds without any defects and with strength equal to that of the base material were produced. Although, Kim et al. 2017 [172] did not perform any analysis of the joining mechanisms and assumed that the welds were produced by FSW.

van der Rest et al. 2014 [2] used pinless tools to produce lap welds between a 0.8 mm thick micro alloyed ultralow carbon steel and 1 mm (Al 1050) or 2 mm (Al 2024 T3) thick aluminium sheets. A tungsten carbide tool with 16 mm diameter, operating at a constant rotational speed of 2000 rpm and varied traverse speeds, between 100 and 700 mm/min, was used. During welding, the higher melting point base material was placed at the top of the joint, for inducing very high temperatures at the plates interface, leading to the partial melting of the bottom plate. According to the authors, the joining between the two plates results from the formation of Al-Fe intermetallics, which lead the authors to label the process as Friction Melt Bonding (FMB). Similarly, Zhang et al. 2011 [173] used a pinless tool for the lap welding of 1.8 mm thick aluminium to low carbon steel plates, using a zinc foil interlayer. Although, in this case, the lower melting point material was placed at the top of the weld and, according to the authors, the joining between the plates resulted from the melting of the 0.1 mm thick zinc foil, placed between the two plates. This process was labelled by the authors as Friction Stir Brazing (FSB).

Pinless tools have also been used by Aota et al. 2009 [174] to produce spot welds in a 0.5 mm thick low carbon steel. Due to the very small thickness of the plates, the authors used a sialon ceramic tool with a diameter of 3.6 mm and a very high rotational speed of 18000 rpm, which is much higher than that generally used in FSW. Nevertheless, the authors were able to produce welds without defects and with good mechanical strength.

Finally, Sun et al. 2012 [175] proposed a novel welding technique, that used pinless tools, to produce steel spot welds without keyhole, in 1 mm thick mild steel. Although, the process proposed by the authors makes use of two operational steps. In the first step, a silicon nitride tool with a pin and a specially designed backing plate, with a round dent on its surface, are used. During this stage, a keyhole and a protuberance are formed on the top and bottom surfaces of the welds. In the second stage, a pinless tool is used to remove the protuberance and the keyhole of the weld. Using this method, the authors were able to obtain sound joints with smooth surfaces and without any internal welding defects.

According to the literature review, even though pinless tools were already used with success in the butt and lap welding of several steels, its feasibility to produce spot and linear steel lap welds, under a varied range of welding conditions, and for diversified base materials, remain an unexplored subject in the literature. So, in this dissertation, the feasibility of using pinless tools to produce spot and linear lap welds, in galvanised and non-galvanised steels, was explored.

### *5.1. Linear welding*

The work carried out to analyse the feasibility of using pinless tools to produce linear lap welds is schematically represented in Figure 46. As shown in the figure, the bonding mechanisms in the linear lap welding of DC steel, with pin and pinless tools, were assessed and compared, by performing a coupled experimental and numerical analysis. In addition, the influence of the process parameters on the joints morphology was also analysed by producing welds in the DXR14 steel under a varied range of tool diameters and rotational and traverse speeds. An analysis of the influence of the process parameters on the linear lap welds strength was also carried out by performing tensile-shear tests. The morphology and strength of the welds were related to the evolution of the contact conditions, with the process parameters, assessed by analysing the welds morphology and the welding torque.



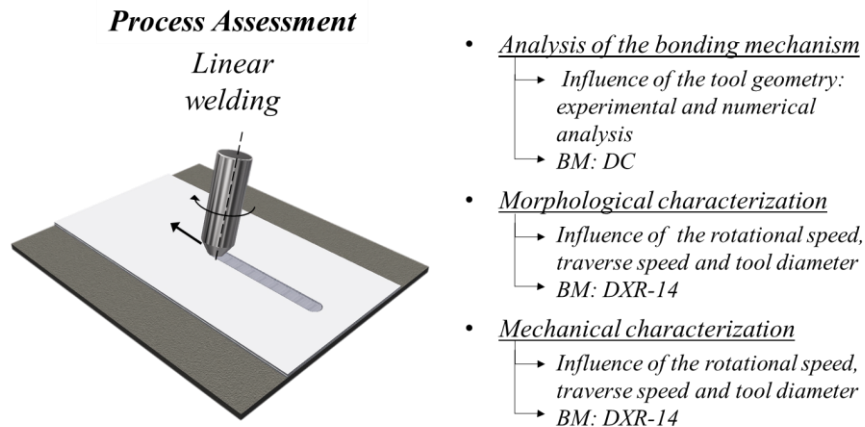


**Figure 46** - Schematic representation of the process assessment analysis performed in current work for the linear welds.

### 5.1.1. Analysis of the bonding mechanisms

In Figure 47a and b are compared the cross sections of steel lap welds, produced with pin and pinless tools, respectively, in 1 mm thick DC steel plates, using rotational and traverse speeds of 1000 rpm and 600 mm/min, respectively. Both tools, the pin and the pinless, had a shoulder diameter of 12 mm. The conventional tool had a conical non-threaded pin, with 1.1 mm length and top and bottom pin diameters of 8 and 4 mm, respectively [4]. In Figure 47c and d are shown the streamlines, representing the material flow around the tool, at the plates lap interface, and the equivalent strain rate distribution maps, obtained when simulating the experimental tests with COMET software, following the procedures explained in Chapter 2. Figure 47a enable to observe that, when using the tool with pin, the joining of the top and bottom plates results from the base material stirring/mixing, promoted by the pin, across the lap interface. The base material stirring conducts to the formation of the onion ring structure, visible in the image, as well as to the formation of the hook and cold lap defects, also signalized in the figure. These defect result from the upward and downward material flow of the bottom and top plates materials, across the lap interface, resulting from the stirring action of the tool. The strong stirring action of the tool, over the base material, is also illustrated by the streamlines in Figure 47c.

## Process Assessment

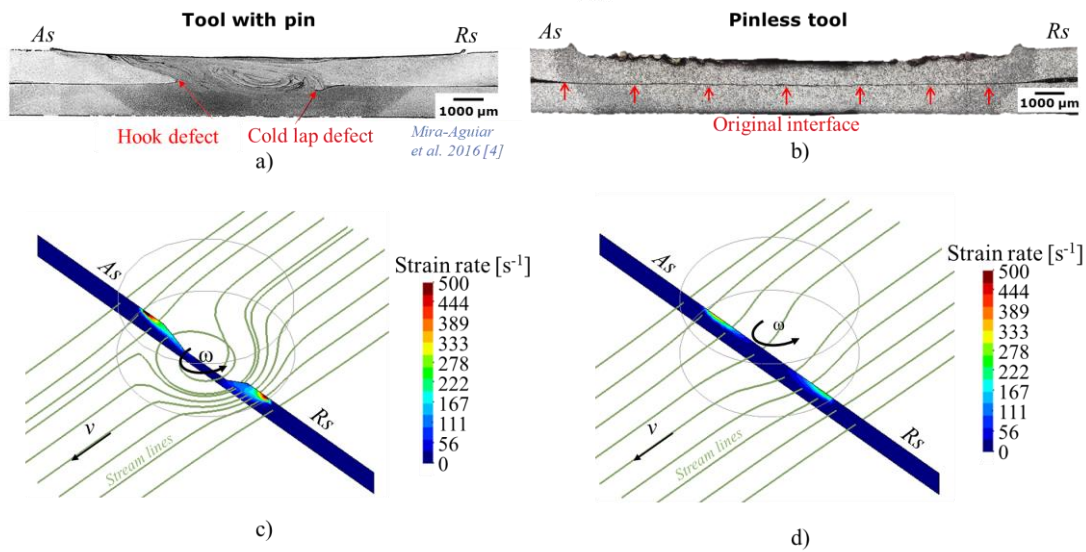


**Figure 47** – Comparison of the cross section (a and b) and material flow (c and d), computed through numerical simulation, of welds produced by pin and pinless tools.

Contrary to this, Figure 47b shows that, for the weld produced with the pinless tool, no material stirring across the lap plates interface took place, as is demonstrated by the continuous line, aligned with the original interface of the plates, which can be observed in the weld cross-section. For this weld, no hook or cold lap defects may be observed in the figure. The absence of material flow across the lap plates interface is also illustrated by the streamlines shown in Figure 47d.

Additionally, in the weld cross section of Figure 47b, it is possible to observe a process affected zone (PAZ), composed by the base material which was subjected to the thermal cycles and the very high pressure promoted by the tool. The PAZ morphology indicates that the tool stirring action was restricted to a very thin region, at the top of the weld. This region, which is shown in more detail in Figure 48a, where it is possible to observe a dark layer containing tool remnants, as revealed by the SEM/EDS analysis (Figure 48b), coincides with the region with non-zero strain rate in the strain rate maps in Figure 47 d. Although no material stirring took place across the lap interface, the joining of the plates occurred, as is shown by the micrograph in Figure 49, where it is possible to observe the microstructural continuity between the top and the bottom sheets. These results demonstrate that for the pinless tool, the joining of the plates results from the plastic deformation and the atomic diffusion across the interface at the very high pressure and temperature developed during welding.

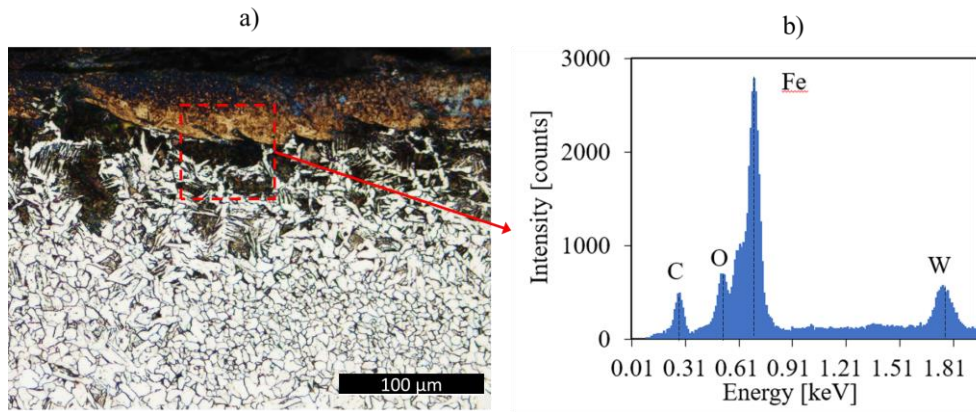


**Figure 48** – Magnification of the weld microstructure at the top surface (a) and SEM/EDS analysis (b).

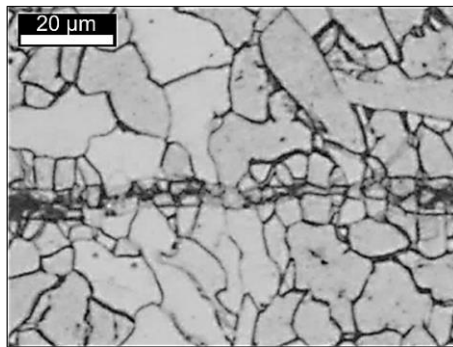


**Figure 49** – Magnification of the weld microstructure at the plates bonding interface.

### 5.1.2. Morphological analysis

The influence of the process parameters on the morphology of the linear lap welds produced with the pinless tools is illustrated in Figure 50 to Figure 52, extracted from “Article A”, which refers to the welding of the DXR14 steel, using tools with different diameters and varying traverse and the rotational speeds. More precisely, in Figure 50 are shown the cross sections of the welds manufactured at a constant tool rotational and traverse speeds of 1000 rpm and 600 mm/min and varying tool diameters, from 10 to 16 mm. The influence of the traverse speed on the PAZ morphology is illustrated in Figure 51, where are shown the cross sections of the welds produced using the PL16 tool, at a constant rotational speed of 1000 rpm and varying traverse speeds from 200 to 1000 mm/min. In Figure 52 are shown the cross sections of the welds manufactured with the PL16 tool, at a constant traverse speed of 600 mm/min and varying rotational speeds from

600 to 1400 rpm. The images in the left side of the figures correspond to photographs of the cross-sections after chemical etching. The images in the right side of the figures were obtained by eliminating the microstructure from the images in the left side, using an image editing software. In all cross-section photographs, except that in Figure 52a, it is possible to observe a PAZ with a microstructure different from that of the base material and a dark line in the middle of the PAZ, aligned with the plates original interface. The images in Figure 50 to Figure 52 also indicate that bonding of the plates was obtained for most of the welding conditions tested. The only exception was reported for the weld performed with the tool PL16 at rotational and traverse speeds of 1000 rpm and 1200 mm/min (Figure 51f), respectively, for which separation of the plates occurred when handling the samples for the metallographic analysis. For the weld produced with the PL16 tool at 600 rpm and 600 mm/min, the formation of cracks at the retreating side was also observed (Figure 52a).

Comparing the cross-sections on the right side of Figure 50 to Figure 52, in which the contour of the PAZ was delimited using dashed lines, it is possible to conclude that the PAZ morphology is symmetrical relative to the weld axis for the welds performed with the different tools, but using similar welding parameters (Figure 50) and for the welds performed with the PL16 tool and low values of tool advancing (Figure 51a to c) and/or rotational (Figure 52b and c) speeds. On the other hand, a strong asymmetry in PAZ morphology/shape, relative to the weld axis, is evident for the welds produced with the PL16 tool and with the highest tool traverse (Figure 51d to f) and rotational (Figure 52d and e) speeds. When increasing the traverse speed, the deepness of the PAZ also diminishes, becoming almost constricted to the upper plate. This is shown by the PAZ thickness,  $z$  in Figure 51d, e and f, which is equal to 1.7 mm, 1.55 mm and 0.95 mm, respectively.

1000 rpm – 600 mm/min

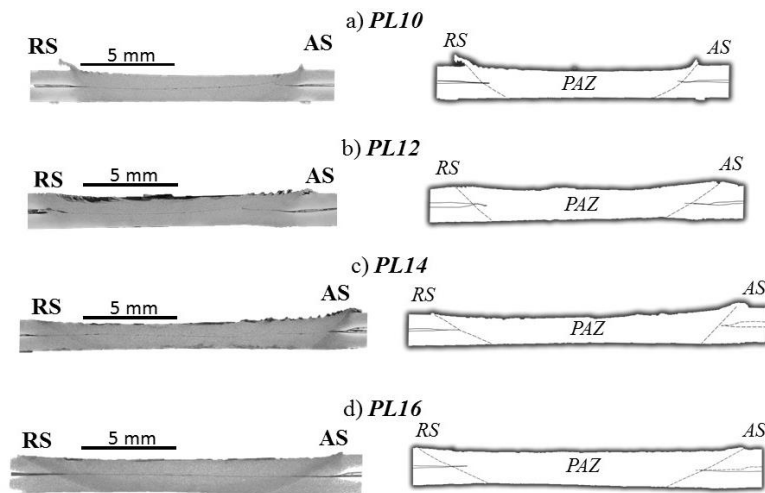


**Figure 50** – Cross sections of the welds manufactured at a constant tool rotational and traverse speeds of 1000 rpm and 600 mm/min and varying tool diameters from 10 to 16 mm (adapted from “Article A”).

PL16 - 1000 rpm

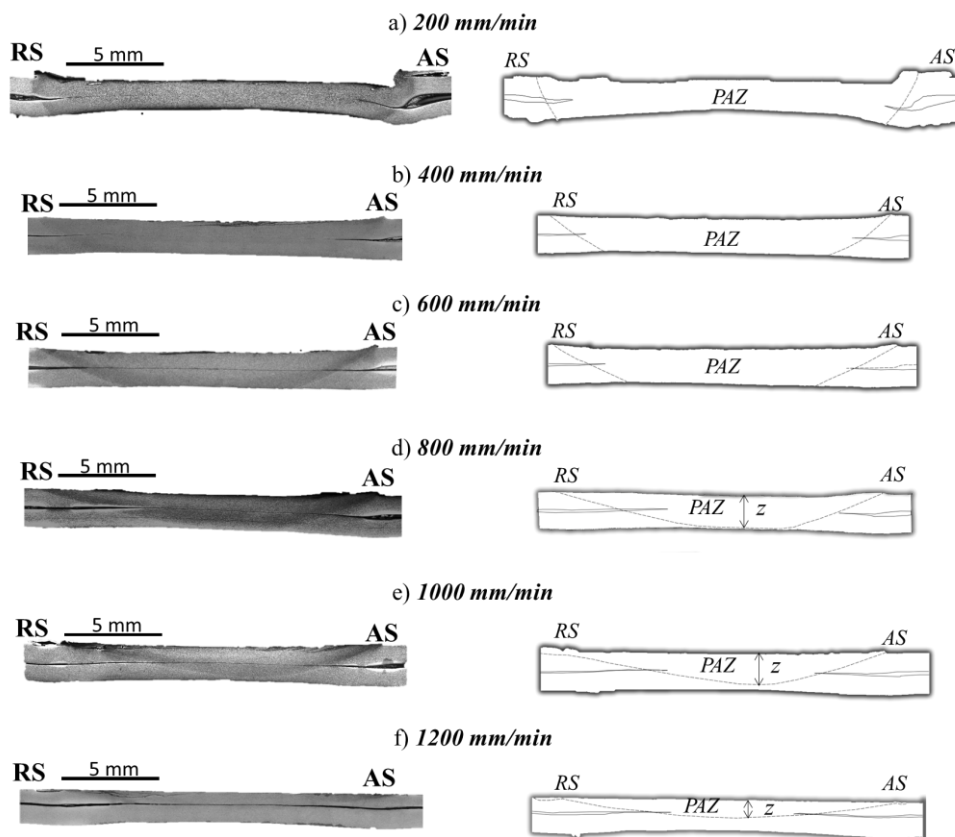


**Figure 51** – Cross sections of the welds manufactured with the PL16 tool, at a constant rotational speed of 1000 rpm and varying traverse speeds (adapted from “Article A”).

*PL16 – 600 mm/min*

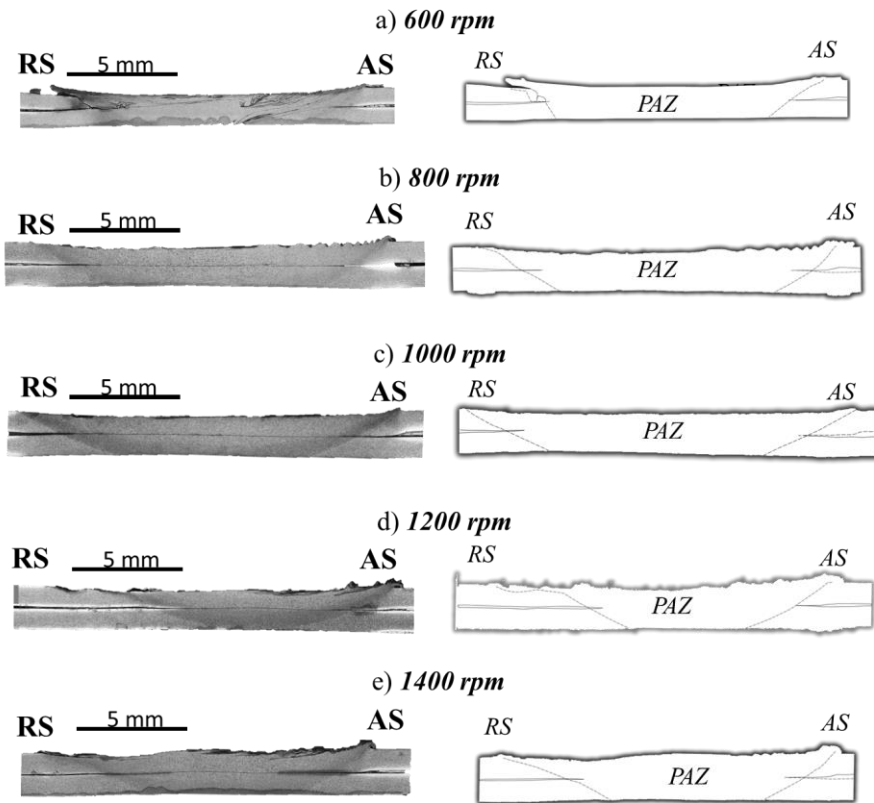


**Figure 52** – Cross sections of the welds manufactured with the PL16 tool, at a constant traverse speed of 600 mm/min and varying rotational speeds (adapted from “Article A”).

Figure 53, Figure 54 and Figure 55 show details of the microstructure at the advancing and retreating sides of the welds in Figure 51c, Figure 51e and Figure 52d, respectively. A dark line was plotted, at the AS and RS of the welds, delimiting a region with a refined microstructure (the PAZ) from a region with a coarser grain structure (the base material). In the middle of the PAZ, a microstructure with coarser grain size than the base material was observed for all the welds (Figure 53c, Figure 54c and Figure 55c). The presence of a coarse grain structure in the PAZ is contradictory to that reported by other authors in FSW [176] and FSP [177] of low carbon steels. This result is another important evidence that the welding mechanisms taking place when using pinless tools are different from those taking place when using tools with pin, since no base material refinement associated with dynamic recrystallization took place in the PAZ, as reported by [176,177].

The images in Figure 53, Figure 54 and Figure 55 also show that the shape of the PAZ boundary at the AS is similar for all the welds (Figure 53d, Figure 54d and Figure 55d). However, the shape of the PAZ boundary at the RS varies according to the welding

conditions (Figure 54a and Figure 55a) showing an asymmetry in PAZ shape, between the AS and RS, for the welds produced at the highest values of tool rotational and traverse speeds. For these welds, the PAZ at the RS is almost restricted to a thin region near the plates surface.

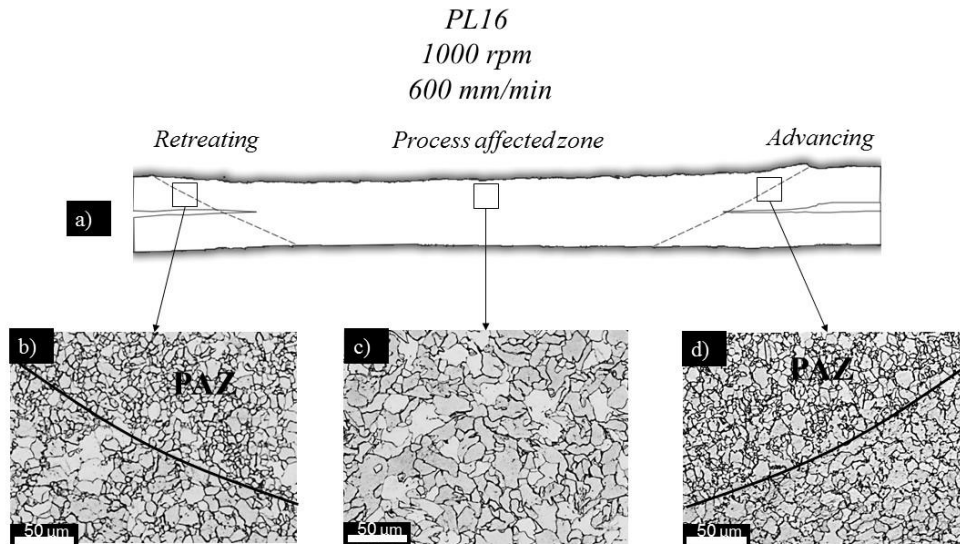


**Figure 53** – Details of the microstructure at the AS and RS of the weld in Figure 51c (adapted from “Article A”).

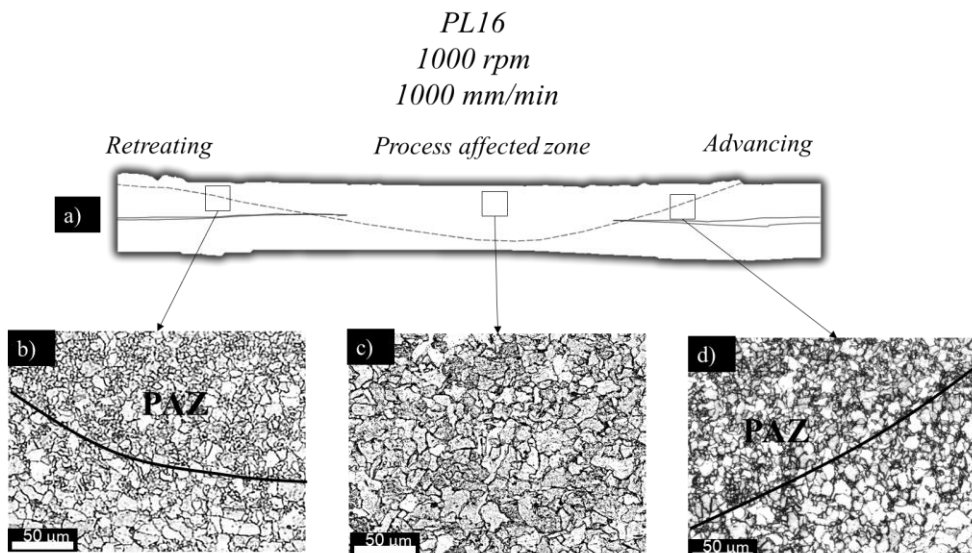


**Figure 54** – Details of the microstructure at the AS and RS of the weld in Figure 51e (adapted from “Article A”).

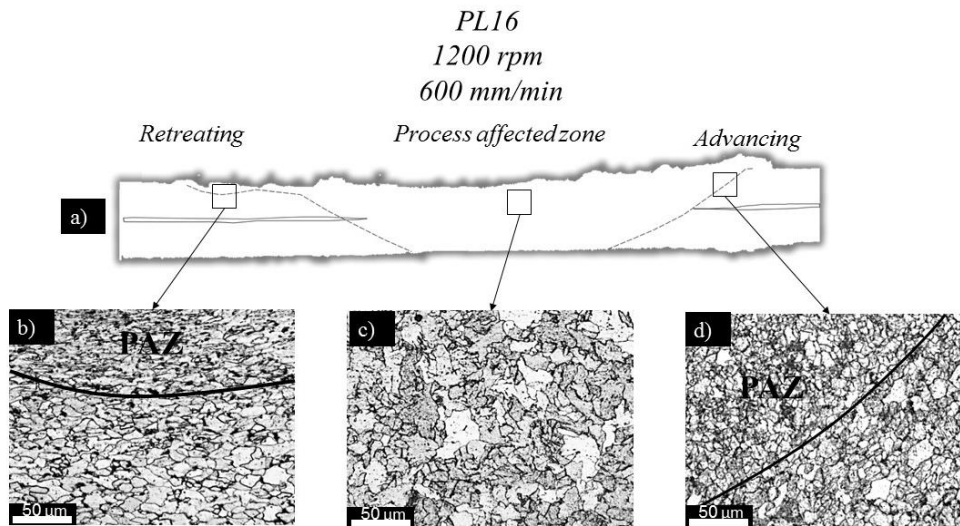


**Figure 55** – Details of the microstructure at the AS and RS of the weld in Figure 52d (adapted from “Article A”).

As already stated in this dissertation, according to Schmidt et al. 2003 [52], the contact conditions at the tool-workpiece interface, in FSW, can be described as a complex combination of slipping and sticking. Present results show that when using pinless tools the contact conditions may be unsymmetrical between the AS and RS, according to the process parameters. More precisely, the symmetry in PAZ morphology, for the welds produced with low values of tool advancing and rotational speeds, prove that the heat generation/distribution was homogeneous at the AS and RS sides of the tool. For these welds, mixed slipping/sticking conditions were prevalent across the entire tool-workpiece contact surface. The asymmetry in PAZ morphology, for the welds produced with high values of tool advancing and rotational speed, prove that the heat generation/distribution was not symmetrical relative to the weld axis. The shape of the PAZ at the RS shows that slipping governed the contact conditions in this side of the tool, where the PAZ is constricted to the upper plate surface. The shape of the PAZ at the AS shows that contact conditions at this side of the tool were similar to that registered for the other welds.

In order to better understand the strong asymmetry in morphology between the AS and RS of the welds produced at highest values of traverse and rotational speeds, an analysis of the process parameters was made. Figure 56 shows a schematic view of the linear velocities of points in the outer radius of the shoulder, at the advancing (point A) and retreating (point B) sides of the tool. The diagram shows that the direction of rotation is the same as that of the linear translation of the tool, at the AS, and opposite at the RS.



So, the linear velocities associated with the advancing ( $v_v$ ) and rotational ( $v_\omega$ ) movements of the tool have the same direction in Point A and the opposite direction in Point B. This way, the difference  $V$  between the linear advancing and the rotational speeds ( $v_v - v_\omega$ ) is higher at the RS than at the AS ( $V_B > V_A$ ).

Figure 57a and b shows the evolution of  $V_B$  with the different traverse and rotational speeds, respectively. It is possible to see that  $V_B$  increases when increasing the traverse and rotational speeds. In both graphs, the points marked in red identify the welds where an asymmetry in morphology, between the AS and the RS was observed, showing that this phenomenon occurred when  $V_B > 1600$  mm/s.

A torque sensitivity analysis was also performed, as shown in Figure 58, where is represented the evolution of the average weld torque with the process parameters ( $v/\omega$ ) for the welds produced with the PL16 tool. Analysing the figure, it is possible to observe two different trends in the torque evolution for the welds produced with  $V_B$  lower (black points) and higher (red points) than 1600 mm/s. The torque tends to stabilise when decreasing  $v/\omega$ , for the welds produced with  $V_B < 1600$  mm/s. For the welds produced with  $V_B \geq 1600$  mm/s, the torque tends to stabilise when increasing  $v/\omega$ . Since no significant base materials stirring takes when pinless tools are used, as when tools with pin are used, the differences in torque evolution for the welds performed with  $V_B$  higher and lower than 1600 mm/s have to be related with the differences in tool-workpiece contact under the different welding conditions.

It is possible to conclude that the asymmetry in welds morphology resulted from the prevalence of slipping contact conditions at the RS of the tool during welding. The torque evolution in Figure 58 is another evidence of the prevalence of slipping contact conditions when  $V_B \geq 1600$  mm/s. More precisely, when increasing the weld pitch, the distance travelled by the tool in each revolution increases, slipping contact conditions become more favourable (independently of  $V_B$ ) and the torque tends to stabilize. This assumption is supported by the fact that the average torque for the weld performed at 600 mm/min and 600 rpm (white point), produced with  $V_B < 1600$  mm/s, follows the red line trend. As can be observed in Figure 52a, this weld has cross-section features characteristic of unstable contact at the tool-workpiece material interface during welding.

When welding with  $V_B < 1600$  mm/s, the torque decreases when decreasing the weld pitch. In this situation, the distance travelled by the tool in each revolution decreases and the conditions for sticking contact become more favourable. The parameter  $V_B$ , in this case, does not enforce slipping contact conditions at the RS of the weld. The evolution

of the contact conditions and torque with the process parameters is governed by the same mechanism operating when using tools with pin.

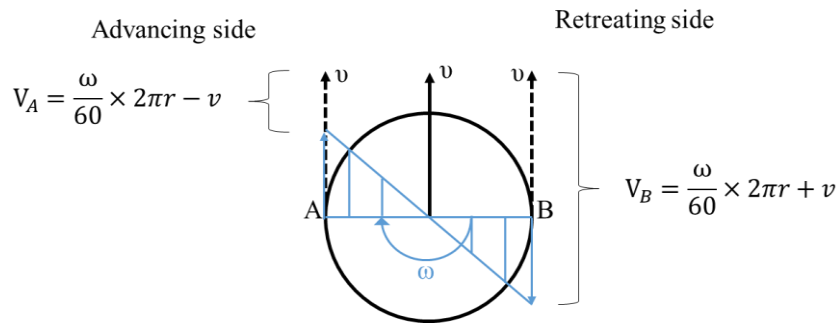


**Figure 56** – Schematic view of the tool, showing the linear velocities of points in the outer radius of the shoulder, at the advancing (point A) and retreating (point B) sides (adapted from “Article A”).

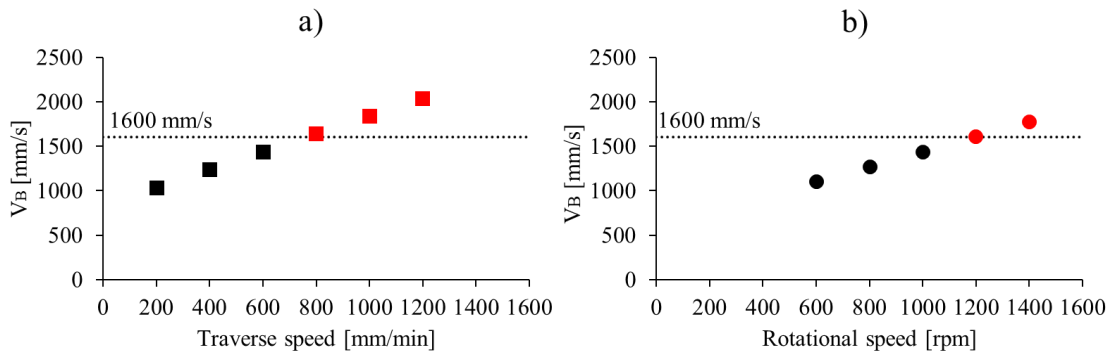


**Figure 57** – Evolution of  $V_B$  with the traverse speed (a) and rotational speed (b) (adapted from “Article A”).

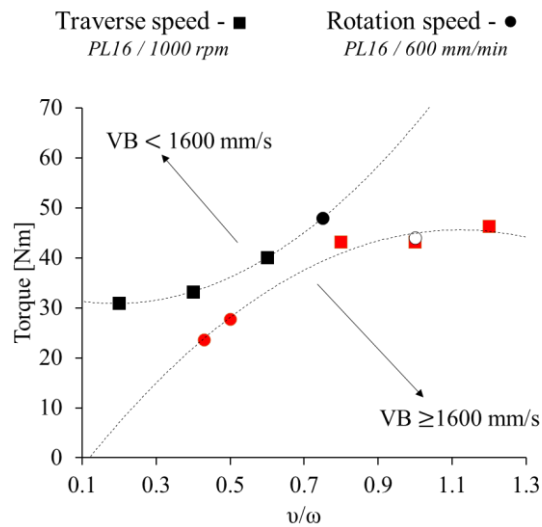


**Figure 58** – Evolution of torque values with the weld pitch  $v/\omega$  (adapted from “Article A”).

### 5.1.3. *Mechanical characterisation*

The strength of all the welds shown in Figure 50 to Figure 52 was evaluated by testing AS and RS loaded samples, following the procedures explained in Chapter 2. The analysis of the results enabled to conclude that most of the samples had lap shear strength similar to the ultimate tensile strength of the base material. The only exception was reported for the weld performed with the PL16 tool at 1000 rpm and 1000 mm/min, for which the lap shear strength of some of the samples did not exceed the yield strength of the base material. Additionally, for most of the welds, no important differences in the lap shear strength of the AS and RS samples were reported.

In order to illustrate the previous statements, Figure 59 to Figure 61 show load-displacement curves of some selected welds. More precisely, Figure 59 shows the load-displacement curves, corresponding to AS and RS samples of the weld produced with the PL16 tool, using rotational and traverse speeds of 1000 rpm and 600 mm/min, respectively, together with the load-displacement curve under tension, of a homogeneous specimen of the base material, with the same width of the lap shear samples. The figure shows that both the AS and RS samples of the weld had mechanical behaviour/strength similar to that of the base material. The Mises strain maps, at maximum load, displayed in Figure 59b and c, also show that both the RS and AS samples failed in the base material far from the weld. In Figure 59d is shown an image of the base material fracture. Since no plastic deformation was recorded inside the PAZ, it is possible to confirm that no lap defects or bonding discontinuities, acting as stress concentrators, were present in the weld. Similar behaviour/strength was reported for most of the welds analysed in this work, except for that produced with the PL16 tool and the highest values of tool rotational and traverse speeds.

In Figure 60a is shown the load-displacement curves, corresponding to AS and RS samples of the weld produced with the PL16 tool, using rotational and traverse speeds of 1000 rpm and 1000 mm/min, respectively. The figure shows that some of the samples of the weld made with a traverse speed of 1000 mm/min had rupture for load values in the range of the yield strength of the base material (red curves in the graph). These samples failed by separation of the plates, at the bonding interface, as shown in Figure 60b. The important differences in strength/behaviour reported for the AS and for the RS samples of this weld, show that the quality of the bonding was not uniform along the weld length. Also, for the weld performed with the PL16 tool at rotational and traverse speeds of 1000

rpm and 1200 mm/min, respectively, the separation of the faying surfaces occurred when handling the samples for the mechanical characterization. In the same way, a non-uniform behaviour in lap shear testing was reported for the weld manufactured with the PL16 tool, at a traverse speed of 600 mm/min and a rotational speed of 1400 rpm, as is shown in Figure 61. For this weld, despite all the samples had strength similar to the UTS of the base material (Figure 61a), the failure modes were different for the AS and for the RS samples. As is shown by the Mises strain maps in Figure 61b and c, while the AS samples failed in the base material, with no plastic deformation in the weld, the RS samples had failure in the top plate, inside the PAZ.

The lap shear testing results show that despite all the welds analysed displayed excellent strength, the loading/failure behaviour was not uniform for the welds with strong asymmetry in PAZ morphology.

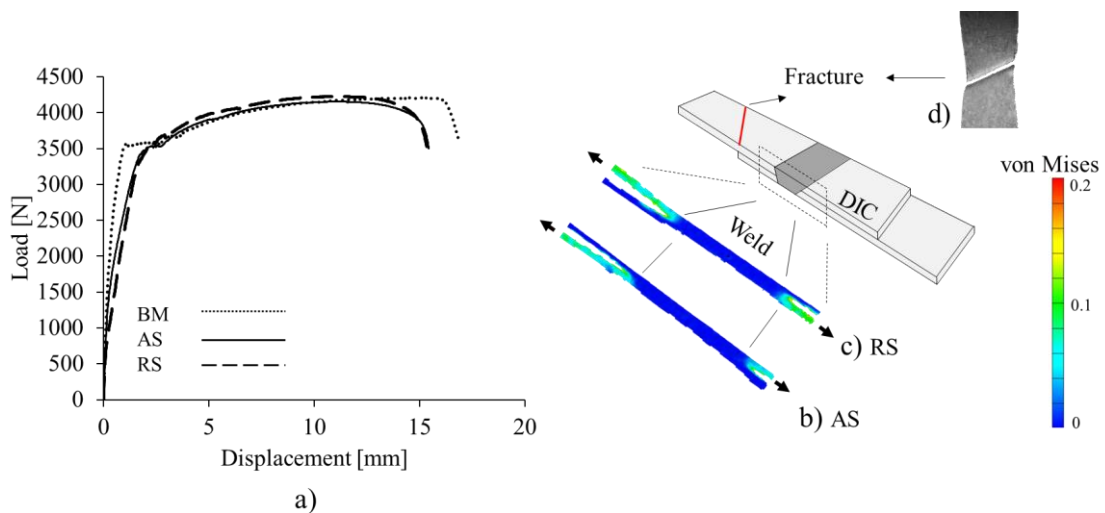


**Figure 59** – Load-displacement curves (a), strain maps (b–c) and fractured sample (d) for the weld produced with the PL16 tool at 600 mm/min and 1000 rpm (adapted from “Article A”).

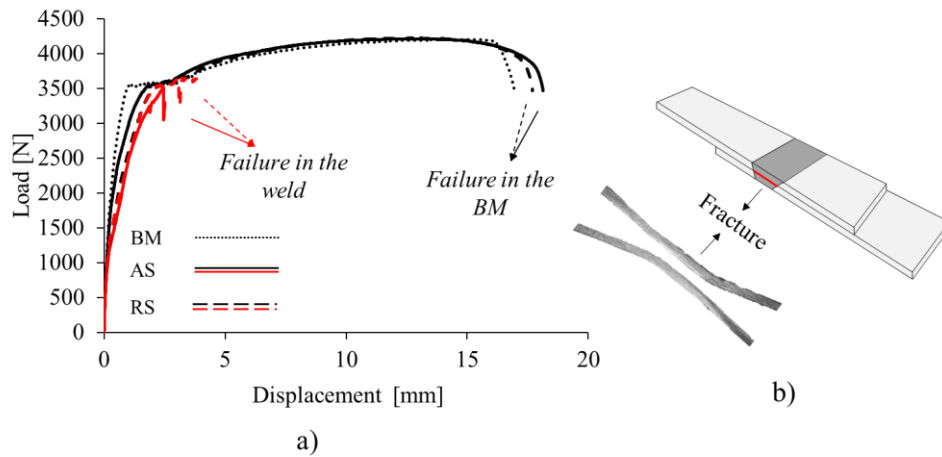


**Figure 60** – Load-displacement curves (a) and fractured sample (b) for the weld produced with the PL16 tool at 1000 mm/min and 1000 rpm (adapted from “Article A”).

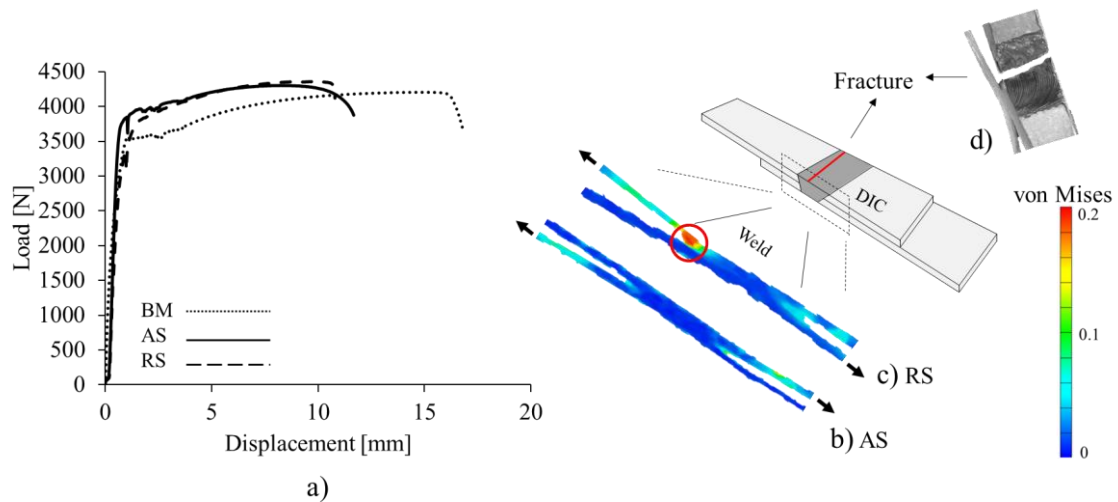


**Figure 61** – Load-displacement curves (a), strain maps (b–c) and fractured sample (d) for the weld produced with the PL16 tool at 600 mm/min and 1400 rpm (adapted from “Article A”).

## 5.2. Spot welding

The work carried out to analyse the feasibility of using pinless tools to produce steel spot welds is schematically represented in Figure 62. Similarly, to what was performed for the linear welds, the bonding mechanisms in spot welding of DC steel, with pinless tools, were analysed by coupling experimental and numerical results. The spot welds strength was evaluated by performing mechanical characterization tests of welds produced in galvanised and non-galvanised steels (DC and DXR14) under a varied range of tool diameters, rotational speeds and dwell times. In addition, special attention was put in

characterizing the influence of the galvanised coating thickness on the thermo-mechanical conditions developed during spot welding. Once again, this analysis was performed by coupling experimental and numerical results.

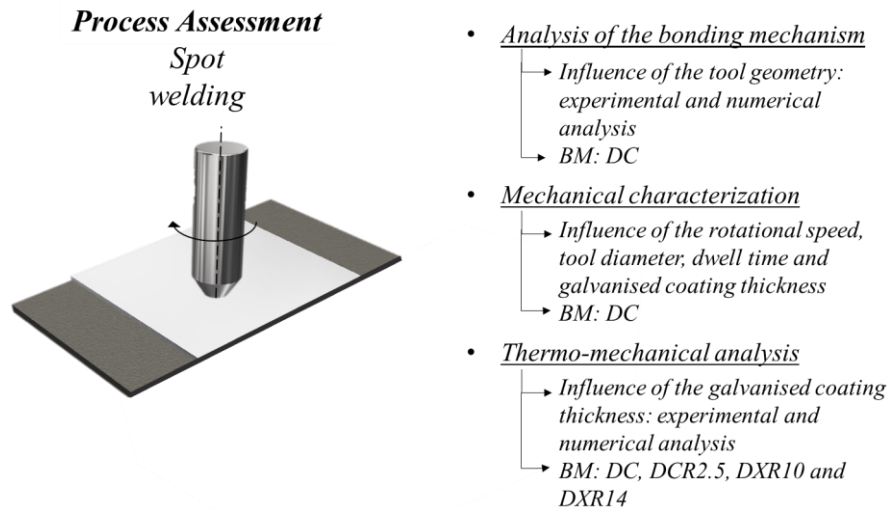


**Figure 62** - Schematic representation of the process assessment analysis performed in current work for spot welds.

### 5.2.1. Analysis of the bonding mechanisms

The bonding mechanisms in spot welding were analysed by producing a weld in DC steel, with the PL12 tool and with a rotational speed of 1140 rpm. In Figure 63a it is shown the cross section of the weld produced, and in Figure 63b it is shown the strain rate distribution map, in the weld cross section, obtained when simulating the experimental conditions in which the weld shown in Figure 63a was produced. Analysing the figure, it is possible to conclude that the weld cross section is very similar to that of the linear weld produced with a pinless tool (Figure 47b). Once again, it is possible to observe a darker region, which corresponds to the PAZ, and a continuous line at the mid thickness of the weld, aligned with the plates original interface. The strain rate map, in Figure 63b, also shows that the stirring action of the tool was limited to a region close to the weld top surface, which correspond to the weld region where higher amount of tool remnants were observed for the linear weld. The computed strain rate values are zero at the plates interface, which supports the previous assumption that no stirring occurred across the base materials thickness. Although no stirring took place at the plates interface, joining of the plates occurred as is shown by the micrograph in Figure 64, where it is possible to

observe the microstructural continuity between the top and the bottom sheets, which shows that the joining between the plates occurred due to diffusion mechanisms associated with the very high pressure and temperatures attained during welding.

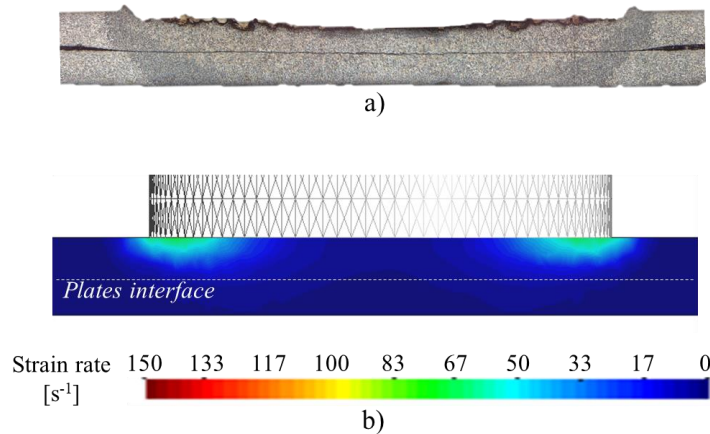


**Figure 63** – Comparison of the weld cross section (a) and strain rate map (b) for the spot weld produced in the DC steel with a rotational speed of 1140 rpm and with a tool diameter of 12 mm (adapted from “Article E”).

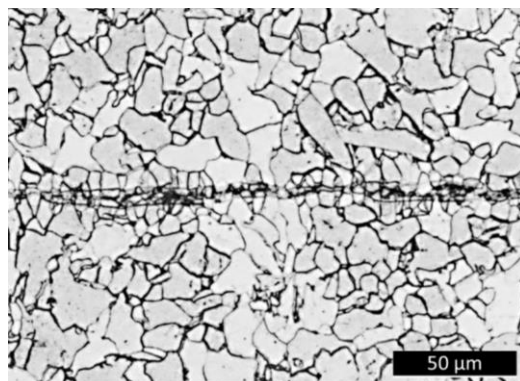


**Figure 64** – Magnification of the weld microstructure at the plates bonding interface (adapted from “Article E”).

### 5.2.2. Mechanical characterisation

The strength of the steel spot welds was evaluated by testing shear tension samples, following the procedures explained in Chapter 2. The influence of the rotational speed, tool diameter, dwell time and galvanised coating thickness, on the strength of the spot welds, is shown in Figure 65. The welds were produced in the DC steel, by varying the rotational speed and the tool diameter between 870 and 1500 rpm and using the PL10 (Figure 65a), PL12 (Figure 65b) and PL16 (Figure 65c) tools, and in the DXR14 steel, by

varying the rotational speed between 870 and 1500 rpm and using the PL12 tool (Figure 65d). Dwelling periods of 5, 15, 30 and 60 s were tested for all the process parameters combinations. In Figure 65e and f are also represented the failure modes identified for the different samples tested.

Analysing Figure 65, it is possible to conclude that the strength of the joints significantly varied according to the welding conditions tested. For the non-galvanised steel, the strength always increased by increasing the tool diameter, irrespective of the rotational speed and dwell time, enabling to conclude that the tool diameter is the main factor determining the metallurgical bonding area. On the other hand, for short process cycle times, when welding with the smaller tool diameters, increasing the rotational speed increased the strength of the joints. When welding with the PL16 tool, no influence of the rotational speed on the joint strength was registered. These results are related to the strong influence of the shoulder diameter and rotational speed on the heat generation, as already shown in Figure 20a. According to Chapter 3 results, in spot welding of steels, for large tool diameters and large rotational speeds, a threshold in heat generation is attained, and the temperature remains constant independently of the processing parameters used. On the other hand, for small tool diameters, the welding temperature keeps increasing with the increase of the rotational speed. Based on these results, it is possible to conclude that increasing the welding heat input improves the spot joints strength.

Another important factor governing the strength of the joints is the welding time. Analysing the figure, it is possible to observe that increasing the welding time from 5 to 15 s, for the PL10 and PL12 tools, at a constant rotational speed of 870 rpm, lead to a substantial increase of the joint strength. It is also important to notice that for welding times higher than 30 s, no influence of the rotational speed or welding time on the joints strength was registered.

Comparing now the strength of the uncoated steel (DC) welds to that of the galvanised steel (DXR14) welds, it is possible to conclude that the galvanised coating has a strong influence on the joint properties. While for the welds produced in the DC steel, with the PL12 tool and a rotational speed of 870 rpm, effective joining between the plates was obtained for 15 s dwell time, for the DXR14 steel welds, produced with the same processing parameters, the joining between plates only occurred for 30 s dwelling time. Also, for the DXR14 steel, no effective joining occurred for a welding time of 5 s, even when using a rotational speed of 1500 rpm.



Finally, according to Figure 65e and f, the fracture behaviour of the samples can be divided into two groups, i.e., interfacial fracture, when the fracture occurred by separation of the faying surfaces (square points), and plug fracture, when the fracture occurred by crack propagation along the weld perimeter (circular points). According to the figure, most of the shear tension samples tested displayed plug fracture mode. The only exceptions were the DC welds produced with the PL12 and PL10 tools, 870 rpm and 5 s dwelling time, and the DXR14 steel welds produced with the PL12 tool, 1500 and 870 rpm and dwelling times lower than 15 s, i.e. the welds with lower mechanical strength.

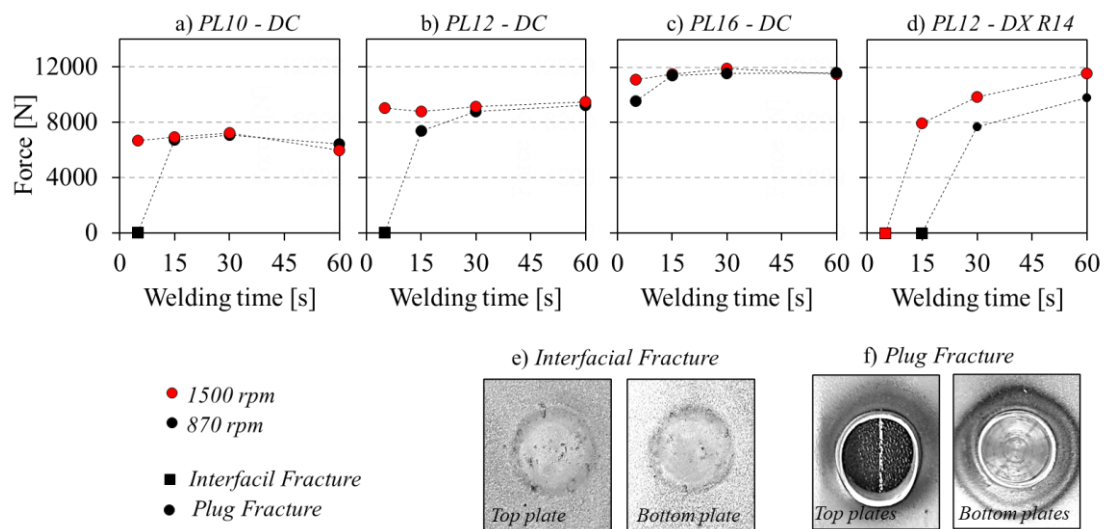


**Figure 65** – Influence of the rotational speed, shoulder diameter, welding time and galvanised coating thickness on the shear tensile load of the welded joints (adapted from “Article E”).

### 5.2.3. Analysis of the thermo-mechanical conditions

To better understand the effect of the galvanised coating on the strength of the spot welds, an analysis on the influence of the galvanised coating thickness on the thermo-mechanical conditions developed during spot welding was conducted. With this aim, spot welds were produced in DC, DCR2.5, DXR10 and DXR14 steels, which had 0, 2.5, 10 and 14  $\mu\text{m}$  thick galvanised coatings, respectively. Rotational speeds from 870 to 1500 rpm and a constant tool diameter of 12 mm were used in this study. The thermo-mechanical conditions developed during welding were assessed by registering the thermal cycles with a thermographic camera and by simulating the experimental tests with COMET software, following the procedures explained in Chapter 2.

In Figure 66 are plotted the thermal cycles registered for all the welds produced. The figure shows that, irrespective of the tool rotational speed, the heating period, was

longer for the galvanised base materials than for the uncoated DC steel. In the same way, meanwhile for the tool rotational speed of 1500 rpm, the threshold temperature of 1000 °C was reached for all the base materials, for the tool rotational speed of 870 rpm, the maximum temperature of 800 °C was not reached in the welding of the DXR10 and DXR14 plates. This behaviour may be associated with the influence of the galvanised zinc layer on the frictional heat generation. When welding at 870 rpm, the temperatures reached are sufficient for melting the galvanised coating (420 °C), which starts acting as a lubricant at the tool/base material interface, lowering the frictional heat generation. However, when welding at 1500 rpm, the heat generated by the tool promotes temperatures higher than the boiling point of the galvanised coating (907 °C), promoting its expulsion from the welding zone and enabling that the threshold temperature is reached independently of the base material.

As highlighted by the blue rectangle, plotted in Figure 66, it is also possible to conclude that the influence of the galvanised coating on the frictional heat generation is even more important for process cycle times lower than 10 s. In these conditions, the use of low tool rotational speeds may be not sufficient for the melting and expulsion of the zinc layer from the welding zone. When increasing the tool rotational speed, to 1500 rpm, the maximum temperature attained during the 10 s cycle period will depend on the thickness of the galvanised coating, but may attain the melting temperature of the zinc, even for thick coatings.

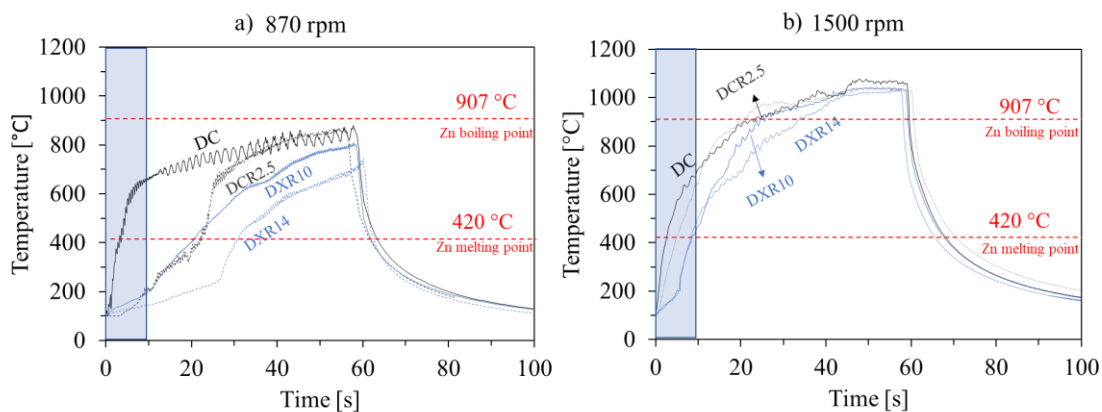


**Figure 66** – Thermal cycles for the welds produced in the steels DC, DCR2.5, DXR10 and DXR14, with the PL12 tool and a rotational speed of 870 rpm (a) and 1500rpm (b) (adapted from “Article B”).

To better understand the effect of the galvanised coating on the heat generation, numerical simulations were performed with different friction values at the tool/workpiece interface, by ranging the consistency parameter ( $a(T)$ ), from Eq. 1, between 0.5 and 500 MPa. To assess the contact conditions at the tool/workpiece interface, the sticking fraction parameter (Eq. 4), proposed by Schmidt et al. 2003 [52] was used.

In Figure 67 is compared the evolution of the welding temperatures, obtained with the numerical simulation (Figure 67a), for different levels of friction, with the welding thermal cycles measured experimentally (Figure 67b) for the DC and DXR14 base materials, i.e. the uncoated base material and the base material with the thicker galvanised coating. The thermal cycles of Figure 67b correspond to the welds produced with a rotational speed of 870 rpm, since according to Figure 66, it is for this rotational speed that the galvanised coating thickness has bigger influence on the heat generation. Finally, in Figure 67c–e are shown the velocity profiles for different friction values between the tool and the base material.

From Figure 67, it is possible to conclude that there was a gradual increase of the welding temperatures and of the sticking fraction when the consistency parameter was increased from 0.5 to 500 MPa. For very low values of  $a(T)$ , fully slipping contact conditions prevailed ( $\delta = 0$ ) and no stirring took place at the tool-workpiece interface, as is possible to conclude from the velocity profile shown in Figure 67c. The tool only starts to stir material for values of  $a(T)$  higher than 30 MPa ( $\delta = 0.1$ ), as shown in Figure 67d. With the gradual increase of  $a(T)$ , there was an increase in the amount of material stirring until a limit is reached at  $a(T)$  equal to 100 MPa (Figure 67e). For  $a(T) > 100$  MPa sticking contact conditions prevailed ( $\delta > 0.6$ ) and the welding temperature becomes independent of the friction value. The evolution of the temperature with  $a(T)$ , obtained through the numerical simulation, is similar to the welding thermal cycles for the galvanised steels, allowing to conclude that the melting and expulsion of the galvanised coating from the tool-workpiece interface during welding has a strong influence on the contact conditions. More precisely, during welding, the tool axial load and centrifugal action expel the galvanised coating from the welding region, which allow a continuous increase of the friction at the tool workpiece interface and of the welding temperature over time. According to Figure 67b, for the DXR14 steel, a large amount of the galvanised coating remained trapped at the tool workpiece interface, promoting prevalent slipping conditions ( $\delta < 0.1$ ), during the 60 s dwelling period, lowering the frictional heat generation.

## Process Assessment

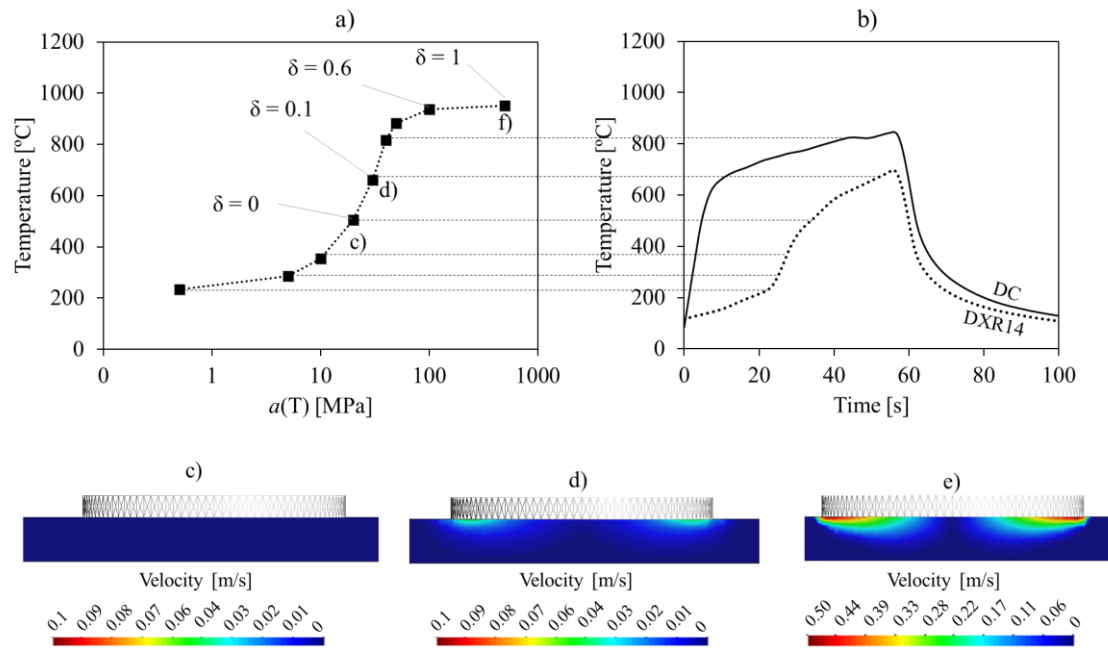


**Figure 67** – Comparison between the welding temperatures, obtained through numerical simulation, for different levels of friction (a), with the welding thermal cycles for the DC and DXR14 welds (b), produced with the PL12 tool at 870 rpm. Velocity profiles, along the weld cross section, for different levels of friction (c–e) (adapted from “Article E”).

## 6. Conclusions and Future Work

---

### *6.1. Conclusions*

In this thesis, a thermal and mechanical analysis of the main friction stir based mechanisms and their relation with the tool dimensions, the rotational and the traverse speeds, the plate thicknesses and the base material properties, were studied by coupling numerical and experimental results. Additionally, the suitability of using pinless tools in the lap joining of thin steel plates was also analysed. The following conclusions were reached:

#### **Thermal Analysis**

- For the linear welding of aluminium alloys and the spot welding of steels it was found that the heat generation is mainly governed by the tool dimensions, due to its important influence on the contact area between the tool and the workpiece and on the amount of material stirred by the tool, and by the rotational speed, due to its important influence on the strain rates. The traverse speed and the base material thickness are secondary parameters governing the welding temperature, since these parameters only have influence on the heat dissipation. Independently of the base material and process parameters used, a threshold in the heat generation was always registered, ensuring that solid-state welding conditions always prevail. The temperature threshold was found to be equal, for the different steels and for the different aluminium alloys.
- For the spot welding of aluminium alloys it was found that the heat generation may be controlled by a proper selection of the pinless tool dimensions. According to the dissertation results, for rotational speeds higher than 600 rpm, for each tool diameter, a threshold in the welding temperatures is reached, independent of the rotational speed and/or of the aluminium alloy being welded. The temperature

## Conclusions and Future Work

threshold is attained for temperatures far below the melting temperature of the alloy being welded and increase with the increase of the tool diameter.

- Temperature coefficients, for spot and linear welding ( $C_T$  and  $C_{T,sw}$ ), were developed to predict the evolution of the welding temperature with the tool dimensions, plate thicknesses, rotational and traverse speeds. The proposed model provided accurate temperature predictions for the very large range of welding conditions and base materials tested. The model constants were found to be different for the different steels, but similar among the different aluminium alloys.

### **Mechanical analysis**

- The material flow during welding is determined by the base material plastic properties and by the contact conditions at the tool/workpiece interface. The material flow was found to be more intense for materials with low mechanical strength and/or high strain rate sensitivity. The results also show that the base material only rotates several times around the tool when the contact conditions are close to full sticking. The formation of welding defects was associated with slipping contact conditions.
- The tool torque was found to decrease with the increase of the rotational speed. On the other hand, although the increase in the tool dimensions conducts to a higher heat generation, the increase of the stirred volume leads to an increase in the tool torque. The traverse speed and the base material thickness were found to be secondary parameters governing the torque, since its influence on the heat input is exclusively related to the heat dissipation.
- Torque coefficients, for spot and linear welding ( $C_M$  and  $C_{M,sw}$ ), were developed to predict the evolution of torque with the tool dimensions, plate thicknesses, rotational and traverse speeds. The proposed model provides better predictions on the torque evolution with process parameters, than other models developed up to

date. The model constants were found to be equal for the different steels and aluminium alloys tested.

### **Process assessment**

- The lap joining mechanisms were found to be different for pin and pinless tools. For the tools with a pin, the joining of the plates resulted from the base material stirring/mixing, promoted by the pin. On the other hand, for the pinless tools, no stirring across the base materials lap interface occurs and the joining of the plates is promoted by the plastic deformation of the interface and by the atomic diffusion at the very high pressure and temperature promoted by the tool.
- The use of pinless tools was found to be effective for the lap welding of thin steel plates. Lap welds without defects and high mechanical strength were produced, even for very high traverse speeds, in linear welding (up to 1000 mm/min), or using very short process cycle times, in spot welding (5 s).
- For steel welds produced with pinless tools, the presence of a thick galvanised coating is an important factor determining the heat generation. The galvanised coating work as a lubricant during welding reducing the sticking fraction and the frictional heat generation. In spot welding the presence of thick galvanised coatings is even more important, since it as a detrimental effect on the joint strength, especially for process cycle times lower than 10 s. For these steels, the effect of the galvanised coating on the joint strength may be suppressed by using very high rotational speeds and/or by adjusting the welding time according to the coating thickness and tool diameter.

### *6.2. Future work suggestions*

Although some progress in the understanding of the thermo-mechanical conditions developed during the FSBT has been achieved, there are still aspects that can be further developed and improved. The following aspects deserve further development:

## Conclusions and Future Work

- Since the slipping/sticking conditions define the tool workpiece interaction, the evolution of the friction coefficient during stir/welding processing needs to be assessed by using high temperature tribology. However, attending to the high complexity of the contact conditions in FSBT, the development of specific devices and/or procedures, for analysing the evolution of the friction coefficient at the temperatures and strain rates envisaged by that processes, is required.
- Using a thermomechanical simulator, such as the *Glebbler* system, for example, for physically simulating stir processes loading conditions, i.e. for performing mechanical tests simulating at the same range of temperatures and strain rates determined in current work, for the FSW process, in order to determine the influence of the base material plastic properties on the  $C_M$  and  $C_T$  coefficients.
- To develop online temperature and torque control systems, for the FSW process, by performing adaptive changes in the controllable parameters through the  $C_T$  and  $C_M$  coefficients.
- Perform a further analysis of the welding mechanisms taking place when the shoulder diameter temperature threshold is observed. To reach this goal, a larger experimental campaign should be performed in several base materials, to verify the welding conditions for which the shoulder diameter temperature threshold occurs, in spot and linear welding. Numerical analysis should also be used to simulate this physical phenomenon. However, the numerical model used in the current work has to be improved in order to include other friction models to simulate the friction at the tool/workpiece interface.



## 7. References

---

- [1] W.M. Thomas, E.D. Nicholas, J.C. Needam, M.G. Murch, P. Templesmith, C.J. Dawes, GB Patent Application No. 9125978.8, December 1991 and US Patent No. 5460317, October. (1995).
- [2] C. van der Rest, P.J. Jacques, A. Simar, On the joining of steel and aluminium by means of a new friction melt bonding process, *Scr. Mater.* 77 (2014) 25–28. doi:<https://doi.org/10.1016/j.scriptamat.2014.01.008>.
- [3] B.T. Gibson, M.C. Ballun, G.E. Cook, A.M. Strauss, Friction stir lap joining of 2198 aluminum-lithium alloy with weaving and pulsing variants, *J. Manuf. Process.* 18 (2015) 12–22. doi:10.1016/j.jmapro.2014.12.002.
- [4] T. Mira-Aguiar, D. Verdera, C. Leitão, D.M.M. Rodrigues, Tool assisted friction welding: A FSW related technique for the linear lap welding of very thin steel plates, *J. Mater. Process. Technol.* 238 (2016) 73–80. doi:10.1016/j.jmatprotec.2016.07.006.
- [5] A. Ebrahimian, A.H. Kokabi, Friction stir soldering: A novel route to produce graphite-copper dissimilar joints, *Mater. Des.* 116 (2017) 599–608. doi:10.1016/j.matdes.2016.12.057.
- [6] R. Sakano, Development of spot FSW robot system for automobile body members, *Proc. 3rd Int. Symp. Frict. Stir Welding, Kobe, Japan, 2004.* (2004). <https://ci.nii.ac.jp/naid/10020488538/en/>.
- [7] R. Stevenson, P.C. Wang, Friction stir riveting - Impact of process parameters on joint performance, *Am. Soc. Mech. Eng. Manuf. Eng. Div. MED.* 16–2 (2005) 1001–1009. doi:10.1115/IMECE2005-79281.
- [8] M.P. Miles, K. Kohkonen, S. Packer, R. Steel, B. Siemssen, Y.S. Sato, Solid state spot joining of sheet materials using consumable bit, *Sci. Technol. Weld. Join.* 14 (2009) 72–77. doi:10.1179/136217108X341193.
- [9] G. Zhang, L. Zhang, C. Kang, J. Zhang, Development of friction stir spot brazing (FSSB), *Mater. Des.* 94 (2016) 502–514. doi:10.1016/j.matdes.2016.01.057.
- [10] R.S. Mishra, M.W. Mahoney, Friction stir processing: a new grain refinement technique to achieve high strain rate superplasticity in commercial alloys, in:

## References

- Mater. Sci. Forum, 2001: pp. 507–514.
- [11] J. Gandra, H. Krohn, R.M. Miranda, P. Vilaça, L. Quintino, J.F. Dos Santos, Friction surfacing - A review, *J. Mater. Process. Technol.* 214 (2014) 1062–1093. doi:10.1016/j.jmatprotec.2013.12.008.
- [12] N. Balasubramanian, R.S. Mishra, K. Krishnamurthy, Friction stir channeling: Characterization of the channels, *J. Mater. Process. Technol.* 209 (2009) 3696–3704. doi:10.1016/j.jmatprotec.2008.08.036.
- [13] M.I. Costa, C. Leitão, A. Ramalho, D.M. Rodrigues, Local improvement of structural steels high-friction properties by friction stir texturing, *J. Mater. Process. Technol.* 217 (2015) 272–277. doi:10.1016/j.jmatprotec.2014.11.026.
- [14] X. Li, D. Baffari, A.P. Reynolds, Friction stir consolidation of aluminum machining chips, *Int. J. Adv. Manuf. Technol.* 94 (2018) 2031–2042. doi:10.1007/s00170-017-1016-4.
- [15] R.S. Mishra, Z.Y. Ma, Friction stir welding and processing, *Mater. Sci. Eng. R Reports.* 50 (2005) 1–78. doi:10.1016/j.mser.2005.07.001.
- [16] W.J. Arbegast, A flow-partitioned deformation zone model for defect formation during friction stir welding, *Scr. Mater.* 58 (2008) 372–376. doi:10.1016/j.scriptamat.2007.10.031.
- [17] R. Rai, A. De, H.K.D.H. Bhadeshia, T. DebRoy, Review: friction stir welding tools, *Sci. Technol. Weld. Join.* 16 (2011) 325–342. doi:10.1179/1362171811Y.0000000023.
- [18] P.L. Threadgill, A.J. Leonard, H.R. Shercliff, P.J. Withers, Friction stir welding of aluminium alloys, *Int. Mater. Rev.* 54 (2009) 49–93. doi:10.1179/174328009X411136.
- [19] G. Çam, S. Mistikoglu, Recent Developments in Friction Stir Welding of Al-alloys, *J. Mater. Eng. Perform.* 23 (2014) 1936–1953. doi:10.1007/s11665-014-0968-x.
- [20] G. Çam, G. İpekoğlu, Recent developments in joining of aluminum alloys, *Int. J. Adv. Manuf. Technol.* 91 (2017) 1851–1866. doi:10.1007/s00170-016-9861-0.
- [21] T.J. Lienert, W.L. Stellwag Jr, B.B. Grimmer, R.W. Warke, Friction stir welding studies on mild steel, *Weld. Journal-New York-*. 82 (2003) 1--S.
- [22] F.C. Liu, Y. Hovanski, M.P. Miles, C.D. Sorensen, T.W. Nelson, A review of friction stir welding of steels: Tool, material flow, microstructure, and properties, *J. Mater. Sci. Technol.* 34 (2018) 39–57.

- doi:<https://doi.org/10.1016/j.jmst.2017.10.024>.
- [23] K. Nakata, Friction stir welding of magnesium alloys, *Weld. Int.* 23 (2009) 328–332. doi:[10.1080/09507110802542668](https://doi.org/10.1080/09507110802542668).
- [24] K. Singh, G. Singh, H. Singh, Review on friction stir welding of magnesium alloys, *J. Magnes. Alloy.* 6 (2018) 399–416. doi:<https://doi.org/10.1016/j.jma.2018.06.001>.
- [25] K. Gangwar, M. Ramulu, Friction stir welding of titanium alloys: A review, *Mater. Des.* 141 (2018) 230–255. doi:<https://doi.org/10.1016/j.matdes.2017.12.033>.
- [26] F. Lambiase, A. Derazkola, A. Simchi, Friction Stir Welding and Friction Spot Stir Welding Processes of Polymers—State of the Art, *Materials (Basel)*. 13 (2020) 2291.
- [27] F. Simões, D.M. Rodrigues, Material flow and thermo-mechanical conditions during Friction Stir Welding of polymers: Literature review, experimental results and empirical analysis, *Mater. Des.* 59 (2014) 344–351. doi:<https://doi.org/10.1016/j.matdes.2013.12.038>.
- [28] S. Eslami, P.J. Tavares, P.M.G.P. Moreira, Friction stir welding tooling for polymers: review and prospects, *Int. J. Adv. Manuf. Technol.* 89 (2017) 1677–1690. doi:[10.1007/s00170-016-9205-0](https://doi.org/10.1007/s00170-016-9205-0).
- [29] R. Nandan, T. DebRoy, H.K.D.H. Bhadeshia, Recent advances in friction-stir welding – Process, weldment structure and properties, *Prog. Mater. Sci.* 53 (2008) 980–1023. doi:<https://doi.org/10.1016/j.pmatsci.2008.05.001>.
- [30] D. Mishra, R.B. Roy, S. Dutta, S.K. Pal, D. Chakravarty, A review on sensor based monitoring and control of friction stir welding process and a roadmap to Industry 4.0, *J. Manuf. Process.* 36 (2018) 373–397. doi:<https://doi.org/10.1016/j.jmapro.2018.10.016>.
- [31] A. Fehrenbacher, N.A. Duffie, N.J. Ferrier, F.E. Pfefferkorn, M.R. Zinn, Toward Automation of Friction Stir Welding Through Temperature Measurement and Closed-Loop Control, *J. Manuf. Sci. Eng.* 133 (2011). doi:[10.1115/1.4005034](https://doi.org/10.1115/1.4005034).
- [32] L. Cederqvist, O. Garpinger, T. Hägglund, A. Robertsson, Cascade control of the friction stir welding process to seal canisters for spent nuclear fuel, *Control Eng. Pract.* 20 (2012) 35–48. doi:<https://doi.org/10.1016/j.conengprac.2011.08.009>.
- [33] J. De Backer, *Feedback Control of Robotic Friction Stir Welding*, University West, 2014.
- [34] D.G. Andrade, C. Leitão, D.M.M. Rodrigues, Properties of lap welds in low carbon

## References

- galvanized steel produced by tool assisted friction welding, *J. Mater. Process. Technol.* 260 (2018) 77–86. doi:<https://doi.org/10.1016/j.jmatprotec.2018.05.018>.
- [35] D.G. Andrade, C. Leitão, D.M. Rodrigues, Influence of base material characteristics and process parameters on frictional heat generation during Friction Stir Spot Welding of steels, *J. Manuf. Process.* 43 (2019) 98–104. doi:<https://doi.org/10.1016/j.jmapro.2019.05.015>.
- [36] D.G. Andrade, C. Leitão, N. Dialami, M. Chiumenti, D.M. Rodrigues, Modelling torque and temperature in friction stir welding of aluminium alloys, *Int. J. Mech. Sci.* 182 (2020). doi:[10.1016/j.ijmecsci.2020.105725](https://doi.org/10.1016/j.ijmecsci.2020.105725).
- [37] D.G. Andrade, C. Leitão, N. Dialami, M. Chiumenti, D.M. Rodrigues, Analysis of contact conditions and its influence on strain rate and temperature in friction stir welding, *Int. J. Mech. Sci.* 191 (2021) 106095. doi:<https://doi.org/10.1016/j.ijmecsci.2020.106095>.
- [38] D.G. Andrade, S.S. Sabari, C. Leitão, D.M. Rodrigues, Influence of the galvanized coating thickness and process parameters on heat generation and strength of steel spot welds, *Thin-Walled Struct.* 160 (2021) 107401. doi:<https://doi.org/10.1016/j.tws.2020.107401>.
- [39] C. Leitão, R. Louro, D.M. Rodrigues, Analysis of high temperature plastic behaviour and its relation with weldability in friction stir welding for aluminium alloys AA5083-H111 and AA6082-T6, *Mater. Des.* 37 (2012) 402–409. doi:<https://doi.org/10.1016/j.matdes.2012.01.031>.
- [40] S. Sabari, I. Galvão, C. Leitão, D.M. Rodrigues, Influence of Softening Mechanisms on Base Materials Plastic Behaviour and Defects Formation in Friction Stir Lap Welding, *J. Manuf. Mater. Process.* 4 (2020) 120. doi:[10.3390/jmmp4040120](https://doi.org/10.3390/jmmp4040120).
- [41] M.I. Costa, D. Verdera, J.D. Costa, C. Leitao, D.M. Rodrigues, Influence of pin geometry and process parameters on friction stir lap welding of AA5754-H22 thin sheets, *J. Mater. Process. Technol.* 225 (2015) 385–392. doi:<https://doi.org/10.1016/j.jmatprotec.2015.06.020>.
- [42] C. Leitão, I. Galvão, R.M. Leal, D.M. Rodrigues, Determination of local constitutive properties of aluminium friction stir welds using digital image correlation, *Mater. Des.* 33 (2012) 69–74. doi:[10.1016/j.matdes.2011.07.009](https://doi.org/10.1016/j.matdes.2011.07.009).
- [43] C. Leitão, M.I. Costa, K. Khanijomdi, D.M. Rodrigues, Assessing strength and local plastic behaviour of welds by shear testing, *Mater. Des.* 51 (2013) 968–974.

- doi:10.1016/j.matdes.2013.04.100.
- [44] M. Chiumenti, M. Cervera, C. Agelet de Saracibar, N. Dialami, Numerical modeling of friction stir welding processes, *Comput. Methods Appl. Mech. Eng.* 254 (2013) 353–369. doi:<https://doi.org/10.1016/j.cma.2012.09.013>.
- [45] N. Dialami, M. Chiumenti, M. Cervera, C. Agelet De Saracibar, An apropos kinematic framework for the numerical modeling of friction stir welding, *Comput. Struct.* 117 (2013) 48–57. doi:10.1016/j.compstruc.2012.12.006.
- [46] N. Dialami, M. Cervera, M. Chiumenti, A. Segatori, W. Osikowicz, Experimental Validation of an FSW Model with an Enhanced Friction Law: Application to a Threaded Cylindrical Pin Tool, *Metals (Basel)*. 7 (2017). doi:10.3390/met7110491.
- [47] N. Dialami, M. Chiumenti, M. Cervera, A. Segatori, W. Osikowicz, Enhanced friction model for Friction Stir Welding (FSW) analysis: Simulation and experimental validation, *Int. J. Mech. Sci.* 133 (2017) 555–567. doi:<https://doi.org/10.1016/j.ijmecsci.2017.09.022>.
- [48] N. Dialami, M. Cervera, M. Chiumenti, C.A. de Saracibar, C. Agelet de Saracibar, C.A. de Saracibar, C. Agelet de Saracibar, C.A. de Saracibar, A fast and accurate two-stage strategy to evaluate the effect of the pin tool profile on metal flow, torque and forces in friction stir welding, *Int. J. Mech. Sci.* 122 (2017) 215–227. doi:10.1016/j.ijmecsci.2016.12.016.
- [49] K.E. Tello, a. P. Gerlich, P.F. Mendez, Constants for hot deformation constitutive models for recent experimental data, *Sci. Technol. Weld. Join.* 15 (2010) 260–266. doi:10.1179/136217110X12665778348380.
- [50] N. Dialami, M. Cervera, M. Chiumenti, Defect formation and material flow in Friction Stir Welding, *Eur. J. Mech. - A/Solids*. 80 (2020) 103912. doi:<https://doi.org/10.1016/j.euromechsol.2019.103912>.
- [51] N. Dialami, M. Cervera, M. Chiumenti, A. Segatori, Prediction of joint line remnant defect in friction stir welding, *Int. J. Mech. Sci.* 151 (2019) 61–69. doi:<https://doi.org/10.1016/j.ijmecsci.2018.11.012>.
- [52] H. Schmidt, J. Hattel, J. Wert, An analytical model for the heat generation in friction stir welding, *Model. Simul. Mater. Sci. Eng.* 12 (2003) 143–157. doi:10.1088/0965-0393/12/1/013.
- [53] R.M. Leal, C. Leitão, A. Loureiro, D.M. Rodrigues, P. Vilaça, Material flow in heterogeneous friction stir welding of thin aluminium sheets: Effect of shoulder

## References

- geometry, *Mater. Sci. Eng. A.* 498 (2008) 384–391. doi:10.1016/j.msea.2008.08.018.
- [54] N. Dialami, M. Chiumenti, M. Cervera, C. de Saracibar, J.P. Ponthot, P. Bussetta, Numerical Simulation and Visualization of Material Flow in Friction Stir Welding via Particle Tracing, in: S.R. Idelsohn (Ed.), *Numer. Simulations Coupled Probl. Eng.*, Springer International Publishing, Cham, 2014: pp. 157–169. doi:10.1007/978-3-319-06136-8\_7.
- [55] K. Huang, R.E. Logé, A review of dynamic recrystallization phenomena in metallic materials, *Mater. Des.* 111 (2016) 548–574. doi:10.1016/j.matdes.2016.09.012.
- [56] Ø. Frigaard, Ø. Grong, O.T. Midling, A process model for friction stir welding of age hardening aluminum alloys, *Metall. Mater. Trans. A.* 32 (2001) 1189–1200. doi:10.1007/s11661-001-0128-4.
- [57] A. Gerlich, G. Avramovic-Cingara, T.H. North, Stir zone microstructure and strain rate during Al 7075-T6 friction stir spot welding, *Metall. Mater. Trans. A.* 37 (2006) 2773–2786. doi:10.1007/BF02586110.
- [58] A. Gerlich, P. Su, M. Yamamoto, T.H. North, Effect of welding parameters on the strain rate and microstructure of friction stir spot welded 2024 aluminum alloy, *J. Mater. Sci.* 42 (2007) 5589–5601. doi:10.1007/s10853-006-1103-7.
- [59] C.I. Chang, C.J. Lee, J.C. Huang, Relationship between grain size and Zener–Holloman parameter during friction stir processing in AZ31 Mg alloys, *Scr. Mater.* 51 (2004) 509–514. doi:https://doi.org/10.1016/j.scriptamat.2004.05.043.
- [60] Y.H. Zhao, S.B. Lin, Z.Q. He, L. Wu, Microhardness prediction in friction stir welding of 2014 aluminium alloy, *Sci. Technol. Weld. Join.* 11 (2006) 178–182. doi:10.1179/174329306X84391.
- [61] T. Sheppard, A. Jackson, Constitutive equations for use in prediction of flow stress during extrusion of aluminium alloys, *Mater. Sci. Technol.* 13 (1997) 203–209. doi:10.1179/mst.1997.13.3.203.
- [62] M.J. Peel, A. Steuwer, P.J. Withers, T. Dickerson, Q. Shi, H. Shercliff, Dissimilar friction stir welds in AA5083-AA6082. Part I: Process parameter effects on thermal history and weld properties, *Metall. Mater. Trans. A.* 37 (2006) 2183–2193. doi:10.1007/BF02586138.
- [63] Y.S. Sato, M. Urata, H. Kokawa, Parameters controlling microstructure and hardness during friction-stir welding of precipitation-hardenable aluminum alloy

- 6063, *Metall. Mater. Trans. A.* 33 (2002) 625–635. doi:10.1007/s11661-002-0124-3.
- [64] W. Xu, J. Liu, G. Luan, C. Dong, Temperature evolution, microstructure and mechanical properties of friction stir welded thick 2219-O aluminum alloy joints, *Mater. Des.* 30 (2009) 1886–1893. doi:https://doi.org/10.1016/j.matdes.2008.09.021.
- [65] L.N. Tufaro, I. Manzoni, H.G. Svoboda, Effect of Heat Input on AA5052 Friction Stir Welds Characteristics, *Procedia Mater. Sci.* 8 (2015) 914–923. doi:10.1016/j.mspro.2015.04.152.
- [66] S.A. Emam, A. El Domiaty, A Refined Energy-Based Model for Friction-Stir Welding, *World Acad. Sci. Eng. Technol.* 29 (2009) 1010–1016.
- [67] A. Arora, A. De, T. Debroy, Toward optimum friction stir welding tool shoulder diameter, *Scr. Mater.* 64 (2011) 9–12. doi:10.1016/j.scriptamat.2010.08.052.
- [68] M.I. Costa, C. Leitão, D.M. Rodrigues, Parametric study of friction stir welding induced distortion in thin aluminium alloy plates: A coupled numerical and experimental analysis, *Thin-Walled Struct.* 134 (2019) 268–276. doi:https://doi.org/10.1016/j.tws.2018.10.027.
- [69] P. Upadhyay, A.P. Reynolds, Effects of thermal boundary conditions in friction stir welded AA7050-T7 sheets, *Mater. Sci. Eng. A.* 527 (2010) 1537–1543. doi:10.1016/j.msea.2009.10.039.
- [70] K. Ramanjaneyulu, G. Madhusudhan Reddy, A. Venugopal Rao, Role of Tool Shoulder Diameter in Friction Stir Welding: An Analysis of the Temperature and Plastic Deformation of AA 2014 Aluminium Alloy, *Trans. Indian Inst. Met.* 67 (2014) 769–780. doi:10.1007/s12666-014-0401-z.
- [71] D. Bakavos, P.B. Prangnell, Effect of reduced or zero pin length and anvil insulation on friction stir spot welding thin gauge 6111 automotive sheet, *Sci. Technol. Weld. Join.* 14 (2009) 443–456. doi:10.1179/136217109X427494.
- [72] M. Mehta, A. Arora, A. De, T. Debroy, Tool geometry for friction stir welding - Optimum shoulder diameter, *Metall. Mater. Trans. A Phys. Metall. Mater. Sci.* 42 (2011) 2716–2722. doi:10.1007/s11661-011-0672-5.
- [73] C. Venkata Rao, G. Madhusudhan Reddy, K. Srinivasa Rao, Influence of tool pin profile on microstructure and corrosion behaviour of AA2219 Al–Cu alloy friction stir weld nuggets, *Def. Technol.* 11 (2015) 197–208. doi:https://doi.org/10.1016/j.dt.2015.04.004.

## References

- [74] M. Wade, A.P. Reynolds, Friction stir weld nugget temperature asymmetry, *Sci. Technol. Weld. Join.* 15 (2010) 64–69. doi:10.1179/136217109X12562846839150.
- [75] H. Papahn, P. Bahemmat, M. Haghpanahi, I.P. Aminaie, Effect of friction stir welding tool on temperature, applied forces and weld quality, *IET Sci. Meas. Technol.* 9 (2015) 475–484.
- [76] P. Upadhyay, A.P. Reynolds, Effects of forge axis force and backing plate thermal diffusivity on FSW of AA6056, *Mater. Sci. Eng. A.* 558 (2012) 394–402. doi:https://doi.org/10.1016/j.msea.2012.08.018.
- [77] L. Giraud, H. Robe, C. Claudin, C. Desrayaud, P. Bocher, E. Feulvarch, Investigation into the dissimilar friction stir welding of AA7020-T651 and AA6060-T6, *J. Mater. Process. Technol.* 235 (2016) 220–230. doi:https://doi.org/10.1016/j.jmatprotec.2016.04.020.
- [78] M. Reza-E-Rabby, A.P. Reynolds, Effect of Tool Pin Thread Forms on Friction Stir Weldability of Different Aluminum Alloys, *Procedia Eng.* 90 (2014) 637–642. doi:https://doi.org/10.1016/j.proeng.2014.11.784.
- [79] Z.-M. Su, Q.-H. Qiu, P.-C. Lin, Design of Friction Stir Spot Welding Tools by Using a Novel Thermal-Mechanical Approach, *Materials (Basel)*. 9 (2016). doi:10.3390/ma9080677.
- [80] A. Kalinenko, K. Kim, I. Vysotskiy, I. Zuiko, S. Malopheyev, S. Mironov, R. Kaibyshev, Microstructure-strength relationship in friction-stir welded 6061-T6 aluminum alloy, *Mater. Sci. Eng. A.* 793 (2020) 139858. doi:https://doi.org/10.1016/j.msea.2020.139858.
- [81] O.S. Salih, N. Neate, H. Ou, W. Sun, Influence of process parameters on the microstructural evolution and mechanical characterisations of friction stir welded Al-Mg-Si alloy, *J. Mater. Process. Technol.* 275 (2020) 116366. doi:https://doi.org/10.1016/j.jmatprotec.2019.116366.
- [82] J.-H. Cho, D.E. Boyce, P.R. Dawson, Modeling strain hardening and texture evolution in friction stir welding of stainless steel, *Mater. Sci. Eng. A.* 398 (2005) 146–163. doi:10.1016/j.msea.2005.03.002.
- [83] E. Hersent, J.H. Driver, D. Piot, C. Desrayaud, Integrated modelling of precipitation during friction stir welding of 2024-T3 aluminium alloy, *Mater. Sci. Technol.* 26 (2010) 1345–1352. doi:10.1179/026708310X12798718274511.
- [84] H.J. Aval, S. Serajzadeh, A.H. Kokabi, The influence of tool geometry on the



- thermo-mechanical and microstructural behaviour in friction stir welding of AA5086, *Proc. Inst. Mech. Eng. Part C J. Mech. Eng. Sci.* 225 (2011) 1–16. doi:10.1243/09544062JMES2267.
- [85] M.S. Chander, M. Ramakrishna, B. Durgaprasad, Experimental investigation on temperature distribution during solid state joining of 5083 aluminium alloy, *Mater. Today Proc.* (2020). doi:<https://doi.org/10.1016/j.matpr.2020.07.037>.
- [86] Y.-M. Hwang, Z.-W. Kang, Y.-C. Chiou, H.-H. Hsu, Experimental study on temperature distributions within the workpiece during friction stir welding of aluminum alloys, *Int. J. Mach. Tools Manuf.* 48 (2008) 778–787. doi:10.1016/j.ijmachtools.2007.12.003.
- [87] F. Rui-dong, S. Zeng-qiang, S. Rui-cheng, L. Ying, L. Hui-jie, L. Lei, Improvement of weld temperature distribution and mechanical properties of 7050 aluminum alloy butt joints by submerged friction stir welding, *Mater. Des.* 32 (2011) 4825–4831. doi:<https://doi.org/10.1016/j.matdes.2011.06.021>.
- [88] H. Fujii, L. Cui, N. Tsuji, M. Maeda, K. Nakata, K. Nogi, Friction stir welding of carbon steels, *Mater. Sci. Eng. A.* 429 (2006) 50–57. doi:10.1016/j.msea.2006.04.118.
- [89] L. Cui, H. Fujii, N. Tsuji, K. Nogi, Friction stir welding of a high carbon steel, *Scr. Mater.* 56 (2007) 637–640. doi:10.1016/j.scriptamat.2006.12.004.
- [90] L. Commin, M. Dumont, J.E. Masse, L. Barrallier, Friction stir welding of AZ31 magnesium alloy rolled sheets: Influence of processing parameters, *Acta Mater.* 57 (2009) 326–334. doi:10.1016/j.actamat.2008.09.011.
- [91] A. Forcellese, M. Martarelli, M. Simoncini, Effect of process parameters on vertical forces and temperatures developed during friction stir welding of magnesium alloys, *Int. J. Adv. Manuf. Technol.* 85 (2016) 595–604. doi:10.1007/s00170-015-7957-6.
- [92] J.W. Pew, T.W. Nelson, C.D. Sorensen, Torque based weld power model for friction stir welding, *Sci. Technol. Weld. Join.* 12 (2007) 341–347. doi:10.1179/174329307X197601.
- [93] S. Cui, Z.W. Chen, J.D. Robson, A model relating tool torque and its associated power and specific energy to rotation and forward speeds during friction stir welding/processing, *Int. J. Mach. Tools Manuf.* 50 (2010) 1023–1030. doi:<https://doi.org/10.1016/j.ijmachtools.2010.09.005>.
- [94] C. Hamilton, S. Dymek, A. Sommers, A thermal model of friction stir welding in

## References

- aluminum alloys, *Int. J. Mach. Tools Manuf.* 48 (2008) 1120–1130. doi:<https://doi.org/10.1016/j.ijmachtools.2008.02.001>.
- [95] C. Hamilton, A. Sommers, S. Dymek, A thermal model of friction stir welding applied to Sc-modified Al–Zn–Mg–Cu alloy extrusions, *Int. J. Mach. Tools Manuf.* 49 (2009) 230–238. doi:<https://doi.org/10.1016/j.ijmachtools.2008.11.004>.
- [96] G.G. Roy, R. Nandan, T. DebRoy, Dimensionless correlation to estimate peak temperature during friction stir welding, *Sci. Technol. Weld. Join.* 11 (2006) 606–608. doi:[10.1179/174329306X122811](https://doi.org/10.1179/174329306X122811).
- [97] A. Arora, T. DebRoy, H.K.D.H. Bhadeshia, Back-of-the-envelope calculations in friction stir welding – Velocities, peak temperature, torque, and hardness, *Acta Mater.* 59 (2011) 2020–2028. doi:<https://doi.org/10.1016/j.actamat.2010.12.001>.
- [98] J.W. Qian, J.L. Li, J.T. Xiong, F.S. Zhang, W.Y. Li, X. Lin, Periodic variation of torque and its relations to interfacial sticking and slipping during friction stir welding, *Sci. Technol. Weld. Join.* 17 (2012) 338–341. doi:[10.1179/1362171812Y.0000000001](https://doi.org/10.1179/1362171812Y.0000000001).
- [99] J.T. Xiong, X.C. Zhang, P. Li, J.W. Qian, J.L. Li, F.S. Zhang, H.B. Dong, Characterisation of periodic variation in torque occurred in friction stir welding process, *Sci. Technol. Weld. Join.* 19 (2014) 350–354. doi:[10.1179/1362171814Y.00000000195](https://doi.org/10.1179/1362171814Y.00000000195).
- [100] D.S. MacKenzie, N. Bogh, T. Croucher, Quenching of Aluminum Alloys, *Heat Treat. Nonferrous Alloy*. 4E (2016) 0. doi:[10.31399/asm.hb.v04e.a0006260](https://doi.org/10.31399/asm.hb.v04e.a0006260).
- [101] Y.N. Zhang, X. Cao, S. Larose, P. Wanjara, Review of tools for friction stir welding and processing, *Can. Metall. Q.* 51 (2012) 250–261. doi:[10.1179/1879139512y.00000000015](https://doi.org/10.1179/1879139512y.00000000015).
- [102] R.A. Prado, L.E. Murr, D.J. Shindo, K.F. Soto, Tool wear in the friction-stir welding of aluminum alloy 6061+20% Al<sub>2</sub>O<sub>3</sub>: a preliminary study, *Scr. Mater.* 45 (2001) 75–80. doi:[https://doi.org/10.1016/S1359-6462\(01\)00994-0](https://doi.org/10.1016/S1359-6462(01)00994-0).
- [103] a. P.P. Reynolds, Visualisation of material flow in autogenous friction stir welds, *Sci. Technol. Weld. Join.* 5 (2000) 120–124. doi:[10.1179/136217100101538119](https://doi.org/10.1179/136217100101538119).
- [104] B.C. Liechty, B.W. Webb, The use of plasticine as an analog to explore material flow in friction stir welding, *J. Mater. Process. Technol.* 184 (2007) 240–250. doi:<https://doi.org/10.1016/j.jmatprotec.2006.10.049>.
- [105] F.C. Liu, T.W. Nelson, In-situ material flow pattern around probe during friction

- stir welding of austenitic stainless steel, *Mater. Des.* 110 (2016) 354–364. doi:<https://doi.org/10.1016/j.matdes.2016.07.147>.
- [106] Z.W. Chen, S. Cui, On the forming mechanism of banded structures in aluminium alloy friction stir welds, *Scr. Mater.* 58 (2008) 417–420. doi:<https://doi.org/10.1016/j.scriptamat.2007.10.026>.
- [107] A.P. Reynolds, Flow visualization and simulation in FSW, *Scr. Mater.* 58 (2008) 338–342. doi:<https://doi.org/10.1016/j.scriptamat.2007.10.048>.
- [108] H.N.B. Schmidt, T.L. Dickerson, J.H. Hattel, Material flow in butt friction stir welds in AA2024-T3, *Acta Mater.* 54 (2006) 1199–1209. doi:<https://doi.org/10.1016/j.actamat.2005.10.052>.
- [109] Z.W. Chen, T. Pasang, Y. Qi, Shear flow and formation of Nugget zone during friction stir welding of aluminium alloy 5083-O, *Mater. Sci. Eng. A.* 474 (2008) 312–316. doi:<https://doi.org/10.1016/j.msea.2007.05.074>.
- [110] K. Kumar, S. V Kailas, The role of friction stir welding tool on material flow and weld formation, *Mater. Sci. Eng. A.* 485 (2008) 367–374. doi:<https://doi.org/10.1016/j.msea.2007.08.013>.
- [111] L.H. Shah, S. Guo, S. Walbridge, A. Gerlich, Effect of tool eccentricity on the properties of friction stir welded AA6061 aluminum alloys, *Manuf. Lett.* 15 (2018) 14–17. doi:<https://doi.org/10.1016/j.mfglet.2017.12.019>.
- [112] I. Galvão, R.M. Leal, D.M. Rodrigues, A. Loureiro, Influence of tool shoulder geometry on properties of friction stir welds in thin copper sheets, *J. Mater. Process. Technol.* 213 (2013) 129–135. doi:<https://doi.org/10.1016/j.jmatprotec.2012.09.016>.
- [113] K. Elangovan, V. Balasubramanian, Influences of pin profile and rotational speed of the tool on the formation of friction stir processing zone in AA2219 aluminium alloy, *Mater. Sci. Eng. A.* 459 (2007) 7–18. doi:<https://doi.org/10.1016/j.msea.2006.12.124>.
- [114] D. Trimble, G.E. O'Donnell, J. Monaghan, Characterisation of tool shape and rotational speed for increased speed during friction stir welding of AA2024-T3, *J. Manuf. Process.* 17 (2015) 141–150. doi:<https://doi.org/10.1016/j.jmapro.2014.08.007>.
- [115] R. Palanivel, P. Koshy Mathews, N. Murugan, I. Dinaharan, Effect of tool rotational speed and pin profile on microstructure and tensile strength of dissimilar friction stir welded AA5083-H111 and AA6351-T6 aluminum alloys, *Mater. Des.*

## References

- 40 (2012) 7–16. doi:<https://doi.org/10.1016/j.matdes.2012.03.027>.
- [116] Y.-H. Zhao, S.-B. Lin, F.-X. Qu, L. Wu, Influence of pin geometry on material flow in friction stir welding process, *Mater. Sci. Technol.* 22 (2006) 45–50. doi:[10.1179/174328406X78424](https://doi.org/10.1179/174328406X78424).
- [117] Z. Sun, C.S. Wu, A numerical model of pin thread effect on material flow and heat generation in shear layer during friction stir welding, *J. Manuf. Process.* 36 (2018) 10–21. doi:<https://doi.org/10.1016/j.jmapro.2018.09.021>.
- [118] P. Motalleb-nejad, T. Saeid, A. Heidarzadeh, K. Darzi, M. Ashjari, Effect of tool pin profile on microstructure and mechanical properties of friction stir welded AZ31B magnesium alloy, *Mater. Des.* 59 (2014) 221–226. doi:<https://doi.org/10.1016/j.matdes.2014.02.068>.
- [119] Y. Li, L.E. Murr, J.C. McClure, Flow visualization and residual microstructures associated with the friction-stir welding of 2024 aluminum to 6061 aluminum, *Mater. Sci. Eng. A.* 271 (1999) 213–223. doi:[https://doi.org/10.1016/S0921-5093\(99\)00204-X](https://doi.org/10.1016/S0921-5093(99)00204-X).
- [120] M.I. Costa, D. Verdera, C. Leitão, D.M. Rodrigues, Dissimilar friction stir lap welding of AA 5754-H22/AA 6082-T6 aluminium alloys: Influence of material properties and tool geometry on weld strength, *Mater. Des.* 87 (2015) 721–731. doi:<https://doi.org/10.1016/j.matdes.2015.08.066>.
- [121] M.I. Costa, C. Leitao, D.M. Rodrigues, Influence of the Aluminium Alloy Type on Defects Formation in Friction Stir Lap Welding of Thin Sheets, *Soldag. Inspeção.* 23 (2018) 32–42. [http://www.scielo.br/scielo.php?script=sci\\_arttext&pid=S0104-92242018000100032&nrm=iso](http://www.scielo.br/scielo.php?script=sci_arttext&pid=S0104-92242018000100032&nrm=iso).
- [122] Y. Morisada, T. Imaizumi, H. Fujii, Determination of strain rate in Friction Stir Welding by three-dimensional visualization of material flow using X-ray radiography, *Scr. Mater.* 106 (2015) 57–60. doi:<https://doi.org/10.1016/j.scriptamat.2015.05.006>.
- [123] Y. Morisada, T. Imaizumi, H. Fujii, Clarification of material flow and defect formation during friction stir welding, *Sci. Technol. Weld. Join.* 20 (2015) 130–137. doi:[10.1179/1362171814Y.0000000266](https://doi.org/10.1179/1362171814Y.0000000266).
- [124] X. He, F. Gu, A. Ball, A review of numerical analysis of friction stir welding, *Prog. Mater. Sci.* 65 (2014) 1–66. doi:<https://doi.org/10.1016/j.pmatsci.2014.03.003>.
- [125] A. Arora, R. Nandan, A.P. Reynolds, T. DebRoy, Torque, power requirement and

- stir zone geometry in friction stir welding through modeling and experiments, *Scr. Mater.* 60 (2009) 13–16. doi:10.1016/j.scriptamat.2008.08.015.
- [126] M. Al-moussawi, A.J. Smith, A. Young, S. Cater, M. Faraji, Modelling of friction stir welding of DH36 steel, *Int. J. Adv. Manuf. Technol.* 92 (2017) 341–360. doi:10.1007/s00170-017-0147-y.
- [127] W. Li, Z. Zhang, J. Li, Y.J. Chao, Numerical Analysis of Joint Temperature Evolution During Friction Stir Welding Based on Sticking Contact, *J. Mater. Eng. Perform.* 21 (2012) 1849–1856. doi:10.1007/s11665-011-0092-0.
- [128] Z. Yu, W. Zhang, H. Choo, Z. Feng, Transient Heat and Material Flow Modeling of Friction Stir Processing of Magnesium Alloy using Threaded Tool, *Metall. Mater. Trans. A.* 43 (2012) 724–737. doi:10.1007/s11661-011-0862-1.
- [129] P.A. Colegrove, H.R. Shercliff, 3-Dimensional CFD modelling of flow round a threaded friction stir welding tool profile, *J. Mater. Process. Technol.* 169 (2005) 320–327. doi:https://doi.org/10.1016/j.jmatprotec.2005.03.015.
- [130] G.Q. Chen, Q.Y. Shi, Y.J. Li, Y.J. Sun, Q.L. Dai, J.Y. Jia, Y.C. Zhu, J.J. Wu, Computational fluid dynamics studies on heat generation during friction stir welding of aluminum alloy, *Comput. Mater. Sci.* 79 (2013) 540–546. doi:10.1016/j.commatsci.2013.07.004.
- [131] G. Chen, Z. Feng, Y. Zhu, Q. Shi, An Alternative Frictional Boundary Condition for Computational Fluid Dynamics Simulation of Friction Stir Welding, *J. Mater. Eng. Perform.* 25 (2016) 4016–4023. doi:10.1007/s11665-016-2219-9.
- [132] H. Robe, C. Claudin, J.M. Bergheau, E. Feulvarch, R-ALE simulation of heat transfer during friction stir welding of an AA2xxx/AA7xxx joint on a large process window, *Int. J. Mech. Sci.* 155 (2019) 31–40. doi:10.1016/j.ijmecsci.2019.02.029.
- [133] M.P. Iqbal, A. Tripathi, R. Jain, R.P. Mahto, S.K. Pal, P. Mandal, Numerical modelling of microstructure in friction stir welding of aluminium alloys, *Int. J. Mech. Sci.* 185 (2020) 105882. doi:https://doi.org/10.1016/j.ijmecsci.2020.105882.
- [134] B.S. Roy, T. Medhi, S.C. Saha, Material Flow Modeling in Friction Stir Welding of AA6061-T6 Alloy and Study of the Effect of Process Parameters, 9 (2015) 641–649.
- [135] K.J. Colligan, R.S. Mishra, A conceptual model for the process variables related to heat generation in friction stir welding of aluminum, *Scr. Mater.* 58 (2008) 327–331. doi:10.1016/j.scriptamat.2007.10.015.

## References

- [136] A. Roth, T. Hake, M.F. Zaeh, An analytical approach of modelling friction stir welding, *Procedia CIRP*. 18 (2014) 197–202. doi:10.1016/j.procir.2014.06.131.
- [137] Y. Zhu, G. Chen, Q. Chen, G. Zhang, Q. Shi, Simulation of material plastic flow driven by non-uniform friction force during friction stir welding and related defect prediction, *Mater. Des.* 108 (2016) 400–410. doi:https://doi.org/10.1016/j.matdes.2016.06.119.
- [138] H. Wang, P.A. Colegrove, J.F. dos Santos, Numerical investigation of the tool contact condition during friction stir welding of aerospace aluminium alloy, *Comput. Mater. Sci.* 71 (2013) 101–108. doi:https://doi.org/10.1016/j.commatsci.2013.01.021.
- [139] G. Chen, Q. Ma, S. Zhang, J. Wu, G. Zhang, Q. Shi, Computational fluid dynamics simulation of friction stir welding: A comparative study on different frictional boundary conditions, *J. Mater. Sci. Technol.* 34 (2018) 128–134. doi:https://doi.org/10.1016/j.jmst.2017.10.015.
- [140] B. Meyghani, C. Wu, Progress in Thermomechanical Analysis of Friction Stir Welding, *Chinese J. Mech. Eng. (English Ed.* 33 (2020). doi:10.1186/s10033-020-0434-7.
- [141] K. Masaki, Y.S. Sato, M. Maeda, H. Kokawa, Experimental simulation of recrystallized microstructure in friction stir welded Al alloy using a plane-strain compression test, *Scr. Mater.* 58 (2008) 355–360. doi:https://doi.org/10.1016/j.scriptamat.2007.09.056.
- [142] R. Kumar, V. Pancholi, R.P. Bharti, Material flow visualization and determination of strain rate during friction stir welding, *J. Mater. Process. Technol.* 255 (2018) 470–476. doi:https://doi.org/10.1016/j.jmatprotec.2017.12.034.
- [143] T. Long, W. Tang, A.P. Reynolds, Process response parameter relationships in aluminium alloy friction stir welds, *Sci. Technol. Weld. Join.* 12 (2007) 311–317. doi:10.1179/174329307X197566.
- [144] P. Tello, K., Duman, U., Mendez, Scaling laws for the welding arc, weld penetration and friction stir welding, in: *Proc. Eighth Trends Weld. Res.*, 2009: pp. 172–181.
- [145] Z.W. Chen, S. Cui, Strain and strain rate during friction stir welding/processing of Al-7Si-0.3Mg alloy, *IOP Conf. Ser. Mater. Sci. Eng.* 4 (2009) 0–5. doi:10.1088/1757-899X/4/1/012026.
- [146] X.C. Liu, Y.F. Sun, T. Nagira, K. Ushioda, H. Fujii, Experimental evaluation of

- strain and strain rate during rapid cooling friction stir welding of pure copper, *Sci. Technol. Weld. Join.* 24 (2019) 352–359. doi:10.1080/13621718.2018.1556436.
- [147] R. Nandan, G.G. Roy, T.J. Lienert, T. DebRoy, Numerical modelling of 3D plastic flow and heat transfer during friction stir welding of stainless steel, *Sci. Technol. Weld. Join.* 11 (2006) 526–537. doi:10.1179/174329306X107692.
- [148] R. Nandan, G.G. Roy, T. Debroy, I. Introduction, Numerical Simulation of Three-Dimensional Heat Transfer and Plastic Flow During Friction Stir Welding, *Metall. Mater. Trans. A.* 37 (2006) 1247–1259. doi:10.1007/s11661-006-1076-9.
- [149] R. Nandan, G.G. Roy, T.J. Lienert, T. Debroy, Three-dimensional heat and material flow during friction stir welding of mild steel, *Acta Mater.* 55 (2007) 883–895. doi:10.1016/j.actamat.2006.09.009.
- [150] S. Mukherjee, A.K. Ghosh, Flow visualization and estimation of strain and strain-rate during friction stir process, *Mater. Sci. Eng. A.* 527 (2010) 5130–5135. doi:https://doi.org/10.1016/j.msea.2010.04.091.
- [151] A.H. Ammouri, G. Kridli, G. Ayoub, R.F. Hamade, Relating grain size to the Zener-Hollomon parameter for twin-roll-cast AZ31B alloy refined by friction stir processing, *J. Mater. Process. Technol.* 222 (2015) 301–306. doi:10.1016/j.jmatprotec.2015.02.037.
- [152] E. Sharghi, A. Farzadi, Simulation of strain rate, material flow, and nugget shape during dissimilar friction stir welding of AA6061 aluminum alloy and Al-Mg<sub>2</sub>Si composite, *J. Alloys Compd.* 748 (2018) 953–960. doi:https://doi.org/10.1016/j.jallcom.2018.03.145.
- [153] Y. Du, T. Mukherjee, P. Mitra, T. DebRoy, Machine learning based hierarchy of causative variables for tool failure in friction stir welding, *Acta Mater.* 192 (2020) 67–77. doi:https://doi.org/10.1016/j.actamat.2020.03.047.
- [154] W.R. Longhurst, A.M. Strauss, G.E. Cook, P.A. Fleming, Torque control of friction stir welding for manufacturing and automation, *Int. J. Adv. Manuf. Technol.* 51 (2010) 905–913. doi:10.1007/s00170-010-2678-3.
- [155] I. Galvão, C. Leitão, A. Loureiro, D.M. Rodrigues, Study of the welding conditions during similar and dissimilar aluminium and copper welding based on torque sensitivity analysis, *Mater. Des.* 42 (2012) 259–264. doi:10.1016/j.matdes.2012.05.058.
- [156] S. Kumari, R. Jain, U. Kumar, I. Yadav, N. Ranjan, K. Kumari, R.K. Kesharwani, S. Kumar, S. Pal, S.K. Pal, D. Chakravarty, Defect identification in friction stir

## References

- welding using continuous wavelet transform, *J. Intell. Manuf.* 30 (2019) 483–494. doi:10.1007/s10845-016-1259-1.
- [157] J. Yan, M.A. Sutton, A.P. Reynolds, Process–structure–property relationships for nugget and heat affected zone regions of AA2524–T351 friction stir welds, *Sci. Technol. Weld. Join.* 10 (2005) 725–736. doi:10.1179/174329305X68778.
- [158] C. Leitão, R. Louro, D.M. Rodrigues, Using torque sensitivity analysis in accessing Friction Stir Welding/Processing conditions, *J. Mater. Process. Technol.* 212 (2012) 2051–2057. doi:10.1016/j.jmatprotec.2012.05.009.
- [159] H. Su, C.S. Wu, A. Pittner, M. Rethmeier, Simultaneous measurement of tool torque, traverse force and axial force in friction stir welding, *J. Manuf. Process.* 15 (2013) 495–500. doi:10.1016/j.jmapro.2013.09.001.
- [160] K.J. Quintana Cuellar, J.L.L. Silveira, Analysis of Torque in Friction Stir Welding of Aluminum Alloy 5052 by Inverse Problem Method, *J. Manuf. Sci. Eng.* 139 (2017). doi:10.1115/1.4035719.
- [161] K.J. Quintana, J.L.L. Silveira, Mechanistic models and experimental analysis for the torque in FSW considering the tool geometry and the process velocities, *J. Manuf. Process.* 30 (2017) 406–417. doi:10.1016/j.jmapro.2017.09.031.
- [162] A. Banik, B. Saha Roy, J. Deb Barma, S.C. Saha, An experimental investigation of torque and force generation for varying tool tilt angles and their effects on microstructure and mechanical properties: Friction stir welding of AA 6061-T6, *J. Manuf. Process.* 31 (2018) 395–404. doi:10.1016/j.jmapro.2017.11.030.
- [163] A.P. Khandkar, M. Z. H., Khan, J. A., Reynolds, Prediction of temperature distribution and thermal history during friction stir welding: input torque based model, *Sci. Technol. Weld. Join.* 8(3) (2003) 165–174.
- [164] P.A. Colegrove, H.R. Shercliff, Experimental and numerical analysis of aluminium alloy 7075-T7351 friction stir welds, *Sci. Technol. Weld. Join.* 8 (2003) 360–368. doi:10.1179/136217103225005534.
- [165] S. Baek, D.-H. Choi, C. Lee, B.-W. Ahn, Y. Yeon, K. Song, S. Jung, Microstructure and Mechanical Properties of Friction Stir Spot Welded Galvanized Steel, *Mater. Trans.* 51 (2010) 1044–1050. doi:https://doi.org/10.2320/matertrans.M2009337.
- [166] M. Santella, Y. Hovanski, A. Frederick, G. Grant, M. Dahl, Friction stir spot welding of DP780 carbon steel, *Sci. Technol. Weld. Join.* 15 (2010) 271–278. doi:10.1179/136217109X12518083193630.



- [167] Y.F. Sun, J.M. Shen, Y. Morisada, H. Fujii, Spot friction stir welding of low carbon steel plates preheated by high frequency induction, *Mater. Des.* 54 (2014) 450–457. doi:<https://doi.org/10.1016/j.matdes.2013.08.071>.
- [168] M. Imam, R. Ueji, H. Fujii, Microstructural control and mechanical properties in friction stir welding of medium carbon low alloy S45C steel, *Mater. Sci. Eng. A.* 636 (2015) 24–34. doi:<https://doi.org/10.1016/j.msea.2015.03.089>.
- [169] B.J. Stringham, T.W. Nelson, C.D. Sorensen, Non-dimensional modeling of the effects of weld parameters on peak temperature and cooling rate in friction stir welding, *J. Mater. Process. Technol.* 255 (2018) 816–830. doi:[10.1016/j.jmatprotec.2017.11.044](https://doi.org/10.1016/j.jmatprotec.2017.11.044).
- [170] G. Çam, Friction stir welded structural materials: beyond Al-alloys, *Int. Mater. Rev.* 56 (2011) 1–48. doi:[10.1179/095066010X12777205875750](https://doi.org/10.1179/095066010X12777205875750).
- [171] D.G. Andrade, I. Galvão, D. Verdera, C. Leitão, D.M. Rodrigues, Influence of the structure and phase composition of the bond interface on aluminium–copper lap welds strength, *Sci. Technol. Weld. Join.* 23 (2018) 105–113. doi:[10.1080/13621718.2017.1329078](https://doi.org/10.1080/13621718.2017.1329078).
- [172] K.H. Kim, H.S. Bang, H.S. Bang, A.F.H. Kaplan, Joint properties of ultra thin 430M2 ferritic stainless steel sheets by friction stir welding using pinless tool, *J. Mater. Process. Technol.* 243 (2017) 381–386. doi:<https://doi.org/10.1016/j.jmatprotec.2016.12.018>.
- [173] G. Zhang, W. Su, J. Zhang, Z. Wei, Friction Stir Brazing: a Novel Process for Fabricating Al/Steel Layered Composite and for Dissimilar Joining of Al to Steel, *Metall. Mater. Trans. A.* 42 (2011) 2850–2861. doi:[10.1007/s11661-011-0677-0](https://doi.org/10.1007/s11661-011-0677-0).
- [174] K. Aota, K. Ikeuchi, Development of friction stir spot welding using rotating tool without probe and its application to low-carbon steel plates, *Weld. Int.* 23 (2009) 572–580. doi:[10.1080/09507110802543054](https://doi.org/10.1080/09507110802543054).
- [175] Y.F. Sun, H. Fujii, N. Takaki, Y. Okitsu, Microstructure and mechanical properties of mild steel joints prepared by a flat friction stir spot welding technique, *Mater. Des.* 37 (2012) 384–392. doi:[10.1016/j.matdes.2012.01.027](https://doi.org/10.1016/j.matdes.2012.01.027).
- [176] S. Karami, H. Jafarian, A.R. Eivani, S. Kheirandish, Materials Science & Engineering A Engineering tensile properties by controlling welding parameters and microstructure in a mild steel processed by friction stir welding, *Mater. Sci. Eng. A.* 670 (2016) 68–74. doi:[10.1016/j.msea.2016.06.008](https://doi.org/10.1016/j.msea.2016.06.008).
- [177] D.M. Sekban, S.M. Aktarer, H. Zhang, P. Xue, Z. Ma, G. Purcek, Microstructural

## References

and Mechanical Evolution of a Low Carbon Steel by Friction Stir Processing, *Metall. Mater. Trans. A.* 48 (2017) 3869–3879. doi:10.1007/s11661-017-4157-z.

# Appendix A

---

## *Article A*

*Andrade, D. G., Leitão, C., & Rodrigues, D. M. (2018). Properties of lap welds in low carbon galvanised steel produced by tool assisted friction welding. Journal of Materials Processing Technology, 260, 77-86.*

<https://doi.org/10.1016/j.jmatprotec.2018.05.018>

### **Properties of lap welds in low carbon galvanised steel produced by tool assisted friction welding.**

#### **Abstract**

Linear lap welds in very thin plates of galvanized steel were produced using tool assisted friction welding, a friction stir welding related technique. The morphological and microstructural analysis of the welds produced with varying tool rotational speed (up to 1400 rpm), tool traverse speed (up to 1200 mm/min) and tool diameter (10 to 16 mm) revealed the absence of stirred material or important welding defects in most of the joints. For the welds produced with the higher tool traverse and rotational speeds, a strong asymmetry in the weld morphology was also observed. A change in the contact conditions between the tool and the workpiece, from sticking to slipping, is appointed as the main factor responsible for the asymmetry in the weld morphology. The asymmetry in welds morphology has important influence in the failure mode of the welds in lap shear test but no influence on the joint strength. Lap shear strengths similar to base material ultimate tensile strength were measured for most of the welds.

**Keywords:** Tool assisted friction welding; Friction stir welding; Galvanized steel; Lap joining.

### 1. Introduction

The Tool Assisted Friction Welding (TAFW) process, proposed by Mira-Aguiar et al. (2016), is similar to Friction Stir Welding (FSW) since it is based on the same operative principles, i.e. the use of a non-consumable tool animated by translational and rotational movements to promote the joining of the base materials. However, in TAFW only pinless tools are used. The use of pinless tools has the advantage of preventing tool pin damage/wear which according to Rai et al. (2011) is one of the most important limitations in welding steel by FSW. Çam 2011, in an extensive review on FSW of non-aluminium alloys, also concludes that the greatest hindrance in the industrial implementation of the FSW of steels is the development of durable and economical tools. The optimization of the tool geometry and/or tool material is indicated as a possible solution for the problem of obtaining durable tools.

In lap welding, the use of pinless tools enables to suppresses the base materials stirring, which prevents the formation of typical friction stir lap welds defects, such as the Hooking or the Cold Lap defects. According to Yadava et al. (2010) and Salari et al. (2014), the pin length and the pin geometry, respectively, both have important influence on the severity and morphology of those defects. Mira-Aguiar et al. (2016) and Kim et al. (2017) had already tested the use of pinless tools in the welding of 1 mm thick DX51D and DC01 steels and 0.5 mm thick 430M2 ferritic stainless steel, respectively. Mira-Aguiar et al. (2016) analysed the welding mechanisms taking place during welding and claim that no stirring takes place, which makes the joining process different from FSW. Kim et al. (2017) did not perform any analysis of the welding mechanisms and assume that FSW was the joining mechanism. In both works, excellent quality welds were obtained without Hooking and Cold Lap defects. Bakavos et al. (2011) also used pinless flat tools in spot welding of 0.93 mm thick plates of AA 6111-T4 aluminium alloy and Zhang et al. (2011) in dissimilar linear lap welding between 1.8 mm thick plates of pure aluminium and low carbon steel. Again, in both works, welds absent of lap defects were obtained in opposition to that usually reported for welds produced using conventional FSW tools, i.e. tools with pin.

The influence of the galvanised coating on the friction stir lap weldability of the galvanised steels, was also addressed by some previous authors. Baek et al. (2010) analysed welds in galvanized steel produced by Friction Stir Spot Welding (FSSW) and concluded that the galvanized layer is expelled from the centre region of the joint due to the very high temperatures (1293 K) reached and due to the pressure and centrifugal force

exerted by the tool. In opposition to this, Chen et al. (2008), in dissimilar friction stir welding of aluminium to galvanized steel, claimed that the presence of the zinc layer was the responsible for the joining of the base materials. Mira-Aguiar et al. (2016) concluded that the zinc has an important influence on the contact conditions at the tool-workpiece material interface, in TAFW, affecting the thermo-mechanical conditions developed during welding. The evolution of the contact conditions in galvanised steel lap welding will be addressed in detail in the current work, as well as the influence of the pinless tools diameter and processing parameters on welds properties.

## 2. Experimental Procedure

Similar lap welds in DX51D z200 galvanized low carbon steel plates, with 1mm thickness, were produced by TAFW. The chemical composition of the base material, from the certificate provided by the supplier, and of the galvanized coating, determined using SEM/EDS analysis, are shown in Table A.1. All the welds were performed in a *MTS I-STIR PDS* machine, in position control, using tungsten carbide tools, with diameters ranging from 10 to 16 mm and tilted backwards by 2°. The plunge depth was set to 0.5 mm in the welding machine.

The welding parameters tested are presented in Figure A.1, in which the different tools were labelled according to the shoulder diameter, i.e. the tool with a 10 mm shoulder diameter was labelled PL10. As is also shown in the figure, the influence of the tool diameter, on the welding conditions, was tested using tool rotation ( $\omega$ ) and traverse ( $v$ ) speeds of 1000 rpm and 600 mm/min, respectively. The analyses of the influence of the traverse speed on the welding conditions was performed using the PL16 tool and ranging  $v$  from 200 to 1200 mm/min, at a constant tool rotational speed of 1000 rpm. The analyses of the influence of the tool rotational speed, on the welding conditions, was performed using the same tool and ranging  $\omega$  from 600 to 1400 rpm, at a constant tool traverse speed of 600 mm/min. The instantaneous evolution of the spindle torque was recorded and analysed as described in Leitão et al. (2012a).

After welding, metallographic samples were extracted from the welds, transverse to the welding direction, polished according to standard procedures, etched with 2% Nital and observed using an optical microscope (*Leica DM 4000 M LED*). The strength of the welds was assessed by performing lap shear tests using a universal tensile testing machine (*Instron 4206*). As schematized in Figures A.2a and A.2b, advancing (AS) and retreating

## Appendix A

(RS) side lap shear specimens, respectively, were prepared and tested according to the procedures described in Costa et al. (2015a). Digital Image Correlation (DIC) was used for strain data acquisition. Samples preparation and strain data analysis was performed following the procedures detailed in Leitão et al. (2012b). Hardness measurements were also performed, transverse to the cross-section of the welds, in the upper and lower plates, using a *Shimadzu Microhardness Tester*, with 200 g load and 15 s holding time.

**Table A.1** – Chemical composition of the base material and of the galvanized coating (in wt%).

Base Material						Coating		
Fe	C	Mn	O	S	Si	Zn	Fe	Al
Bal.	0.05	0.35	0.008	0.01	0.02	Bal.	1.5	0.3

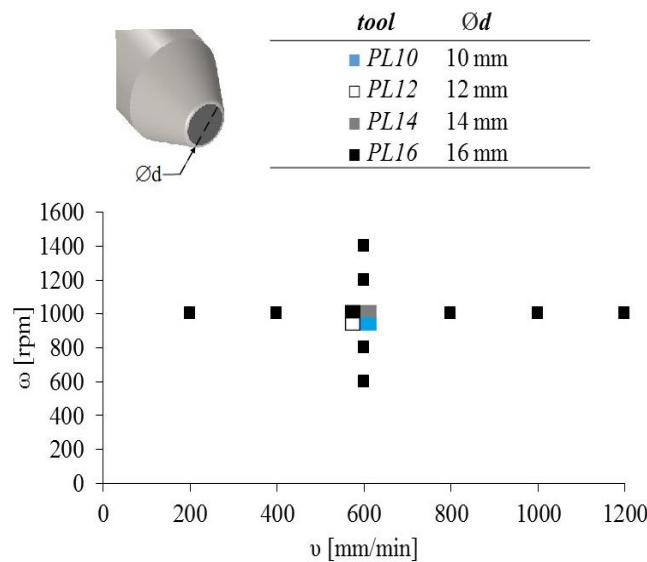


**Figure A.1** – Process parameters.

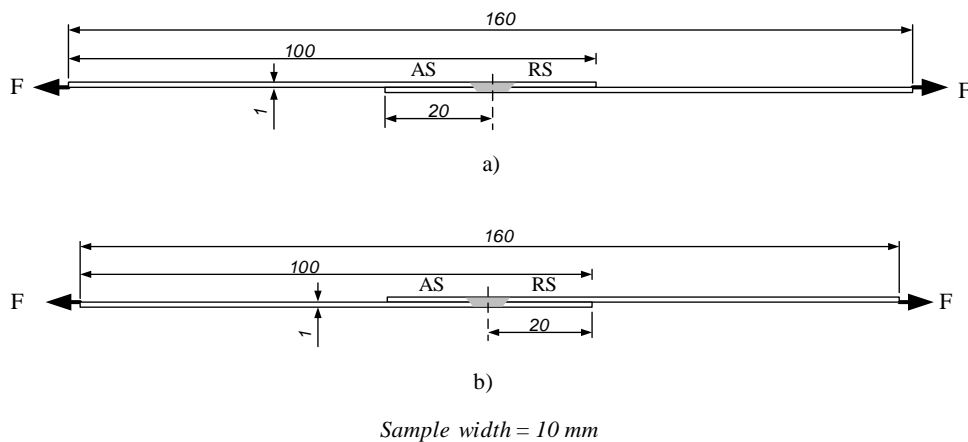


**Figure A.2** – Scheme of the advancing (a) and retreating (b) lap shear samples.

### 3. Results and Discussion

#### 3.1. Morphological analysis

The cross sections of the welds produced using tools with different diameters, traverse speeds and rotational speeds are compared in Figures A.3, A.4 and A.5, respectively. The images in the left side of the figures correspond to photographs of the cross-sections after chemical etching. The images in the right side of the figures were obtained by eliminating the microstructure from the images in the left side, using an image editing software. In all cross-section photographs, except that in Figure A.5a, it is possible to observe a process affected zone (PAZ) with a microstructure different from that of the base material and a dark line in the middle of the PAZ, aligned with the plates original interface. The weld interface, represented in Figure A.6 at higher magnification, for the weld produced with the PL16 tool at 600 rpm and 600 mm/min, shows microstructural continuity and the absence of voids inside the dark line. As in Mira-Aguiar et al. (2016), the dark line was found to correspond to remnants of the galvanized coating of the plates. The continuity of the line, across the PAZ, proves that no cross-interface base material stirring took place during welding, as in FSW. According to these authors, the joining of the plates result from diffusion across the base materials interface, due to the very high contact pressure of the surfaces, heated to very high temperature by the rotating tool, instead from base materials stirring, as in FSW. The images in Figures A.3, A.4 and A.5 also indicate that bonding of the plates was obtained for most of the welding conditions tested. The only exception was reported for the weld performed with the tool PL16 at rotational and traverse speeds of 1000 rpm and 1200 mm/min (Figure A.4f), respectively, for which separation of the plates occurred when handling the samples for the metallographic analysis. For the weld produced with the PL16 tool at 600 rpm and 600 mm/min, the formation of cracks at the retreating side was also observed (Figure 5a).

Comparing the cross-sections on the right side of Figures A.3, A.4 and A.5, in which the contour of the PAZ was delimited using dashed lines, it is possible to conclude that the PAZ morphology is symmetrical relative to the weld axis for the welds performed with the different tools using similar welding parameters (Figure A.3) and for the welds performed with the PL16 tool and low values of tool advancing (Figures A.4a to A.4c) and/or rotational (Figures A.5b and A.5c) speeds. On the other hand, a strong asymmetry in PAZ morphology/shape, relative to the weld axis, is evident for the welds produced with the PL16 tool and with the highest tool traverse (Figures A.4d to A.4f) and rotational (Figures A.5d and A.5e) speeds. When increasing the traverse speed, the deepness of the

## Appendix A

PAZ also diminishes, becoming almost constricted to the upper plate. This is shown by the PAZ thickness,  $z$  in Figures A.4d, A.4e and A.4f, which is equal to 1.7 mm, 1.55 mm and 0.95 mm, respectively.

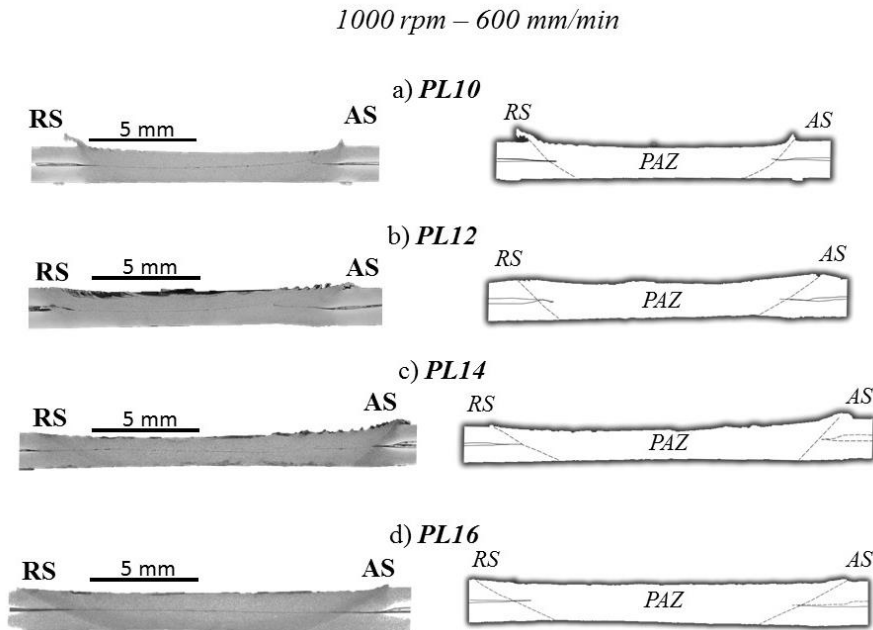


**Figure A.3** – Cross sections of the welds manufactured at a constant tool rotational and traverse speeds of 1000 rpm and 600 mm/min and varying tool diameters.

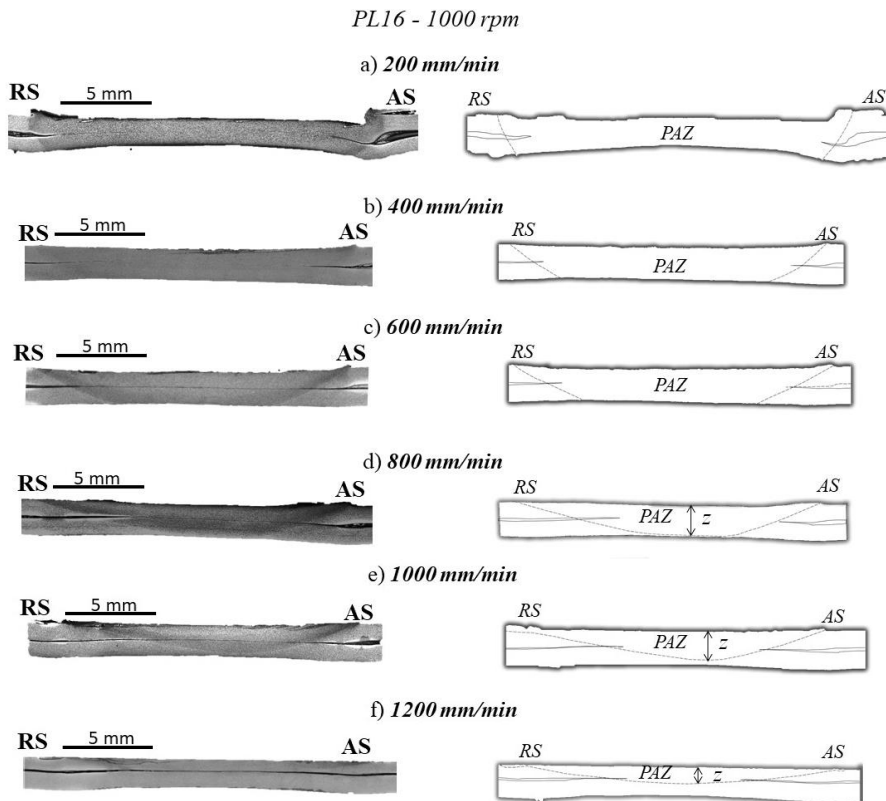


**Figure A.4** – Cross sections of the welds manufactured with the PL16 tool, at a constant rotational speed of 1000 rpm and varying traverse speeds.



PL16 – 600 mm/min

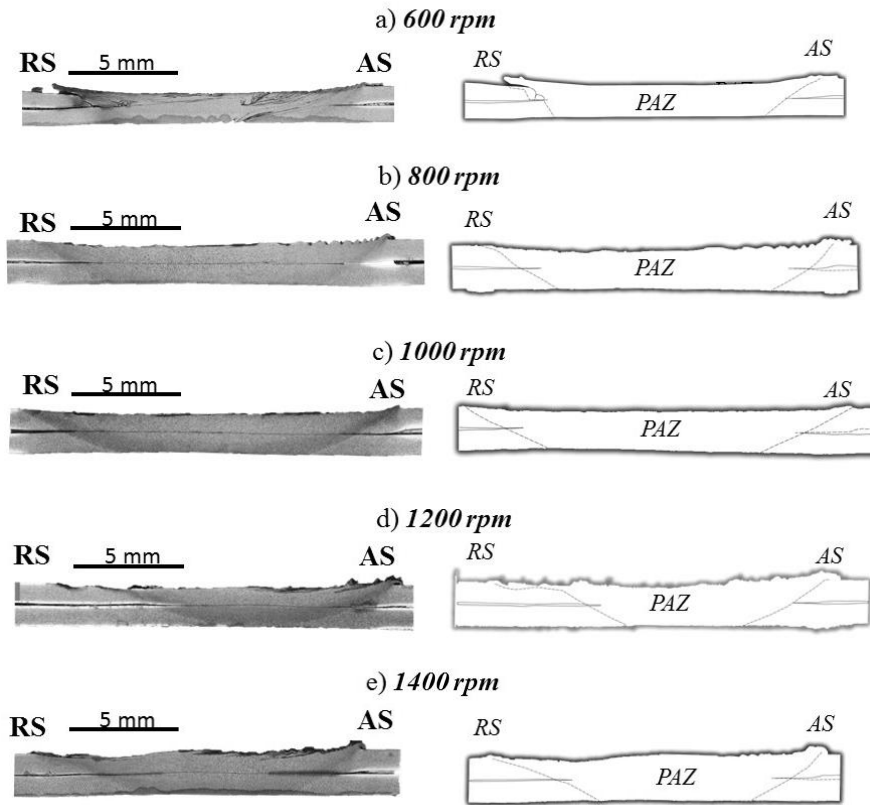


**Figure A.5** – Cross sections of the welds manufactured with the PL16 tool, at a constant traverse speed of 600 mm/min and varying rotational speeds.

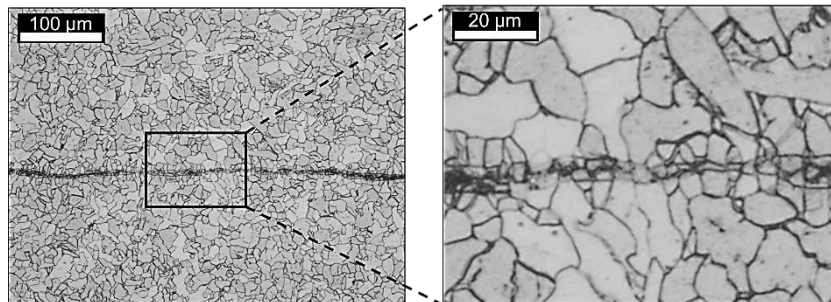


**Figure A.6** – Bonding interface for the weld produced with the PL16 tool at 600 rpm and 600 mm/min.

Figures A.7, A.8 and A.9 show details of the microstructure at the advancing (AS) and retreating (RS) sides of the welds in Figures A.4c, A.4e and A.5d, respectively. A dark line was plotted, at the AS and RS of the welds, delimiting a region with a refined microstructure (the PAZ) from a region with a coarser grain structure (the base material). In the middle of the PAZ, a microstructure with coarser grain size than the base material was observed for all the welds (Figures A.7c, A.8c and A.9c). The presence of a coarse grain structure in the PAZ is contradictory to that reported by Karami et al. (2016) and

## Appendix A

Sekban et al. (2017) in FSW and FSP, respectively, of low carbon steels. This result is an important evidence that the welding mechanisms taking place during TAFW are different from those taking place during FSW/P, since no base material refinement associated with dynamic recrystallization took place in the PAZ, as reported by the above authors. Despite the coarser grain structure in the welds, the average hardness registered for the PAZ material was higher than that of the base material, independently of the processing parameters, as shown in Figure A.10. The figure also shows that the average hardness of the PAZ was similar for all the welds, independently of the tool and process parameters used in the production of the welds. The main differences in joint characteristics, between the welds analysed in this work, were in PAZ morphology but not in PAZ hardness. The images in Figures A.7, A.8 and A.9 show that the shape of the PAZ boundary at the AS is similar for all the welds (Figures A.7d, A.8d and A.9d). However, the shape of the PAZ boundary at the RS varies according to the welding conditions (Figures A.8a and A.9a) showing an asymmetry in PAZ shape, between the AS and RS, for the welds produced at the highest values of tool rotational and traverse speeds. For these welds, the PAZ at the RS is almost restricted to a thin region near the plates surface.

According to Schmidt et al. (2003), the contact conditions at the tool-workpiece interface, in FSW, can be described as a complex combination of sliding and sticking. Present results show that in TAFW the contact conditions may be unsymmetrical between the AS and RS, according to the process parameters. More precisely, the symmetry in PAZ morphology, for the welds produced with low values of tool advancing and rotational speeds, prove that the heat generation/distribution was homogeneous at the AS and RS sides of the tool. For these welds, mixed sliding/sticking conditions were prevalent across the entire tool-workpiece contact surface. The asymmetry in PAZ morphology, for the welds produced with high values of tool advancing and rotational speed, prove that the heat generation/distribution was not symmetrical relative to the weld axis. The shape of the PAZ at the RS shows that sliding governed the contact conditions in this side of the tool, where the PAZ is constricted to the upper plate surface. The shape of the PAZ at the AS shows that contact conditions at this side of the tool were similar to that registered for the other welds.

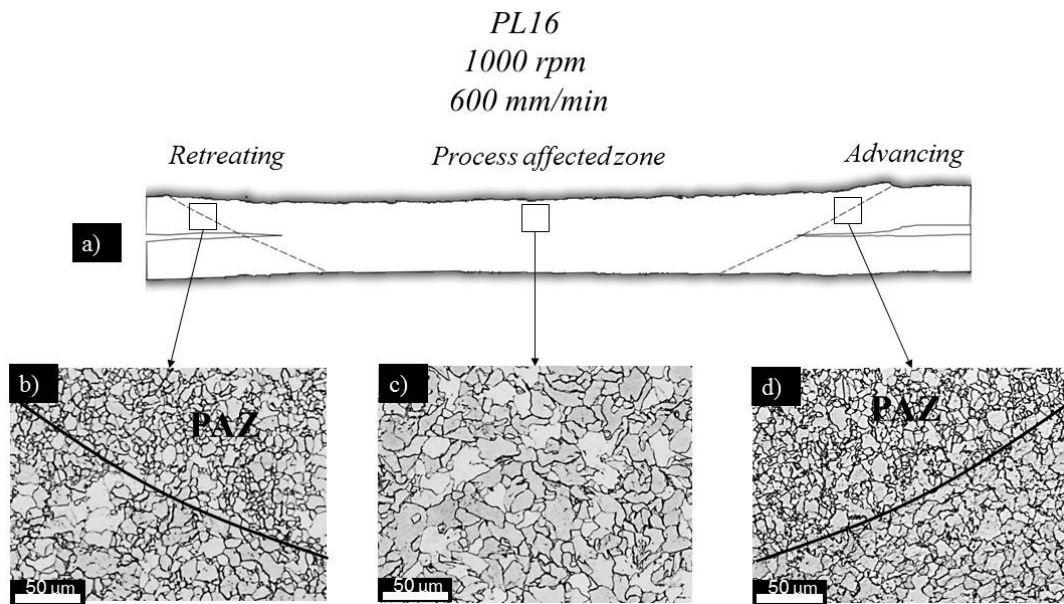


**Figure A.7** – Details of the microstructure at the AS and RS of the weld in Figure A.4c (1000 rpm – 600 mm/min).

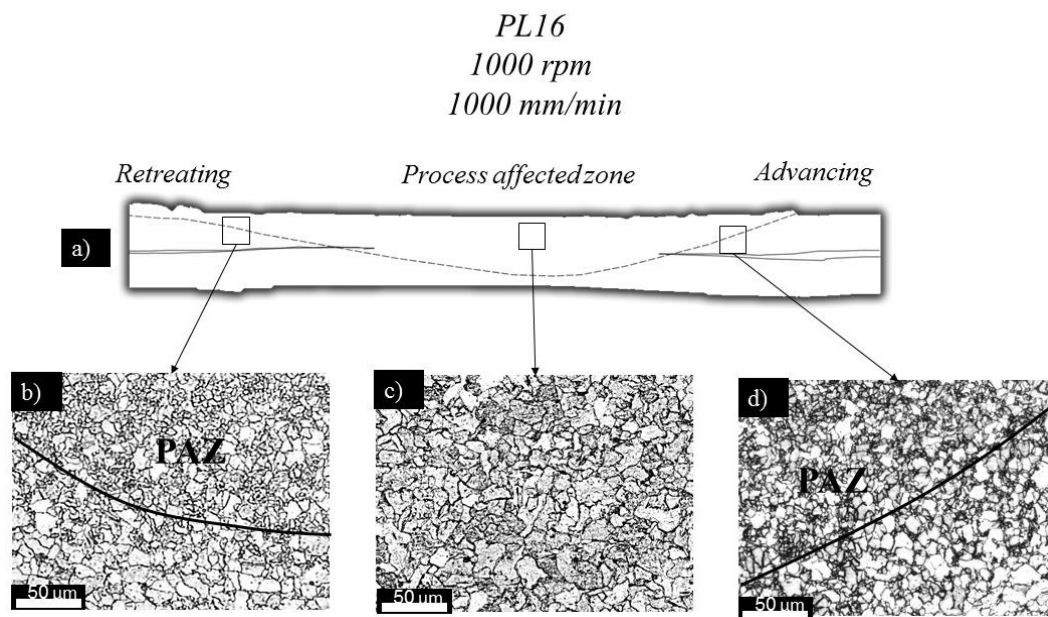


**Figure A.8** - Details of the microstructure at the AS and RS of the weld in Figure A.4e (1000 rpm – 1000 mm/min).

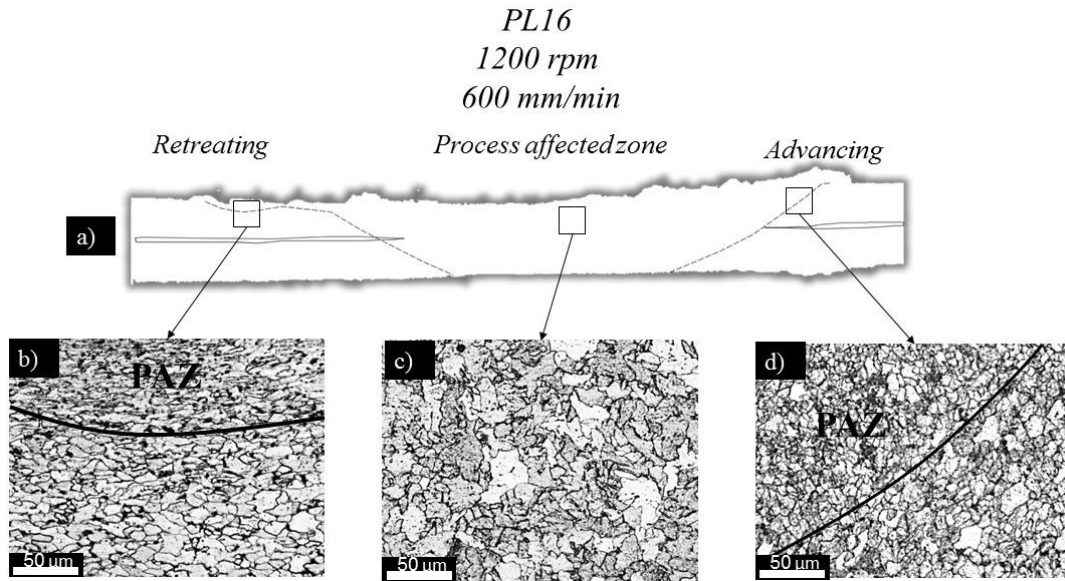


**Figure A.9** - Details of the microstructure at the AS and RS of the weld in Figure A.5d (1200 rpm – 600 mm/min).

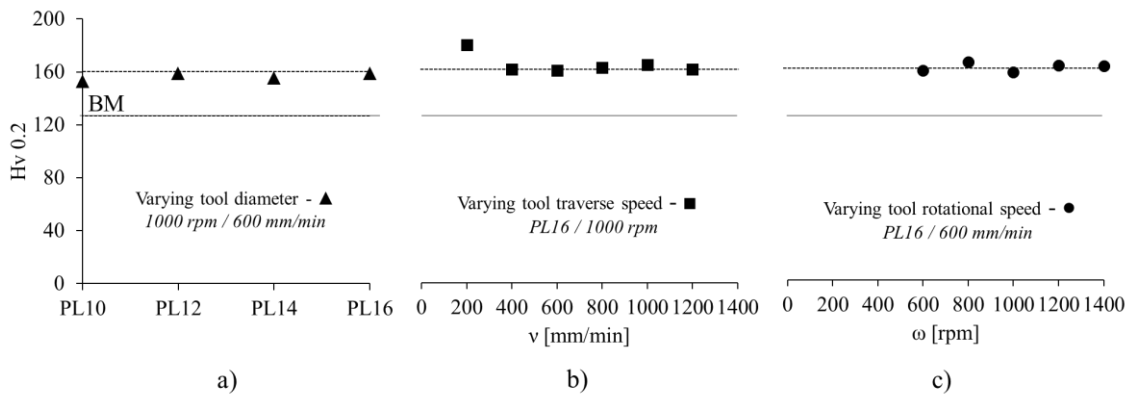


**Figure A.10** – Evolution of the average hardness in the PAZ with the process parameters: tool diameter (a), traverse speed (b) and rotational speed (c).

Figure A.11 shows now the evolution of the width of the PAZ (Figure A.11a), with the tool diameter and traverse and rotational speeds (Figures A.11b to A.11d). It is possible to see that the width of the PAZ increases linearly when increasing the tool diameter and decreases linearly when increasing the tool traverse speed. This is related to the increase in heat generation with the increase in tool diameter, and the increase in heat dissipation with the increase in tool traverse speed. The shape of the PAZ, which becomes constricted to the upper plate (Figures A.4e and A.4f), also reflects the increase in heat dissipation when increasing the tool traverse speed. Analysing the evolution of the PAZ width with the tool rotational speed (Figure A.11d) it can be concluded that it varies non-

linearly with the tool rotational speed, increasing when the tool rotational speed was increased from 600 to 1000 rpm, but decreasing when the tool rotational speed was further increased to values higher than 1000 rpm. The decrease in PAZ width, for the welds produced with high rotational speeds, is associated with the asymmetry in the shape of the PAZ (Figures A.5d and A.5e) reported in the previous paragraph, which was attributed to the asymmetrical contact conditions between the AS and RS of the tool.

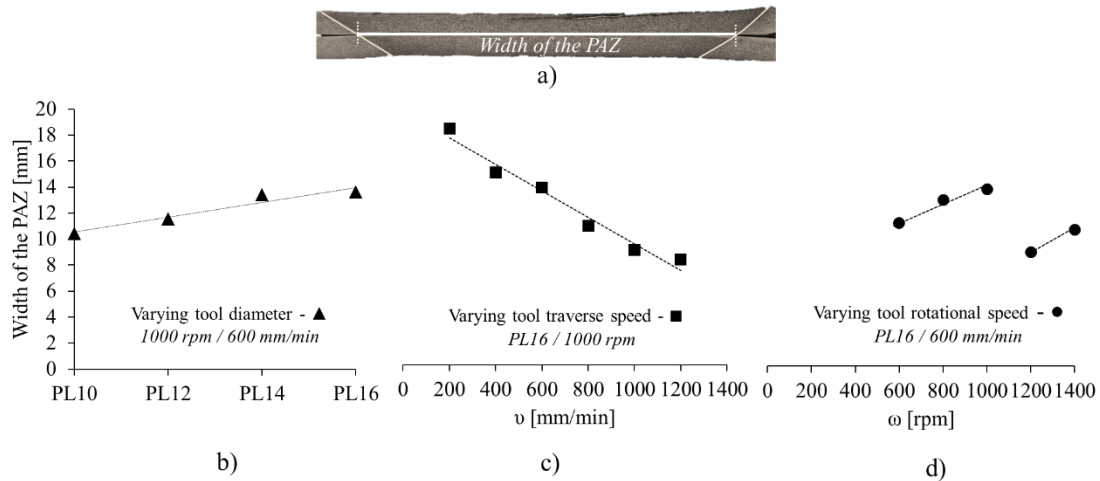


**Figure A.11** - Evolution of the width of the PAZ (a) with the process parameters: tool diameter (b), traverse speed (c) and rotational speed (d).

### 3.2 Mechanical Characterisation

The strength of the welds was evaluated by testing AS and RS loaded samples. The analysis of the results enabled to conclude that most of the samples had lap shear strength similar to the ultimate tensile strength (UTS) of the base material. The only exception was reported for the weld performed with the PL16 tool at 1000 rpm and 1000 mm/min, for which the lap shear strength of some of the samples did not exceed the yield strength of the base material. Additionally, for most of the welds, no important differences in the lap shear strength of the AS and RS samples were reported, as is usual in lap welds produced by FSW (Costa et al. 2015b).

In order to illustrate the previous statements, Figures A.12 to A.13 show load-displacement curves of some selected welds. More precisely, Figure A.12a shows the load-displacement curve for the weld produced with the PL16 tool and rotational and traverse speeds of 1000 rpm and 600 mm/min, respectively, together with the load-displacement curve under tension, of a homogeneous specimen of base material, with the

## Appendix A

same width of the lap shear samples. The figure shows that both the AS and RS samples of the weld had mechanical behaviour/strength similar to that of the base material. The Mises strain deformation map, at maximum load, displayed in Figure A.12b and A.12c, also show that both the RS and AS samples failed in the base material far from the weld. In Figure A.12d is shown an image of the base material fracture. Since no plastic deformation was recorded inside the PAZ, it is possible to confirm that no lap defects or bonding discontinuities, acting as stress concentrators, were present in the weld. Similar behaviour/strength was reported for most of the welds analysed in this work, except for that produced with the PL16 tool and the highest values of tool rotational and traverse speeds, as is shown in Figures A.13 and A.14, respectively.

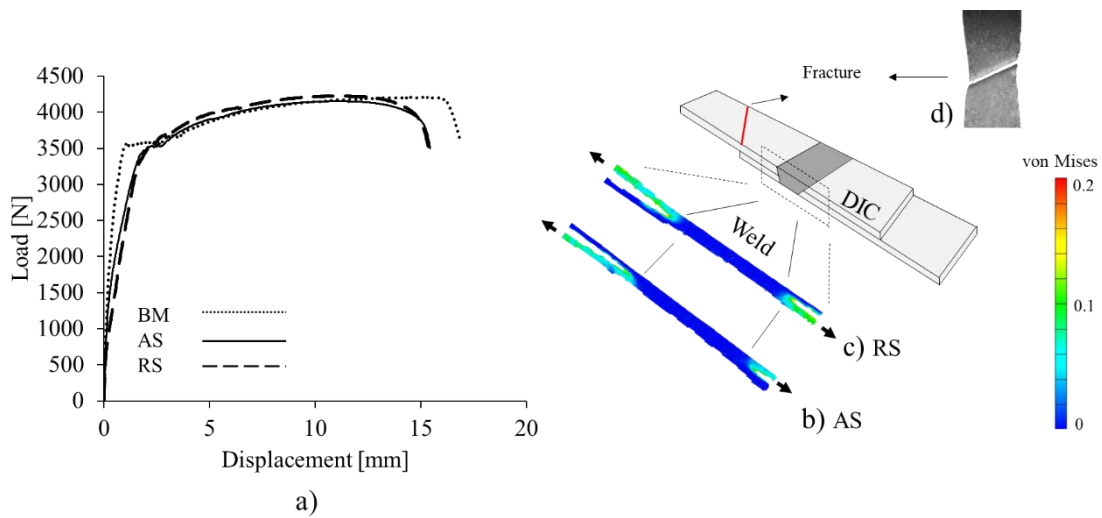


**Figure A.12** – Load-displacement curves (a), strain maps (b-c) and fractured sample (d) for the weld produced with the PL16 tool at 600 mm/min and 1000 rpm.

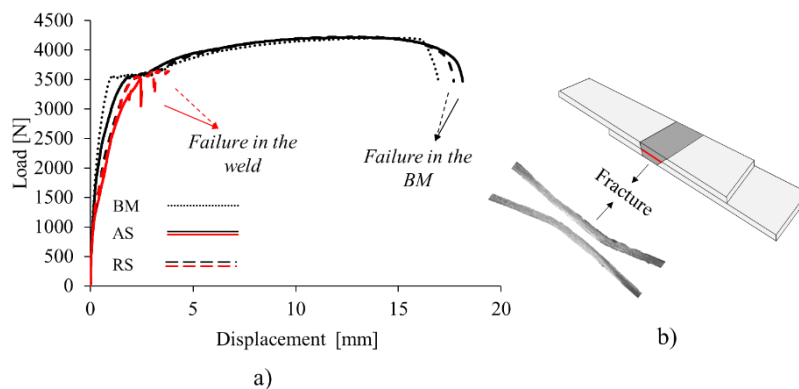


**Figure A.13** – Load-displacement curves (a) and fractured sample (b) for the weld produced with the PL16 tool at 1000 mm/min and 1000 rpm.

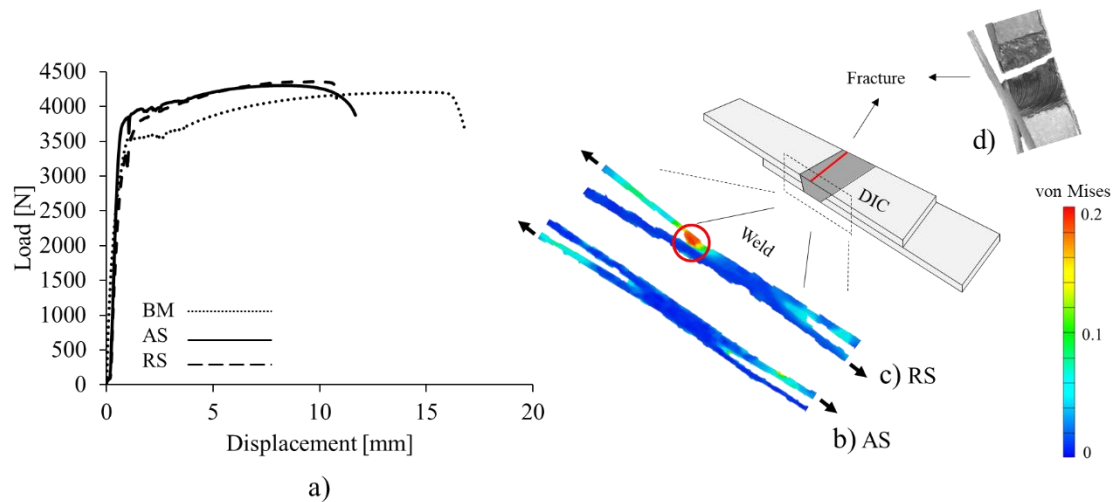


**Figure A.14** – Load-displacement curves (a), strain maps (b-c) and fractured sample (d) for the weld produced with the PL16 tool at 600 mm/min and 1400 rpm.

The load-displacement curves in Figure A.13a show that some of the samples of the weld made with a traverse speed of 1000 mm/min had rupture for load values in the range of the yield strength of the base material (red curves in the graph). These samples failed by separation of the plates, at the bonding interface, as shown in Figure A.13b. The important differences in strength/behaviour reported for the AS and for the RS samples of this weld, show that the quality of the bonding was not uniform along the weld length. In the same way, a non-uniform behaviour in lap shear testing was reported for the weld manufactured with the PL16 tool and the highest rotational speed (1400 rpm), as is shown in Figure A.14. For this weld, despite all the samples had strength similar to the UTS of the base material (Figure A.14a), the failure modes were different for the AS and for the RS samples. As is shown by the Mises strain deformation maps in Figures A.14b and A.14c, while the AS samples failed in the base material, with no plastic deformation in the weld, the RS samples had failure in the top plate, inside the PAZ (Figures A.14c and 14d). This mode of failure is associated with the asymmetrical morphology of the joint.

The lap shear testing results show that despite all the welds analysed displayed excellent strength, the loading/failure behaviour was not uniform for the welds with strong asymmetry in PAZ morphology. In the next section, the contact conditions associated with the unsymmetrical welds properties are discussed based on process parameters and torque sensitivity analysis.

### 3.3. Contact conditions in TAFW

In order to better understand the strong asymmetry in morphology between the AS and RS of the welds produced at highest values of traverse and rotational speeds, an analysis of the process parameters was made. Figure A.15 shows a schematic view of the linear velocities of points in the outer radius of the shoulder, at the advancing (point A) and retreating (point B) sides of the tool. The diagram shows that the direction of rotation is the same as that of the linear translation of the tool, at the AS, and opposite at the RS. So the linear velocities associated with the advancing ( $v_v$ ) and rotational ( $v_\omega$ ) movements of the tool have the same direction in Point A and the opposite direction in Point B. This way, the difference  $V$  between the linear advancing and the rotational speeds ( $v_v - v_\omega$ ) is higher at the RS than at the AS ( $V_B > V_A$ ).

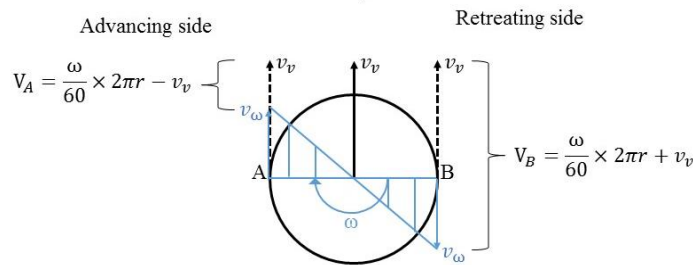


**Figure A.15** – Schematic view of the tool, showing the linear velocities of points in the outer radius of the shoulder, at the advancing (point A) and retreating (point B) sides.

Figures A.16a and A.16b shows the evolution of  $V_B$  with the different traverse and rotational speeds, respectively. It is possible to see that  $V_B$  increases when increasing  $v$  and  $\omega$ . In both graphs, the points marked in red identify the welds where an asymmetry in morphology, between the AS and the RS was observed, showing that this phenomenon occurred when  $V_B > 1600$  mm/s.

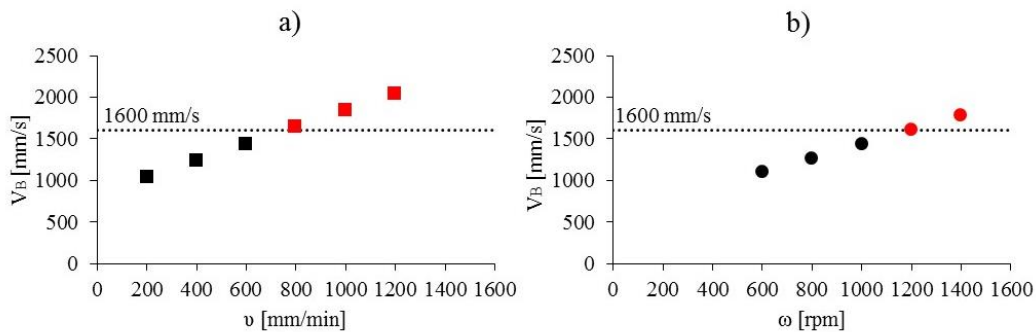


**Figure A.16** – Evolution of  $V_B$  with the traverse speed (a) and rotational speed (b).



A torque sensitivity analysis was also performed, as made by Leitão et al. 2012a in FSW of aluminium alloys. Figure A.17 shows the evolution of the average weld torque with the process parameters ( $v/\omega$ ) for the welds produced with the PL16 tool. Analysing the figure, it is possible to observe two different trends in the torque evolution for the welds produced with  $V_B$  lower (black points) and higher (red points) than 1600 mm/s. The torque tends to stabilise when decreasing  $v/\omega$ , for the welds produced with  $V_B < 1600$  mm/s. For the welds produced with  $V_B \geq 1600$  mm/s, the torque tends to stabilise when increasing  $v/\omega$ . Since no significant base materials stirring takes place during TAFW, as in FSW, the differences in torque evolution for the welds performed with  $V_B$  higher and lower than 1600 mm/s have to be related with the differences in tool-workpiece contact under the different welding conditions.

The differences in contact conditions, between the AS and RS of the tool, for the welds performed with  $V_B \geq 1600$  mm/s, were already addressed when analysing the asymmetries in the morphology of the welds in Figures A.4d to A.4f and Figures A.5d and A.5e. It was concluded that the asymmetry in welds morphology resulted from the prevalence of sliding contact conditions at the RS of the tool during welding. The torque evolution in Figure 17 is another evidence of the prevalence of sliding contact conditions when  $V_B \geq 1600$  mm/s. More precisely, when increasing the weld pitch, the distance travelled by the tool in each revolution increases, sliding contact conditions become more favourable (independently of  $V_B$ ) and the torque tends to stabilize. This assumption is supported by the fact that the average torque for the weld performed at 600 mm/min and 600 rpm (white point), produced with  $V_B < 1600$  mm/s, follows the red line trend. As can be observed in Figure A.5a, this weld has cross-section features characteristic of unstable contact at the tool-workpiece material interface during welding.

When welding with  $V_B < 1600$  mm/s the torque decreases when decreasing the weld pitch, as observed by other authors in FSW of aluminium (Leitão et al. 2012a) and aluminium-copper (Galvão et al. 2012) alloys. In this situation, the distance travelled by the tool in each revolution decreases and the conditions for sliding/sticking contact become more favourable. The parameter  $V_B$ , in this case, does not enforce sliding contact conditions at the RS of the weld. The evolution of the contact conditions with the process parameters is governed by the same mechanism operating in FSW (Arora et al. 2009), and the torque evolution follows the same trends as in FSW.

## Appendix A

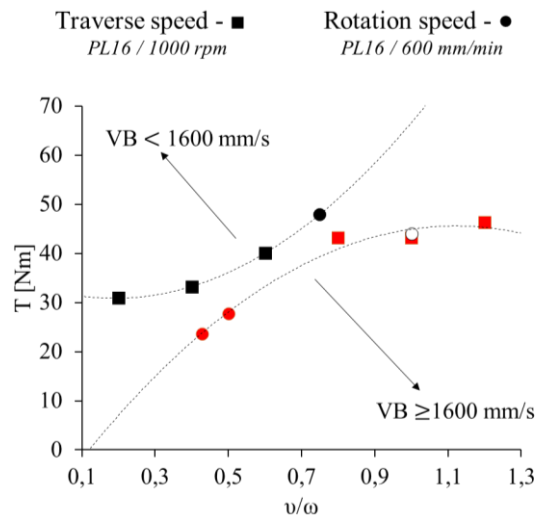


**Figure A.17** - Evolution of average torque values with the weld pitch ( $v/\omega$ ).

### 4. Conclusions

- It is possible to produce steel lap welds with joint strength similar to the UTS of the base material using TAFW.
- The morphology of the welds evolves with the traverse and rotational speeds of the tool, becoming asymmetrical between the AS and the RS for critical combinations of rotational and traverse speeds ( $V_B > 1600$  mm/s).
- The asymmetry in welds morphology determines the mode of failure of the joints but has small influence on the joints strength in monotonic loading.
- No hooking or cold lap defects were observed for any of the lap welds produced by TAFW.

### References

- Arora, A., Nandan, R., Reynolds, A. P., DebRoy, T., 2009. Torque, power requirement and stir zone geometry in friction stir welding through modeling and experiments. Scripta matter, 60(1), 13-16.
- Baek, S. W., Choi, D. H., Lee, C. Y., Ahn, B. W., Yeon, Y. M., Song, K., Jung, S. B., 2010. Microstructure and mechanical properties of friction stir spot welded galvanized steel. Mater Trans. 51(5), 1044-1050.

- Bakavos, D., Chen, Y., Babout, L., Prangnell, P., 2011. Material interactions in a novel pinless tool approach to friction stir spot welding thin aluminum sheet. *Metall Mater Trans A*. 42(5), 1266-1282.
- Çam, G., 2011. Friction stir welded structural materials: beyond Al-alloys. *Int Mater Rev*, 56(1), 1-48.
- Chen, Y. C., Komazaki, T., Tsumura, T., Nakata, K., 2008. Role of zinc coat in friction stir lap welding Al and zinc coated steel. *Mater Sci Tech*. 24(1), 33-39.
- Costa, M. I., Verdera, D., Costa, J. D., Leitao, C., Rodrigues, D. M., 2015a. Influence of pin geometry and process parameters on friction stir lap welding of AA5754-H22 thin sheets. *J Mater Process Tech*. 225, 385-392.
- Costa, M. I., Verdera, D., Leitão, C., Rodrigues, D. M., 2015b. Dissimilar friction stir lap welding of AA 5754-H22/AA 6082-T6 aluminium alloys: Influence of material properties and tool geometry on weld strength. *Mater Design*. 87, 721-731.
- Galvão, I., Leitão, C., Loureiro, A., Rodrigues, D. M., 2012. Study of the welding conditions during similar and dissimilar aluminium and copper welding based on torque sensitivity analysis. *Mater Design*, 42, 259-264.
- Karami, S., Jafarian, H., Eivani, A. R., Kheirandish, S., 2016. Engineering tensile properties by controlling welding parameters and microstructure in a mild steel processed by friction stir welding. *Mat Sci Eng A*. 670, 68-74.
- Kim, K. H., Bang, H. S., Kaplan, A. F. H., 2017. Joint properties of ultra thin 430M2 ferritic stainless steel sheets by friction stir welding using pinless tool. *J Mater Process Tech*. 243, 381-386.
- Leitão, C., Louro, R., Rodrigues, D. M., 2012a. Using torque sensitivity analysis in accessing Friction Stir Welding/Processing conditions. *J Mater Process Tech*. 212(10), 2051-2057.
- Leitão, C., Galvão, I., Leal, R. M., Rodrigues, D. M., 2012b. Determination of local constitutive properties of aluminium friction stir welds using digital image correlation. *Mater Design*. 33, 69-74.
- Mira-Aguiar, T., Verdera, D., Leitão, C., Rodrigues, D. M., 2016. Tool assisted friction welding: A FSW related technique for the linear lap welding of very thin steel plates. *J Mater Process Tech*. 238, 73-80.

## Appendix A

- Rai, R., De, A., Bhadeshia, H. K. D. H., DebRoy, T., 2011. friction stir welding tools. *Sci Technol Weld Joi.* 16(4), 325-342.
- Salari, E., Jahazi, M., Khodabandeh, A., Ghasemi-Nanesa, H., 2014. Influence of tool geometry and rotational speed on mechanical properties and defect formation in friction stir lap welded 5456 aluminum alloy sheets. *Mater Design.* 58, 381-389.
- Schmidt, H., Hattel, J., Wert, J., 2003. An analytical model for the heat generation in friction stir welding. *Model Simul Mater Sc.* 12(1), 143.
- Sekban, D. M., Aktarer, S. M., Zhang, H., Xue, P., Ma, Z., Purcek, G., 2017. Microstructural and mechanical evolution of a low carbon steel by friction stir processing. *Metall Mater Trans A.* 1-11.
- Yadava, M. K., Mishra, R. S., Chen, Y. L., Carlson, B., Grant, G. J., 2010. Study of friction stir joining of thin aluminium sheets in lap joint configuration. *Sci Technol Weld Joi.* 15(1), 70-75.
- Zhang, G., Su, W., Zhang, J., Wei, Z., 2011. Friction stir brazing: a novel process for fabricating Al/steel layered composite and for dissimilar joining of Al to steel. *Metall Mater Trans A.* 42(9), 2850-2861.

# Appendix B

---

## *Article B*

*Andrade, D. G., Leitão, C., & Rodrigues, D. M. (2019). Influence of base material characteristics and process parameters on frictional heat generation during friction stir spot welding of steels. Journal of Manufacturing Processes, 43, 98-104.*

<https://doi.org/10.1016/j.jmapro.2019.05.015>

**Influence of base material characteristics and process parameters on frictional heat generation during Friction Stir Spot Welding of steels.**

### **Abstract**

Frictional heat generation, in Friction Stir Spot Welding of steels, was assessed by producing welds with pinless tools. In order to analyse the influence of base material characteristics on heat generation, spot welds were produced, using varied process parameters, in DC01, DX51D and HC420 LA steel sheets (1 mm thick). Uncoated and coated sheets, with galvanised films of different thicknesses, were tested in order to assess the influence of surface properties on heat generation. The welding thermal cycles were measured using thermography and hardness measurements were done to evaluate the influence of the maximum temperature, maintenance time and cooling rates on welds properties. It was found that the main factors influencing the frictional heat generation are, by order of importance, the tool diameter, the tool rotation speed and the presence of low melting point coatings. Differences in frictional heat generation, for the different base materials, were only registered when welding with a 10 mm diameter tool. The analysis of the average welds hardness enabled to conclude that the hardness increase in the weld region, relative to the base material, is determined by the maximum temperature reached during welding and by the grain size of the base material.

**Keywords:** FSSW; Heat generation; Thermal cycle; Process parameters; Steel

### 1. Introduction

In welding engineering, it is well known that the maximum temperatures reached during welding, as well as the heating and cooling rates associated with it, influence the final microstructure and mechanical properties of steel welds. This is true in both fusion and solid state welding. However, meanwhile in fusion welding the maximum temperatures are always above the melting temperature of the base materials, in solid state welding the maximum temperatures reached are always below the melting temperature and may be controlled by an accurate selection of process parameters. In Friction Stir Welding (FSW) and Friction Stir Spot Welding (FSSW), it is expected that the maximum temperatures reached during welding are determined by the tool geometry, the welding parameters and the base materials properties/characteristics.

In Figure B.1 are listed the experimental works that have reported temperature measurements in FSW and FSSW of carbon steels. Analysing the figure, it is possible to conclude that the maximum temperature registered in the different studies on FSW and FSSW of steels were in the range of 400 to 1300, which confirms the previous assumption that the maximum temperatures in stir welding vary according to the process parameters. According to Cui et al. [1] and Santella et al. [2], who analyse the thermal cycles in FSW of S70C and FSSW of DP780 steels, respectively, increasing the tool rotation speed increases the maximum temperatures reached during welding. According to Fujii et al. [3], who analysed the influence of the welding speed on thermal cycles in FSW of IF (0% C), S12C (0,12% C) and S35C (0,34% C) steels, and Imam et al. [4], who performed the same type of analysis in FSW of S45C steel, the maximum temperatures registered during welding decreases as the welding speed increases. Comparing the different studies, it is also possible to conclude that maximum temperatures above 1100 °C were only registered by Lienert et al. [5] and Stringham et al. [6], who used very large shoulder diameter tools ( $D_s > 19$  mm).

Finally, Santella et al. [2], who performed FSW of galvanised steels, observed that the presence of a galvanised coating in steel sheets reduced the welding temperatures, up to 110 °C, when compared to uncoated welds produced under the same welding conditions. Baek et al. [7], Mazzaferro et al. [8] and Mira-Aguiar et al. [9], who also analysed galvanised steel welds, concluded, based on metallographic analysis, that the galvanised coating melted during the welding process, working as a lubricant at the tool-plates interface, which prevented base materials stirring and lowered the welding temperatures.

In current work, the influence of tool diameter, rotational speed and base material properties, on frictional heat generation during Friction Stir Spot Welding of steels, was analysed by measuring the welding thermal cycles in spot welding of a varied range of base materials. In order to evaluate the frictional heat generation, a pinless tool was used, which according to Mira-Aguiar et al. [9] and Andrade et al.[10,11], enables to suppress base materials stirring during welding.

2003	2006	2007	2010	2014	2015	2018
<u>Lienert et al. [5]</u> BM: AISI 1018 Ds = 19 mm $\omega = 650 \text{ rpm}$ $v = 25.2 \text{ mm/min}$ $T_{max} = 1100 \text{ }^\circ\text{C}$	<u>Cui et al. [1]</u> BM: S70C Ds = 12 mm $\omega = 200-800 \text{ rpm}$ $v = 400 \text{ mm/min}$ $T_{max} = 600-900 \text{ }^\circ\text{C}$	<u>Sun et al. [15]</u> BM: S12C Ds = 12 mm $\omega = 800 \text{ rpm}$ $T_{max} = 700 \text{ }^\circ\text{C}$	<u>Stringham et al. [6]</u> BM: HSLA-65 Ds = 36.8 mm $\omega = 350-550 \text{ rpm}$ $v = 72-264 \text{ mm/min}$ $T_{max} = 825-1327 \text{ }^\circ\text{C}$	<u>Fujii et al. [3]</u> BM: IF, S12C, S35C Ds = 12 mm $\omega = 400 \text{ rpm}$ $v = 100-400 \text{ mm/min}$ $T_{max} = 643-873 \text{ }^\circ\text{C}$	<u>Baek et al. [7]</u> BM: Galvanised steel Ds = 13.5 mm $\omega = 1600 \text{ rpm}$ $T_{max} = 1020 \text{ }^\circ\text{C}$	<u>Imam et al. [4]</u> BM: S45C $\omega = 400 \text{ rpm}$ $v = 100-500 \text{ mm/min}$ $T_{max} = 527-825 \text{ }^\circ\text{C}$
		<u>Santella et al. [2]</u> BM: DP780 Ds = 9.5 mm $\omega = 800-1600 \text{ rpm}$ $T_{max} = 410-683 \text{ }^\circ\text{C}$				

FSW  
 FSSW

**Figure B.1** – Experimental works that have reported temperatures measurements in FSW and FSSW of carbon steels.

## 2. Experimental Procedure

In current work, spot welds, in 1 mm thick steel plates of several steels, were produced using pinless tools. In Table B.1 are identified the different base materials together with some properties considered of interest in current work, more precisely: the carbon content ( $C_{eq}$ ), the hardness ( $HV_{0.2}$ ), the ultimate tensile strength ( $\sigma_{max}$ ), the galvanised coating thickness ( $CT$ ) and the average grain size ( $GS$ ). The carbon content of the different alloys was evaluated using the IIW carbon equivalent equation [12]. As shown in the table, two DC steels (DC and DC-R2.5), two DX51D steels (DX51D-R10 and DX51D-R14) and a high strength steel (HC420) were used in the investigation. The DC-R2.5, DX-R10 and DX-R14 plates had 2.5, 10 and 14  $\mu\text{m}$  thick galvanised coatings, respectively. The DC and HC420 plates were uncoated.

The experimental setup used for producing the spot welds, in 80x80 mm sheets, is schematized in Figure B.2a. The welds were produced in a three-step operation: (1)

## Appendix B

The plunging period, during which the tool moved vertically until the desired plunging depth (0.5 mm) was reached; (2) The dwell period (60s), during which the rotating tool remained in contact with the upper plate surface, heating the base materials; (3) The drawing-out period, which corresponded to the removal of the tool. During the welding process, the temperatures at the outer interface, between the tool and the workpiece, were measured using a thermographic camera (Figure B.2b). As can be seen in Figure B.2c, only tungsten carbide pinless tools with flat shoulder were used in the investigation. In the text, the tools with a shoulder diameter of 10 mm, 12 mm and 16 mm will be labelled as PL10, PL12 and PL16, respectively. The welds were produced, in position control, using a Cincinnati universal milling machine.

**Table B.1** –Base materials and their properties: carbon content ( $C_{eq}$ ), hardness ( $HV_{0.2}$ ), ultimate tensile strength ( $\sigma_{max}$ ), galvanised coating thickness ( $CT$ ) and average grain size ( $GS$ ).

Material	Nomenclature	$C_{eq}$ [%]	$HV_{0.2}$	$\sigma_{max}$ [MPa]	$CT$ [ $\mu\text{m}$ ]	$GS$ [ $\mu\text{m}$ ]
DC01	DC	0.13	105	452	0	7.1
DC01-ZE25/25	DC-R2.5	0.13	106	461	2.5	9.3
DX51D-Z140	DX-R10	0.11	108	461	10	7.4
DX51D-Z200	DX-R14	0.19	127	483	14	5.9
HC 420 LA	HC420	0.37	183	670	0	3.3

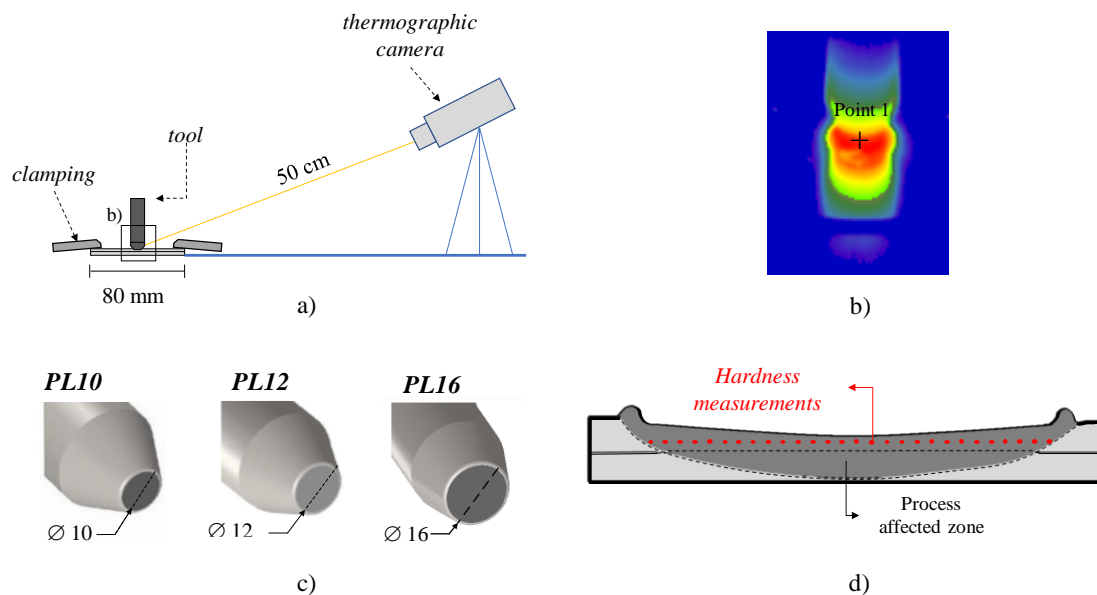


**Figure B.2** – Experimental procedure: assembly used for the production of the spot welds (a); thermographic analysis (b), tools geometry (c) and hardness measurements scheme (d).

The welding parameters tested, shown in Figure B.3, were chosen in order to enable performing a sensitivity analysis on the influence of base materials characteristics,



tool geometry and process parameters on heat generation, i.e. different rotational speeds and tools were used to weld steels with different mechanical properties and surface conditions. The tool penetration depth and the dwell time were selected, not to reproduce industrial welding conditions, but for enabling capturing the differences in heat generation and thermal cycles between the different welding conditions.

After welding, metallographic samples were removed from the welds, polished according to standard procedures, etched with 2% Nital and observed using an optical microscope (Leica DM 4000 M LED). The hardness of the welds was assessed by averaging the results of hardness measurements performed transverse to the cross section, in the upper sheet, as schematized in Figure B.2d. Hardness measurements were done using a Shimadzu microhardness tester, with 200 g load and 15 s holding time.

<b>Material \ Tool</b>	<b>PL10</b>	<b>PL12</b>	<b>PL16</b>
<b>HC420</b>	870;1500 rpm	870;1140;1500 rpm	870;1500 rpm
<b>DC</b>	870;1500 rpm	870;1140;1500 rpm	870;1500 rpm
<b>DC-R2.5</b>	-	870;1140;1500 rpm	-
<b>DX-R10</b>	-	870;1140;1500 rpm	-
<b>DX-R14</b>	-	870;1140;1500 rpm	-

- Sensitivity analysis on rotational speed and tool geometry
- Sensitivity analysis on base material strength
- Sensitivity analysis on surface conditions

**Figure B.3** – Process parameters.

### 3. Results and Discussion

#### 3.1. Morphological and thermal analysis

The metallographic analysis enabled to conclude that all the welds produced had similar morphology, characterised by a bowl shape process affected zone encompassing both lap plates thickness. This morphology is exemplified in Figure B.4, where is shown a cross section of a DC weld produced with the PL12 tool with a rotational speed of 1140 rpm. The image enables to observe that no cross-interface base material stirring took place during welding, since a straight dark line marked by arrows in Figure B.4 may still be observed in the same position of the original plates interface. The absence of intense base

## Appendix B

material stirring is also indicative that frictional heat generation was the main mechanism governing the welding induced thermal cycles.

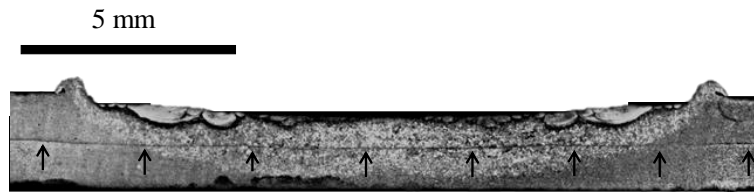


**Figure B.4** – Morphology of the weld cross-section, produced in DC steel with the PL12 tool with a rotational speed of 1140 rpm.

In Figure B.5 is shown a thermal cycle for the weld in Figure B.4. The thermal cycle enables to identify three main welding stages: a heating period ( $t_h$ ), during which the temperature rises, a steady state period ( $t_{ss}$ ), during which the temperature remains almost constant, and a cooling period ( $t_c$ ), during which the temperature decreases, after welding. In Figure B.5 is also represented the instantaneous derivative of the temperature ( $dT/dt$ ), used in current work to determine the duration of the three different stages. The instantaneous derivative corresponds to the instantaneous heating rate, when displays positive values, and to the instantaneous cooling rate, when reaching negative values. In order to determine the length of the steady state period, at the maximum temperature, it was assumed that the heating period ends when  $0 \leq dT/dt \leq 4 \text{ }^\circ\text{C/s}$ . Once the duration of the steady state period was set, the maximum temperature reached during welding ( $T_{max}$ ) was determined by calculating the average of the temperatures recorded during that period. The cooling rate ( $V_c$ ) was determined by calculating the cooling time from 800 to 500  $^\circ\text{C}$  ( $\Delta t_{8/5}$ ).

### 3.1.1. Welding of uncoated based materials

In Figure B.6 are shown the thermal cycles acquired in the welding of the DC01 and HC420 steels, with different rotational speeds and tool diameters. In each figure is plotted a rectangle, in blue, highlighting the evolution of temperature in the first 10s of the welding operation, which corresponds to the average duration of the process cycle time in a large number of studies on FSSW of steels [2,13,14,15]. In Figure B.7 are plotted the maximum temperatures determined from the thermal cycles in Figure B.6, using the procedure explained in Figure B.5.

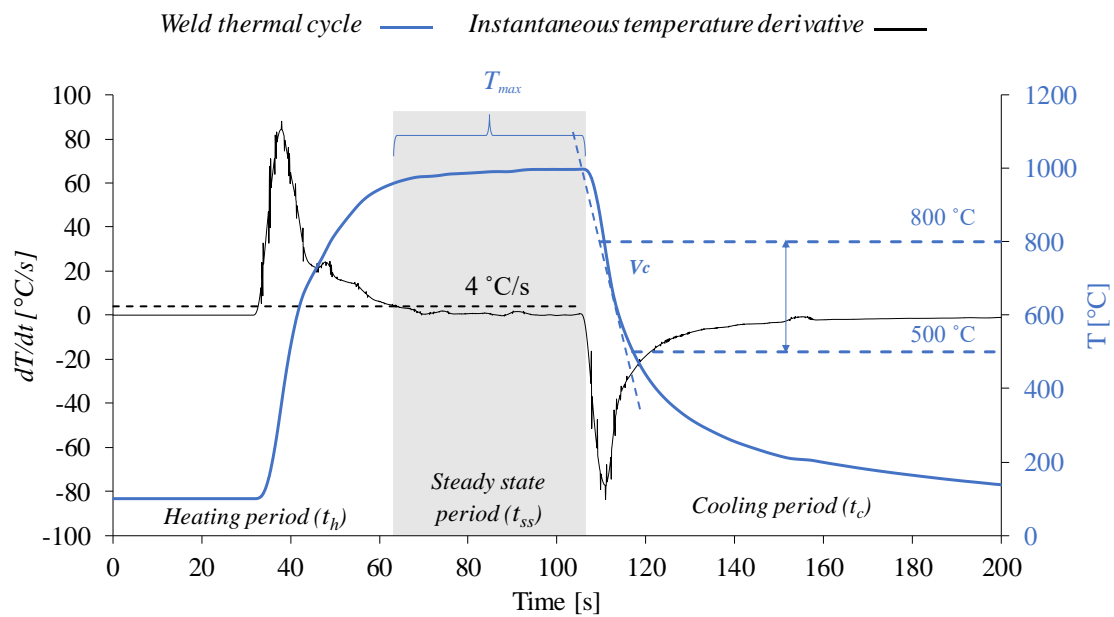


**Figure B.5** – Weld thermal cycle, represented by a blue line, and instantaneous temperature derivative in order of time ( $dT/dt$ ), represented by a black line, for the weld produced in DC steel with the PL12 tool and a rotational speed of 1140 rpm.

Analysing Figures B.6 and B.7 it is possible to conclude that there was an important influence of the tool diameter on heat generation during welding. Figure B.7 shows that not only different maximum temperature ranges were registered for the different tools, but also that the evolution of  $T_{max}$  with the base material and tool rotation speed varied according to the tool diameter. More precisely, for the PL16 tool, no important differences in  $T_{max}$  were registered, independently of the base material and tool rotation speed, indicating that a threshold in heat generation was attained. The invariability in the maximum temperature registered for this tool, which was in the range of 1100 °C, indicates that the tool diameter was the main factor governing heat generation.

For the PL12 tool, the maximum temperatures were all lower than those registered for the PL16 tool. Despite similar temperatures were registered for the two base materials, an increase in  $T_{max}$  was registered when increasing the tool rotation speed, indicating that the tool diameter was no more the only factor governing the heat generation. For this tool diameter, a maximum threshold temperature was registered for each tool rotation speed, independently of the base material. The maximum temperatures increased with the rotational speed, stabilising in a value near to 1000 °C, when the rotational speed was

## Appendix B

increased to values higher than 1000 rpm, which is the maximum threshold temperature for the PL12 tool.

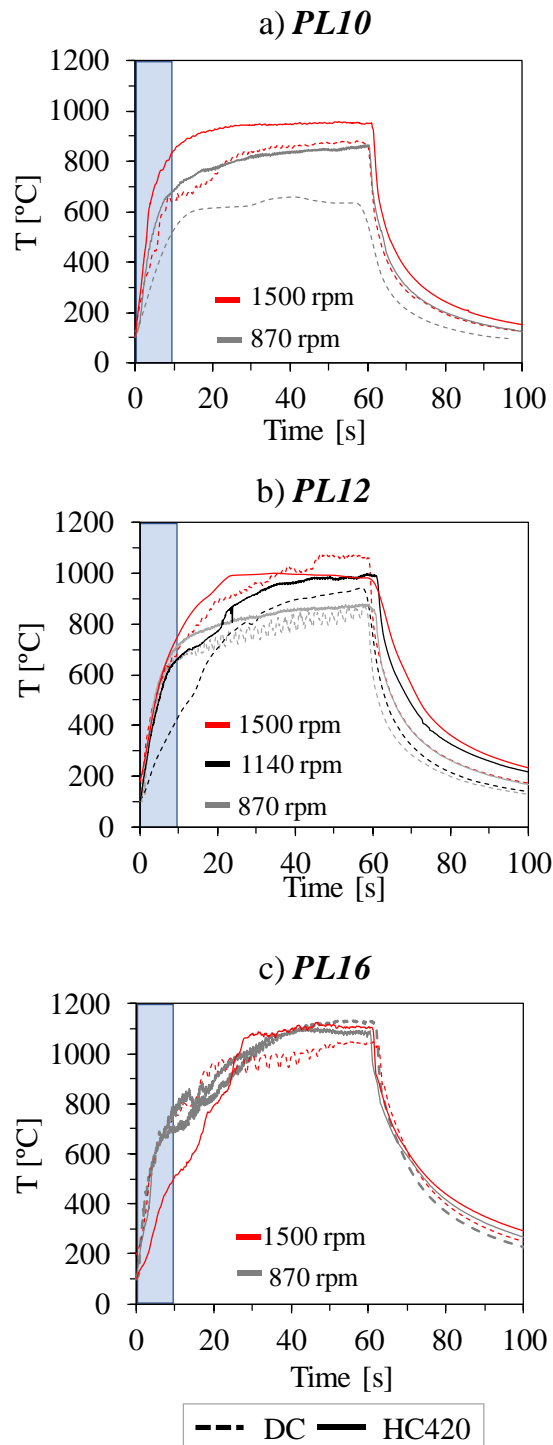


**Figure B.6** – Evolution of the acquired thermal cycles with the rotational speed and with the tool diameter, for the DC and HC420 steels.

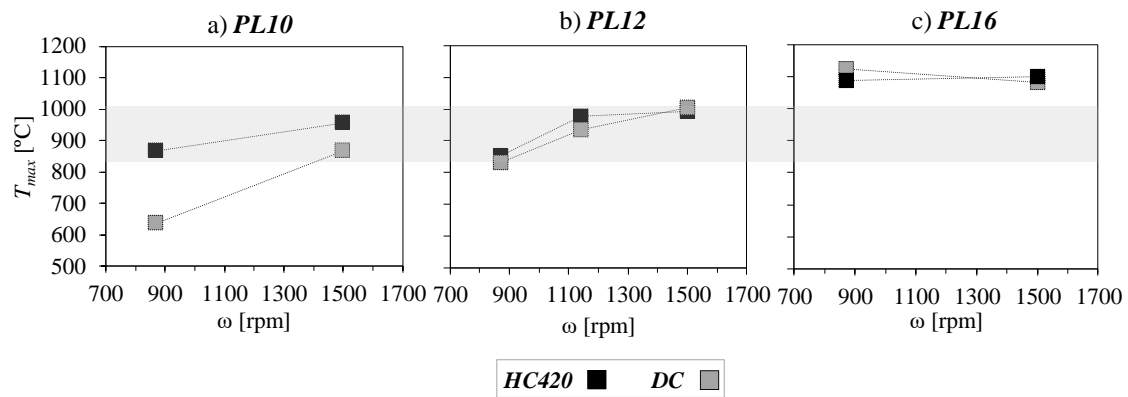


**Figure B.7** – Evolution of  $T_{max}$  with the rotational speed and with the tool diameter, for the DC and HC420 steels.

Finally, for the PL10 tool, contrary to that registered for the PL16 and PL12 tools, the maximum temperatures were different for the two base materials and rotational speeds, indicating that heat generation had an important influence from the base material properties and tool rotation speeds. In fact, despite  $T_{max}$  increased when the tool rotation speed was increased, for a same rotational speed,  $T_{max}$  was higher for the higher strength base material. The figure also enables to observe that, the differences in  $T_{max}$ , between the two base materials diminished for the higher tool rotation speed, and also, that the increase in  $T_{max}$  with the tool rotation speed, was much narrower for the HC420 steel, for which the highest temperatures were registered. This evolution in maximum temperatures enables to conclude that a maximum threshold temperature, of around 950 °C, may also be associated with the PL10 tool.

Figure B.6 also shows that for the welding operations conducted with the PL12 and PL16 tools, no important differences in temperature evolution were registered for the first 10s of the welding operation. The only exceptions correspond to the welding of the DC and HC420 steels at 1440 and 1500 rpm, respectively, which resulted from the use of slower plunging speeds. These thermal cycles were included in the figure to prove that the maximum threshold temperatures registered for the PL12 and PL16 tools were independent of the heating history.

Contrary to that reported for the PL16 and PL12 tools, the temperature evolution in the first 10s, for the PL10 tool, varied according to the base material and tool rotational speed. Additionally, these results indicate that, for the very short process cycle times required in industrial production, the maximum temperatures attained during welding may be independent of base material and tool rotation speeds, when welding with large

diameter tools, but may be controlled to low values, by a proper choice of the tool rotation speed, when small tool diameters are used.

### 3.1.2. Welding of galvanised based materials

The analysis of the influence of the galvanised coating on heat generation during welding was made by performing spot welds with the PL12 tool. According to Figure B.6, when welding with this tool, the maximum temperatures attained during welding did not varied when changing the base material, but increased non-linearly with the tool rotation speed, reaching a threshold near 1000 °C. In Figure B.8 is shown the evolution of  $T_{max}$  with the tool rotation speed, for the DC, DC-R2.5, DX-R10 and DX-R14 welds. From the graphic, in which  $T_{max}$  is plotted against the coating thickness, it is possible to conclude that, for each base material,  $T_{max}$  increased with the tool rotation speed until the threshold temperature of 1000 °C was reached. However, it is also possible to observe, that for tool rotation speeds lower than 1500 rpm  $T_{max}$  decreased when the galvanised plates were welded. Meanwhile for the DC-R2.5 steel, with the smallest coating thickness of 2.5 µm, the maximum temperatures were very close to that of the non-galvanised DC steel, for the DX-R10 and DX-R14 steels, with 10 and 14 µm thick coatings, the decrease in maximum temperature, relative to the DC steel, was of the range of 100 °C.

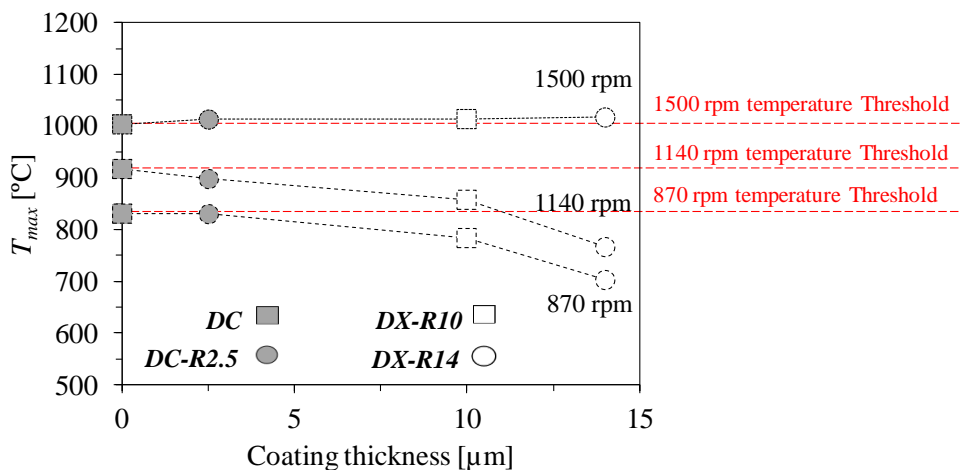


**Figure B.8** – Evolution of  $T_{max}$  with the galvanised coating thickness for the welds produced in the steels DC, DC-R2.5, DX-R10 and DX-R14, with the PL12 tool and a rotational speed of 870 rpm and 1500rpm.

In Figure B.9 are plotted the thermal cycles registered during the welding of the base materials in Figure B.8, with the rotational speeds of 870 and 1500 rpm. The figure

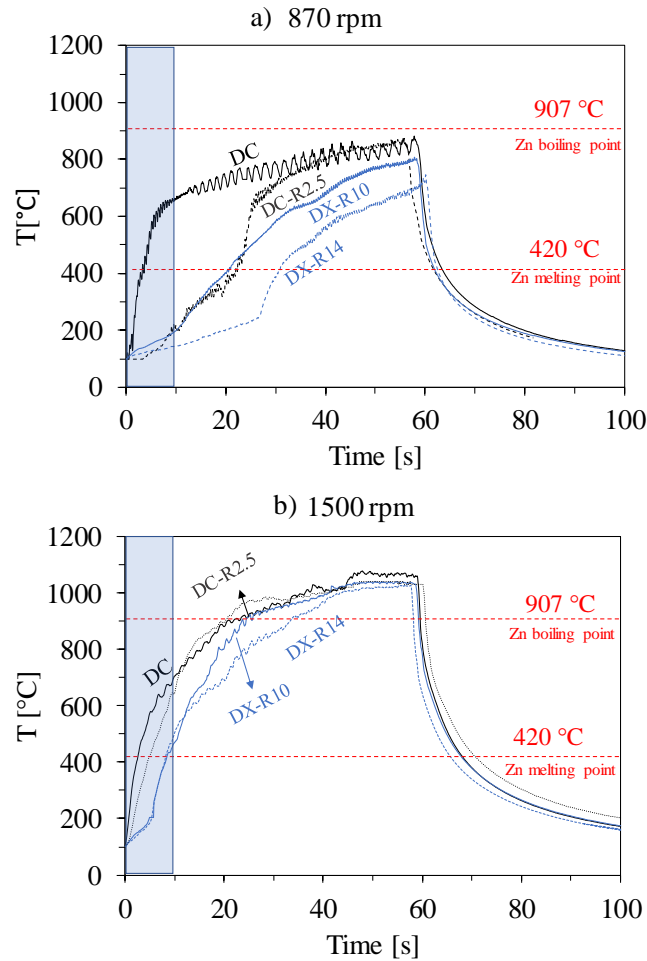
shows that, irrespectively of the tool rotation speed, the heating period (before  $T_{max}$  was reached), was longer for the galvanised base materials than for the uncoated DC steel. In the same way, meanwhile for the tool rotation speed of 1500 rpm, the threshold temperature of 1000 °C was reached for all the base materials, for the tool rotation speed of 870 rpm, the maximum temperature threshold of 800 °C was not reached in the welding of the DX-R10 and DX-R14 plates. This behaviour may be associated with the influence of the galvanised zinc layer on frictional heat generation. When welding at 870 rpm, the temperatures reached are sufficient for melting the galvanised coating (420 °C), which starts acting as a lubricant at the tool/base material interface, lowering the frictional heat generation. However, when welding at 1500 rpm, the heat generated by the tool promotes temperatures higher than the boiling point of the galvanised coating (907 °C), promoting its expulsion from the welding zone and enabling that the threshold temperature is reached independently of the base material.

Figure B.9 also shows that the influence of the galvanised coating on the frictional heat generation is even more important for process cycle times lower than 10s. In these conditions, the use of low tool rotation speeds may be not sufficient for the melting and expulsion of the zinc layer from the welding zone. When increasing the tool rotation speeds, to 1500 rpm, the maximum temperature attained during the 10s cycle period will depend on the thickness of the galvanised coating, but may attain the melting temperature of the zinc, even for thick coatings.

### 3.2. Influence of thermal cycles on welds properties

In order to analyse the influence of the thermal cycles on welds properties, hardness measurements were performed, enabling to conclude that, irrespectively of the welding conditions, the hardness of the base materials was always increased in the welding zone. This increase in hardness was quantified using the ratio  $RHV$  between the average hardness of the welds ( $HV^{weld}$ ) and the base material hardness ( $HV^{bm}$ ), calculated as follows:

$$RHV = \frac{HV^{weld}}{HV^{bm}}. \quad (B.1)$$



**Figure B.9** – Thermal cycles for the welds produced in the steels DC, DC-R2.5, DX-R10 and DX-R14, with the PL12 tool and a rotational speed of 870 rpm (a) and 1500rpm (b).

From Figure B.10, where is plotted the hardness ratio against the carbon equivalent of the base materials, it is possible to conclude that the hardness increase was highest for the base materials with the lower carbon equivalent, which is in contradiction with the common assumption that the hardness increase is higher for steels with higher alloy strength [16]. However, according to Nelson & Rose [16] and Wei & Nelson [17], the microstructure and mechanical properties of friction stir welds in steel are correlated with the heat input and the cooling rates during welding. Therefore, an analysis on the influence of the thermal cycles on hardness increase was performed. In Figure B.11 is plotted the evolution of the ratio  $RVH$  against  $T_{max}$  (Figure B.11a), the cooling rate (Figure B.11b) and the steady state period at high temperatures (Figure B.11c). Analysing the figure, it is possible to conclude that there is a very poor correlation between the hardness increase and the thermal parameter analysed in each graph ( $R^2 < 0.1$  in all graphs).



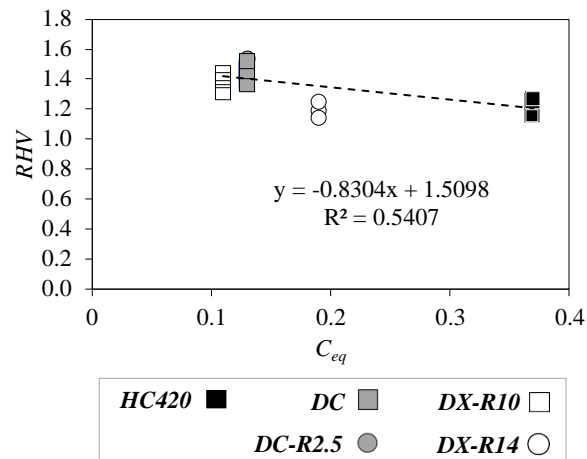


**Figure B.10** – Evolution of  $RHV$  as a function of the base material carbon equivalent for all base materials and welding conditions.

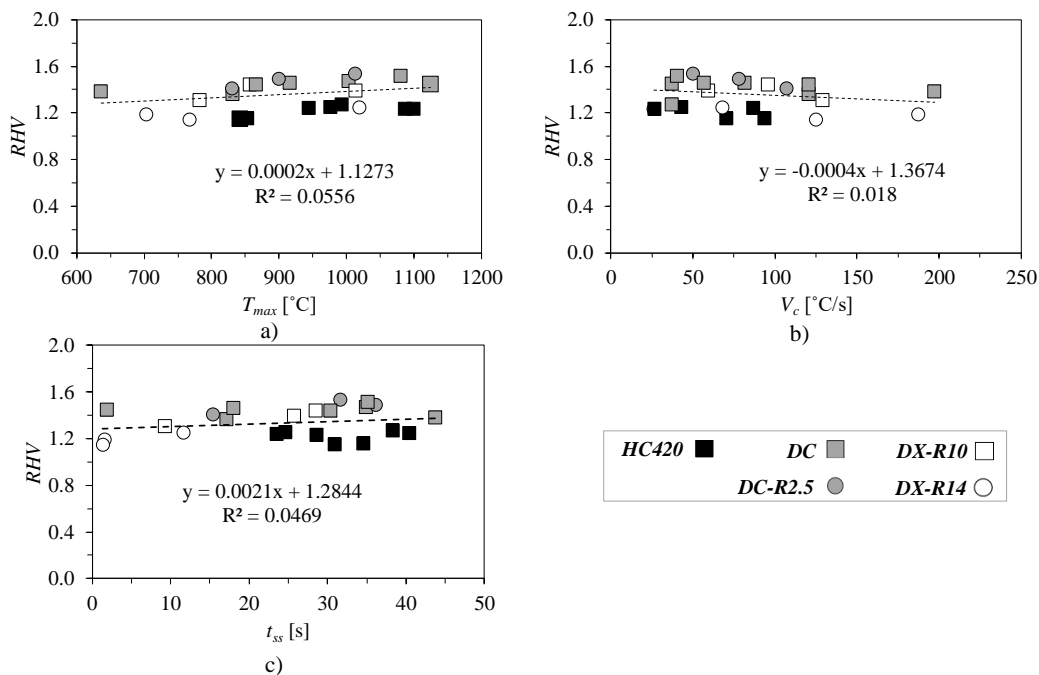


**Figure B.11** – Evolution of  $RHV$  with  $T_{max}$ ,  $V_c$  and  $t_{ss}$  for all base materials and welding conditions.

So, a new parameter to predict the hardenability of the different steel alloys, calculated by multiplying  $T_{max}$  by the base material grain size ( $T_{max} \times \mu m$ ), was tested. This parameter was developed after Brooks [18] and Bodnar & Hansen [19], according to whom the hardness increase in steel welds is related to the maximum temperatures reached during welding and to the austenitic grain size, Analysing Figure B.12, where is plotted the evolution of  $RHV$  as a function of  $T_{max} \times \mu m$ , it is possible to conclude that, unlike the trends in Figure B.11, there is a strong relationship between  $RHV$  and  $T_{max} \times \mu m$

## Appendix B

( $R^2 = 0.79$ ). These results indicate that the microstructural embrittlement in steel spot welding may be controlled, or even suppressed, by an appropriate choice of the tool diameter and tool rotation speed, which are the main parameters in determining  $T_{max}$ .

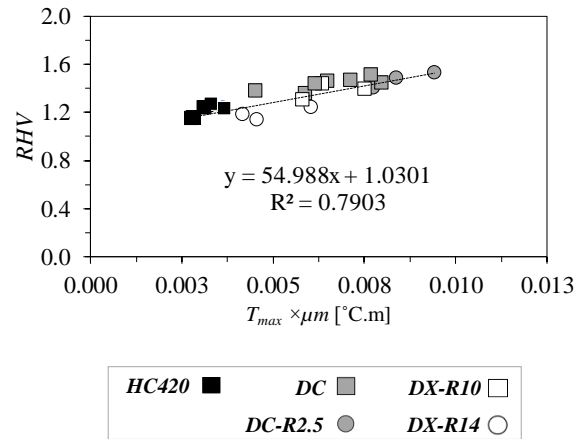


**Figure B.12** – Evolution of  $RHV$  with the  $T_{max} \times \mu m$  for all base materials and welding conditions.

## 4. Conclusions

In the present work, the influence of the process parameters and of the base material properties in the thermo-mechanical conditions developed during FSSW was analysed. The following conclusions were reached:

- The tool diameter is an important factor determining the maximum temperatures reached during FSSW. For each tool diameter, there is a threshold in the maximum temperature that can be reached during welding. The threshold temperature increases with the tool diameter.
- Meanwhile, for large tool diameters, the maximum welding temperature may be constant and independent of the base material and tool rotation speed, for small tool diameters, the maximum welding temperature varies according to the base material and tool rotation speed.
- For small tool diameters, the presence of a thick galvanised coating may be also an important factor determining the heat generation during welding. For rapid process cycle times ( $< 10s$ ), the presence of thick galvanised coatings may obstruct the bonding process.
- In FSSW, the hardness increase in the welds, relative to the base material, is governed by the maximum temperatures reached during the welding and by

the initial base material grain size. Nor the cooling rate, nor the time at high temperature, have strong influence on the final weld hardness.

## References

- [1] Cui L, Fujii H, Tsuji N, Nogi K. Friction stir welding of a high carbon steel. *Scr Mater* 2007;56:637–40. doi:<https://doi.org/10.1016/j.scriptamat.2006.12.004>.
- [2] Santella M, Hovanski Y, Frederick A, Grant G, Dahl M. Friction stir spot welding of DP780 carbon steel. *Sci Technol Weld Join* 2010;15:271–8. doi:<https://doi.org/10.1179/136217109X12518083193630>.
- [3] Fujii H, Cui L, Tsuji N, Maeda M, Nakata K, Nogi K. Friction stir welding of carbon steels. *Mater Sci Eng A* 2006;429:50–7. doi:<https://doi.org/10.1016/j.msea.2006.04.118>.
- [4] Imam M, Ueji R, Fujii H. Microstructural control and mechanical properties in friction stir welding of medium carbon low alloy S45C steel. *Mater Sci Eng A* 2015;636:24–34. doi:<https://doi.org/10.1016/j.msea.2015.03.089>.
- [5] Lienert TJ, Stellwag WL, Grimmer BB, Warke RW. Friction stir welding studies on mild steel. *Weld J* 2003;82:1–9.
- [6] Stringham BJ, Nelson TW, Sorensen CD. Non-dimensional modeling of the effects of weld parameters on peak temperature and cooling rate in friction stir welding. *J Mater Process Technol* 2018;255:816–30. doi:<https://doi.org/10.1016/j.jmatprotec.2017.11.044>.
- [7] Baek S-W, Choi D-H, Lee C-Y, Ahn B-W, Yeon Y-M, Song K, et al. Microstructure and Mechanical Properties of Friction Stir Spot Welded Galvanized Steel. *Mater Trans* 2010;51:1044–50. doi:<https://doi.org/10.2320/matertrans.M2009337>.
- [8] Mazzaferro CCP, Rosendo TS, Tier MAD, Mazzaferro JAE, Dos Santos JF, Strohaecker TR. Microstructural and Mechanical Observations of Galvanized TRIP Steel after Friction Stir Spot Welding. *Mater Manuf Process* 2015;30:1090–103. doi:<https://doi.org/10.1080/10426914.2015.1004699>.
- [9] Mira-Aguiar T, Verdera D, Leitão C, Rodrigues DM. Tool assisted friction welding: A FSW related technique for the linear lap welding of very thin steel plates. *J Mater Process Technol* 2016;238:73–80. doi:<https://doi.org/10.1016/J.JMATPROTEC.2016.07.006>.

## Appendix B

- [10] Andrade DG, Galvão I, Verdera D, Leitão C, Rodrigues DM. Influence of the structure and phase composition of the bond interface on aluminium–copper lap welds strength. *Sci Technol Weld Join* 2018;23:105–13. doi:<https://doi.org/10.1080/13621718.2017.1329078>.
- [11] Andrade DG, Leitão C, Rodrigues DM. Properties of lap welds in low carbon galvanized steel produced by tool assisted friction welding. *J Mater Process Technol* 2018;260:77–86. doi:<https://doi.org/10.1016/J.JMATPROTEC.2018.05.018>.
- [12] British Standards Institution. BS EN 1011-2:2001: Welding — Recommendations for welding of metallic materials — Part 2: Arc welding of ferritic steels 2001.
- [13] Hovanski Y, Santella ML, Grant GJ. Friction stir spot welding of hot-stamped boron steel. *Scr Mater* 2007;57:873–6. doi:<https://doi.org/10.1016/j.scriptamat.2007.06.060>.
- [14] Bakavos D, Chen Y, Babout L, Prangnell P. Material Interactions in a Novel Pinless Tool Approach to Friction Stir Spot Welding Thin Aluminum Sheet. *Metall Mater Trans A* 2011;42:1266–82. doi:<http://dx.doi.org/10.1007/s11661-010-0514-x>.
- [15] Sun YF, Shen JM, Morisada Y, Fujii H. Spot friction stir welding of low carbon steel plates preheated by high frequency induction. *Mater Des* 2014;54:450–7. doi:<https://doi.org/10.1016/j.matdes.2013.08.071>.
- [16] Nelson TW, Rose SA. Controlling hard zone formation in friction stir processed HSLA steel. *J Mater Process Technol* 2016;231:66–74. doi:<https://doi.org/10.1016/j.jmatprotec.2015.12.013>.
- [17] Wei L, Nelson TW. Influence of heat input on post weld microstructure and mechanical properties of friction stir welded HSLA-65 steel. *Mater Sci Eng A* 2012;556:51–9. doi:<https://doi.org/10.1016/j.msea.2012.06.057>.
- [18] Brooks C. Principles of the Austenitization of Steels. 1992.
- [19] Bodnar RL, Hansen SS. Effects of austenite grain size and cooling rate on Widmanstätten ferrite formation in low-alloy steels. *Metall Mater Trans A* 1994;25:665–75. doi:<http://dx.doi.org/10.1007/BF02665443>.

# Appendix C

---

## *Article C*

*Andrade, D. G., Leitão, C., Dialami, N., Chiuementi, M., & Rodrigues, D. M. (2020). Modelling torque and temperature in Friction Stir Welding of Aluminium Alloys. International Journal of Mechanical Sciences, 105725.*

<https://doi.org/10.1016/j.ijmecsci.2020.105725>

### **Modelling torque and temperature in Friction Stir Welding of Aluminium Alloys**

#### **Abstract**

An analysis of the evolution of the torque and of the temperature with welding conditions, in Friction Stir Welding (FSW) of aluminium alloys, was conducted. More precisely, torque and temperature results from a large number of publications, on FSW of AA2xxx, AA5xxx, AA6xxx and AA7xxx aluminium alloys series, were collected. The literature data was complemented with results from a fully coupled thermo-mechanical analysis of the FSW welding process. Coupling the experimental data, from the literature, with numerical simulation results, the individual influence of the main process parameters, tools and plates characteristics, on the torque and on the temperatures in FSW was assessed. It was found that the tool rotational speed govern the heat generation, while the tool dimensions have a very important influence, not only on the heat generation but also on the volume of material being stirred during welding, which is another important factor determining the welding torque. The traverse speed and the base material thickness were also found to be important factors governing the torque during welding. However, the influence of the traverse speed on torque evolution is conditioned by the tool dimensions. A parametric analysis enabling to understand the relation between process parameters, heat generation, heat dissipation and base material stirring, was conducted. Analytical relations, which enable calculating the torque and the temperature, in FSW of aluminium

alloys, were developed based on numerical results and tested using the data from the literature review.

**Keywords:** FSW; Torque; Temperature; Modelling.

### 1. Introduction

The proper application of the Friction Stir Welding (FSW) technique requires the identification of the primary process parameters, i.e. those controlling the heat generation and dissipation, as well as the amount of material flow during welding. Nowadays, since no model relating FSW parameters, machine output data, heat generation and base material stirring during welding is available, any new process application needs to be planned based on trial and error experiments, which according to Magalhães et al. [1] is an important drawback in FSW industrialisation. The development of process control strategies, enabling online quality control, is another critical issue in assisting FSW industrialisation.

Several works analysed the viability of using the tool torque as a process response to the thermo-mechanical conditions developed during FSW. Longhurst et al. [2] proposed the use of the torque, instead of force, as a process control parameter. According to the authors, the control of the torque allows to produce welds without defects and adapt the weld process to the changes in the surface conditions of the workpiece. Bachmann et al. [3] developed a temperature control system based on an analytical torque model. The authors observed that the welds produced with this control system displayed higher quality and higher homogeneity along the weld length. Leitão et al. [4], in FSW of 5xxx and 6xxx aluminium alloys, also found that when welds without defects were produced, the torque registered during welding could be related to the process parameters, following a well defined empirical relationship. However, when using process parameters conducting to the production of welds with defects, no clear relationship could be established between torque evolution and process parameters, since the torque results were almost aleatory. In the same way, Galvão et al. [5], in dissimilar friction stir welding of aluminium and copper, registered that analysing the torque evolution during welding it is possible to determine the formation of defects resulting from the realising of important quantities of intermetallics from under the tool. Kumar et al. [6] also related the variation of the torque during welding with the formation of surface defects. From all these works, it is possible to conclude that understanding and modelling the influence of process parameters on torque can be an important instrument, not only in selecting

process parameters for different applications, but also in controlling the process itself and detecting the formation of welding defects. Other works have also shown the importance of controlling the torque in different production processes such as friction welding [7], rolling [8–10], machining [11,12], among others.

Khandkar et al. [13] and Schmidt et al. [14] proposed the following model

$$M = M_{shoulder} + M_{pin\ surface} + M_{pin\ bottom} \quad (C.1)$$

$$M = \int_{r_p}^{r_s} (r\tau)2\pi r dr + (r_p\tau)2\pi r_p p_l + \int_0^{r_p} (r\tau)2\pi r dr \quad (C.2)$$

to predict the torque ( $M$ ), taking into account the individual contribution of the different tool components and base material properties on the torque values. In the above equations,  $r$  is the radial distance from the centre of rotation to the outer edge of the tool shoulder,  $r_s$  and  $r_p$  are the tool shoulder and pin radius,  $p_l$  is the pin length and  $\tau$  is the shear stress at the tool-base material interface. According to Schmidt et al. [14], the shear stress, which varies according to the contact conditions, i.e. the occurrence of slipping or sticking contact, can be estimated using the equation

$$\tau = (1 - \delta)\tau_{plastic} + \delta\tau_{friction} \quad (C.3)$$

where  $\delta$  is the slipping fraction,  $\tau_{plastic}$  is the shear stress due to the sticking contact and  $\tau_{friction}$  is the shear stress due to the slipping contact. The shear associated with the sticking contact is estimated based on the yield stress of the base material ( $\sigma_y$ ), using the von Mises yield criterion:

$$\tau_{plastic} = \frac{\sigma_y}{\sqrt{3}}. \quad (C.4)$$

The shear stress associated to the slipping contact is estimated using the Coulomb's friction law,

$$\tau_{friction} = \mu_f P \quad (C.5)$$

where  $P$  is the contact pressure and  $\mu_f$  is the friction coefficient between the tool and the workpiece. The previous model requires the knowledge of the slipping fraction and of the friction coefficient, under the thermo-mechanical conditions imposed by the FSW process, which are very difficult to determine. Those uncertainties lead to the development of other analytical models, relating the torque with process parameters.

## Appendix C

Colegrove and Shercliff [15] proposed a model that includes the effect of the traverse ( $v$ ) and rotational ( $\omega$ ) speeds on the torque, which is given by the equation,

$$M = K \frac{v^\alpha}{\omega^\beta} \quad (\text{C.6})$$

where  $\beta$ ,  $\alpha$  and  $K$  are constants. If both  $\alpha$  and  $\beta$  are equal to 1, the previous model displays a linear relation between the torque with the welding heat input. Arbogast and Hartley [16] have used this heat index to represent the welding temperature evolution, where  $\alpha$  and  $\beta$  were taken as 1 and 2, respectively. However, none of the previous models take explicitly into account the influence of the tool geometry and/or the plate thickness, i.e. the amount of material dragged by the tool, on the torque registered during welding. However, in Colegrove and Shercliff [15] it may be assumed that the influence of those parameters on the torque evolution may be taken into account through the constant  $K$ .

It is also important to enhance that the Colegrove and Shercliff [15] model can only predict the evolution of the torque with the process parameters if the values of  $\omega$  and  $v$  are kept inside a certain range. For instance, when  $\omega$  is close to 0,  $M$  values become too high, and for high values of  $\omega$ ,  $M$  becomes 0. Based on this model limitation, Cui et al. [17] developed an alternative model:

$$M = M_0 + M_f e^{-n\omega}. \quad (\text{C.7})$$

In the previous equations,  $M_0$  is the minimum torque value for the different traverse speeds,  $n$  is a decay parameter and  $M_f$  is a pre-exponential parameter. According to this model, the maximum torque value ( $M_{max}$ ), that occurs when  $\omega$  is close to 0, do not vary with the rotational and traverse speeds, being determined by the alloy strength at room temperature.

Pew et al. [18] also reported a strong relation between the welding temperature and the welding power, obtained by multiplying the torque by the tool rotational speed. Tello et al. [19] even developed an analytical model correlating the torque with the welding temperature, given by the equation

$$M = \frac{2\pi k \Delta T_w}{\eta \omega K_0} \quad (\text{C.8})$$

where  $k$  is the thermal conductivity of the base material,  $\eta$  is the efficiency of the process,  $K_0$  is the modified Bessel function of the second kind and 0 order and  $\Delta T_w$  is the difference between the temperature at the shear layer interface and the initial temperature of the base material.



In the present work, experimental values of torque and welding temperatures were collected, for a very large range of experimental conditions, by performing a literature review. The influence of the different FSW process parameters, as well as of the plates thicknesses and tool dimensions, on the torque evolution, was also analysed using numerical simulation. This study allowed to expand the Colegrove and Shercliff [15] model, by adding a larger number of process variables to the equation. In the proposed model, the influence of the tool dimensions, rotational speed, traverse speed and base material thickness, on the stirring volume, welding heat input and torque are taken into account. The analytical equations developed for calculating the torque and welding temperatures in aluminium alloys, were fitted successfully to the very large range of welding conditions obtained from the literature.

## 2. Experimental data

In order to analyse the influence of the process parameters on the FSW torque and temperature, a literature review was performed and a database containing data from more than 300 different friction stir welding tests, in AA2xxx, AA5xxx, AA6xxx and AA7xxx aluminium alloys, in lap and butt joint configurations, was created. The references used to collect the data are presented in Table C.1. The database generated contains not only the tool torque and the maximum welding temperatures ( $T$ ) registered by the different authors, but also the process parameters, i.e. the rotational and traverse speeds, the pin diameter ( $D_p$ ), the pin length ( $p_l$ ) and the shoulder diameter ( $D_s$ ) used in each work.

In Figures C.1a and C.1b it is represented the range of torque and maximum temperature values obtained from the different authors. It should be noted that the temperature measurement position and/or technique varied according to the different works, which may have important influence on the range of results collected. Analysing these figures, in which the results are grouped according to the base material tested, it is possible to conclude that a larger amount of results were available for the AA5xxx and AA6xxx aluminium alloys, since these alloys series are the most common base materials studied in FSW.

In order to take into account the influence of the tool dimensions on the welding outputs, a geometry parameter ( $G$ ) was developed

$$G = \frac{\pi}{4} D_p^2 + \pi D_p p_l + \frac{\pi}{4} (D_s - D_p)^2, \quad (\text{C.9})$$

## Appendix C

which corresponds to the contact area between the tool and the workpiece, as in Khandkar et al. [13] and Schmidt et al. [14]. For complex pin or shoulder geometries,  $G$  was calculated assuming an equivalent cylindrical geometry to determine  $D_p$ . Analysing the  $G$  parameters corresponding to all the tools used by the different authors, which are represented in Figure C.1c, it is possible to conclude that a large range of tool dimensions was tested. More precisely, among the different works,  $D_p$ ,  $p_l$  and  $D_s$  varied in the range of 3 to 16 mm, 1 to 12.5 mm and 10 to 35 mm, respectively. Due to the large variety of process parameters and tool dimensions considered in the database, the values registered for  $M$  varied in the range of 6 to 320 Nm.

**Table C.1** – Experimental works used to construct the database.

AA 2xxx	AA 5xxx	AA 6xxx	AA 7xxx
• Yan et al. [20]	• Peel et al. [21]	• Peel et al. [21]	• Long et al. [22]
• Long et al. [22]	• Long et al. [22]	• Emam and Domiaty [23]	• Emam and Domiaty [23]
• Arora et al. [24]	• Leitão et al. [4]	• Cui et al. [17]	• Upadhyay and Reynolds [25]
• Su et al. [26]	• Quintana and Silveira [27]	• Wade and Reynolds [28]	• Mehta et al. [29]
• Ramanjaneyulu et al. [30]	• Cuellar and Silveira [31]	• Leitão et al. [4]	
	• Costa et al. [32]	• Reza-E-Rabby and Reynolds [33]	
		• Banik et al. [34]	
		• Costa et al. [32]	

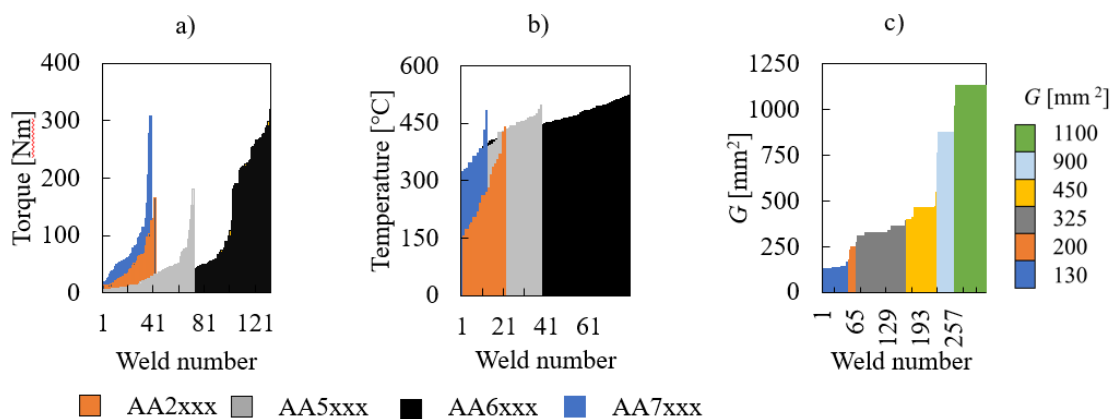


**Figure C.1** – Range of torque (a), temperature (b) and geometry parameter (c) values covered by the database.

The evolution of the torque with  $\omega$ ,  $v$  and  $G$  is shown in Figures C.2a to c, respectively. The figure enables to observe that the rotational and traverse speeds tested

by the different authors vary in the range of 55 to 1700 rpm and 25 to 2000 mm/min, respectively. The effect of the different process parameters on torque was ranked based on the Pearson correlation coefficient ( $R^2$ ). From the figure, it is possible to conclude that both the tool dimensions and the tool rotational speed may be statistically related to the torque, while no important relation between the traverse speed with the torque may be inferred. Comparing the evolution of torque with  $\omega$  and  $G$ , it is also possible to conclude that both have a comparable influence on the torque since the Pearson correlation coefficients are similar.

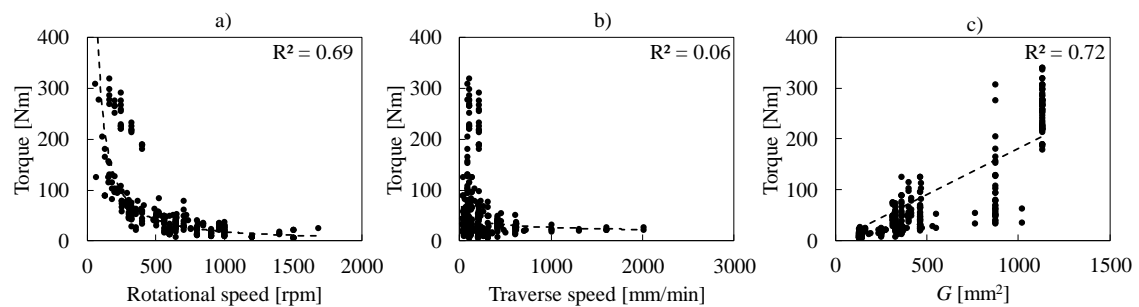


**Figure C.2** – Evolution of torque with the rotational speed (a), traverse speed (b) and geometry parameter (c). Experimental values from the literature.

Based on the previous conclusion, the evolution of torque versus the product  $G\omega$  was analysed and plotted in Figures C.3a, for each base material. In the figure, each colour identifies different torque evolutions corresponding to different levels of  $G$ , established according to Figure C.1c. Analysing the results, it is possible to conclude that irrespective of the base material welded, the torque results may be divided in different curves/trends in accordance to the tool dimensions ( $G$ ). For each curve, the torque decreases exponentially with the increase of the rotational speed. However, meanwhile for the lower  $G$  values a trend line may be plotted fitting almost accurately the decrease of the torque with  $\omega$ , for all the materials, for the larger  $G$  value (green symbols), an important dispersion of results may be observed. This dispersion is shown in more detail in Figure C.3b, where the different traverse speeds used are identified. Analysing Figures C.3a and b it is possible to conclude that the traverse speed only has important influence on the torque values when tools with large dimensions are used. To the authors knowledge no previous work report the same type of conclusion. In order to understand the influence of  $G$ ,  $\omega$  and  $v$  on the torque evolution/values, a parametric analysis was conducted using numerical simulation.

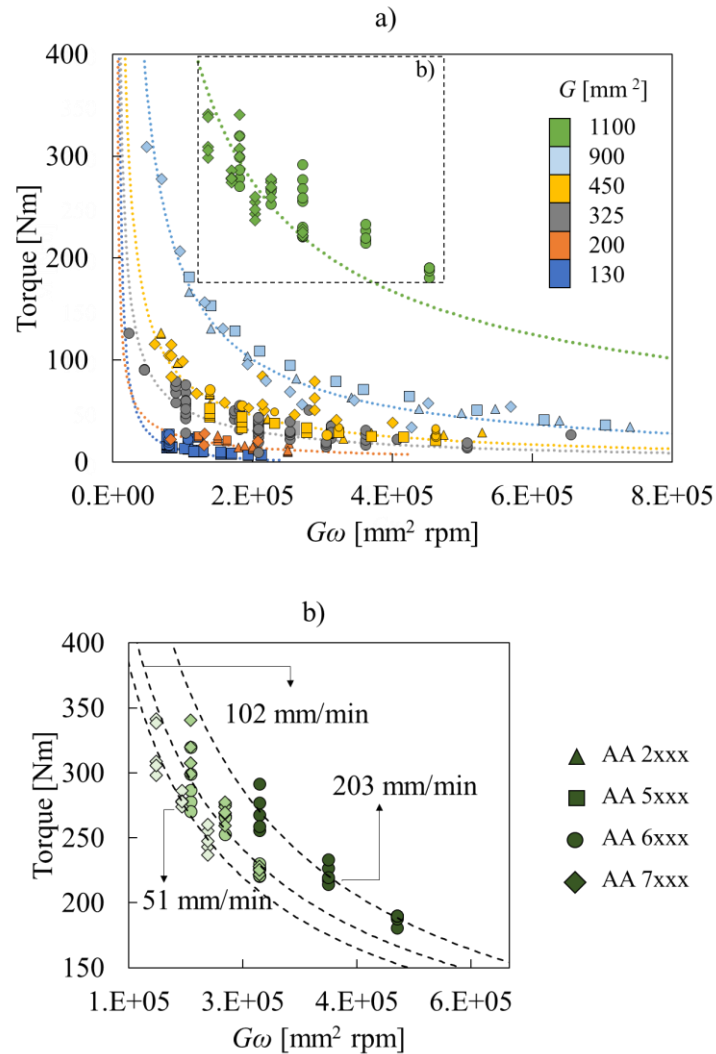


**Figure C.3** – Evolution of torque with the geometry parameter multiplied by the rotational speed ( $G\omega$ ). Experimental values from the literature.

### 3. Numerical Simulation

#### 3.1. Numerical model

The welding mechanisms that govern the tool torque and the welding temperatures were studied through numerical simulation of the FSW process. Three sections including the tool, the stir zone and the workpiece were considered in the finite element model. As in Dialami et al. [35–37], an apropos kinematic framework was adopted consolidating three frameworks for the different weld subdomains. Namely, the tool was modelled in a Lagrangian framework and the stir zone and the rest of the workpiece were described using Arbitrary Lagrangian/Eulerian (ALE) and Eulerian frameworks, respectively. The forces acting on the tool were calculated by appropriate integration of the tractions at the

tool-stirred material interface. In order to save computation time, a fast and accurate two-stage solution strategy was adopted [38]. More precisely, during an initial speed up stage, the steady state solution is calculated by decreasing the thermal capacity of the transient problem. The problem at this phase is defined in a fixed configuration. The periodic stage starts by taking the solution obtained in the first step, as the initial condition, and modelling the movement of the tool. This strategy reduces the FSW simulation time drastically and, at the same time, makes possible the modelling of asymmetrical pin shapes and the visualisation of the material flow during welding. Full sticking contact conditions between the tool and the workpiece were considered in the numerical simulations.

In Figure C.4 is shown the workpiece, the tool geometry and the mesh used in the numerical simulation. The FE mesh contained around 32000 nodes and 180000 tetrahedral elements. The base material plates were modelled with 160 mm width and length. The tool was modelled with a cylindrical pin and a flat shoulder. A more refined mesh was used in modelling the tool/workpiece interface, in order to capture the temperature and strain rate gradients. A convection coefficient ( $h_{conv}$ ) equal to 25 W/m<sup>2</sup>k and a conduction coefficient ( $h_{cond}$ ) equal to 1000 W/m<sup>2</sup>k were used to model the heat exchanges with the surrounding environment and with the backing plate, respectively.

The Norton-Hoff constitutive model was considered to model the base material behaviour,

$$\sigma_{eq}(\dot{\epsilon}_{eq}, T) = \sqrt{3} \mu(T) (\sqrt{3} \dot{\epsilon}_{eq})^{m(T)}, \quad (C.10)$$

where  $\sigma_{eq}$  is the equivalent stress,  $\dot{\epsilon}_{eq}$  the equivalent strain rate and  $\mu(T)$  and  $m(T)$  are the viscosity parameter and exponent, respectively. The base material constitutive properties used in the numerical simulations were taken from Dialami et al. [38]. The remaining governing equations of the numerical model are summarised in Table C.2 and the respective nomenclature in Table C.3. For a detailed explanation of the computational framework, see Ref. [35-38].

## Appendix C

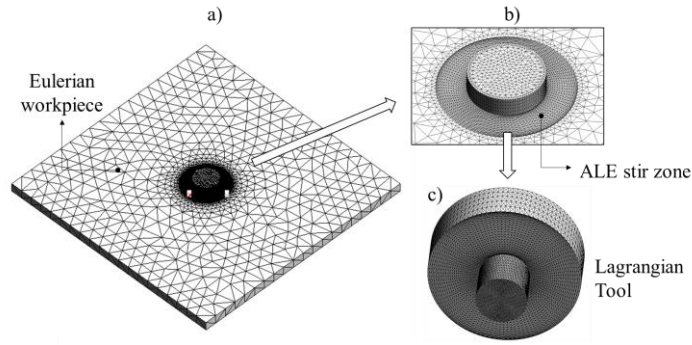


**Figure C.4** – Finite element model: workpiece geometry (a), stirring zone (b) and tool geometry (c).

**Table C.2** – Thermo-mechanical formulation.

<b>Mechanical partition</b>	
$\nabla \cdot s + \nabla p + \rho_0 b = 0$	Momentum balance equation
$\nabla \cdot v = 0$	Continuity equation
$\dot{\varepsilon} = \nabla^s v$	Kinematic equation
$\sigma_{eq} = \sqrt{\frac{3}{2} (s : s)^{1/2}}$	Equivalent stress
$\dot{\varepsilon}_{eq} = \sqrt{\frac{2}{3} (\dot{\varepsilon} : \dot{\varepsilon})^{1/2}}$	Equivalent strain rate
<b>Thermal partition</b>	
$\rho_0 c \left( \frac{1}{\xi} \frac{dT}{dt} + (v - v_{mesh}) \cdot \nabla T \right) - \nabla \cdot (k \nabla T) = D_{mesh}$	Energy balance equation
$D_{mesh} = \theta s : \dot{\varepsilon}$	Viscoplastic dissipation
$q_{conv} = h(T - T_{env})$	Heat convection
$q_{cond} = h_{cond}(T - T_{tool})$	Heat conduction

**Table C.3** – Nomenclature.

$s$	Stress deviator
$p$	Pressure
$\rho_0$	Density in the reference configuration
$b$	Body forces vector per unit of mass
$v$	Velocity field
$\dot{\varepsilon}$	Strain rate
$\mu$	Viscosity parameter
$m$	Viscosity exponent
$c$	Specific heat
$T$	Temperature
$v_{mesh}$	Velocity of the mesh
$k$	Thermal conductivity
$\theta$	Fraction of plastic dissipation
$h_{conv}$	Heat transfer coefficient by convection
$h_{cond}$	Heat transfer coefficient by conduction
$\xi$	Speed-up factor
$T_{env}$	Environmental temperature
$T_{tool}$	Tool temperature

A sensitivity analysis was performed in order to analyse individually the influence of the tool dimensions and of the tool rotational and traverse speeds on the torque and temperature evolution during welding. In the numerical simulations, the tool rotational and traverse speeds were varied in the same range of the welding speeds used in the literature analysed (shown in Figures C.1a and b), i.e.  $\omega$  was varied between 300 to 1500 rpm and  $v$  was varied between 250 to 2000 mm/min. The tool dimensions were also selected based on the experimental works using the data in Figure C.5, where are plotted the shoulder diameters and the base material thicknesses ( $t$ ) for the welding conditions covered by the database. In the figure, it is also plotted, by a dashed line, the shoulder diameter to plate thickness ratios recommended by Zhang et al. [39],

$$D_s = 2.2t + 7.3 \quad (\text{C.11})$$

for obtaining non-defective welds. The range of tool dimensions used in the numerical simulations, which are represented in the figure by the red box, were defined in order to consider two situations: (1) shoulder diameters proportional to the plate thickness, calculated using Eq. C.11, and (2) constant shoulder diameters and varying plate thicknesses. The pin dimensions were established using a  $D_s/D_p$  ratio of 3, as recommended by Prado et al. [40], and a  $p/t$  ratio of 0.85. This way, the thickness of the base material and the shoulder diameter were varied between 1 to 10 mm and 12 to 30 mm, respectively.

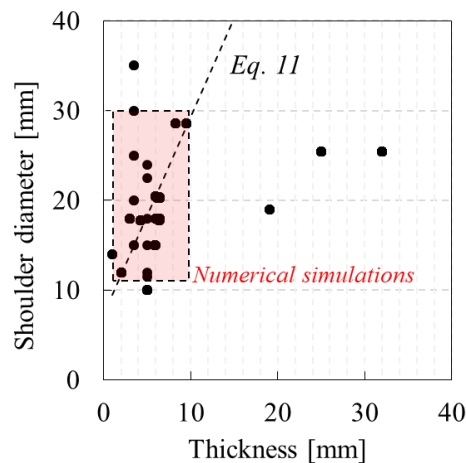


**Figure C.5** – Tool shoulder diameter versus base material thickness, for all the experimental conditions considered in the database and FE modelling.

### 3.2. Numerical results

The influence of the different welding parameters on the torque evolution during welding was analysed by measuring the maximum welding temperatures ( $T$ ) and the amount of material stirred by the tool, quantified by the stirred area ( $SA$ ), and relating it to the average torque registered in the numerical simulation. The procedures used to quantify  $T$  and  $SA$  are exemplified in Figures C.6a and b, where it is shown the temperature and the logarithmic equivalent strain rate distribution, respectively, in the weld cross section, when steady-state conditions are reached during welding. As shown in Figure C.6a the temperature distribution in the welds was asymmetrical, with maximum temperatures registered at the advancing side of the weld. The temperatures used in the analysis were measured in a point located at the outer shoulder radius, at the advancing side of the tool. The amount of material stirred by the tool was evaluated by measuring the area of material with equivalent strain rate higher than zero, as shown in Figure C.6b.

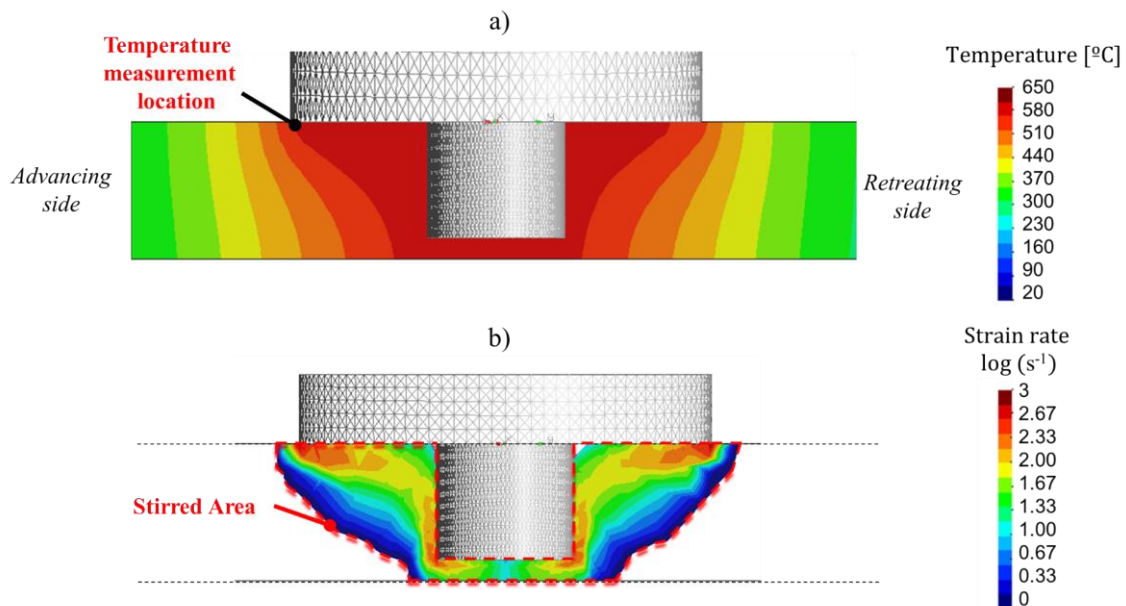


**Figure C.6** – Distribution maps of temperature (a) and logarithmic equivalent strain rate (b). Results for the weld cross section.

In Figure C.7 is shown the evolution of the welding torque (continuous lines) with  $\omega$  and  $G$ . The results were obtained by varying  $\omega$  between 300 and 1500 rpm and using a constant welding speed of 250 mm/min. The  $G$  values were set assuming a proportionality between the shoulder diameter and the plates thickness, i.e. using Eq. C.11 for calculating the shoulder diameter and assuming plate thicknesses varying between 2 to 10 mm.



Analysing the figure, it is possible to conclude that, in accordance to the experimental results, for constant tool rotational speeds, the torque registered in the numerical simulations increased with  $G$ , and for constant  $G$  values, the torque decreased with increasing  $\omega$ . However, the figure also shows that the influence of  $G$  on the torque evolution is more significant for low than for high rotational speeds and, on the other hand, the influence of the rotational speed on the torque evolution is more significant for large than for low values of  $G$ .

The evolution of the torque with  $\omega$  and  $G$  may be explained analysing the evolution of the maximum welding temperatures (coloured map) and of the stirred area (dashed lines) with the process parameters. The colour map in Figure C.7 shows that the welding temperatures increase with the tool rotational speed, irrespective of the tool dimensions, and stabilise in maximum values for large values of  $\omega$  and  $G$ . The stabilisation of the maximum temperature corresponds to the threshold in heat generation which is known to prevent the welding temperature from reaching the base material melting temperature, ensuring solid-state welding in FSW irrespective of the welding parameters. However, meanwhile for low values of  $G$ , the decrease of the torque with  $\omega$ , reported in the previous paragraph, may be attributed to the base material softening with increasing temperatures, for high  $G$  values the same is not true, since high torque values were registered in the very high temperature domain. Therefore, the increase in the torque with  $G$  has to be related to the increase of the amount of material stirred by the tool. Analysing Figure C.7 it is possible to confirm that, independent of  $\omega$ , the stirred area increases with  $G$ , i.e. with increasing tool dimensions and plate thickness. The only exception is in the very high temperature domain, where a gradual decrease in the stirred area with increasing  $\omega$  may be observed.

In Figure C.8 is now shown the evolution of the torque (continuous lines) with the shoulder diameter and thickness for two different values of rotational speed (300 and 900 rpm) and two different values of traverse speed (250 and 1000 mm/min). In these numerical simulations, no proportionality between the tool dimensions and plate thickness was assumed, i.e. in each simulation the  $D_s/t$  ratio was not set according to Eq. C.11, being selected in order to cover the full range of tool dimensions highlighted by the red shaded area in Figure C.5. As shown in Figure C.8, tools with shoulder diameters varying from 12 to 30 mm were tested for the welding of 1 to 9 mm thick plates. Analysing the torque results it is possible to conclude that, irrespective of  $\omega$  and  $v$ , the

## Appendix C

larger torque values were always registered for the simulations corresponding to the tools with the larger shoulder diameter and the larger thicknesses, i.e. for the larger  $G$  values, which is in accordance with the experimental results. Comparing the four plots, it is also possible to conclude that for the same range of shoulder diameters and plate thicknesses, the torque values were higher in the simulations performed with the lower tool rotational speed and/or the higher traverse speed.

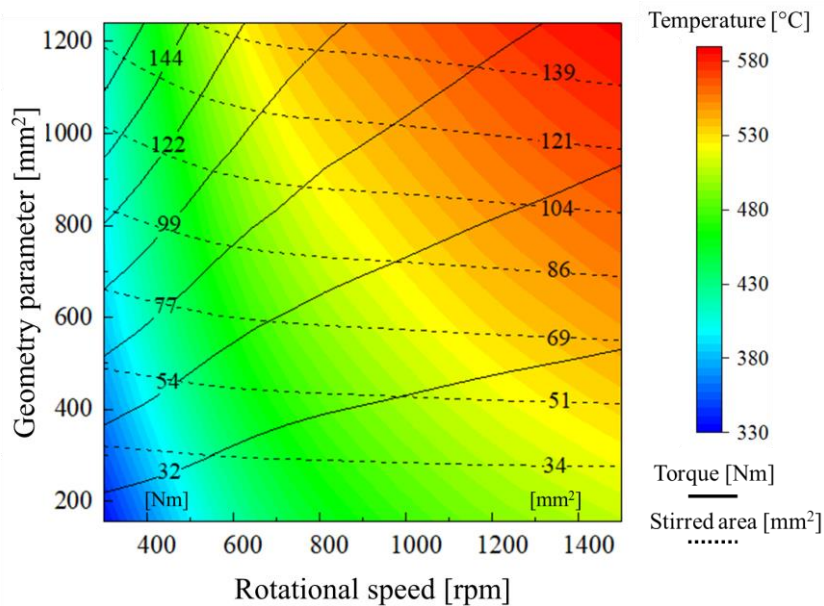


**Figure C.7** – Numerical results concerning the evolution of the torque, temperature and area of material stirred with the rotational speed and geometry parameter.

Analysing in Figure C.8 the evolution of the temperature (coloured maps) with process parameters it is possible to conclude that the welding temperatures were higher in the numerical simulations performed with the higher tool rotational speed of 900 rpm and the higher shoulder diameters. Comparing the temperature values in Figures C.8a and b and Figures C.8c and d it is even possible to conclude that heat generation was determined by the tool rotation, in first, and by the shoulder diameter, in second. On the other hand, the evolution of the temperatures in each graph also enables to conclude that for constant shoulder diameters, the temperature decreases with increasing plate thicknesses. In the same way, the differences in temperature fields between Figures C.8a and c and Figures C.8b and d, also enable to conclude that irrespective of  $D_s$  and  $\omega$ , the temperatures decrease when increasing the traverse speed. Those results point for the

strong influence of  $v$  and  $t$  on the welding temperature, indicating that these parameters should also be considered in the modelling of the torque evolution with process parameters. However, these results also enhance that the influence of  $v$  on the torque and temperature is more pronounced for welding conditions corresponding to large  $G$  values, as already stressed when analysing the results in Figure C.3b.

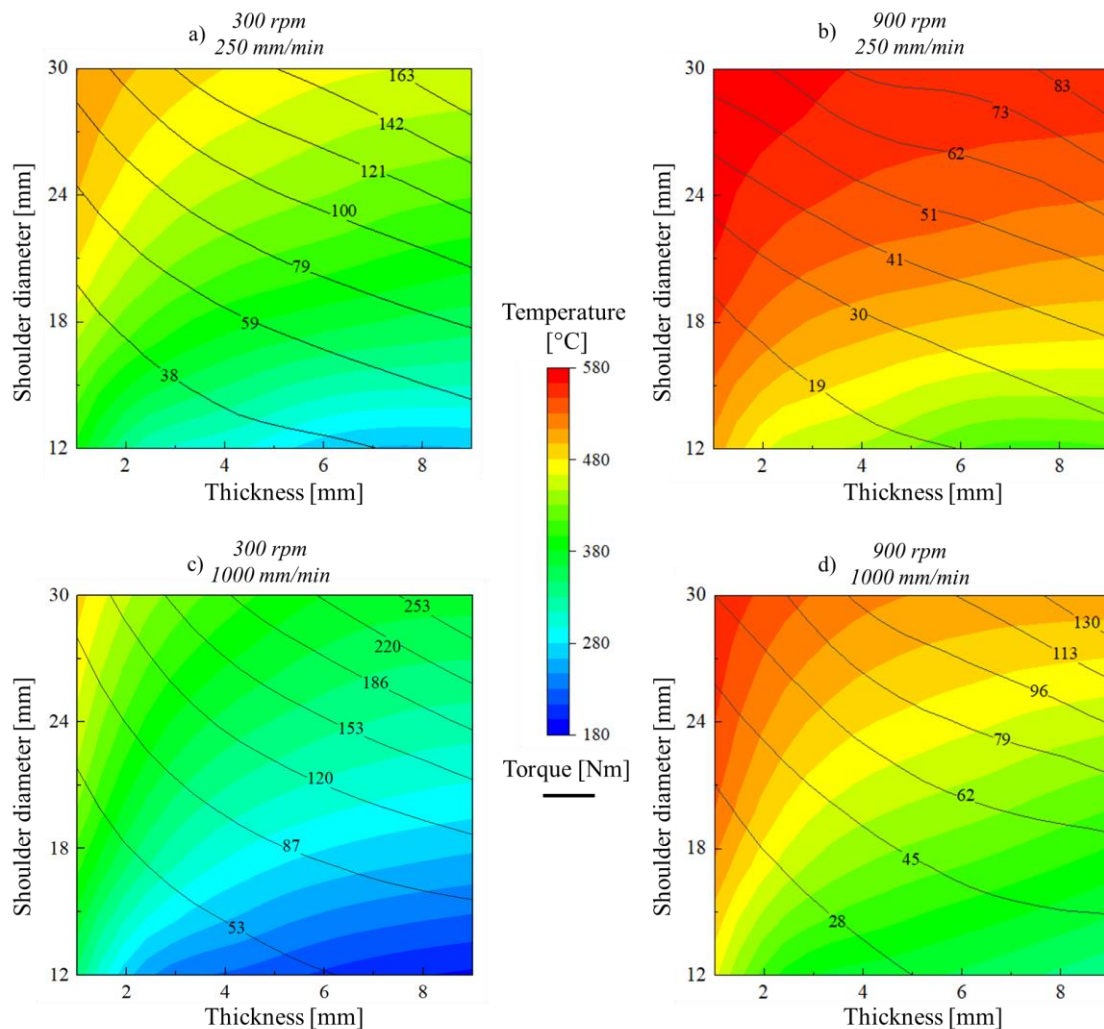


**Figure C.8** – Numerical results concerning the evolution of torque and temperature with the shoulder diameter and thickness, for rotational and traverse speeds of 300 to 900 rpm and 250 to 1000 mm/min, respectively.

#### 4. Modelling torque and temperature

Figures C.9a and b show the evolution of the temperature and torque, respectively, versus the product of the traverse speed by the plate thickness ( $vt$ ). Both parameters were found to be important factors in determining the welding heat dissipation in the previous analysis. In the figure, the results plotted with red squares correspond to the numerical simulations of Figure C.7, in which heat dissipative effects associated with the thickness and the traverse speed were minimised by assuming a constant value for  $v$  and setting the

## Appendix C

shoulder diameter proportional to the plates thickness. The results plotted with circles correspond to the numerical simulations of Figure C.8, in which the shoulder diameters, plate thicknesses and traverse speeds were selected in order to enhance the heat dissipative effects on the temperature fields.

Analysing Figure C.9a, it is possible to conclude that the welding temperature increases with  $G$  and  $\omega$ , which were found as the main factors in heat generation in the previous analysis, but decrease non-linearly with the  $vt$  product. Analysing now the evolution of the torque in Figure C.9b, it is possible to conclude that the torque decreases with  $\omega$ , which is the main factor in heat generation, but increases with  $G$ , which is the main factor in determining the volume of material stirred by the tool. The torque also increases non-linearly with the product ( $vt$ ), due to the important influence of both parameters in heat dissipation, i.e. in decreasing the welding temperature.

From the results in Figure C.9, two coefficients, relating the heat generation and the volume of stirred material, governed by  $\omega$  and  $G$ , respectively, and the heat dissipation, governed by  $v$  and  $t$ , are proposed to be used in quantifying the average torque and the maximum temperature attained during welding. The torque ( $C_M$ ) and temperature ( $C_T$ ) coefficients are given by

$$C_M = \frac{G}{\omega} \sqrt[4]{vt}, \quad (\text{C.12})$$

and,

$$C_T = \frac{G\omega}{\sqrt{vt}}. \quad (\text{C.13})$$

Assuming  $\alpha = 1/4$  and  $K = G\sqrt[4]{t}$ , these coefficients resembles Colegrove and Shercliff [15] model for torque. However, a larger number of process parameters, enabling to better describe the welding conditions in use, is taken into account in the proposed coefficients. In Figure C.10a are plotted the torque values obtained in the numerical simulations performed in current work versus the torque coefficient  $C_M$ . Based on the figure, it is possible to establish a linear relationship between the torque and  $C_M$

$$M = K_M \frac{G}{\omega} \sqrt[4]{vt}. \quad (\text{C.14})$$

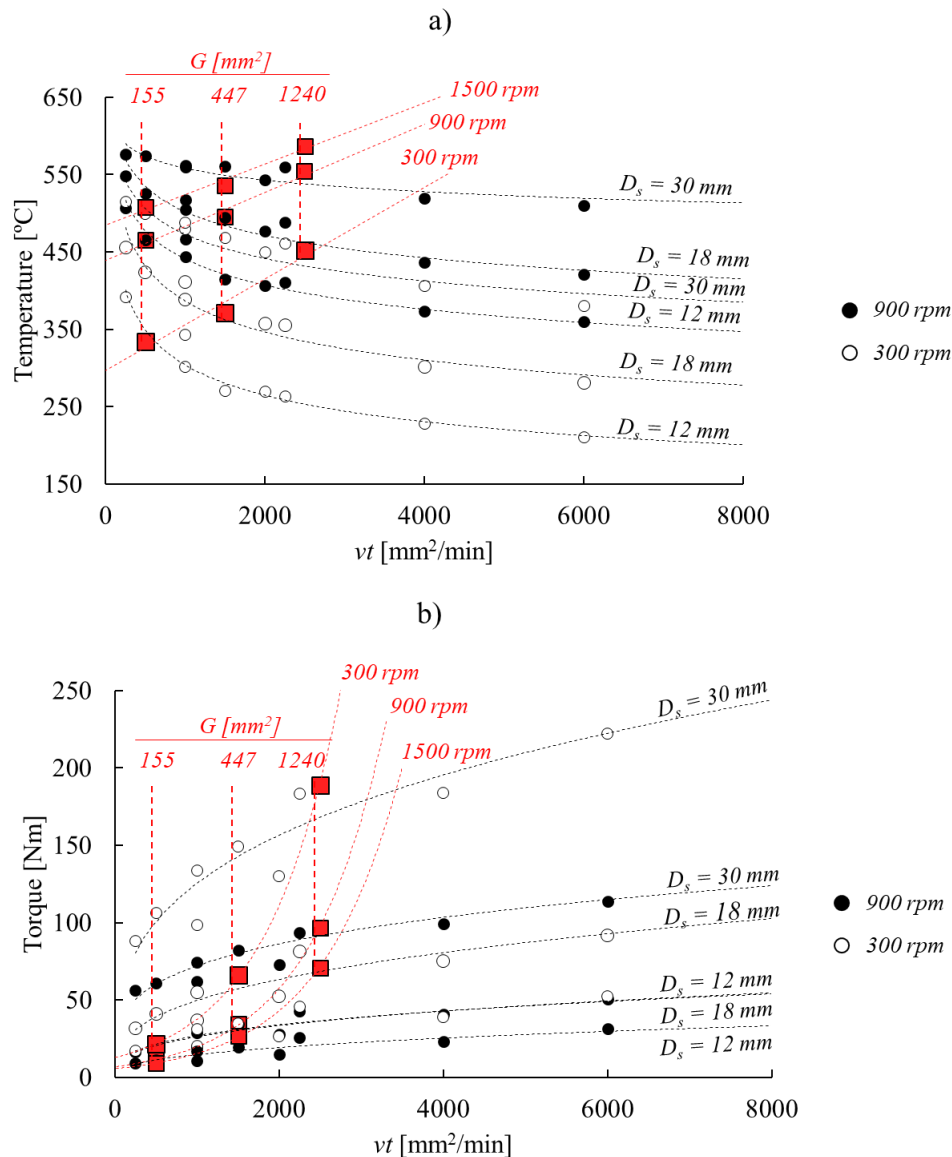


**Figure C.9** – Evolution of temperature (a) and torque (b) with the traverse speed multiplied by the plate thickness ( $vt$ ) when heat dissipative effects are minimized (red squares) and maximized (black circles).

In this equation, a new constant  $K_M$  is introduced, which resembles the  $M_{max}$  in Cui et al. [17] model. According to this author,  $M_{max}$  is determined by the strength of the base materials at room temperature. According to present authors,  $K_M$  is determined by the plastic properties of the alloy being welded, which were already found to determine the weldability in FSW of aluminium alloys in a previous work [41]. For the aluminium alloy tested in the numerical simulation work, fitting the numerical results it was determined that  $K_M = 6$ . The torque values obtained from Eq. C.14 are compared to the torque values obtained in the numerical simulations in Figures C.10b to d. In these figures, the torque results are plotted versus the plate thickness (Figure C.10b), the rotational

## Appendix C

speed (Figure C.10c) and the traverse speed (Figure C.10d). All the figures show that the proposed model satisfactorily reflects the evolution of the average torque with process parameters.

In Figure C.11 the model previsions are now compared with some of the experimental results from the database. Since different aluminium alloys were used by the different authors, and  $K_M$  is a material property related parameter, its value had to be adjusted according to the base material in use in each reference. Analysing the figure, it is possible to conclude that the  $C_M$  coefficient is able to reproduce satisfactorily the torque evolution for the experimental welding conditions covered by the database.

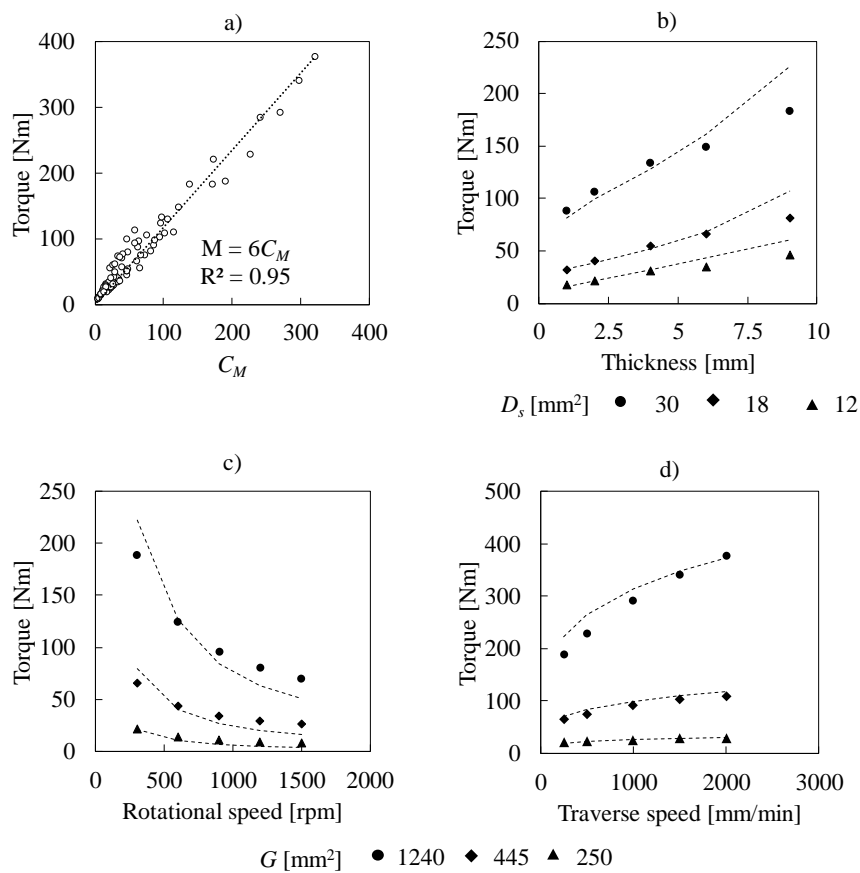


**Figure C.10** – Evolution of the torque values, obtained in the numerical simulations, with the torque coefficient (a). Comparison between the torque values, obtained in the numerical simulations, for different plate thicknesses (b), rotational speeds (c) and traverse speeds (d) with the torque values calculated with Eq. C.14 (dashed lines).

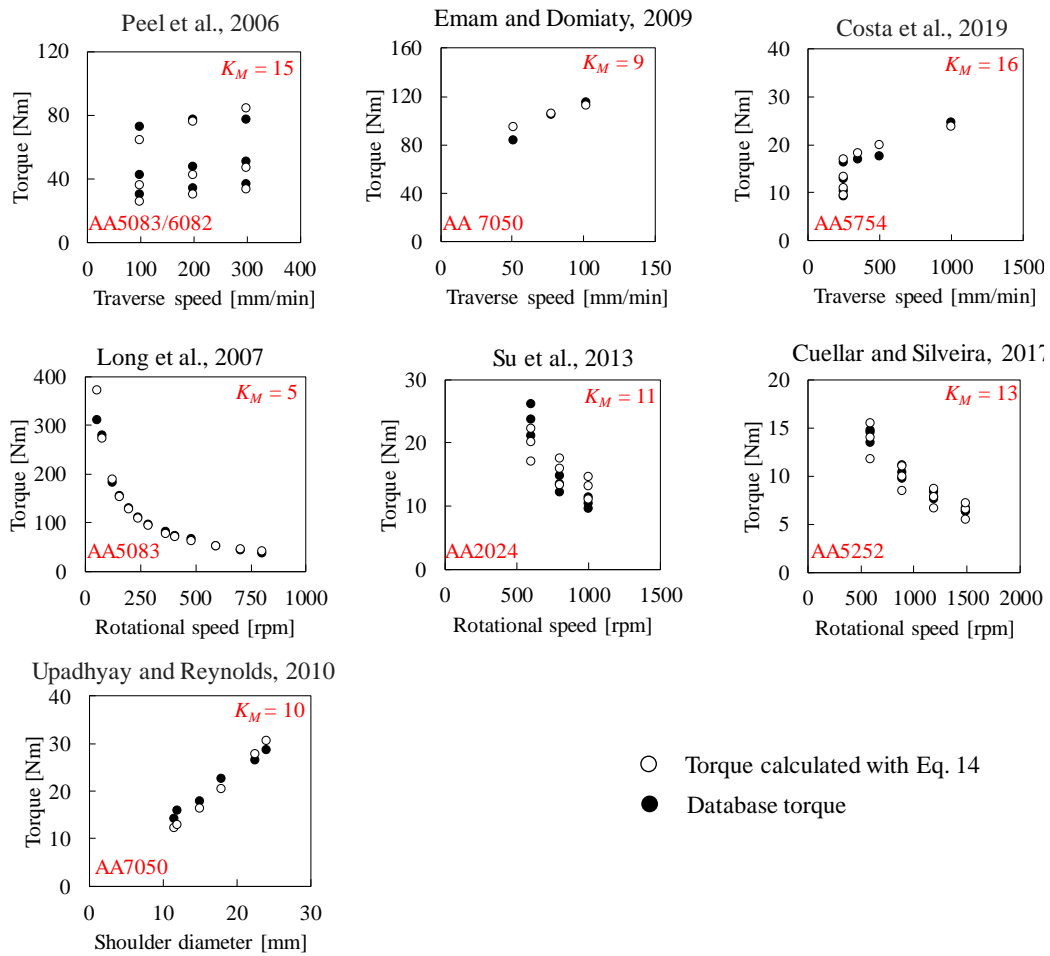


**Figure C.11** – Comparison of the experimental torque results, from the database, with the torque values calculated with Eq. C.14.

In Figure C.12 are now plotted the maximum welding temperatures, obtained in the numerical simulations, versus the temperature coefficient  $C_T$ . The figure clearly shows that for  $C_T$  higher than 20000, the maximum welding temperatures remain constant, indicating that this value of  $C_T$  may be considered as a heat generation threshold indicator for aluminium alloys. As was done for the torque, the  $C_T$  coefficient was correlated with the temperature values, being obtained an equation to predict the welding temperature. So, according to the figure, the temperatures in FSW of aluminium alloys may be estimated as follows:

$$\begin{cases} T = K_T C_T^\phi & \text{for } C_T < 20000, \\ T = 590^\circ\text{C} & \text{for } C_T \geq 20000. \end{cases} \quad (\text{C.15})$$

## Appendix C

In this case,  $K_T$  and  $\varphi$  are related to the base material properties that determine heat generation and dissipation. From the numerical simulation results it was determined that  $K_T = 50$  and  $\varphi = 0.25$ .

In Figure C.13, the temperature values previewed by the model are compared with the experimental results from the database. In order to fit accurately the experimental results, the temperature values computed using Eq. C.15 and making  $K_T = 50$  and  $\varphi = 0.25$ , had to be multiplied by a  $\lambda$  constant. The need for this constant may be associated with important influence of the different experimental techniques, followed by the different authors, in acquiring the maximum temperature, i.e. differences in temperature measurement techniques, differences in the position at which the temperature was measured relative to the weld axis, or even, differences in the backing plate material, among others. Therefore,  $\lambda$  factors were determined individually for each one of the experimental works, due to the strong dependence of the maximum temperatures registered from the experimental apparatus. However, it is important to enhance that no adjustment in  $K_T$  and  $\varphi$  parameters was necessary, indicating that these parameters are constant for all aluminium alloys. In fact, analysing Figure C.13, it is possible to see that despite the different welding conditions, i.e. different shoulder diameters, traverse and rotational speeds, the temperature values computed through  $C_T$  always follow the temperature results obtained by the different authors.

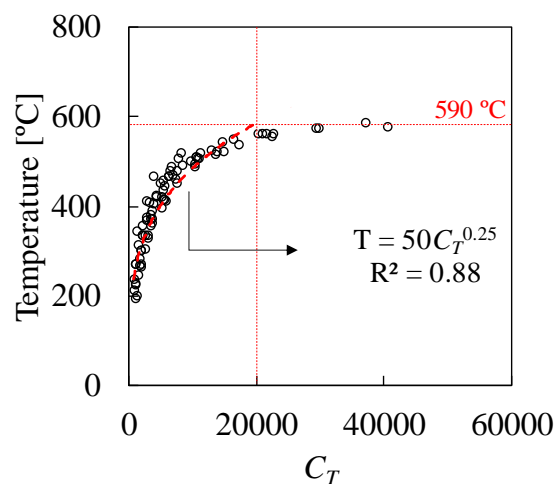


**Figure C.12** – Evolution of the maximum welding temperatures, obtained in the numerical simulations, with the temperature coefficient.



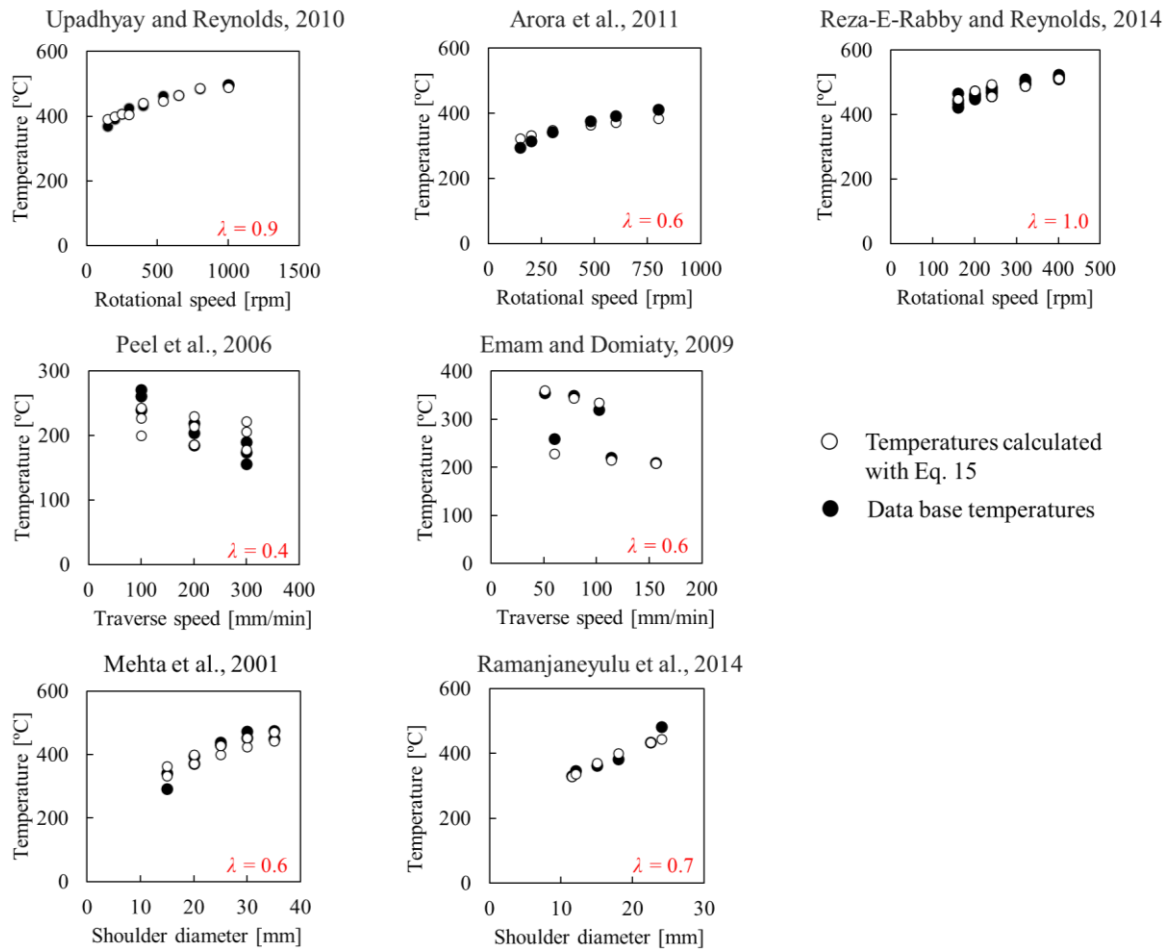


**Figure C.13** – Comparison between the experimental temperature values, from the database, with the temperature values calculated with Eq. C.15.

#### 4. Conclusions

In the present work, the influence of the process parameters, tool dimensions and plate thickness on the torque and welding temperatures was analysed. The main findings of the investigation may be summarized as follows:

- Analytical coefficients ( $C_M$  and  $C_T$ ) were determined for calculating the average torque and the maximum temperature as a function of the welding parameters. The proposed analytical coefficients were validated using experimental results from the literature.
- The tool dimensions and the rotational speed have strong influence on torque and temperature. The proposed coefficients enable to quantify their influence on torque and temperature.

## Appendix C

- The traverse speed and the base material thickness are secondary parameters governing the torque and temperature. Their influence on torque is only noticeable when large shoulder tools are used and/or in thick plates welding.
- $C_M$  and  $C_T$  coefficients enable to quantify the influence of the traverse speed and plates thickness on torque and temperature.
- The temperature coefficient  $C_T$  enables to determine a threshold in the heat generation in FSW, i.e. for  $C_T > 20000$  no temperature increase is expected by changing the welding parameters/conditions.

## References

- [1] Magalhães VM, Leitão C, Rodrigues DM. Friction stir welding industrialisation and research status. *Sci Technol Weld Join* 2018;23:400–9. doi:10.1080/13621718.2017.1403110.
- [2] Longhurst WR, Strauss AM, Cook GE, Fleming PA. Torque control of friction stir welding for manufacturing and automation. *Int J Adv Manuf Technol* 2010;51:905–13. doi:10.1007/s00170-010-2678-3.
- [3] Bachmann A, Gamper J, Krutzlinger M, Zens A, Zaeh MF. Adaptive model-based temperature control in friction stir welding. *Int J Adv Manuf Technol* 2017;93:1157–71. doi:10.1007/s00170-017-0594-5.
- [4] Leitão C, Louro R, Rodrigues DM. Using torque sensitivity analysis in accessing Friction Stir Welding/Processing conditions. *J Mater Process Technol* 2012;212:2051–7. doi:10.1016/j.jmatprotec.2012.05.009.
- [5] Galvão I, Leitão C, Loureiro A, Rodrigues DM. Study of the welding conditions during similar and dissimilar aluminium and copper welding based on torque sensitivity analysis. *Mater Des* 2012;42:259–64. doi:10.1016/j.matdes.2012.05.058.
- [6] Kumar U, Yadav I, Kumari S, Kumari K, Ranjan N, Kesharwani RK, et al. Defect identification in friction stir welding using discrete wavelet analysis. *Adv Eng Softw* 2015;85:43–50. doi:10.1016/j.advengsoft.2015.02.001.
- [7] Jin F, Li J, Liu P, Nan X, Li X, Xiong J, et al. Friction coefficient model and joint formation in rotary friction welding. *J Manuf Process* 2019;46:286–97. doi:https://doi.org/10.1016/j.jmapro.2019.09.008.
- [8] Duan X, Sheppard T. Three dimensional thermal mechanical coupled simulation

- during hot rolling of aluminium alloy 3003. *Int J Mech Sci* 2002;44:2155–72. doi:[https://doi.org/10.1016/S0020-7403\(02\)00164-9](https://doi.org/10.1016/S0020-7403(02)00164-9).
- [9] Shi J, McElwain DLS, Langlands TAM. A comparison of methods to estimate the roll torque in thin strip rolling. *Int J Mech Sci* 2001;43:611–30. doi:[https://doi.org/10.1016/S0020-7403\(00\)00049-7](https://doi.org/10.1016/S0020-7403(00)00049-7).
- [10] Zhang SH, Zhao DW, Gao CR. The calculation of roll torque and roll separating force for broadside rolling by stream function method. *Int J Mech Sci* 2012;57:74–8. doi:<https://doi.org/10.1016/j.ijmecsci.2012.02.006>.
- [11] Oezkaya E, Biermann D. Segmented and mathematical model for 3D FEM tapping simulation to predict the relative torque before tool production. *Int J Mech Sci* 2017;128–129:695–708. doi:<https://doi.org/10.1016/j.ijmecsci.2017.04.011>.
- [12] Lu S, Gao H, Bao Y, Xu Q. A model for force prediction in grinding holes of SiCp/Al composites. *Int J Mech Sci* 2019;160:1–14. doi:<https://doi.org/10.1016/j.ijmecsci.2019.06.025>.
- [13] Khandkar, M. Z. H., Khan, J. A., Reynolds AP. Prediction of temperature distribution and thermal history during friction stir welding: input torque based model. *Sci Technol Weld Join* 2003;8(3):165–74.
- [14] Schmidt H, Hattel J, Wert J. An analytical model for the heat generation in friction stir welding. *Model Simul Mater Sci Eng* 2003;12:143–57. doi:10.1088/0965-0393/12/1/013.
- [15] Colegrove PA, Shercliff HR. Experimental and numerical analysis of aluminium alloy 7075-T7351 friction stir welds. *Sci Technol Weld Join* 2003;8:360–8. doi:10.1179/136217103225005534.
- [16] Arbegast WJ, Hartley PJ. Friction stir weld technology development at Lockheed Martin Michoud Space System--an overview. *ASM Int Trends Weld Res* 1999:541–6.
- [17] Cui S, Chen ZW, Robson JD. A model relating tool torque and its associated power and specific energy to rotation and forward speeds during friction stir welding/processing. *Int J Mach Tools Manuf* 2010;50:1023–30. doi:10.1016/j.ijmachtools.2010.09.005.
- [18] Pew JW, Nelson TW, Sorensen CD. Torque based weld power model for friction stir welding. *Sci Technol Weld Join* 2007;12:341–7. doi:10.1179/174329307X197601.
- [19] Tello, K., Duman, U., Mendez P. Scaling laws for the welding arc, weld

## Appendix C

- penetration and friction stir welding. *Proc. Eighth Trends Weld. Res.*, 2009, p. 172–81.
- [20] Yan J, Sutton MA, Reynolds AP. Process–structure–property relationships for nugget and heat affected zone regions of AA2524–T351 friction stir welds. *Sci Technol Weld Join* 2005;10:725–36. doi:10.1179/174329305X68778.
- [21] Peel MJ, Steuwer A, Withers PJ, Dickerson T, Shi Q, Shercliff H. Dissimilar friction stir welds in AA5083-AA6082. Part I: Process parameter effects on thermal history and weld properties. *Metall Mater Trans A Phys Metall Mater Sci* 2006;37:2183–93. doi:10.1007/BF02586138.
- [22] Long T, Tang W, Reynolds AP. Process response parameter relationships in aluminium alloy friction stir welds. *Sci Technol Weld Join* 2007;12:311–7. doi:10.1179/174329307X197566.
- [23] Emam SA, Domiaty A El. A Refined Energy-Based Model for Friction-Stir Welding. *World Acad Sci Eng Technol* 2009;29:1010–6.
- [24] Arora A, De A, Debroy T. Toward optimum friction stir welding tool shoulder diameter. *Scr Mater* 2011;64:9–12. doi:10.1016/j.scriptamat.2010.08.052.
- [25] Upadhyay P, Reynolds AP. Effects of thermal boundary conditions in friction stir welded AA7050-T7 sheets. *Mater Sci Eng A* 2010;527:1537–43. doi:10.1016/j.msea.2009.10.039.
- [26] Su H, Wu CS, Pittner A, Rethmeier M. Simultaneous measurement of tool torque, traverse force and axial force in friction stir welding. *J Manuf Process* 2013;15:495–500. doi:10.1016/j.jmapro.2013.09.001.
- [27] Quintana KJ, Silveira JLL. Mechanistic models and experimental analysis for the torque in FSW considering the tool geometry and the process velocities. *J Manuf Process* 2017;30:406–17. doi:10.1016/j.jmapro.2017.09.031.
- [28] Wade M, Reynolds AP. Friction stir weld nugget temperature asymmetry. *Sci Technol Weld Join* 2010;15:64–9. doi:10.1179/136217109X12562846839150.
- [29] Mehta M, Arora A, De A, DebRoy T. Tool Geometry for Friction Stir Welding-Optimum Shoulder Diameter. *Metall Mater Trans A* 2011;42:2716–22. doi:10.1007/s11661-011-0672-5.
- [30] Ramanjaneyulu K, Madhusudhan Reddy G, Venugopal Rao A. Role of Tool Shoulder Diameter in Friction Stir Welding: An Analysis of the Temperature and Plastic Deformation of AA 2014 Aluminium Alloy. *Trans Indian Inst Met* 2014;67:769–80. doi:10.1007/s12666-014-0401-z.

- [31] Cuellar, Karen Johanna Quintana Silveira JLL. Analysis of Torque in Friction Stir Welding of Aluminum Alloy 5052 by Inverse Problem Method. *J Manuf Sci Eng* 2017;139:41017–8.
- [32] Costa MI, Leitão C, Rodrigues DM. Parametric study of friction stir welding induced distortion in thin aluminium alloy plates: A coupled numerical and experimental analysis. *Thin-Walled Struct* 2019;134:268–76. doi:<https://doi.org/10.1016/j.tws.2018.10.027>.
- [33] Reza-E-rabby M, Reynolds AP. Effect of tool pin thread forms on friction stir weldability of different aluminum alloys. *Procedia Eng* 2014;90:637–42. doi:10.1016/j.proeng.2014.11.784.
- [34] Banik A, Saha Roy B, Deb Barma J, Saha SC. An experimental investigation of torque and force generation for varying tool tilt angles and their effects on microstructure and mechanical properties: Friction stir welding of AA 6061-T6. *J Manuf Process* 2018;31:395–404. doi:10.1016/j.jmapro.2017.11.030.
- [35] Dialami N, Chiumenti M, Cervera M, Agelet de Saracibar C. An apropos kinematic framework for the numerical modeling of friction stir welding. *Comput Struct* 2013;117:48–57. doi:<https://doi.org/10.1016/j.compstruc.2012.12.006>.
- [36] Dialami N, Chiumenti M, Cervera M, Segatori A, Osikowicz W. Enhanced friction model for Friction Stir Welding (FSW) analysis: Simulation and experimental validation. *Int J Mech Sci* 2017;133:555–67. doi:<https://doi.org/10.1016/j.ijmecsci.2017.09.022>.
- [37] Dialami N, Cervera M, Chiumenti M, Segatori A. Prediction of joint line remnant defect in friction stir welding. *Int J Mech Sci* 2019;151:61–9. doi:<https://doi.org/10.1016/j.ijmecsci.2018.11.012>.
- [38] Dialami N, Cervera M, Chiumenti M, de Saracibar CA, Agelet de Saracibar C, de Saracibar CA, et al. A fast and accurate two-stage strategy to evaluate the effect of the pin tool profile on metal flow, torque and forces in friction stir welding. *Int J Mech Sci* 2017;122:215–27. doi:10.1016/j.ijmecsci.2016.12.016.
- [39] Zhang YN, Cao X, Larose S, Wanjara P. Review of tools for friction stir welding and processing. *Can Metall Q* 2012;51:250–61. doi:10.1179/1879139512Y.0000000015.
- [40] Prado RA, Murr LE, Shindo DJ, Soto KF. Tool wear in the friction-stir welding of aluminum alloy 6061+20 Al 2 O 3 : a preliminary study. *Scr Mater* 2001;45:75–80.

## Appendix C

- [41] Leitão C, Louro R, Rodrigues DM. Analysis of high temperature plastic behaviour and its relation with weldability in friction stir welding for aluminium alloys AA5083-H111 and AA6082-T6. *Mater Des* 2012;37:402–9. doi:<https://doi.org/10.1016/j.matdes.2012.01.031>.

# Appendix D

---

## *Article D*

*Andrade, D. G., Leitão, C., Dialami, N., Chiuementi, M., & Rodrigues, D. M. (2021). Analysis of contact conditions and its influence on strain rate and temperature in Friction Stir Welding. International Journal of Mechanical Sciences, 191, 106095.*

<https://doi.org/10.1016/j.ijmecsci.2020.106095>

### **Analysis of contact conditions and its influence on strain rate and temperature in Friction Stir Welding**

#### **Abstract**

In friction stir welding (FSW), the real contact conditions between the tool and the workpiece and the range of strain rates experienced remain quite unclear. In this work, a coupled 3D thermo-mechanical numerical model was used to simulate the FSW process. A Parametric finite element analysis of the evolution of the contact conditions, strain rates and temperatures with the processing parameters, tool dimensions and base material plastic properties was conducted. The numerical model was able to capture the evolution of the mixed slipping/sticking contact conditions with the welding time and welding parameters. The temperature and strain rate gradients obtained in the numerical simulations were validated with experimental data, by calculating the grain size distribution, in the stirred volume, using the Zener-Hollomon parameter. Full sticking, full slipping and mixed slipping-sticking contact domains were identified in a process parameters chart. It was found that, meanwhile the temperature and the sticking fraction evolve in the same way with the processing parameters, the strain rate is mainly determined by the tool rotation speed, varying from an average of 68 to 324 s<sup>-1</sup>, when the tool rotation speed is increased from 300 to 1200 rpm. The contact conditions and the base material plastic properties were also found to mutually influence the material flow.

## Appendix D

In full sticking contact, high strength materials, with high strain rate sensitivity, may display a similar flow pattern to that of low strength materials. However, coarser and more uniform grain structures may result from the welding of high strength materials, as a result of the narrower range of strain rates experienced during welding combined with high heat input.

**Keywords:** FSW; Contact conditions; Strain rate; Numerical simulation.

### 1. Introduction

During Friction Stir Welding (FSW), the tool rotation and translation movements promote not only the heating by friction of the materials to be joined, but also its plastic deformation under complex loading conditions and variable strain rates. The complex loading conditions, at high temperatures, are responsible for the material flow and for the microstructural phenomena taking place during welding. So the understanding of the mechanisms that govern the plastic deformation during welding, which are conditioned by the contact conditions at the tool/workpiece interface, temperature and strain rates inside the stirred volume, are very important to predict the final microstructure of the welded materials as well as the possibility of defect formation.

Several works attempted to analyse and measure the plastic deformation and the strain rates during FSW, by using different techniques, such as microstructural analysis, tracing materials, analytical models and numerical simulation. Table D.1 summarises the strain rate values reported in the literature, determined using the above described techniques, for different base materials and process conditions. Frigaard et al., 2001 [1], Gerlich et al., 2006 [2] and Gerlich et al., 2007 [3] measured the grain size in the stirring zone to compute the strain rate values by using the Zener–Hollomon parameter, in FSW and Friction Stir Spot Welding (FSSW) of Aluminium alloys. Frigaard et al., 2001 [1] calculated strain rate values, between 1 to 20 s<sup>-1</sup> in FSW of AA6082 and AA7018. According to the authors, these results indicated the occurrence of slipping contact conditions between the tool and the workpiece, since the calculated strain rate values were very low when compared to the angular velocity of the tool. On the other hand, Gerlich et al., 2006 [2] and Gerlich et al., 2007 [3] in FSSW of AA7075 and AA2024, respectively, reported a decrease in the strain rates, from 650 to 20s<sup>-1</sup> and 1600 to 0.6s<sup>-1</sup>, by increasing the rotation speed from 1000 to 3000 rpm and 750 to 3000 rpm, respectively. They attributed these results to the local melting of second phase particles. Masaki et al., 2008 [4] determined the strain rate values during FSW of AA1050, by



comparing the grain size in the welded zone, with the grain size of specimens loaded in plane-strain compression, under various temperatures and strain rates. Using this technique, the authors found that by increasing the rotation speed from 600 to 1200 rpm the strain rates varied between 1.7 to 2.7 s<sup>-1</sup>.

Chen and Cui, 2009 [5] and Liu et al., 2019 [6] determined the strain rates in FSW of A356 alloy and C1100P copper, respectively, by measuring the distortion of tracer materials in the post-weld microstructure. Chen and Cui, 2009 [5] calculated strain rates between 3.5 to 85 s<sup>-1</sup> in the leading side of the tool, while Liu et al., 2019 [6] calculated an average strain rate of 20.8 s<sup>-1</sup> in the band formation zone. The use of tracers has also been used to determine the strain rates and the material flow velocity during FSW by Morisada et al., 2015 [7], Morisada et al., 2015 [8] and Kumar et al., 2018 [9]. Morisada et al., 2015 [7] calculated a maximum strain rate value of almost 15 s<sup>-1</sup>, for the FSW of A1050 at 1000 rpm. Also, in the FSW of A1050 Morisada et al., 2015 [8], observed that the tracing particles rotated around the tool several times, when the rotation speed was higher than 400 rpm, although the angular velocity of the tracer was always lower than the angular velocity of the tool. For rotation speeds lower than 300 rpm the tracing particles stopped rotating around the tool and defects were observed in the weld. Kumar et al., 2018 [9] analysed the influence of the rotation and traverse speeds on the strain rate, in the FSW of a viscoplastic fluid. According to the authors, the tracing particles also rotated several times around the tool pin, up to a maximum velocity of 60 % of the pin angular speed. The tool rotational speed was found to be the main factor governing the strain rates. Increasing the rotation speed from 75 to 425 rpm lead to an increase in the strain rates between 8 and 44 s<sup>-1</sup>.

Chang et al., 2004 [10] and Long et al., 2007 [11] proposed analytical models to estimate the strain rates during welding. Chang et al., 2004 [10] proposed that the strain rates are proportional to the size of the dynamically recrystallised zone and to a fraction of the tool rotational speed, due to the sticking/slipping contact condition at the tool/workpiece interface. Using the previous model, Chang et al., 2004 [10] calculated an increase in the strain rates between 5 to 50 s<sup>-1</sup> by increasing the rotation speed from 180 to 1800 rpm. The Long et al., 2007 [11] model estimated the strain rates by considering the distance that the tool advance in one rotation, as the initial length of the undeformed material. Then, during the tool rotation, this portion of material is stretched in the front side of the pin and is finally compressed in the trailing side of the pin, where it is deposited. Considering the previous model, Long et al., 2007 [11] calculated an increase

## Appendix D

in the average strain rates from 20 to 350 s<sup>-1</sup> by increasing the rotation speed from 544 to 844 rpm, respectively.

Due to the difficulty in calculating the strain rates experimentally during welding, numerical simulation has been used as a tool to determine the strain rates experienced during FSW. Nandan et al., 2006 [12], Nandan et al., 2006 [13] and Nandan et al., 2007 [14] used a three-dimensional viscoplastic model to simulate the FSW of 304 stainless steel, AA6061 aluminium and AISI 1018 steel, respectively. The authors determined maximum strain rate values of 130 s<sup>-1</sup>, 150 s<sup>-1</sup> and 40 s<sup>-1</sup>, for rotation speeds equal to 344, 300 and 450 rpm, respectively. Du et al., 2020 [15] used numerical simulation to model the FSW of AA2017, AA5083 and AA6082 aluminium alloys and computed strain rate values between 23.16 to 434.25 s<sup>-1</sup> by varying the rotation speed from 100 to 1100 rpm. Mukherjee and Ghosh, 2010 [16] used two-dimensional finite-element simulation using ABAQUS, to model the FSW of AA5083 aluminium alloy. The authors concluded that a 0.1 ratio between the base material velocity matrix and the tool velocity, best characterised the material flow. For these conditions, a maximum strain rate of 87 s<sup>-1</sup> was determined. Ammouri et al., 2015 [17] used a 3D thermo-mechanically coupled FE model to simulate the FSW of AZ31B, under different rotation and traverse speeds. The authors observed that the strain rates increased with the rotation and traverse speeds. Although, the rotation speed presented higher influence on the strain rate values than the traverse speed. Sharghi and Farzadi, 2018 [18] used a three-dimensional model based on the computational fluid dynamics to simulate dissimilar welding of AA6061/Al-Mg<sub>2</sub>Si aluminium alloys. The authors computed a maximum strain rate of 975 s<sup>-1</sup> near the top surface of the workpiece at the outer edge of the tool shoulder.

The contact conditions at the tool/workpiece interface are also critical to understand the welding mechanisms occurring during FSW, although they are difficult to study experimentally. In general, the contact conditions are considered to be fully sticking [19–27] or fully slipping [19,24,28–30]. However, this assumption may be restrictive in order to simulate the welding process accurately. Some works have also considered the partial slipping/sticking phenomena during the welding process by prescribing imposed velocity profiles at the tool/workpiece interface [19,24,31–33].

Considering all the works analysed, it is possible to conclude that the calculated strain rate values widely vary, in accordance with the different measurement techniques, process parameters, contact conditions and base materials used. In current work, a coupled three-dimensional thermo-mechanical model was used to simulate the evolution

of the mixed slipping/sticking contact conditions and to compute the strain rates and temperatures during FSW of different base materials under a wide range of parametrically varied welding conditions. The range of temperatures and strain rate obtained in the numerical simulations were validated with experimental results and extrapolated to predict the evolution of the weld microstructure for the different welding conditions tested.

**Table D.1** – Range of strain rates reported in the literature.

Technique	Author	Base Material	Rotation speed [rpm]	Traverse speed [mm/min]	Strain rate [ $s^{-1}$ ]
<b>Microstructural</b>	Frigaard et al., 2001 [1]	AA6082 and AA7018	1500	720	1 - 20
	Gerlich et al., 2006 [2]	AA7075-T6	1000 - 3000	0	20 - 650
	Gerlich et al., 2007 [3]	AA2024 T351	750 - 3000	0	0.6 - 1600
	Masaki et al., 2008 [4]	AA1050	600 - 1200	100	1.7 - 2.7
<b>Tracers</b>	Chen and Cui, 2009 [5]	A356 (Al-7Si-0.3Mg)	740	168	3.5 - 85
	Morisada et al., 2015 [7]	A1050	1000	400	13.4 - 15
	Kumar et al., 2018 [9]	Visco-plastic fluid	75 - 425	50-110	8 - 44
	Liu et al., 2019 [6]	Copper C1100P	800	150	20.8
<b>Analytical model</b>	Chang et al., 2004 [10]	AZ31	180 - 1800	90	5 - 50
	Long et al., 2007 [11]	5083-O, 2219-T87 and 7050-T751	544 - 844	76.2	20 - 350
<b>Numerical</b>	Nandan et al., 2006 [12]	304 Stainless Steel	300	101	130
	Nandan et al., 2006 [13]	AA6061	344	95	150
	Nandan et al., 2007 [14]	AISI 1018	450	25.2	40
	Mukherjee and Ghosh, 2010 [16]	AA5083	1500	50.8	87
	Ammouri et al., 2015 [17]	AZ31B alloy	600 - 2000	75 - 900	34.8 - 122.5
	Sharghi and Farzadi, 2018 [18]	AA6061/ Al-Mg2Si	1120	120	975
	Du et al., 2020 [15]	AA2219, AA5083 and AA6082	150-1302	100-1100	23.16-434.25

## 2. Numerical simulation

### 2.1. The finite element model

The contact conditions and the plastic deformation during FSW were studied by using the three-dimensional numerical model proposed by Chiumenti et al., 2013 [34] and Dialami et al., 2013 [35]. As shown in Figure D.1, the finite element model combines three different kinematic frameworks. The tool is modelled in a Lagrangian framework, while the stirring zone and the base material are modelled using Arbitrary Lagrangian/Eulerian (ALE) and Eulerian frameworks, respectively. In order to reduce the computational time, the two-stage solution strategy proposed by Dialami et al., 2017 [36] was used. The coupled thermo-mechanical problem is solved by using the thermal and mechanical sub-problems, shown in Table D.2, sequentially for each time step. The nomenclature of the variables used is shown in Table D.3. In the numerical model it was assumed that 90% of the plastic dissipation was converted into heat. For a more detailed explanation of the thermal and mechanical models, and of the computational framework, see Refs. [35–39].

**Table D.2** – Formulation.

<b>Mechanical partition</b>	
$\nabla \cdot s + \nabla p + \rho_o b = 0$	Momentum balance equation
$\nabla \cdot v = 0$	Continuity equation
$\dot{\varepsilon} = \nabla^s v$	Kinematic equation
$\sigma_{eq} = \sqrt{\frac{3}{2} (s:s)^{1/2}}$	Equivalent stress
$\dot{\varepsilon}_{eq} = \sqrt{\frac{2}{3} (\dot{\varepsilon}:\dot{\varepsilon})^{1/2}}$	Equivalent strain rate
<b>Thermal partition</b>	
$\rho_o c \left( \frac{1}{\xi} \frac{dT}{dt} + (v - v_{mesh}) \cdot \nabla T \right) - \nabla \cdot (k \nabla T) = D_{mesh}$	Energy balance equation
$D_{mesh} = \theta s:\dot{\varepsilon}$	Viscoplastic dissipation
$q_{conv} = h(T - T_{env})$	Heat convection
$q_{cond} = h_{cond}(T - T_{tool})$	Heat conduction

In this work, a square shaped workpiece with 160×160 mm was used to simulate the base material. The tool was simulated with a flat shoulder with a concentric cylindrical pin. A mesh with 32000 nodes and 180000 tetrahedral elements was used in the numerical simulations. In order to understand the influence of the process parameters on the contact conditions and on the plastic deformation during welding, in the numerical simulations, the rotation ( $\omega$ ) and traverse ( $v$ ) speeds were varied between 300 to 1200 rpm and 250 to

1000 mm/min, respectively. The tool pin diameter ( $D_p$ ), pin length ( $p_l$ ), shoulder diameter ( $D_s$ ) and base material thickness ( $t$ ) were varied in the range of 4 to 10 mm, 1.8 to 8.5 mm, 12 to 30 mm and 2 to 10 mm, respectively. According to Andrade et al., 2020 [40], this range of welding velocities, tool dimensions and plate thicknesses represent the majority of the welding conditions tested in the FSW works on aluminium alloys. As in Andrade et al., 2020 [40], in current work, the influence of the tool dimensions on the welding outputs was considered by using the geometry parameter ( $G$ ), that corresponds to the contact area between the tool and the workpiece,

$$G = \frac{\pi}{4} D_p^2 + \pi D_p p_l + \frac{\pi}{4} (D_s - D_p)^2. \quad (\text{D.1})$$

The combination of base material thicknesses, pin and shoulder diameters and respective geometry parameters used in current numerical simulations are summarised in Table D.4. These combinations were set according to Zhang et al., 2012 [41] and Prado et al., 2001 [42], who recommended a shoulder diameter to plate thickness relation equal to  $D_s = 2.2t + 7.3$  and a shoulder to pin diameter ratio equal to  $D_s/D_p = 3$ , respectively. Also, a pin length to plate thickness ratio equal to 0.85 was considered.

**Table D.3** – Nomenclature.

$s$	Stress deviator
$p$	Pressure
$\rho_0$	Density in the reference configuration
$b$	Body forces vector per unit of mass
$v$	Velocity field
$\dot{\epsilon}$	Strain rate
$c$	Specific heat
$T$	Temperature
$v_{mesh}$	Velocity of the mesh
$k$	Thermal conductivity
$\theta$	Fraction of plastic dissipation
$h_{conv}$	Heat transfer coefficient by convection
$h_{cond}$	Heat transfer coefficient by conduction
$\xi$	Speed-up factor
$T_{env}$	Environmental temperature
$T_{tool}$	Tool temperature

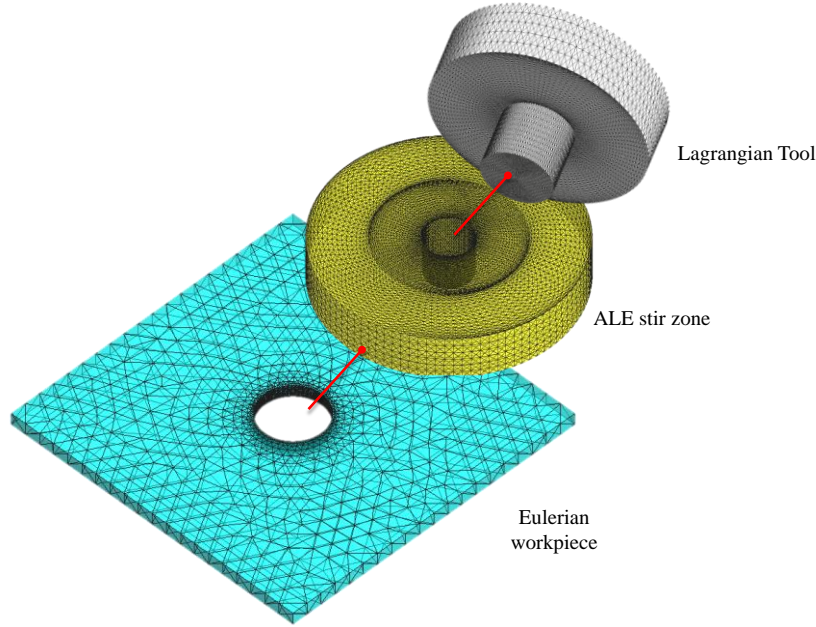


**Figure D.1** – Numerical model and respective subdomains: Lagrangian, ALE and Eulerian zones.

**Table D.4** – Base material thicknesses, shoulder diameters, pin diameters and geometry parameters used in the numerical simulations.

$t$ [mm]	$D_s$ [mm]	$D_p$ [mm]	$G$ [mm <sup>2</sup> ]
2	12	4	134
6	18	6	351
10	30	10	974

## 2.2. The base materials modelled

The base material plastic behaviour was modelled by using the Norton-Hoff constitutive model,

$$\sigma_{eq}(\dot{\epsilon}_{eq}, T) = \sqrt{3}\mu(\sqrt{3}\dot{\epsilon}_{eq})^m, \quad (\text{D.2})$$

where  $\sigma_{eq}$  is the equivalent stress,  $\dot{\epsilon}_{eq}$  is the equivalent strain rate and  $\mu$  and  $m$  are constants that determine the strength and the strain rate sensitivity, respectively, of the base material. Some conceptual materials were considered in this analysis. The base materials stress-strain rate curves, for a constant temperature of 25 °C and 550 °C, and the stress-temperature curves, for a constant strain rate of 100 s<sup>-1</sup>, are represented in Figure D.2a to D.2c. In the figure, the base material represented by the yellow line was modelled using the AA6063-T6 constitutive properties from Dialami et al., 2017 [37]. The constitutive properties of this material, which will be labelled as reference material, were

used in most of the analysis that follows. The remaining base materials used in the analysis were conceptually developed by varying  $\mu$  and  $m$  values, taken from the reference material, from -90 % to +100 % as shown in Figure D.2. The *HSHSRS* and the *HLSRS* are high strength materials ( $\mu = +100\%$ ) but with high ( $m = +100\%$ ) and low ( $m = -90\%$ ) strain rate sensitivity, respectively. On the other hand, the *LSHSRS* and *LLSRS* are low strength materials ( $\mu = -90\%$ ), but with high ( $m = +100\%$ ) and low ( $m = -90\%$ ) strain rate sensitivity, respectively. The conceptual materials were exclusively used in a parametric analysis on the influence of the plastic properties of the base materials on the material flow and temperature and strain rate distributions during welding.

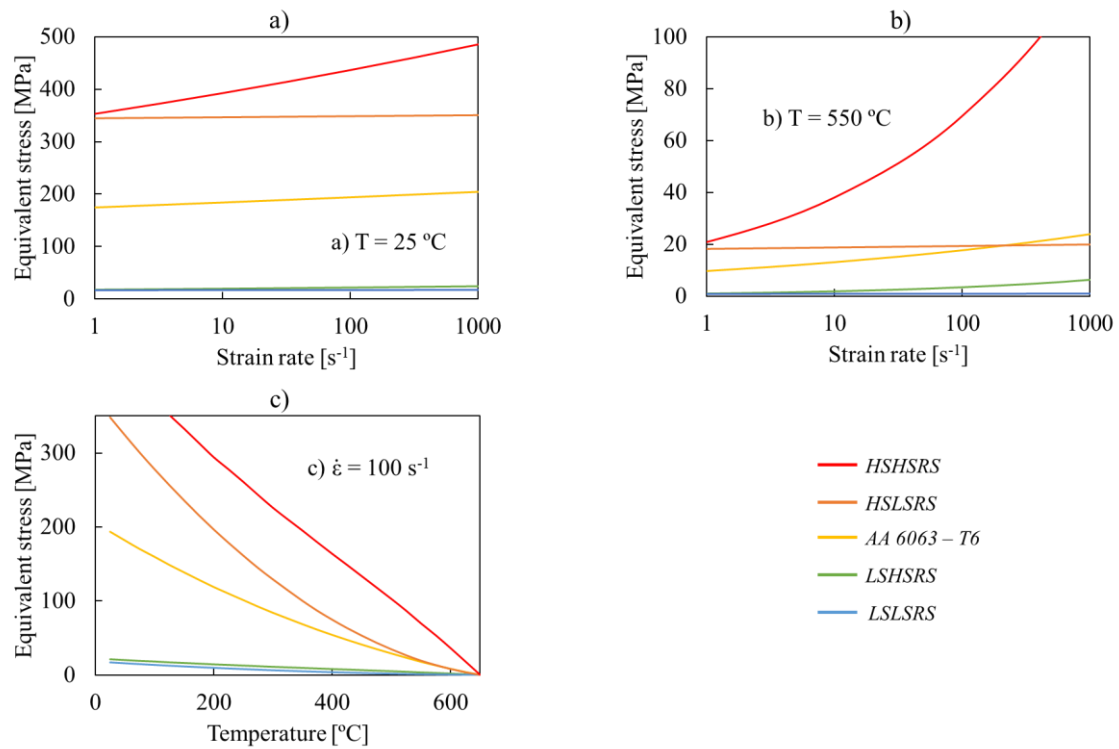


**Figure D.2** – Stress-strain rate curves at a constant temperature of 25 °C (a) and 550 °C (b), and stress-temperature curves at a constant strain rate of 100 s<sup>-1</sup> (c). Labels *HSHSRS* and *HLSRS* denote high strength materials with high and low strain rate sensitivity, respectively. Labels *LSHSRS* and *LLSRS* denote low strength materials with high and low strain rate sensitivity, respectively.

### 2.3. The friction law and the contact conditions

The Norton's friction law was used to model the friction between the tool and the workpiece:

$$\tau = a(T) \|\Delta v_s\|^{q-1} \Delta v_s. \quad (\text{D.3})$$

## Appendix D

In the equation,  $\tau$  is the friction shear stress,  $\Delta v_s$  is the relative sliding velocity between the tool and the workpiece,  $q$  is the sensitivity to the sliding velocity and  $a(T)$  is the consistency parameter given by

$$a(T) = -\alpha_f K(T), \quad (D.4)$$

where  $\alpha_f$  is the friction coefficient and  $K(T)$  is the temperature dependent material consistency. Considering an almost uniform temperature distribution at the contact interface,  $a(T)$  may be assumed constant. In order to ensure that the mixed contact conditions characteristic of the FSW process were accurately captured by the numerical model,  $a(T)$  values ranging from 50 to 500 MPa, were tested. With this selection, several friction coefficients were assumed, since  $K(T)$  is a material related constant. The sensitivity to the sliding velocity parameter was assumed to be constant ( $q = 0.5$ ) [37].

The contact conditions between the tool and the workpiece were assessed by measuring the sticking fraction ( $\delta$ ), as suggested by Schmidt et al., 2003 [43]:

$$\delta = \frac{v_{BM}}{v_{tool}}. \quad (D.5)$$

In the equation,  $v_{BM}$  represents the velocity of the base material, at the tool/workpiece interface, and  $v_{tool}$  is the tool velocity. According to Schmidt et al., 2003 [43], when the sticking fraction is equal to one, it means that the contact is 100 % sticking. When the sticking fraction is equal to zero, it means that the contact is 100 % slipping.

### 3. Analysis of results

#### 3.1. Sensitivity analysis on contact conditions

To determine whether the mixed slipping/sticking contact conditions occurring in the FSW process were accurately captured by the numerical model,  $a(T)$  values ranging from 50 to 500 MPa were tested using the AA6063 alloy constitutive properties for modelling the base material, a tool with geometry parameter  $G = 351 \text{ mm}^2$  and rotation and traverse speeds of 600 rpm and 250 mm/min, respectively.

Figures D.3a and D.3b compare the evolution of the base material and tool velocities, at the tool/workpiece interface, in two different stages of the FSW process, i.e. at the beginning of the welding process ( $t = 0.04\text{s}$ ) and after steady state conditions are reached ( $t = 5\text{s}$ ). The figure refers to numerical simulations performed using  $a(T)$  equal to 90 and 500 MPa. In Figures D.3c and D.3d is compared the distribution of the sticking fraction, calculated using the velocity profiles of Figures D.3a and b, respectively. In the



next, to characterise the contact conditions, the average sticking fraction ( $\delta_{avg}$ ), which is the average of the sticking fraction values calculated for all the points along the tool/workpiece interface, will be used.

Analysing Figure D.3 it is possible to conclude that, in both numerical simulations, the tool and the material velocities increase with the radial distance from the tool axis, and its maximum values are reached at the outer shoulder edge. The figure also enables to conclude that, irrespective of  $a(T)$ , the sticking fraction increased with the welding time, satisfactorily reproducing the evolution of the contact conditions during the dwelling period at the beginning of the FSW process. Although, meanwhile for the simulations performed with  $a(T) = 90$  MPa, slipping contact conditions ( $\delta_{avg} \approx 0$ ) prevailed at the initial stage of the welding process ( $t = 0.04$ s), for the simulations performed with  $a(T) = 500$  MPa, a large sticking fraction ( $\delta_{avg} \approx 0.8$ ) was registered since the beginning of the welding process. When using  $a(T) = 90$  MPa, once steady state conditions were reached ( $t = 5$ s), mixed slipping/sticking contact conditions ( $\delta_{avg} \approx 0.7$ ) were developed. On the other hand, when using  $a(T) = 500$  MPa, full sticking ( $\delta_{avg} \approx 1$ ) prevailed after steady state conditions were reached. Another important difference between the simulations performed with the different consistency parameter values is that, for the simulations ran with  $a(T) = 90$  MPa, the contact conditions were not symmetrical nor uniform along the tool diameter, since the beginning of the welding process, being registered higher sticking fractions at the retreating side (*RS*) than at the advancing side (*AS*) of the tool. However, for the simulations ran with  $a(T) = 500$  MPa, contact conditions were almost symmetrical and became uniform, at the shoulder/workpiece interface, when steady state conditions were reached. For  $a(T) = 90$  MPa, the sticking fraction was also higher, at the inner shoulder diameter, where the tool velocity is lower and the weld nugget is formed due to the dragging of the material from the shoulder influence zone to the pin influence zone [44].

The analysis performed in the previous paragraph showed important differences in contact conditions at the tool/workpiece interface when different values were assumed for the consistency parameter in the Norton friction law. So, in order to better understand the evolution of the contact conditions with  $a(T)$ , and its influence on heat generation and material flow, numerical simulations were ran using a varied range of tool rotational speeds (300, 600, 900 and 1200 rpm), which is the main factor governing the heat generation in FSW [40]. Figures D.4a and D.4b show the evolution of the average sticking

## Appendix D

fraction with  $a(T)$  and with the rotation speed, respectively. In the figures, it is also plotted the evolution of the welding temperature for the range of welding conditions tested. The welding temperature was calculated by computing the average temperature in the stirring volume, i.e. considering only the amount of material with equivalent strain rate values higher than zero.

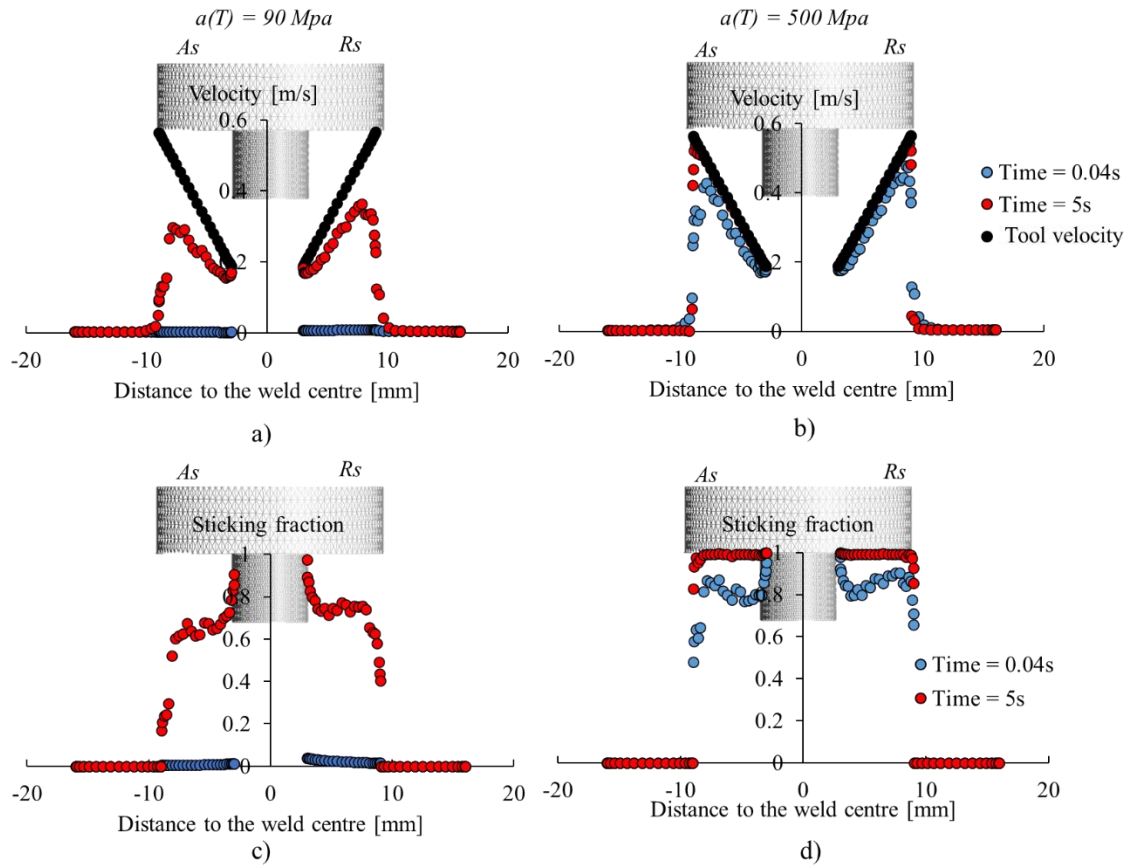


**Figure D.3** – Evolution of the base material velocity at the tool/workpiece interface (a and b) and of the sticking fraction (c and d) with the welding time. Labels  $a(T)$ ,  $As$ ,  $Rs$  denote consistency parameter, advancing side and retreating side, respectively.

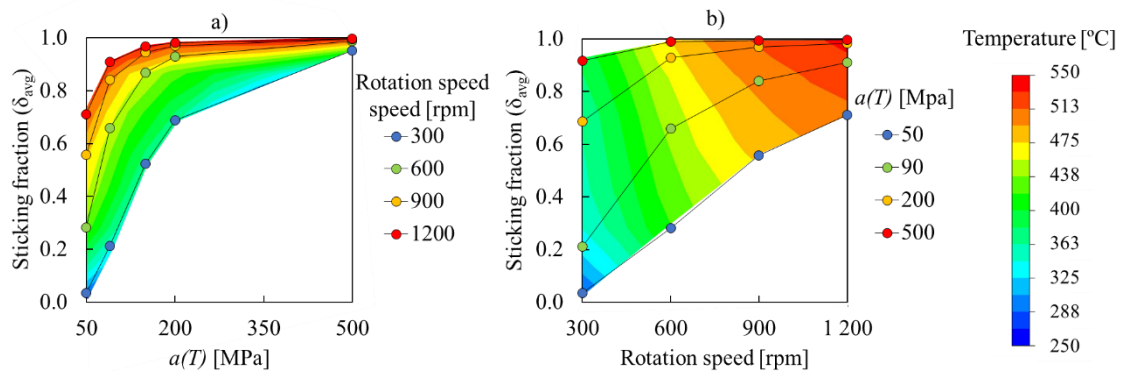


**Figure D.4** – Evolution of the average sticking fraction with  $a(T)$  (a) and rotation speed (b). Label  $a(T)$ , denote consistency parameter.

Analysing Figure D.4a, it can be concluded that, independently of the rotation speed, the sticking fraction increases with  $a(T)$ . For  $a(T) < 200$  MPa, slipping contact and mixed slipping/sticking contact prevail, depending on the tool rotational speed. For  $a(T) > 200$  MPa, sticking contact prevails, mainly for rotation speeds higher than 600 rpm. Figure D.4 also shows that the low temperatures associated with the very low rotation speed of 300 rpm [40], is only simulated for  $a(T) < 100$  MPa and that the transition between prevalent slipping, at low rotation speeds, to prevalent sticking, at high rotation speeds, is only simulated for  $a(T) = 90$  MPa. Based on these results,  $a(T) = 90$  MPa was selected to be used in the analysis of the evolution of the contact conditions and strain rate with process parameters. In the next, this option will be validated based on literature and experimental results.

### 3.2. Validation of the model

A relationship between the process parameters and the welding temperatures was already established and validated by Andrade et al., 2020 [40]:

$$\begin{cases} T = K_T C_T^\varphi & \text{for } C_T < 20000 \\ T = 590^\circ\text{C} & \text{for } C_T \geq 20000 \end{cases} \quad (\text{D.6})$$

In these relationships,  $C_T$  is the temperature coefficient and  $K_T$  and  $\varphi$  are constants related to the base material properties. For aluminium alloys, the authors determined that for  $K_T$  and  $\varphi$  equal to 50 and 0.25, respectively, a good fitting for a large number of literature results was obtained. The temperature coefficient is given by

$$C_T = \frac{G\omega}{\sqrt{vt}}. \quad (\text{D.7})$$

In Figure D.5 the temperature values previewed by the analytical model (Eq. D.6) are compared with the numerical results obtained in the numerical simulations, using  $a(T) = 90$  MPa and considering the constitutive properties of the AA6063 alloy and all welding conditions tested in this work. In the figure is plotted a rectangle in blue, highlighting the evolution of temperature for predominant sliding conditions ( $\delta_{avg} \leq 0.2$ ) and a rectangle in grey highlighting the evolution of temperature results for the simulations in which  $\delta_{avg} > 0.2$ . The correlation between the analytical model and the results of the numerical simulations was assessed by the percentage error between the

## Appendix D

average of the temperatures obtained from the numerical simulations and the average of the temperatures previewed by the model. Analysing the figure, it is possible to conclude that for sticking fraction values lower than 0.2, the percentage error between the analytical and the numerical simulation results is 25 %. For these welding conditions, the temperatures were always inferior to the ones predicted by the analytical model. For sticking fraction values higher than 0.2, the percentage error is inferior to 3 %, showing a very good agreement between the numerical results with the ones predicted by the analytical model. These results indicate that, in the domain of mixed contact conditions and full sticking, the welding temperatures are determined by the process parameters and tool dimensions, but the same is not true when sliding contact prevails, i.e. in a temperature interval conducting to the production of defective welds due to the very low heat input [8,45]. This may be explained assuming that in the full sliding domain an accurate knowledge of the friction coefficient ( $\alpha_f$ ) is required in order to accurately model the FSW process. However, the figure also shows that for mixed sliding/sticking conditions, the temperature may be accurately previewed using  $a(T) = 90$  MPa for modelling the contact conditions.

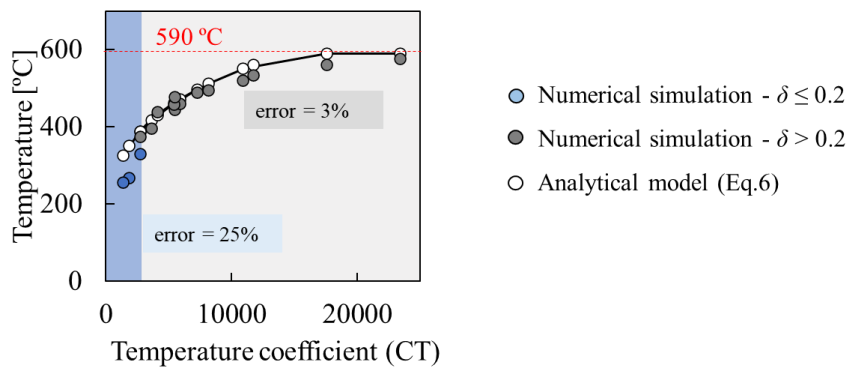


**Figure D.5** – Comparison between the temperature values previewed by the analytical model (Eq. D.6) with the temperatures computed by the numerical results, for  $\delta_{avg} \leq 0.2$  (a) and  $\delta_{avg} > 0.2$  (b). Label  $\delta_{avg}$ , denote average sticking fraction.

In Figure D.6 is now shown a cross-section of a weld performed in the AA6082-T6 aluminium alloy using a tool with a geometry parameter of  $475 \text{ mm}^2$  and rotation and traverse speeds of 500 rpm and 200 mm/min, respectively. In figure are displayed the streamlines representing the material flow around the tool, determined as in Dialami et al., 2014 [46]. The figure also shows the strain rate and temperature distributions, in the

weld cross section, obtained when simulating the experimental FSW test. Despite the room temperature properties of the AA6063-T6, to which refer the material constitutive properties used in the numerical simulations, and the AA6082-T6 alloys, used to fabricate the weld in the figure, are different, at the very high temperatures reached during FSW, it is expected that both alloys display similar properties and that the numerical and experimental results may be compared. Actually, analysing the streamlines in Figure D.6 it is possible to conclude that, for the FSW conditions modelled, the numerical simulations preview that the material is stirred under the shoulder for more than one revolution. This prevision is corroborated by the cross-section of the weld, which displays a large shoulder influence zone. However, in order to better demonstrate the good agreement between the numerical and the experimental results, the grain size (GS) distribution in weld nugget, represented in Figure D.7, was compared with the grain size distribution calculated using the temperature and strain rate distributions displayed in Figure D.6.

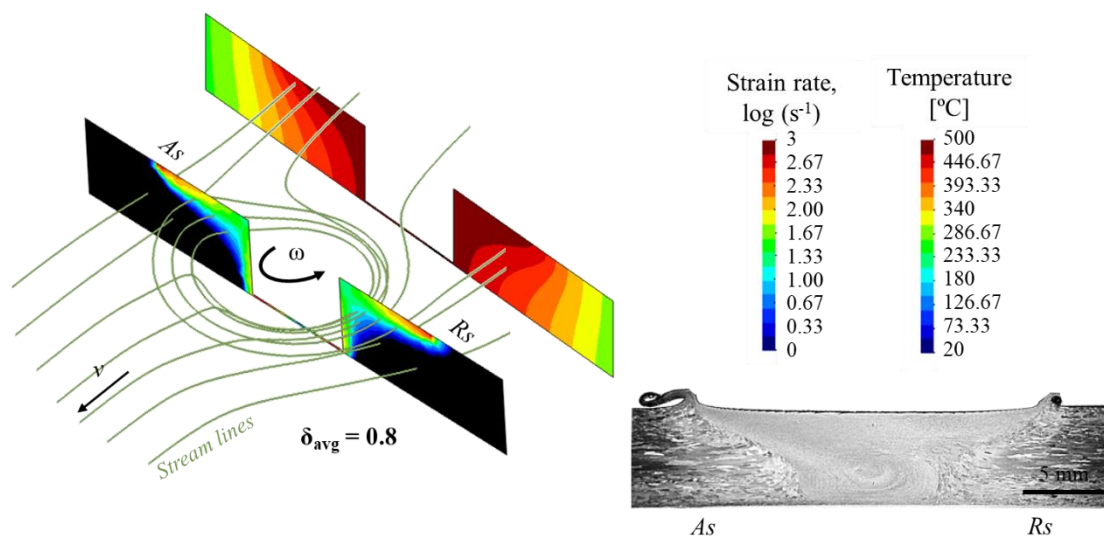


**Figure D.6** – Comparison between the AA6082-T6 weld cross section, with the streamlines, temperature and strain rate fields obtained through numerical simulation. Labels  $A_s$ ,  $R_s$ ,  $\delta$ ,  $\omega$  and  $v$  denote advancing side, retreating side, sticking fraction, rotation speed and traverse speed, respectively.

Figure D.7a and D.7b clearly illustrate the large dispersion in GS inside the nugget of the weld in Figure D.6. According to Leal et al., 2008, [44] the onion rings are composed by intercalated layers, which result from the incorporation of the plasticised material dragged under the shoulder into to the shear layer around the pin. Magnifications of the microstructure in different locations of the nugget, identified by numbers 1 to 5 in Figure D.7a, as well as the grain size distribution in these different regions, are shown in

## Appendix D

Figures D.7c to D.7m. Analysing the figure, it is possible to observe zones with smaller grain size intercalated with zones with larger grain size. As it is known, in thermo-mechanical processes with severe plastic deformation, such as FSW, the dynamic recrystallisation phenomena contribute to the grain refinement in the weld nugget. According to Huang and Logé, 2016 [47], the recrystallisation kinetics and the recrystallised grain size increases with increasing temperatures and decreasing strain rates. The Zener-Hollomon parameter ( $Z$ )

$$Z = \dot{\epsilon} \left( \frac{Q}{RT} \right), \quad (\text{D.8})$$

have been used to incorporate the strain rates ( $\dot{\epsilon}$ ) and the deformation temperature ( $T$ ) into a single parameter by several works in FSW [1-3,10,48]. In the equation,  $R$  is the gas constant and  $Q$  is the deformation activation energy. The relation between the Zener-Hollomon parameter and the recrystallised grain size ( $d$ ) is given by [10,48]

$$\ln(d) = a - b \times \ln(Z), \quad (\text{D.9})$$

where  $a$  and  $b$  are material constants. For the AA6063 aluminium alloy, the activation energy is about 153 kJ/mol [49]. Fitting the experimental results in Figure D.7, it was determined that  $a$  and  $b$  constants are equal to 15 and 0.44, respectively. In Figure D.7b, the grain size distribution obtained from the microstructural analysis is compared with the grain size distribution obtained through the numerical simulation, using Eq. D.8 and 9 and the constants determined using the experimental results. Analysing the figure, it is possible to conclude that the grain size distribution estimated using the numerical results satisfactorily reproduce the experimental ones, which validates the numerical model. The differences between the numerical and experimental results may be explained considering the differences in constitutive properties between the AA6063 and AA6082 alloys, and also, by the fact that no mesh refinement was performed in order to capture more accurately the strain rate and temperature gradients inside the stirred volume.

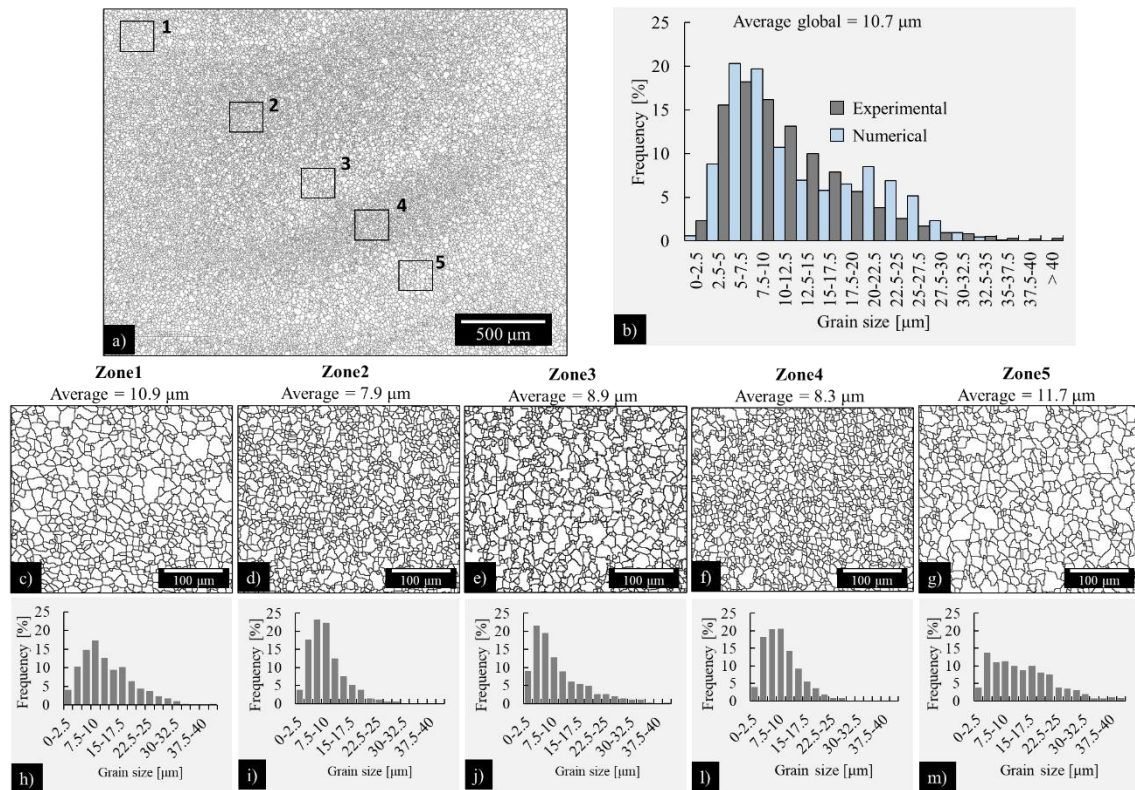


Figure D.7 – Microstructure and grain size distribution in the weld nugget.

### 3.3. Influence of process parameters on the thermo-mechanical conditions

The influence of the process parameters on the contact conditions and strain rates developed during FSW was analysed by performing numerical simulations, using the constitutive properties of the AA6063-T6 alloy, the reference material in this study,  $a(T) = 90$  MPa and varying the tool traverse and rotation speeds, as well as the tool dimensions, represented by the geometry parameter.

In a previous investigation, from the current authors [40], it was already demonstrated that the rotation speed and the tool dimensions were the main factors governing the heat generation in FSW. This conclusion is also illustrated in Figure D.8 of this manuscript, which shows the evolution of the temperature (coloured maps) as a function of  $\omega$  and  $G$ . However, in addition to the temperature evolution, the figure also shows the evolution of the average sticking fraction (discontinuous lines) and of the average strain rate (continuous lines), in the stirred material volume. Analysing the results, it is possible to conclude that in the lower temperatures domain, the sticking fraction evolves with  $G$  and  $\omega$  in the same way as the temperature, i.e. the dashed lines almost follow the contour of the isotherms. On the other hand, in the higher temperatures



## Appendix D

domain, corresponding to large values of  $G$  and  $\omega$ , meanwhile the sticking fraction becomes very high and almost constant, the temperature continues to increase with  $G$  and  $\omega$ . The graphic also shows that the average strain rate also increases with the rotation speed, being mainly determined by this parameter.

Since both the temperature and the strain rate deeply vary in the full sticking domain ( $\delta > 0.9$ ), it is possible to conclude that the increase in heat generation is due to an increase in the adiabatic heat generation associated with the plastic deformation of the stirred material at very high strain rates [50-52]. Actually, Andrade et al., 2020 [40], showed that the volume of the stirred material deeply increases in this domain of temperature and tool dimensions. In order to illustrate the previous assumptions, in Figure 9 are now shown the streamlines that represent the material flow around the tool during welding, together with the distribution of the logarithmic equivalent strain rate in the weld cross-sections, for some of the welding conditions whose temperatures are represented in Figure D.8. Analysing the figure, it is possible to conclude that irrespective of the welding parameters, the computed strain rate values widely vary in the weld cross-section. It is also important to observe that the strain rate values are very high at the outer edge of the tool shoulder, where the tool velocity gradients are higher and a singularity in the strain rate distribution is determined by the numerical model.

Analysing the streamlines for the weld produced with a tool with geometry parameter of  $351 \text{ mm}^2$  and rotation and traverse speeds of 600 rpm and 250 mm/min, respectively, it is possible to conclude that the material is stirred from the advancing to the retreating side, being deposited approximately one pin diameter backwards, relative to the tool translational movement. Increasing the traverse speed from 250 to 1000 mm/min lead to a slight decrease in the sticking fraction, from 0.7 to 0.5, but the material is still extruded around the tool and deposited at the advancing side, in the rear of the tool. The streamlines are nearest to the tool pin, since the stirred volume decreases when increasing the traverse speed. When the rotation speed is decreased to 300 rpm, the sticking fraction reduces to 0.2 and the material does not complete a full rotation around the tool, which is usually associated to the formation of tunnel defects at the advancing side of the tool [8,45]. On the other hand, when increasing the rotation speed to 1200 rpm, it is possible to observe that the material rotated several times under the shoulder, increasing the strain rate in the stirred volume. A similar material flow pattern was registered when welding with rotation and traverse speeds of 600 rpm and 250 mm/min,



respectively, but increasing the tool dimensions from a geometry factor of 351 to 974 mm<sup>2</sup>. Actually, the figure shows that the material only rotated several times around the tool when the contact conditions were close to full sticking ( $\delta_{avg} \geq 0.9$ ), i.e. in the very high temperatures domain of Figure D.8. Another important remark is that the formation of weld defects, due to the absence of proper material stirring, was only previewed when the contact conditions were close to full sliding ( $\delta_{avg} = 0.2$ ).

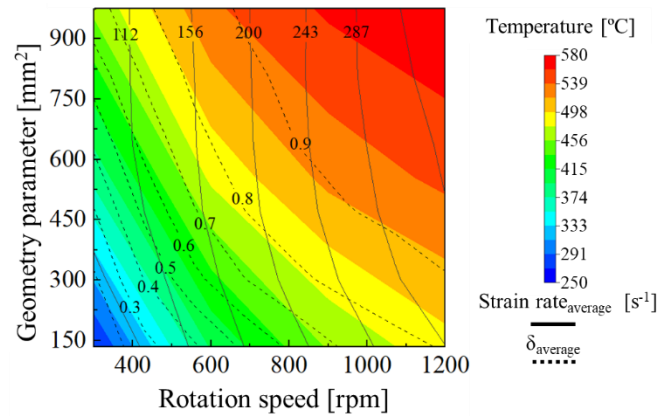


**Figure D.8** – Evolution of the welding temperatures, average strain rate (continuous lines) and average sticking fraction (discontinuous lines) with the rotational speed and geometry parameter.

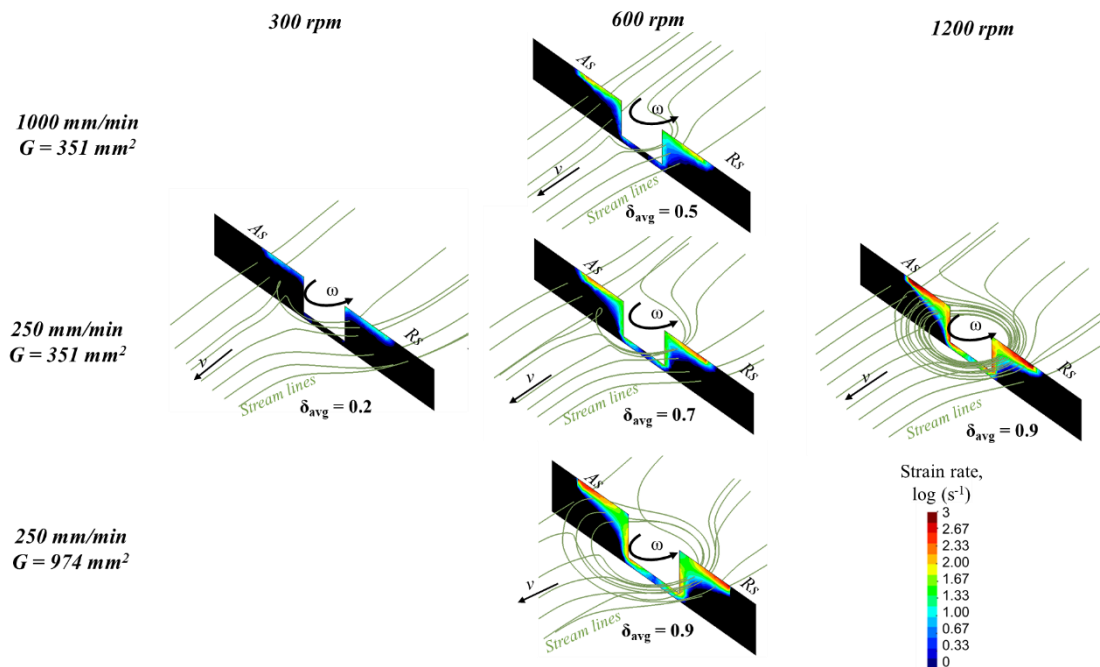


**Figure D.9** – Evolution of the welding streamlines and logarithmic equivalent strain rate maps with the processing parameters. Labels  $A_s$ ,  $R_s$ ,  $\delta$ ,  $\omega$  and  $v$  denote advancing side, retreating side, sticking fraction, rotation speed and traverse speed, respectively.

## Appendix D

In the previous section it was demonstrated that the strain rate and the temperature fields, obtained in the numerical simulation, enabled to preview with reasonable accuracy the grain size distribution in the stirred volume. In this way, in the next, the influence of the process parameters on the thermo-mechanical conditions in FSW will be analysed by plotting the GS distribution, for different welding conditions, versus the strain rate and temperature. In Figure D.10 the evolution of the grain size versus the temperature and strain rate is compared for samples processed with different traverse speeds (Figure D.10a), rotation speeds (Figure D.10b) and geometry parameters (Figure D.10c). In each figure, the largest strain rate values, corresponding to local singularities at the outer tool diameter, were excluded from the graphics, by only considering the values within the strain rate 99th percentile.

Analysing Figure D.10a, where it is represented the grain size distribution for the samples welded with two different traverse speeds and two different tools, using 600 rpm rotation speed, it is possible to conclude that meanwhile the range of strain rates was similar in all welding conditions, the temperature ranges were markedly different. For the smaller tool modelled, was registered a much broader welding temperatures range when welding at 250 mm/min ( $\approx 445\text{ }^{\circ}\text{C}$ ) than when welding at 1000 mm/min ( $\approx 376\text{ }^{\circ}\text{C}$ ). However, when welding at 1000 mm/min, with a tool with much higher shoulder diameter ( $G = 974\text{ mm}^2$ ), the average temperature ( $\approx 480\text{ }^{\circ}\text{C}$ ) was higher than when welding at 250 mm/min and with the lower shoulder diameter tool ( $\approx 445\text{ }^{\circ}\text{C}$ ). The similarities in strain rate values between the three welding conditions are associated to the fact of being used the same rotation speed in all cases, i.e. the main parameter governing the strain rate in the stirred volume. So, based on the analysis of the data provided in the graphic, it can be concluded that the important differences in grain size distribution between the welds performed with the different traverse speeds, and the same tool, results from the differences in temperature distribution, in the two samples, associated to the strong influence of the traverse speed on the heat dissipation during welding [40]. The heat dissipative effect of the high traverse speed was suppressed when the heat generation was increased by increasing the shoulder diameter. This conducted to an important rise in the maximum temperature and the production of a coarse grain microstructure is previewed.

Analysing now Figure D.10b, where is plotted the prevision for the grain size distribution in the nugget of welds performed with different rotation speeds but a constant traverse speed of 250 mm/min and the same tool ( $G = 351\text{ mm}^2$ ), it can be concluded that

the coarser grain sizes were previewed for the sample processed with the highest rotation speed. Actually, the figure once again demonstrates that the maximum strain rate deeply increases when increasing the rotation speed. However, since the temperature follows the same trend, and its influence on grain size prevail over that of the strain rate, the use of high rotation speeds conduct to the production of welds with a large number of coarse grains intercalated with bands of very small grain size. When diminishing the rotation speed, the average grain size diminishes and the grain size distribution becomes narrower.

Finally, Figure D.10c refers to welds produced with constant rotation and traverse speeds of 600 rpm and 250 mm/min, respectively, but with tools with different sizes. The figure shows that, since the same rotation speed was used in all tests, the strain rate range was very similar for all the samples. However, due to the strong influence of the tool dimensions on the heat generation, the temperatures were very different, being much higher for the weld produced with the larger tool. For these welding conditions, an almost uniform coarse grain structure is previewed by the numerical simulation. Figure D.10c also shows the important influence of the tool dimensions on the microstructure, which is illustrated by the results relative to welds performed with the largest tool geometry and a rotation speed of 300 rpm. For this welding condition, larger grain sizes are previewed than when welding with lower tool dimensions but a higher tool rotational speed of 600 rpm. This result is mainly a consequence of the lower strain rates associated with the rotation speed of 300 rpm, since the temperatures are similar to that of welding operations performed with smaller tools but higher rotation speeds.

### **3.4. Influence of base materials plastic properties on the thermo-mechanical conditions**

As previously described, when introducing the base materials modelled, several conceptual materials were generated in order to analyse the influence of the plastic properties of the base materials on the thermo-mechanical conditions developed during FSW. The base materials plastic behaviour, for temperatures of 25 °C and 550°C, and for a constant strain rate of 100 s<sup>-1</sup>, was already represented in Figures D.2a to D.2c. The figure shows that meanwhile for the low strength conceptual materials the strain rate sensitivity has no important influence on the material strength at very high temperatures, for the high strength conceptual material, the strain rate sensitivity may be responsible for a large difference in strength, at high temperatures, relative to lower strength materials and the high strength material with lower strain rate sensitivity. Actually, Figure D.2

## Appendix D

shows that the strength of the HLSRS, at high temperatures and high strain rates, is even lower than that of the reference material, which has much lower strength at room temperature but higher strain rate sensitivity.

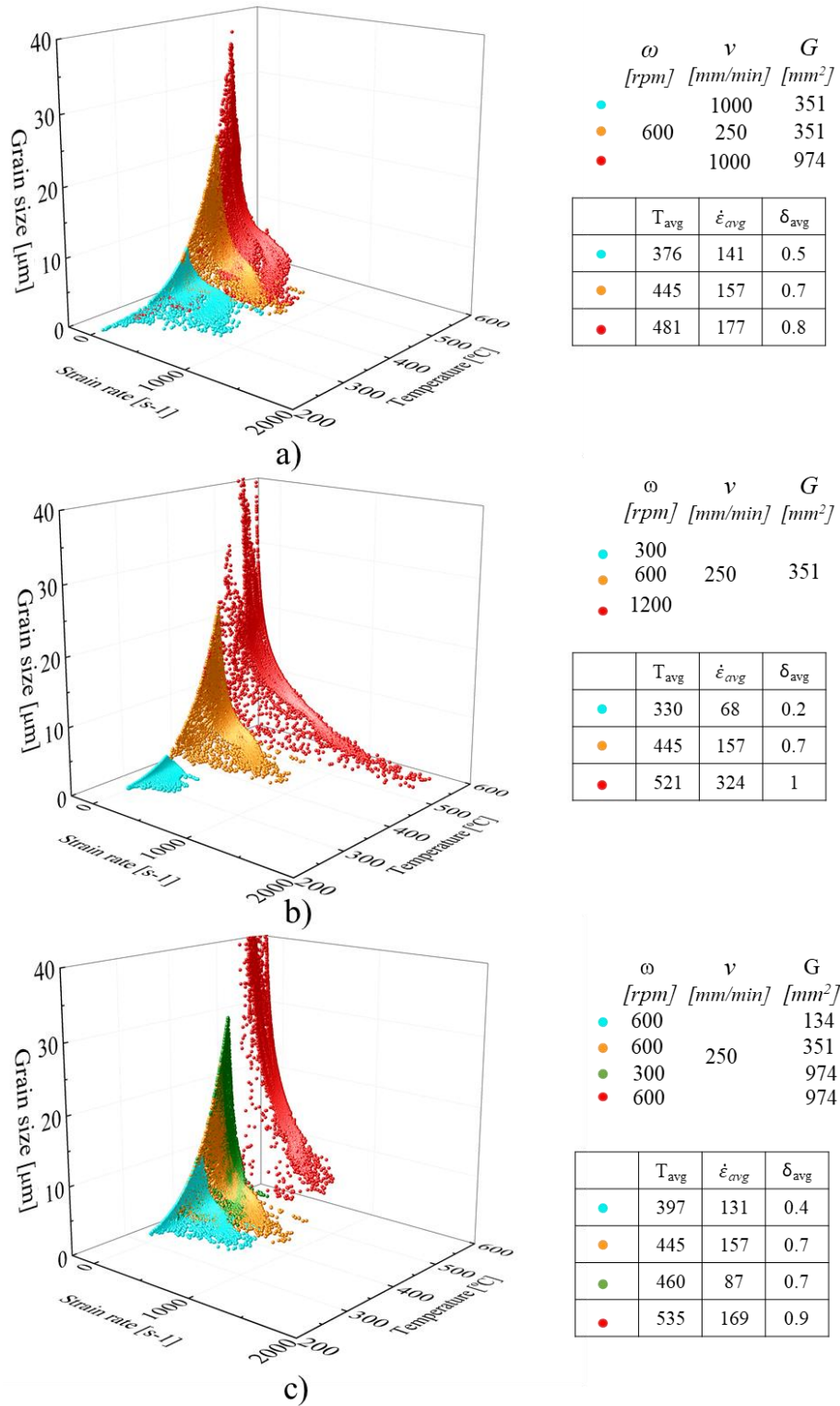


**Figure D.10** – Evolution of the grain size versus the temperature and strain rate for different traverse speeds (a), rotation speeds (b) and geometry parameters (c). Labels  $\omega$ ,  $v$  and  $G$  denote rotation speed, traverse speed and geometry parameter, respectively. Labels  $T_{avg}$ ,  $\dot{\epsilon}_{avg}$  and  $\delta_{avg}$  denote average temperature, strain rate and sticking fraction, respectively.

In Figure D.11 are now compared, for all the base materials modelled, the streamlines that represent the material flow around the tool during welding, as well as the distribution of the logarithmic equivalent strain rate in the weld cross-sections. The results shown in the figure were obtained for constant rotational and traverse speeds of 600 rpm and 250 mm/min, respectively, and a tool with a geometry parameter of 351 mm<sup>2</sup>. A consistency parameter  $a(T) = 500$  MPa was used in order to ensure full sticking contact for all the materials, enhancing the influence of the plastic properties of the base materials on the material flow and heat generation in FSW. Analysing the figure, it is possible to conclude that, in spite full sticking contact was simulated for all the base materials ( $\delta_{avg} = 1$ ), the material flow varied according to the base material plastic properties. In fact, meanwhile for the reference (AA6063-T6) and HSLRS materials, it was previewed that the material is dragged from the advancing to the retreating side of the tool, being deposited approximately one pin diameter backwards, after one revolution, for the low strength materials (LSHSRS and LSLSR) and for the high strength material with high strain rate sensitivity (HSHSRS), it was previewed that the material is stirred under the shoulder for more than one revolution before being deposited in the rear of the tool.

In Figure D.12 are now shown the strain rates and temperatures registered for the different materials once steady state conditions were reached during welding. The figure shows that meanwhile the temperatures reached during welding increase with the materials strength at high temperatures, the strain rates diminish, being lower for the materials with higher strain rate sensitivity. So, from the results in Figure D.12, it is possible to conclude that welds with the coarser and more uniform grain structure result from the welding of high strength materials, as a result of the narrower range of strain rates experienced during welding.

## Appendix D

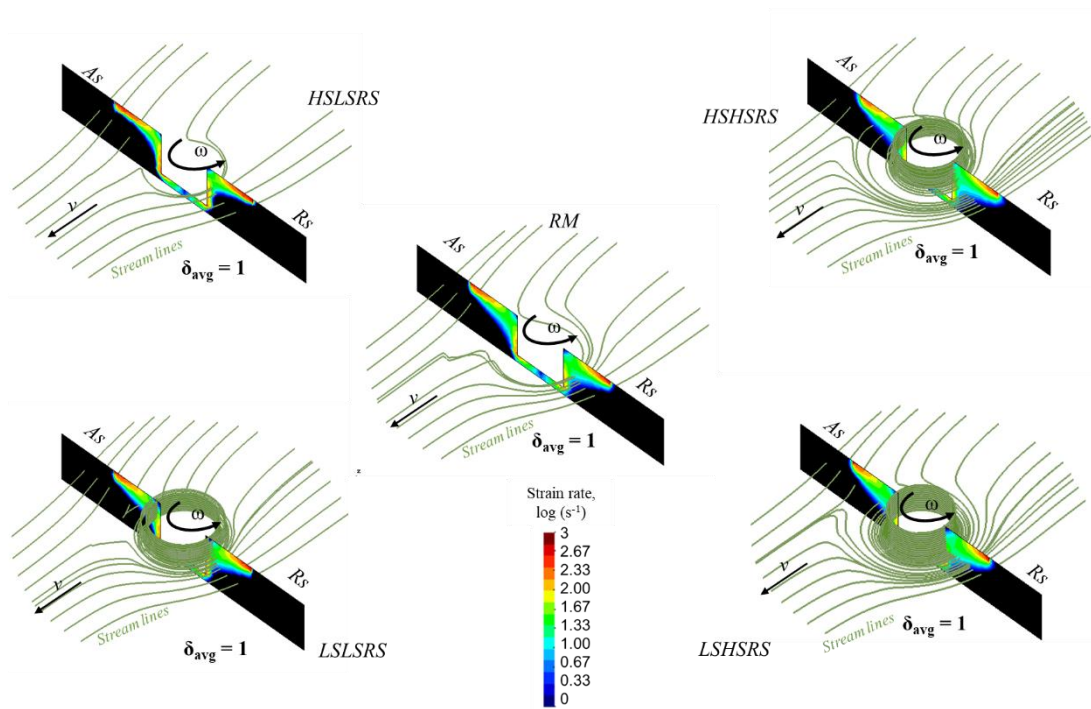


**Figure D.11** – Evolution of the welding streamlines and logarithmic equivalent strain rate with the base material plastic properties. Labels  $A_s$ ,  $R_s$ ,  $\delta$ ,  $\omega$  and  $v$  denote advancing side, retreating side, sticking fraction, rotation speed and traverse speed, respectively.

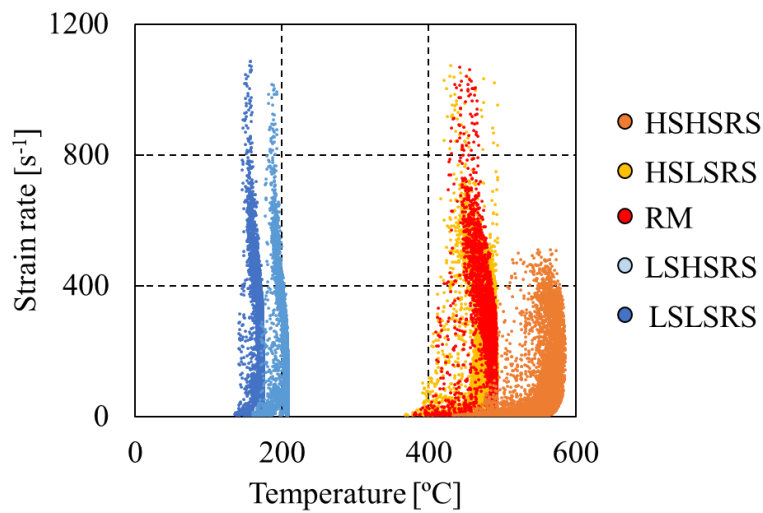


**Figure D.12** – Strain rates and temperatures registered for the different materials. Labels *HSHRS* and *HSLRS* denote high strength materials with high and low strain rate sensitivity, respectively. Labels *LSHRS* and *LSLRS* denote low strength materials with high and low strain rate sensitivity, respectively. Label *RM* denote reference material.

#### 4. Conclusions

In the present work, the influence of the welding velocities, tool dimensions and base material plastic properties on the contact conditions, strain rates and temperatures in FSW was analysed by using a coupled 3D thermo-mechanical numerical model. The following conclusions were reached:

- The numerical model is able to predict the evolution of the contact conditions with the welding time and processing parameters, as well as of capturing the non-uniform contact conditions at the tool/workpiece interface.
- The numerical model is able to predict with satisfactory accuracy the temperature and strain rate gradients in the stirred volume, enabling to calculate the grain size distribution in the stirred volume using the Zener-Hollomon parameter ( $Z$ ). Using this parameter, it was concluded that in order to obtain a refined microstructure in the welds it is advisable the use of small diameter tools, to minimise heat generation, and high rotation speeds, to maximise the strain rate.
- The welding temperatures may be estimated using processing parameters and tool dimensions, for welding conditions corresponding to an average sticking fraction larger than 20%. The highest temperatures are reached for sticking fractions higher than 80% and/or high strength materials.
- The material flow during welding is determined by the base material plastic properties, in first, and by the contact conditions at the tool/workpiece interface, in second. Independently of the base material properties, non-defective welds may be produced when the average sticking fraction is higher than 50%.
- High strength materials with high strain rate sensitivity are more likely to display coarse grain structures than low strength materials, due to the important influence of the plastic properties on the strain rate and heat generation.

#### References

- [1] Frigaard Ø, Grong Ø, Midling OT. A process model for friction stir welding of age hardening aluminum alloys. *Metall Mater Trans A* 2001;32:1189–200. doi:10.1007/s11661-001-0128-4.
- [2] Gerlich A, Avramovic-Cingara G, North TH. Stir zone microstructure and strain rate during Al 7075-T6 friction stir spot welding. *Metall Mater Trans A* 2006;37:2773–86. doi:10.1007/BF02586110.

## Appendix D

- [3] Gerlich A, Su P, Yamamoto M, North TH. Effect of welding parameters on the strain rate and microstructure of friction stir spot welded 2024 aluminum alloy. *J Mater Sci* 2007;42:5589–601. doi:10.1007/s10853-006-1103-7.
- [4] Masaki K, Sato YS, Maeda M, Kokawa H. Experimental simulation of recrystallized microstructure in friction stir welded Al alloy using a plane-strain compression test. *Scr Mater* 2008;58:355–60. doi:https://doi.org/10.1016/j.scriptamat.2007.09.056.
- [5] Chen ZW, Cui S. Strain and strain rate during friction stir welding/processing of Al-7Si-0.3Mg alloy. *{IOP} Conf Ser Mater Sci Eng* 2009;4:12026. doi:10.1088/1757-899x/4/1/012026.
- [6] Liu XC, Sun YF, Nagira T, Ushioda K, Fujii H. Experimental evaluation of strain and strain rate during rapid cooling friction stir welding of pure copper. *Sci Technol Weld Join* 2019;24:352–9. doi:10.1080/13621718.2018.1556436.
- [7] Morisada Y, Imaizumi T, Fujii H. Determination of strain rate in Friction Stir Welding by three-dimensional visualization of material flow using X-ray radiography. *Scr Mater* 2015;106:57–60. doi:https://doi.org/10.1016/j.scriptamat.2015.05.006.
- [8] Morisada Y, Imaizumi T, Fujii H. Clarification of material flow and defect formation during friction stir welding. *Sci Technol Weld Join* 2015;20:130–7. doi:10.1179/1362171814Y.0000000266.
- [9] Kumar R, Pancholi V, Bharti RP. Material flow visualization and determination of strain rate during friction stir welding. *J Mater Process Technol* 2018;255:470–6. doi:https://doi.org/10.1016/j.jmatprotec.2017.12.034.
- [10] Chang CI, Lee CJ, Huang JC. Relationship between grain size and Zener–Holloman parameter during friction stir processing in AZ31 Mg alloys. *Scr Mater* 2004;51:509–14. doi:https://doi.org/10.1016/j.scriptamat.2004.05.043.
- [11] Long T, Tang W, Reynolds AP. Process response parameter relationships in aluminium alloy friction stir welds. *Sci Technol Weld Join* 2007;12:311–7. doi:10.1179/174329307X197566.
- [12] Nandan R, Roy GG, Lienert TJ, DebRoy T. Numerical modelling of 3D plastic flow and heat transfer during friction stir welding of stainless steel. *Sci Technol Weld Join* 2006;11:526–37. doi:10.1179/174329306X107692.
- [13] Nandan R, Roy GG, DebRoy T. Numerical simulation of three-dimensional heat transfer and plastic flow during friction stir welding. *Metall Mater Trans A*



- 2006;37:1247–59. doi:10.1007/s11661-006-1076-9.
- [14] Nandan R, Roy GG, Lienert TJ, Debroy T. Three-dimensional heat and material flow during friction stir welding of mild steel. *Acta Mater* 2007;55:883–95. doi:<https://doi.org/10.1016/j.actamat.2006.09.009>.
- [15] Du Y, Mukherjee T, Mitra P, DebRoy T. Machine learning based hierarchy of causative variables for tool failure in friction stir welding. *Acta Mater* 2020;192:67–77. doi:<https://doi.org/10.1016/j.actamat.2020.03.047>.
- [16] Mukherjee S, Ghosh AK. Flow visualization and estimation of strain and strain-rate during friction stir process. *Mater Sci Eng A* 2010;527:5130–5. doi:<https://doi.org/10.1016/j.msea.2010.04.091>.
- [17] Ammouri AH, Kridli G, Ayoub G, Hamade RF. Relating grain size to the Zener-Hollomon parameter for twin-roll-cast AZ31B alloy refined by friction stir processing. *J Mater Process Technol* 2015;222:301–6. doi:10.1016/j.jmatprotec.2015.02.037.
- [18] Sharghi E, Farzadi A. Simulation of strain rate, material flow, and nugget shape during dissimilar friction stir welding of AA6061 aluminum alloy and Al-Mg<sub>2</sub>Si composite. *J Alloys Compd* 2018;748:953–60. doi:<https://doi.org/10.1016/j.jallcom.2018.03.145>.
- [19] Hamilton C, Dymek S, Sommers A. A thermal model of friction stir welding in aluminum alloys. *Int J Mach Tools Manuf* 2008;48:1120–30. doi:<https://doi.org/10.1016/j.ijmachtools.2008.02.001>.
- [20] Li W, Zhang Z, Li J, Chao YJ. Numerical Analysis of Joint Temperature Evolution During Friction Stir Welding Based on Sticking Contact. *J Mater Eng Perform* 2012;21:1849–56. doi:10.1007/s11665-011-0092-0.
- [21] Yu Z, Zhang W, Choo H, Feng Z. Transient Heat and Material Flow Modeling of Friction Stir Processing of Magnesium Alloy using Threaded Tool. *Metall Mater Trans A* 2012;43:724–37. doi:10.1007/s11661-011-0862-1.
- [22] Colegrove PA, Shercliff HR. 3-Dimensional CFD modelling of flow round a threaded friction stir welding tool profile. *J Mater Process Technol* 2005;169:320–7. doi:<https://doi.org/10.1016/j.jmatprotec.2005.03.015>.
- [23] Chen GQ, Shi QY, Li YJ, Sun YJ, Dai QL, Jia JY, et al. Computational fluid dynamics studies on heat generation during friction stir welding of aluminum alloy. *Comput Mater Sci* 2013;79:540–6. doi:10.1016/j.commatsci.2013.07.004.
- [24] Chen G, Feng Z, Zhu Y, Shi Q. An Alternative Frictional Boundary Condition for

## Appendix D

- Computational Fluid Dynamics Simulation of Friction Stir Welding. *J Mater Eng Perform* 2016;25:4016–23. doi:10.1007/s11665-016-2219-9.
- [25] Robe H, Claudin C, Bergheau J-M, Feulvarch E. R-ALE simulation of heat transfer during friction stir welding of an AA2xxx/AA7xxx joint on a large process window. *Int J Mech Sci* 2019;155:31–40. doi:https://doi.org/10.1016/j.ijmecsci.2019.02.029.
- [26] Ghate ND, Sood A, Srivastava A, Shrivastava A. Ductile fracture based joint formation mechanism during friction stir welding. *Int J Mech Sci* 2020;168:105293. doi:https://doi.org/10.1016/j.ijmecsci.2019.105293.
- [27] Iqbal MP, Tripathi A, Jain R, Mahto RP, Pal SK, Mandal P. Numerical modelling of microstructure in friction stir welding of aluminium alloys. *Int J Mech Sci* 2020;185. doi:10.1016/j.ijmecsci.2020.105882.
- [28] Colligan KJ, Mishra RS. A conceptual model for the process variables related to heat generation in friction stir welding of aluminum. *Scr Mater* 2008;58:327–31. doi:https://doi.org/10.1016/j.scriptamat.2007.10.015.
- [29] Hamilton C, Sommers A, Dymek S. A thermal model of friction stir welding applied to Sc-modified Al–Zn–Mg–Cu alloy extrusions. *Int J Mach Tools Manuf* 2009;49:230–8. doi:https://doi.org/10.1016/j.ijmachtools.2008.11.004.
- [30] Roth A, Hake T, Zaeh MF. An Analytical Approach of Modelling Friction Stir Welding. *Procedia CIRP* 2014;18:197–202. doi:https://doi.org/10.1016/j.procir.2014.06.131.
- [31] Wang H, Colegrove PA, dos Santos JF. Numerical investigation of the tool contact condition during friction stir welding of aerospace aluminium alloy. *Comput Mater Sci* 2013;71:101–8. doi:https://doi.org/10.1016/j.commatsci.2013.01.021.
- [32] Chen G, Ma Q, Zhang S, Wu J, Zhang G, Shi Q. Computational fluid dynamics simulation of friction stir welding: A comparative study on different frictional boundary conditions. *J Mater Sci Technol* 2018;34:128–34. doi:https://doi.org/10.1016/j.jmst.2017.10.015.
- [33] Meyghani B, Wu C. Progress in Thermomechanical Analysis of Friction Stir Welding. *Chinese J Mech Eng* 2020;33:12. doi:10.1186/s10033-020-0434-7.
- [34] Chiumenti M, Cervera M, Agelet de Saracibar C, Dialami N. Numerical modeling of friction stir welding processes. *Comput Methods Appl Mech Eng* 2013;254:353–69. doi:https://doi.org/10.1016/j.cma.2012.09.013.
- [35] Dialami N, Chiumenti M, Cervera M, Agelet de Saracibar C. An apropos kinematic

- framework for the numerical modeling of friction stir welding. *Comput Struct* 2013;117:48–57. doi:<https://doi.org/10.1016/j.compstruc.2012.12.006>.
- [36] Dialami N, Cervera M, Chiumenti M, Agelet de Saracibar C. A fast and accurate two-stage strategy to evaluate the effect of the pin tool profile on metal flow, torque and forces in friction stir welding. *Int J Mech Sci* 2017;122:215–27. doi:<https://doi.org/10.1016/j.ijmecsci.2016.12.016>.
- [37] Dialami N, Chiumenti M, Cervera M, Segatori A, Osikowicz W. Enhanced friction model for Friction Stir Welding (FSW) analysis: Simulation and experimental validation. *Int J Mech Sci* 2017;133:555–67. doi:<https://doi.org/10.1016/j.ijmecsci.2017.09.022>.
- [38] Dialami N, Chiumenti M, Cervera M, de Saracibar C, Ponthot JP. Material flow visualization in Friction Stir Welding via particle tracing. *Int J Mater Form* 2015;8:167–81. doi:10.1007/s12289-013-1157-4.
- [39] Dialami N, Cervera M, Chiumenti M, Segatori A. Prediction of joint line remnant defect in friction stir welding. *Int J Mech Sci* 2019;151:61–9. doi:<https://doi.org/10.1016/j.ijmecsci.2018.11.012>.
- [40] Andrade DG, Leitão C, Dialami N, Chiumenti M, Rodrigues DM. Modelling torque and temperature in Friction Stir Welding of Aluminium Alloys. *Int J Mech Sci* 2020:105725. doi:<https://doi.org/10.1016/j.ijmecsci.2020.105725>.
- [41] Zhang YN, Cao X, Larose S, Wanjara P. Review of tools for friction stir welding and processing. *Can Metall Q* 2012;51:250–61. doi:10.1179/1879139512Y.0000000015.
- [42] Prado RA, Murr LE, Shindo DJ, Soto KF. Tool wear in the friction-stir welding of aluminum alloy 6061+20 Al 2 O 3 : a preliminary study. *Scr Mater* 2001;45:75–80.
- [43] Schmidt H, Hattel J, Wert J. An analytical model for the heat generation in friction stir welding. *Model Simul Mater Sci Eng* 2003;12:143–57. doi:10.1088/0965-0393/12/1/013.
- [44] Leal RM, Leitão C, Loureiro A, Rodrigues DM, Vilaça P. Material flow in heterogeneous friction stir welding of thin aluminium sheets: Effect of shoulder geometry. *Mater Sci Eng A* 2008;498:384–91. doi:<https://doi.org/10.1016/j.msea.2008.08.018>.
- [45] Arbogast WJ. A flow-partitioned deformation zone model for defect formation during friction stir welding. *Scr Mater* 2008;58:372–6.

## Appendix D

- doi:<https://doi.org/10.1016/j.scriptamat.2007.10.031>.
- [46] Dialami N, Chiumenti M, Cervera M, Agelet de Saracibar C, Ponthot JP, Bussetta P. Numerical Simulation and Visualization of Material Flow in Friction Stir Welding via Particle Tracing BT - Numerical Simulations of Coupled Problems in Engineering. In: Idelsohn SR, editor., Cham: Springer International Publishing; 2014, p. 157–69. doi:10.1007/978-3-319-06136-8\_7.
- [47] Huang K, Logé RE. A review of dynamic recrystallization phenomena in metallic materials. *Mater Des* 2016;111:548–74. doi:<https://doi.org/10.1016/j.matdes.2016.09.012>.
- [48] Zhao Y-H, Lin S-B, He Z-Q, Wu L. Microhardness prediction in friction stir welding of 2014 aluminium alloy. *Sci Technol Weld Join* 2006;11:178–82. doi:10.1179/174329306X84391.
- [49] Sheppard T, Jackson A. Constitutive equations for use in prediction of flow stress during extrusion of aluminium alloys. *Mater Sci Technol* 1997;13:203–9. doi:10.1179/mst.1997.13.3.203.
- [50] Fonda RW, Knipling KE. Texture development in friction stir welds. *Sci Technol Weld Join* 2011;16:288–94. doi:10.1179/1362171811Y.0000000010.
- [51] Balachandran S, Mishra RS, Banerjee D. Friction stir processing of a metastable  $\beta$  titanium alloy in  $\beta$  and  $\alpha+\beta$  phase fields. *Mater Sci Eng A* 2020;772:138705. doi:<https://doi.org/10.1016/j.msea.2019.138705>.
- [52] Jia B, Rusinek A, Pesci R, Bahi S, Bernier R. Thermo-viscoplastic behavior of 304 austenitic stainless steel at various strain rates and temperatures: Testing, modeling and validation. *Int J Mech Sci* 2020;170:105356. doi:<https://doi.org/10.1016/j.ijmecsci.2019.105356>.

# Appendix E

---

## *Article E*

*Andrade, D. G., Sree Sabari, S., Leitão, C., M., & Rodrigues, D. M. (2021). Influence of the galvanized coating thickness and process parameters on heat generation and strength of steel spot welds. Thin-Walled Structures, 160, 107401.*

<https://doi.org/10.1016/j.tws.2020.107401>

### **Influence of the galvanized coating thickness and process parameters on heat generation and strength of steel spot welds**

#### **Abstract**

The influence of galvanized coating thickness, tool diameter and rotational speed, on the thermal cycles, in spot welding of steels produced by Tool Assisted Friction Welding (TAFW), a Friction Stir Spot Welding (FSSW) related technique, is analysed. To study the influence of the galvanized coating thickness on the thermal cycles, thin steel plates commonly used in steel construction and automotive industry with galvanized coatings of varied thicknesses were welded. Numerical simulation of the welding process was conducted to understand some of the physical phenomena observed experimentally. Numerical and experimental results were compared and discussed. The influence of the above described parameters, as well as of the dwell time, on welds strength was also characterized. The results showed that steel spot welds with very good mechanical strength can be obtained in very short process cycle times. It was also determined that the welds strength was much higher than the minimum strength recommended for resistance spot welds (RSW).

**Keywords:** TAFW, FSSW, Steel, Heat generation, Numerical modelling, Mechanical strength.

### 1. Introduction

Spot welds are mainly used in the automotive, shipbuilding, railway and aeronautical industries, in thin plates joining, due to the very fast processing cycle time, in comparison to riveted joining. Spot welding also ensures low plates distortion, in comparison to seam welding. At the industrial level, steels spot welding is mainly done by Resistance Spot Welding (RSW). However, some difficulties may arise when using RSW to weld galvanised and high strength steels. The galvanised coating causes inadequate heat conduction during welding and diminishes the electrode life [1,2]. Also, when welding high strength steels, the high temperatures and fast cooling rates associated with RSW may lead to the formation of brittle microstructures [3]. Friction Stir Spot Welding (FSSW), a solid state welding process, which is a variant of the Friction Stir Welding (FSW) technology, is a very promising technique to overcome these RSW limitations. According to some authors, FSSW is also an energy-efficient alternative to RSW [4].

In the FSW and FSSW of steels and other high melting point materials, the intense tool pin damage and/or wear represents, according to Çam, 2011 [5] and Rai et al., 2011 [6], a huge drawback. In spite of this, the development of durable and economic tools, capable of welding such kind of materials, as not yet been achieved. However, in the welding of thin plates, one possible solution for this problem may be the use of pinless tools. These tools were already used with success in butt and lap welding of several steels, as well as in spot welding.

Mira-Aguiar et al., 2016 [7] used a tungsten carbide pinless tool, with a diameter of 12 mm, in the linear lap welding of 1mm thick DX51D and DC01 steels, with rotational and traverse speeds of 1000 rpm and 600 mm/min, respectively. According to the authors, due to the absence of the tool pin no material mixing along the base material thickness was observed, and the welding occurs due to the combination of very high pressure and temperature at the plates interface. Since the welding mechanisms were reported to be different from the ones in FSW, the authors labelled the process as Tool Assisted Friction Welding (TAFW). Andrade et al., 2018 [8] also used the TAFW process to produce lap welds in 1mm thick DX51D steel plates, under a varied range of tool diameters (10 to 16 mm), rotational speeds (600 to 1400 rpm) and traverse speeds (200 to 1200 mm/min). The authors obtained welds with mechanical strength equal to the base material ultimate tensile strength, for traverse speeds up to 1000 mm/min. For the range of process parameters tested no hook or cold-lap defects were found.

Kim et al., 2017 [9] tested a WC-Co pinless tool in the butt welding of 1mm thick 430M2 ferritic stainless steel. Welds without any defects and with mechanical strength equal to the base material were produced using a tool with 6 mm diameter and rotational and traverse speeds of 900 rpm and 96 mm/min, respectively.

Sun et al., 2019 [10] analysed the influence of the rotational speed in the mechanical strength of low carbon steel spot welds produced with pinless tools. The steel welds were produced using very low rotational speeds, between 5 to 50 rpm, but high axial loads, between 6 to 8 t. Due to the very low heat input, a dwell time of 30 s was used in order to obtain good quality welds. According to the authors, the weld metallurgical bonding at the plates interface resulted from plastic deformation enhanced atomic inter-diffusion. It was found that increasing the rotational speed and axial load leads to an increase in the welds mechanical strength.

Pinless tools have also been used by van der Rest et al., 2014 [11], to produce lap welds between a 0.8 mm thick microalloyed ultralow carbon steel and 1 mm thick Al 1050 or 2 mm thick Al 2024 T3 sheets. A tungsten carbide tool with 16 mm, with a constant rotational speed of 2000 rpm and varied traverse speeds between 100 to 700 mm/min were used. During welding, the higher melting point material was placed in the top of the joint, enabling very high temperatures at the plates interface that lead to partial melting of the bottom sheet. The joining between the two sheets occurred due to the formation of Al-Fe intermetallics, which lead the authors to label the process as Friction Melt Bonding (FMB). Similarly, Zhang et al., 2011 [12] used a pinless tool for the lap welding of 1.8 mm thick aluminium to low carbon steel plates. Although, in this case, the lower melting point material was placed at the top of the weld and the joining between the plates resulted from the melting of a 0.1 mm thick zinc foil, placed between the two sheets.

The feasibility of the TAFW process to produce steel lap welds at very high traverse speeds and with good mechanical strength was already demonstrated by Mira-Aguiar et al., 2016 [7] and Andrade et al., 2018 [8]. On the other hand, the feasibility of the TAFW process to produce steel spot welds with good mechanical strength at short process cycle times remains unexplored. The present work aimed to analyse the influence of the process parameters and galvanized coating thickness on the heat generation and mechanical strength of steel spot welds, produced using TAFW. Numerical simulation of the process was performed in order to provide a better insight into the heat generation and

bonding mechanisms. Welds strength was evaluated by performing shear tension tests of specimens produced for a wide range of welding conditions.

## 2. Experimental procedure

In this work, friction stir spot welds in a mild steel (DC01) and three galvanized steels (DC01-ZE25/25, DX51D-Z140 and DX51D-Z200) were produced. The base materials ultimate tensile strength (UTS), hardness ( $HV_{0.2}$ ), equivalent carbon content ( $C_{eq}$ ) and galvanized coating thickness (CT) are shown in Figure E.1. The base materials were properly selected in order to have similar chemical composition and mechanical properties, while having different galvanized coating thicknesses. Throughout the text, the base materials DC01, DC01-ZE25/25, DX51D-Z140 and DX51D-Z200 will be labelled as DC, DCR2.5, DXR10 and DXR14, respectively.

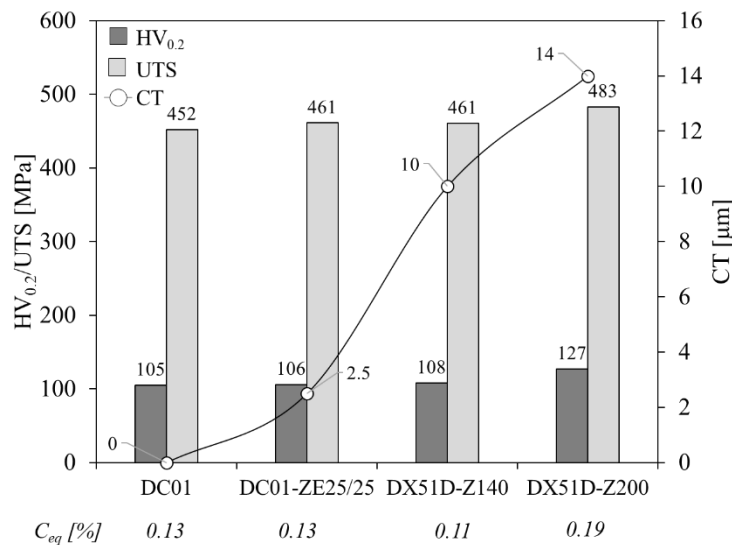


**Figure E.1** – Base material properties: carbon content ( $C_{eq}$ ), galvanized coating thickness (CT), hardness ( $HV_{0.2}$ ) and ultimate tensile strength (UTS).

The spot welds were produced in position control using tungsten carbide pinless tools with flat shoulders. Plates dimensions were 80x80x1 mm. As in FSSW, a three-stage welding operation was adopted, consisting of the tool penetration, the dwell period and the tool removal. To analyse the influence of the tool diameter, rotational speed, galvanized coating thickness and dwell time on the heat generation, three different experimental trials were conducted as described in Table E.1. the influence of the process parameters on the heat generation was assessed by producing welds in DC steel, the uncoated reference material, and varying the rotational speed and tool diameter between



870 to 1500 rpm and 10 to 16 mm, respectively. The influence of the galvanized coating thickness on the heat generation was analysed by producing welds in DC, DCR2.5, DXR10 and DXR14 steels with rotational speeds between 870 and 1500 rpm and a constant tool diameter equal to 12 mm. In all these tests, a plunge depth of 0.5 mm and a dwelling period of 60 s were used. Finally, the influence of the above described parameters, as well as the influence of the dwell time, on the welds strength, was assessed by testing dwelling periods of 5, 15, 30 and 60 s, in DC and DXR14 steels, i.e. in the uncoated steel and the steel with the highest coating thickness, for all the rotational speeds and tool diameters tested in this work. In order to ensure the reproducibility of the results, for each welding condition, at least, two welding trials were performed. Along the text, the tools will be labelled according to the shoulder diameter, for example, the tool with a 16 mm shoulder diameter will be labelled PL16.

**Table E.1** – Welding parameters.

<i>Experimental trial</i>	<i>Base material</i>	<i>Tool diameter [mm]</i>	<i>Rotational speed [rpm]</i>	<i>Dwell time [s]</i>
1	DC	10 - 16	870 - 1500	60
2	DC DCR2.5 DXR10 DXR14	12	870 - 1500	60
3	DC DXR14	10 - 16	870 - 1500	5 - 60

The welds strength was evaluated by performing shear tension tests, in quasi-static loading conditions ( $2 \text{ mm/min}^{-1}$ ). Digital Image Correlation (DIC) was used for strain data acquisition following the practices described in Leitão et al., 2012 [13] and Leitão et al., 2013 [14]. The shear tension sample is schematized in Figure E.2. In order to prevent bending of the samples during testing, plates with thickness equal to that of the welded sheets were attached at each end of the shear tension samples.

The welding thermal cycles were recorded with a thermographic camera and analysed as described in Andrade et al., 2019 [15]. After welding, transverse samples were cut from the welds, prepared according to standard metallographic practice, etched with 2% Nital and observed using an optical microscope. Grain size measurements were conducted by using an image analysing software.

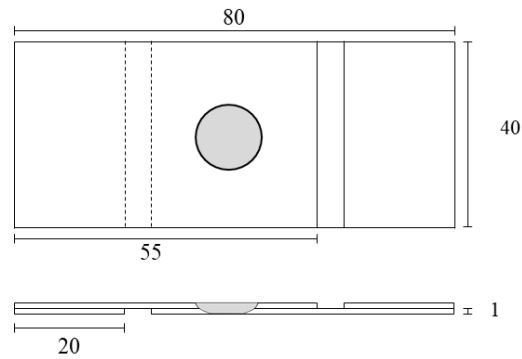


**Figure E.2** – Schematic representation of the shear tension sample.

### 3. Numerical model

The TAFW process was modelled by using an already developed three-dimensional numerical model proposed by Chiumenti et al., 2013 [16] and Dialami et al., 2013 [17]. In this model, a Lagrangian formulation is used for the rotating tool, while ALE and Eulerian formulations are used for the stir zone and the rest of the workpiece, respectively. The coupled thermo-mechanical model, as well as the numerical strategies used to solve the problem, are described in detail in Dialami et al., [18–20]. The Norton's friction law was used to model the friction at the tool/workpiece interface:

$$\tau = a(T) \|\Delta v_s\|^{q-1} \Delta v_s. \quad (\text{E.1})$$

In the equation,  $\tau$  is the friction shear stress,  $\Delta v_s$  is the relative sliding velocity between the tool and the workpiece,  $q$  is the sensitivity to the sliding velocity and  $a(T)$  is the consistency parameter. The geometry of the model and the mesh discretisation are shown in Figure E.3. For the tool and the workpiece, a computational mesh of around 21000 nodes and 115000 tetrahedral elements were used.

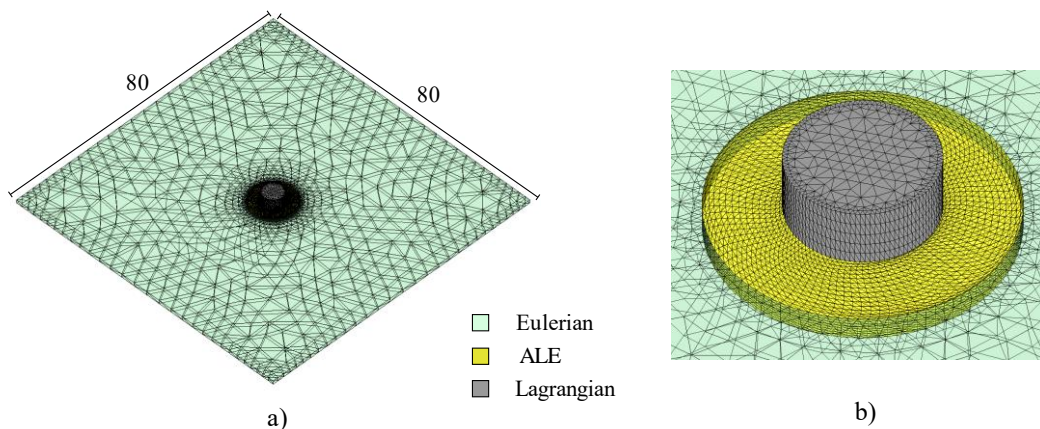


**Figure E.3** – Model geometry and mesh discretisation: workpiece (a) and tool (b).

## 4. Results and discussion

### 4.1. Influence of process parameters on heat generation

The thermal cycle and the cross section of the weld produced in DC steel, with the PL12 tool and with a rotational speed of 1140 rpm, are shown in Figure E.4a and E.4b, respectively. Analysing the welding thermal cycle, it is possible to observe that the temperature rapidly increased as soon as the tool was plunged in the workpiece. A peak temperature, of around 935 °C, was reached at the end of the dwelling period (60 s). After the tool removal, the temperature started to decrease. In Figure E.4b it is shown a weld cross section, after chemical etching, where it is possible to observe a darker region that corresponds to the process affected zone (PAZ), with a microstructure different from that of the base material. Since pinless tools were used, the material stirring across the plates thickness was suppressed, as is shown by the continuous line at the mid thickness of the weld. Although no stirring took place at the plates interface, joining of the plates occurred as is shown by the micrograph in Figure E.5a, where it is possible to observe the microstructural continuity between the top and the bottom sheets, which shows that the joining between the plates occurred due to diffusion mechanisms associated with the very high pressure and temperatures attained during welding. Actually, the only tool/workpiece interaction was observed in a thin region at the top of the welds. This region is shown in more detail in Figure E.5b, where it is possible to observe a dark layer containing tool remnants, as revealed by the SEM/EDS analysis (Figure E.5c). Concentric rings are also observed in the weld surface in Figure E.4, which resulted from the intense wear that the tool is subjected during the welding process. Independently of the process parameters tested and tool geometries used, all the spot welds produced presented similar morphology.

The microstructural evolution from the PAZ to the non-affected base material is shown in more detail in Figure E.6a, using a grain size (GS) distribution map. In Figure E.6b and c are shown the GS distribution and GS average values, respectively, for the regions 1, 2 and 3, identified in the cross section of Figure E.6a. In the figures, it is also shown the GS distribution and the average GS for the base material. The figures enable to observe a continuous decrease in the grain size from zone 1, outside the PAZ, to zone 3, inside the PAZ. These grain size refinement in zone 3 is due to the high temperatures, higher than  $A_1$ , that allow the steel allotropic transformations to occur. On the other hand, an increase in the grain size, relative to the base material was observed in zones 1 and 2, due to the long exposure (60 s) of these regions to temperatures below  $A_1$ . A similar

## Appendix E

microstructural evolution was already reported by Lienert et al., 2003 [21], Fujii et al., 2006 [22], Karami et al., 2016 [23] and Sekban et al., 2017 [24] in the heat affected zone (HAZ) of steel welds produced by FSW. The similarities between the PAZ and the HAZ, of welds produced by FSW, once again prove the absence of base materials stirring in the spot welds produced by TAFW.

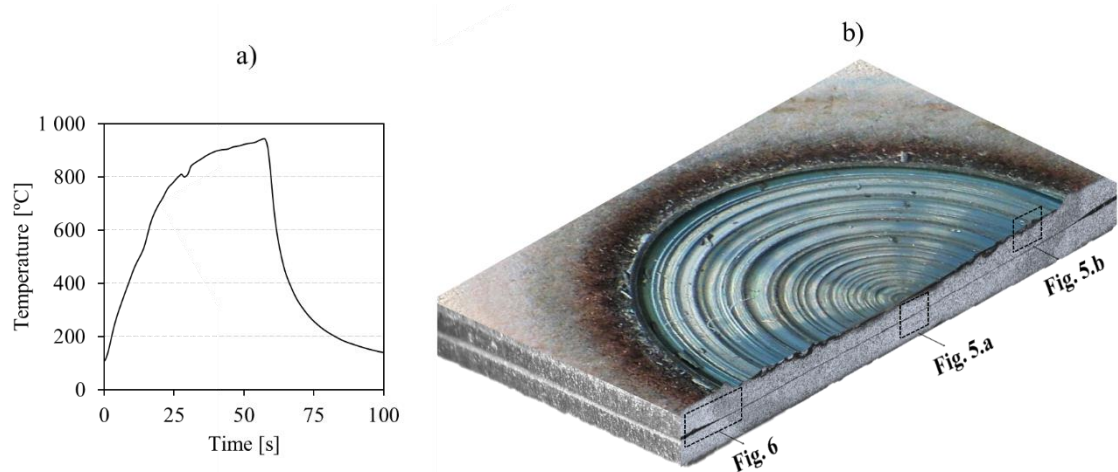


**Figure E.4** – Welding thermal cycle (a) and cross section view (b) for the weld produced in DC steel with a rotational speed of 1140 rpm and with a tool diameter of 12 mm.

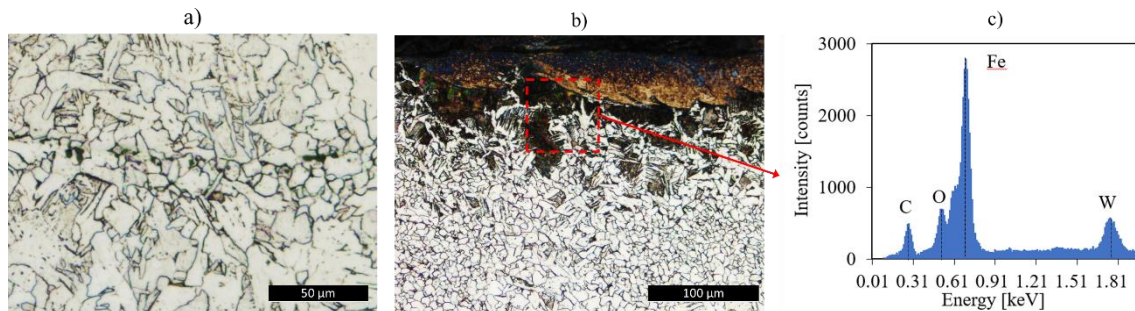


**Figure E.5** – Magnification of the weld microstructure at the plates bonding interface (a), at the top of the weld (b), and SEM/EDS analysis (c).

In Figures E.7a and b are now shown the velocity and temperature map distributions along the weld cross section, respectively, obtained when simulating the experimental conditions of the weld shown in Figure E.4. In Figure E.7b it is also represented, using a black dashed line, the shape of PAZ in Figure E.4, obtained by eliminating the microstructure with an image editing software. The velocity profile, in Figure E.7a, shows that the stirring action of the tool was limited to a region close to the weld top surface, which correspond to the weld region where higher amount of tool remnants were observed. The computed velocity values are zero at the plates interface,

which supports the previous assumption that no stirring occurred across the base materials thickness. The regions where the velocity values are higher also correspond to the regions with higher welding temperatures. For this weld, the thermographic camera registered a maximum temperature of 935 °C, which corresponds to the temperature obtained through the numerical simulation near the tool/workpiece outer edge interface, as shown in Figure E.7b. The temperature distribution also shows that the PAZ starts in a region where the temperatures are around 730 °C, which correspond to the  $A_1$  temperature of the DC steel. The temperature gradient in Figure E.7b is also in good agreement with the GS distribution in Figure E.6.

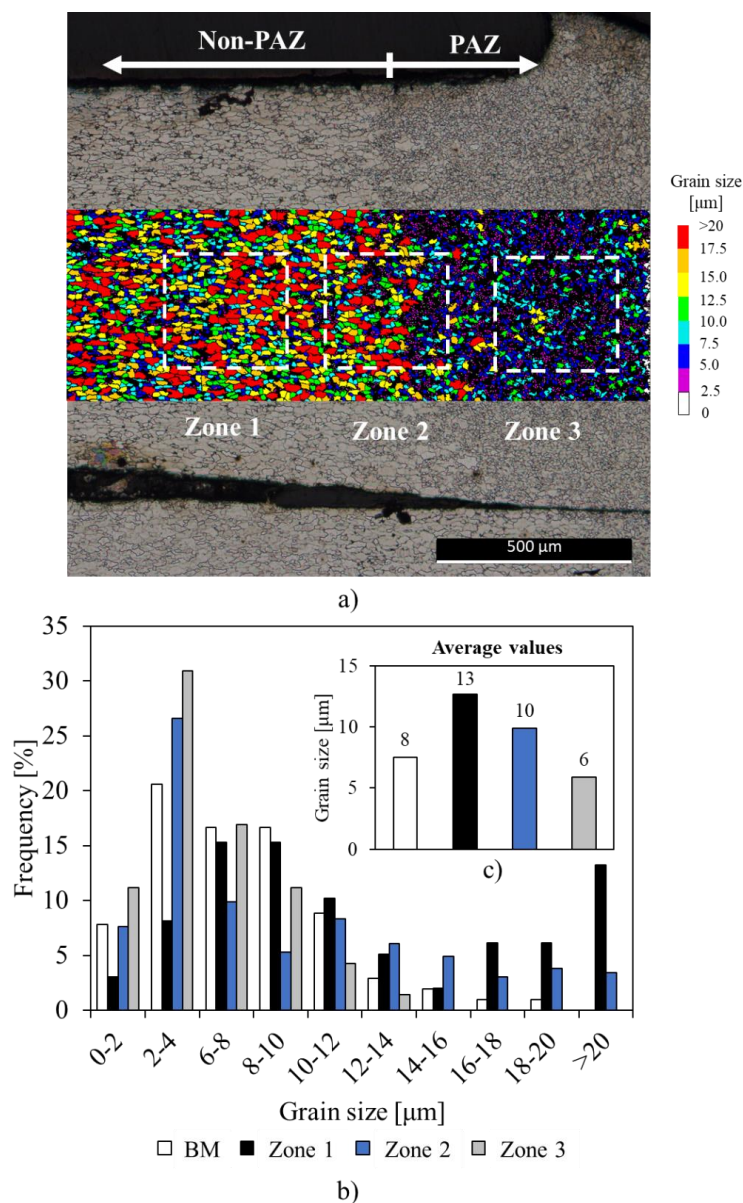


**Figure E.6** – Microstructural evolution from the non-PAZ to the PAZ (a). Grain size distribution for the welding zones 1, 2 and 3 and for the DC base material (b-c).

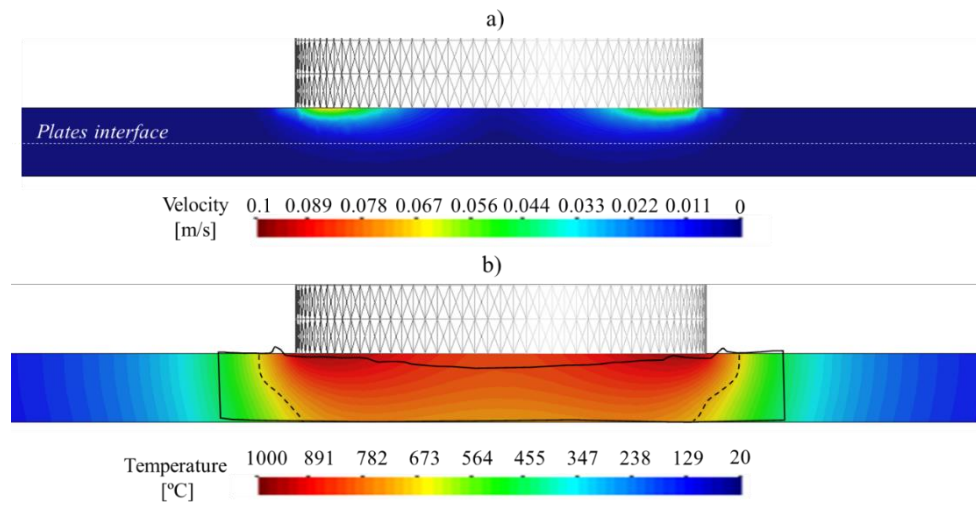


**Figure E.7** – Velocity (a) and temperature profiles (b), along the weld cross section, produced with a rotational speed of 1140 rpm and with a tool diameter of 12 mm.

In Figure E.8 is now shown the evolution of the maximum welding temperatures registered in the experimental tests, i.e. using different rotational speeds and tool diameters. Analysing the figure, it is possible to conclude that the welding temperature always increased with the increase of the tool diameter, independently of the rotational speed used. Although, the influence of the tool diameter in the temperature is higher when lower rotational speeds are used. For a rotational speed of 870 rpm, increasing the tool diameter from 10 to 16 mm lead to an increase in temperature of 480° C, while for a rotational speed of 1500 rpm, the same variation in the tool diameter only lead to a variation in temperature of 220 °C. On the other hand, the rotational speed only affects the maximum welding temperatures for small tool diameters. For the PL10 and PL12 tools, increasing the rotational speed from 870 to 1500 rpm lead to a variation of 200 °C in the welding temperature. For the larger tool diameter tested no influence of the rotational speed on the welding temperatures was observed. Instead, a temperature threshold of around 1100 °C was registered.



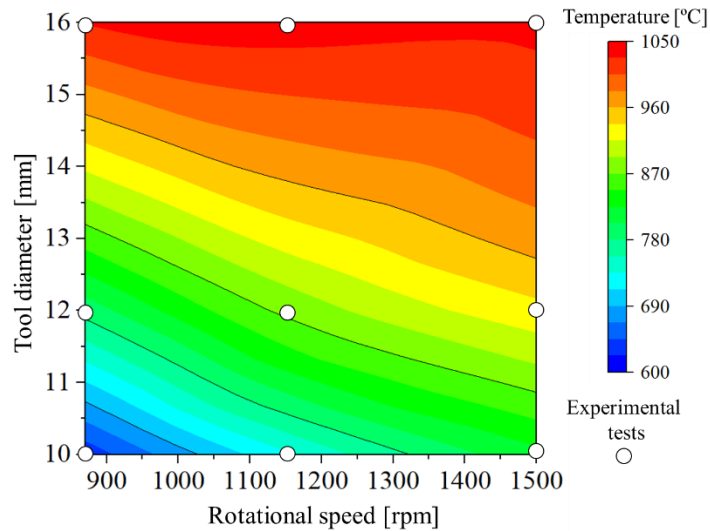


**Figure E.8** – Evolution of the welding temperatures with the rotational speed and tool diameter, for the DC steel.

#### 4.2. Influence of the galvanized coating on heat generation

The influence of the galvanized coating thickness on the maximum welding temperatures is shown in Figure E.9. These results were obtained for welds produced in DC, DCR2.5, DXR10 and DXR14 steels, with the PL12 tool and by varying the rotational speed from 870 to 1500 rpm. Analysing the figure, it is possible to conclude that for low rotational speeds, the maximum welding temperature decreased with the increase of the galvanized coating thickness. Although, by increasing the rotational speed, the effect of the galvanized coated thickness on the welding temperature decreased. More precisely, for the rotational speeds of 870 and 1140 rpm, increasing the galvanized coating thickness from 0 to 14  $\mu\text{m}$ , resulted in a variation of around 100 °C in the welding temperature, while for the rotational speed of 1500 rpm only a small variation of 15 °C was registered.

Figures E.10a and b show the evolution of the welding thermal cycles, obtained for the rotational speeds of 870 and 1500 rpm, respectively, with the galvanized coating thickness. In the figures, it is also shown the galvanized coating melting (420 °C) and boiling (709 °C) temperatures. From the figure, it is possible to conclude that, at 870 rpm, the rate of heat generation was lower for the welds performed with the thicker galvanized coatings. For this rotational speed, the welding temperatures were always higher than the melting temperature of the galvanized coating but lower than its boiling temperature. The only exception was in the welding of the DCR2.5 steel, which was the steel with the lowest galvanized coating thickness, which reached temperatures similar to the ones registered for the DC steel at the end of the dwelling stage. On the other hand, increasing

## Appendix E

the rotational speed to 1500 rpm, increased the centrifugal action of the tool, allowing the welding temperatures to be superior to the boiling temperature of the galvanized coating due to the removal of the coating from the tool-workpiece interface. So, for these welding conditions, the galvanized coating did not affect the heat generation and a threshold in the welding temperature was reached independently of the galvanized coating thickness used.

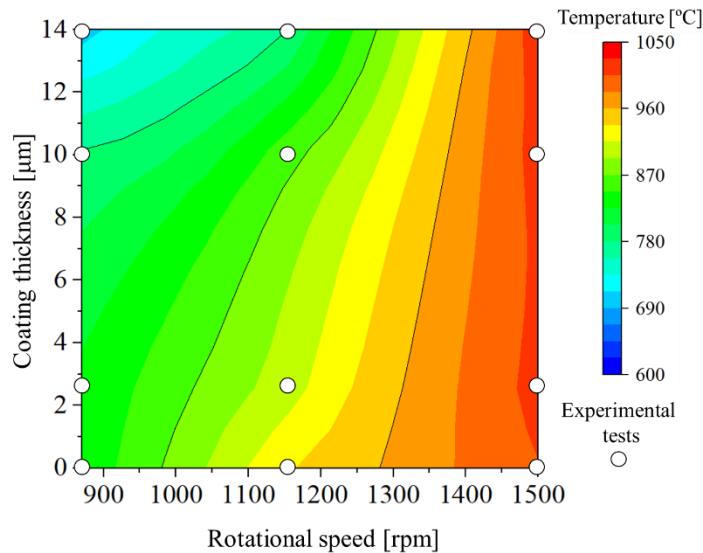


**Figure E.9** – Evolution of the welding temperature with the rotational speed and galvanized coating thickness.

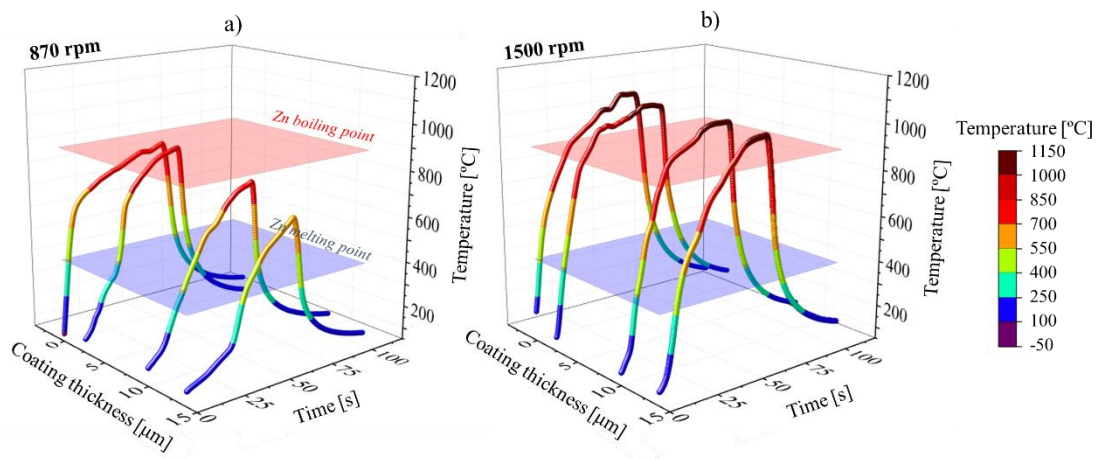


**Figure E.10** – Evolution of the welding thermal cycles with the galvanized coating thickness for a rotational speed of 870 rpm (a) and 1500 rpm (b).

To better understand the effect of the galvanized coating on the heat generation, numerical simulations were performed with different friction values at the tool/workpiece interface. The friction values were varied by ranging the consistency parameter ( $a(T)$ ),



from Eq. E.1, between 0.5 to 500 MPa. By using such a wide range of  $a(T)$  values, it is expected to simulate different contact conditions at the tool/workpiece interface, i.e. slipping, mixed slipping/sticking and sticking. In order to assess the contact conditions between the tool and the workpiece, the contact state variable proposed by Schmidt et al., 2003 [25] was used:

$$\delta = \frac{v_{BM}}{v_{tool}}. \quad (E.2)$$

In the equation,  $\delta$  is the sticking fraction,  $v_{BM}$  is the velocity of the base material at the tool/workpiece interface, and  $v_{tool}$  is the tool velocity. According to the previous equation, when the contact state variable is equal to one, it means that the base material velocity at the tool/workpiece is equal to the tool velocity, and fully sticking contact conditions are reached. On the other hand, when the contact state variable is equal to zero, it means that no material is extruded around the tool, and the contact is fully slipping. In the next, the contact conditions were characterized by calculating the average sticking fraction for all the points along the tool/workpiece interface.

In Figure E.11 is compared the evolution of the welding temperatures, obtained numerically (Figures E.11a), for different levels of friction, with the welding thermal cycles measured experimentally (Figures E.11b) for the DC and DXR14 base materials, i.e. the uncoated base material and the base material with the thicker galvanized coating. The results in the figure correspond to the welding operations conducted with the PL12 tool and the rotational speed of 870 rpm. In Figures E.11c to f are shown the velocity profiles for different friction values between the tool and the base material. From the figure, it is possible to conclude that there was a gradual increase of the welding temperatures and of the sticking fraction when the consistency parameter was increased. For very low values of  $a(T)$ , fully slipping contact conditions prevailed ( $\delta = 0$ ) and no stirring took place at the tool-workpiece interface, as is possible to see in the velocity profile shown in Figure E.11c. The tool only starts to stir material for values of  $a(T)$  higher than 30 MPa ( $\delta = 0.1$ ), as shown in Figure E.11d. With the gradual increase of  $a(T)$  there was an increase in the amount of material stirring until a limit is reached at  $a(T)$  equal to 100 MPa (Figure 11f). For  $a(T) > 100$  MPa sticking contact conditions prevailed ( $\delta > 0.6$ ) and the welding temperature becomes independent of the friction value. The evolution of the temperature with  $a(T)$ , obtained through the numerical simulation, is similar to the welding thermal cycles for the galvanized steels, allowing to conclude that the melting and expulsion of the galvanized coating from the tool-workpiece interface during welding

has a strong influence on the contact conditions. More precisely, during welding, the tool axial load and centrifugal action expel the galvanized coating from the welding region, which allow a continuous increase of friction at the tool workpiece interface and of the welding temperature over time. According to Figures E.11 b, for the DXR14 steel, a large amount of the galvanized coating remained trapped at the tool workpiece interface, promoting prevalent sliding conditions ( $\delta < 0.1$ ), during the 60 s dwelling period.

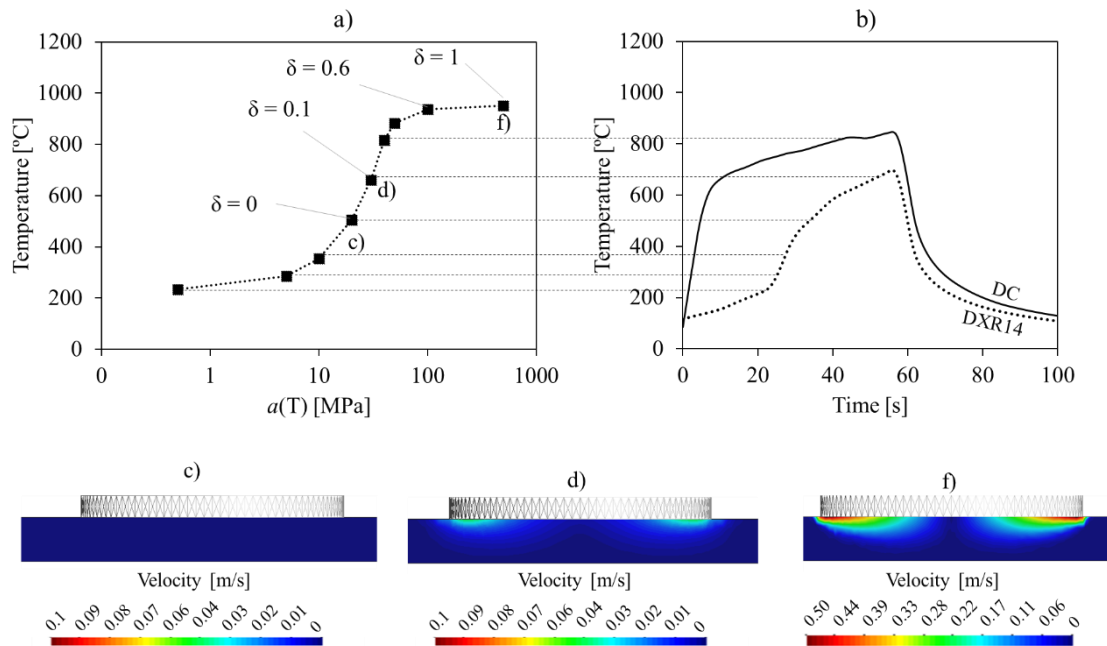


**Figure E.11** – Comparison between the welding temperatures, obtained through numerical simulation, for different levels of friction (a), with the welding thermal cycles for the DC and DXR14 welds (b), produced with the PL12 tool at 870 rpm. Velocity profiles, along the weld cross section, for different levels of friction (c-f).

### 4.3. Influence of the process parameters on welds strength

The load-displacement curves obtained in the shear tension tests of the DC steel welds, produced with the PL12 tool, at 870 rpm and welding times of 5, 15, 30 and 60 s, are shown in Figure E.12a. In Figure E.12b are shown the fractured shear tensile specimens and the respective failure modes, and in Figure E.12c is shown the Mises strain distribution maps, at maximum load, for the specimens tested. Since the weld produced in 5 s experienced premature failure, while preparing the samples for the shear tensions tests, no load-displacement curves or strain distribution maps were added in the figure for this welding condition. Analysing the figure, it is possible to conclude that the weld produced with a welding time of 60 s showed the highest mechanical strength. This weld also had higher elongation and plastic deformation than the other welds, as it is possible

to conclude from the load-displacement curves and the strain distribution maps. Reducing the welding time leads to a decrease in both strength and plastic deformation.

According to Figure E.12b, the fracture behaviour of the samples can be divided into two groups, i.e. interfacial fracture, in which fracture occurs by separation of the faying surfaces, and plug fracture, in which the fracture occurs by crack propagation along the weld perimeter. Actually, for these welds, all produced with dwell times equal or higher than 15 s, no plastic deformation was recorded inside the PAZ (Figure E.12c), which shows the very good quality of the bonding.

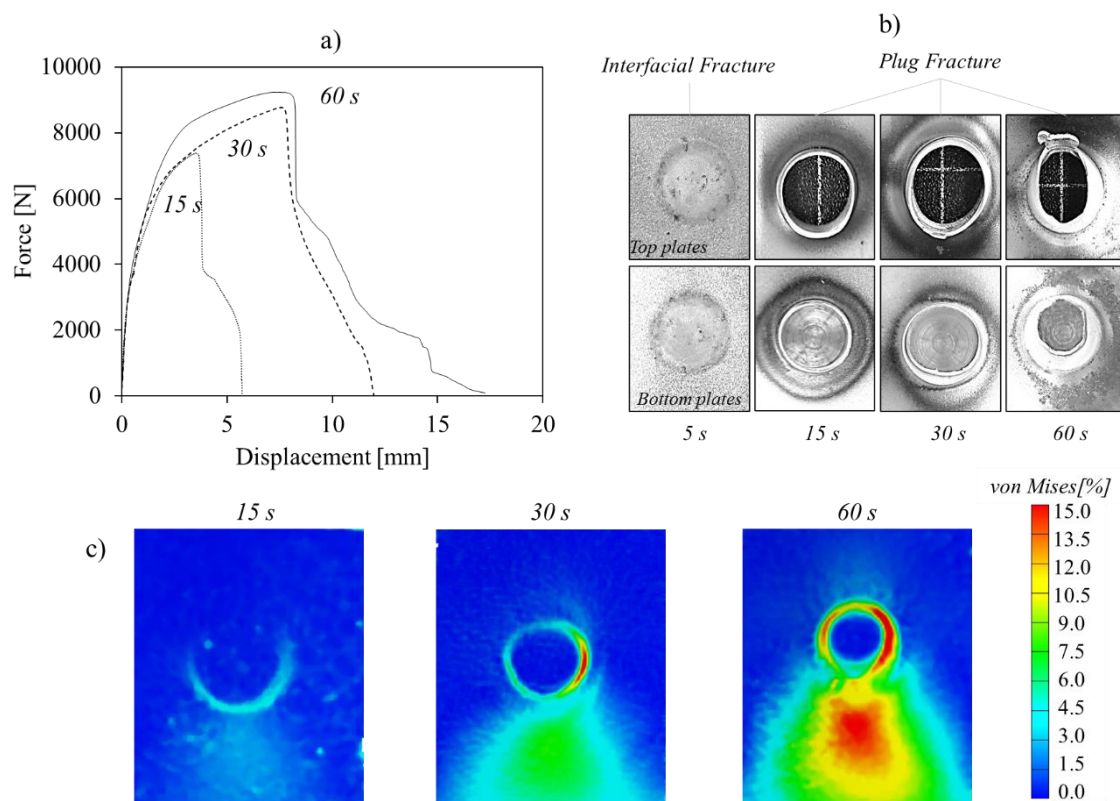


**Figure E.12** – Load-displacement curves (a), fractured tensile specimens (b) and Mises strain distribution maps (b-d) for the welds produced in the DC steel at 870 rpm and with the PL12 tool.

The influence of the rotational speed, tool diameter, welding time and galvanized coating thickness on the strength of the welds is shown in Figure E.13. It is important to enhance that most of the shear tension samples, which strength is shown in the figure, displayed plug fracture mode. The only exceptions were for the welds produced in DC steel, with the PL12 and PL10 tools, 870 rpm and 5 s dwelling time, and for the DXR14 steel welds produced with the PL12 tool, 1500 and 870 rpm and dwelling times lower than 15 s. Analysing the figure, it is possible to observe that the strength of the joints significantly varied according to the welding conditions used. For the non-galvanized

## Appendix E

steels, the strength always increased by increasing the tool diameter, irrespective of the rotational speed and dwell time, enabling to conclude that the tool diameter is the main factor determining the metallurgical bonding area. On the other hand, for short process cycle times, when welding with small tool diameters, PL10 and PL12, increasing the rotational speed increased the strength of the joints. When welding with the PL16 tool, no influence of the rotational speed on the joint strength was registered. These results are related to the strong influence of the shoulder diameter and rotational speed on the heat generation shown in Figure E.8. According to this figure, for the large tool diameters, the temperature remained constant independently of the rotational speed used, while for the smaller tool diameters, the maximum welding temperature increased with the increase of the rotational speed. It is possible to conclude that increasing the welding heat input improved the joint strength.

Another important factor governing the strength of the joints is the welding time. Analysing the figure, it is possible to observe that increasing the welding time from 5 to 15 s, for the PL10 and PL12 tools, at a constant rotational speed of 870 rpm, lead to a substantial increase in the joint strength. It is also important to notice that for welding times higher than 30 s, no influence of the rotational speed or welding time on the joints strength was registered.

Comparing now the strength of the uncoated steel (DC) to that of the galvanized steel (DXR14), it is possible to conclude that the galvanized coating has a strong influence on the joint properties. While for the welds produced in the DC steel with the PL12 tool and a rotational speed of 870 rpm, effective joining between the plates interface was obtained for 15 s dwell time, for the DXR14 steel welds produced with the same processing parameters, the joining between plates only occurred for 30 s dwelling time. Also, for the DXR14 steel, no effective joining occurred for a welding time of 5 s, even when using a rotational speed of 1500 rpm. According to the analysis performed in the previous section, these results are related to the fact that the galvanized coating works as a lubricant at the tool/workpiece interface, reducing the heat generation.

Finally, it is also important to notice that the maximums loads were always higher than the minimum shear tension strength recommended for joints produced by resistance spot welding, according to the AWS D8.1 [26] standard. This is represented in the figure by the red line. Despite the use of a pinless tool, which, as already demonstrated, suppresses the base materials stirring across the faying surfaces, the joints produced by TAFW showed very good mechanical performance.

According to the previous results, for the spot welding of non-galvanised steels, in order to obtain welds with high mechanical strength, at fast production rates, it is recommended the use of a rotational speed of 1500 rpm, independently of the tool diameter. At this rotation speed, current results indicate that the welding time may be less than 5s. On the other hand, for galvanised steels, it is recommended the use of welding times higher than 5s, to ensure that the galvanised coating, which as a detrimental effect on the joint strength, is expelled from the weld region. For these steels, the welding time should be optimized according to the coating thickness and tool diameter.

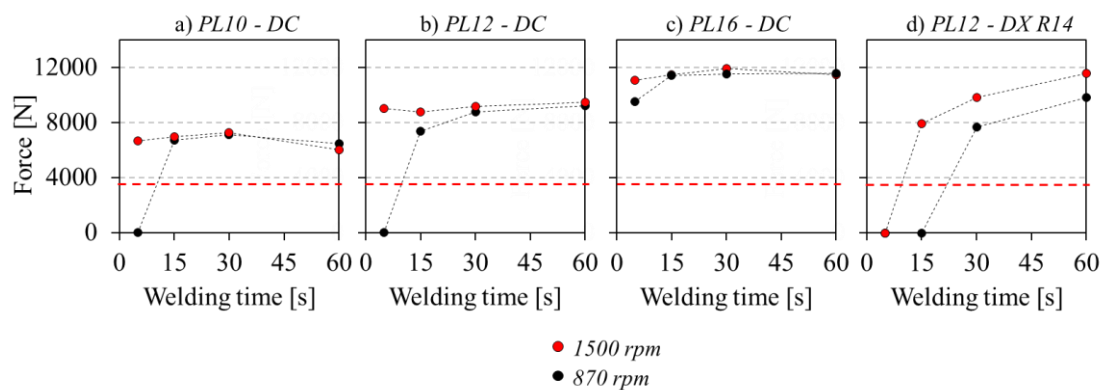


**Figure E.13** – Influence of the rotational speed, shoulder diameter, welding time and galvanized coating thickness on the shear tensile load of the welded joints.

#### 4. Conclusions

In the present work, the influence of the welding time on the joint strength, and the influence of the rotational speed, tool diameter and galvanized coating thickness on the welding thermal cycles during TAFW of steels were studied. In the analysis performed, the experimental results were coupled with a numerical analysis of the welding process. The following conclusions can be drawn:

- The numerical model used was able to reproduce the evolution of the welding temperatures registered under different process parameters and contact conditions.
- The welding temperatures always increases with the tool diameter, that was found to be the main factor governing the heat generation. For small tool diameters, the increase of the rotational speed increases the welding temperatures. For large tool diameters, no variation on the welding temperatures with the rotational speed occurs.

## Appendix E

- During welding, the galvanized coating reduces the friction and the heat generation at the tool/workpiece interface. The effect of the galvanized coating may be suppressed by using very high rotational speeds.
- Despite the absence of a pin and base material stirring across the plates interface, the joints present very good strength. In order to obtain welds with good strength while using very short process cycle times (5 s), required in industrial applications, the use of large tool diameters and high values of rotational speed is recommended.

## References

- [1] M. Spitz, M. Fleischanderl, R. Sierlinger, M. Reischauer, F. Perndorfer, G. Fafilek, Surface lubrication influence on electrode degradation during resistance spot welding of hot dip galvanized steel sheets, *J. Mater. Process. Technol.* 216 (2015) 339–347. doi:<https://doi.org/10.1016/j.jmatprotec.2014.09.011>.
- [2] H.C. Lin, C.A. Hsu, C.S. Lee, T.Y. Kuo, S.L. Jeng, Effects of zinc layer thickness on resistance spot welding of galvanized mild steel, *J. Mater. Process. Technol.* 251 (2018) 205–213. doi:<https://doi.org/10.1016/j.jmatprotec.2017.08.035>.
- [3] N. Saunders, M. Miles, T. Hartman, Y. Hovanski, S.-T. Hong, R. Steel, Joint strength in high speed friction stir spot welded DP 980 steel, *Int. J. Precis. Eng. Manuf.* 15 (2014) 841–848. doi:10.1007/s12541-014-0407-9.
- [4] Z. Shen, Y. Ding, A.P. Gerlich, Advances in friction stir spot welding, *Crit. Rev. Solid State Mater. Sci.* 45 (2020) 457–534. doi:10.1080/10408436.2019.1671799.
- [5] G. Çam, Friction stir welded structural materials: beyond Al-alloys, *Int. Mater. Rev.* 56 (2011) 1–48. doi:10.1179/095066010X12777205875750.
- [6] R. Rai, A. De, H.K.D.H. Bhadeshia, T. DebRoy, Review: friction stir welding tools, *Sci. Technol. Weld. Join.* 16 (2011) 325–342. doi:10.1179/1362171811Y.0000000023.
- [7] T. Mira-Aguiar, D. Verdera, C. Leitão, D.M.M. Rodrigues, Tool assisted friction welding: A FSW related technique for the linear lap welding of very thin steel plates, *J. Mater. Process. Technol.* 238 (2016) 73–80. doi:10.1016/j.jmatprotec.2016.07.006.
- [8] D.G.G. Andrade, C. Leitão, D.M.M. Rodrigues, Properties of lap welds in low carbon galvanized steel produced by tool assisted friction welding, *J. Mater. Process. Technol.* 260 (2018) 77–86.

- doi:<https://doi.org/10.1016/j.jmatprotec.2018.05.018>.
- [9] K.H. Kim, H.S. Bang, H.S. Bang, A.F.H.H. Kaplan, Joint properties of ultra thin 430M2 ferritic stainless steel sheets by friction stir welding using pinless tool, *J. Mater. Process. Technol.* 243 (2017) 381–386. doi:[10.1016/j.jmatprotec.2016.12.018](https://doi.org/10.1016/j.jmatprotec.2016.12.018).
- [10] Y.F. Sun, H. Fujii, Y. Sato, Y. Morisada, Friction stir spot welding of SPCC low carbon steel plates at extremely low welding temperature, *J. Mater. Sci. Technol.* 35 (2019) 733–741. doi:[10.1016/j.jmst.2018.11.011](https://doi.org/10.1016/j.jmst.2018.11.011).
- [11] C. van der Rest, P.J. Jacques, A. Simar, On the joining of steel and aluminium by means of a new friction melt bonding process, *Scr. Mater.* 77 (2014) 25–28. doi:<https://doi.org/10.1016/j.scriptamat.2014.01.008>.
- [12] G. Zhang, W. Su, J. Zhang, Z. Wei, Friction Stir Brazing: a Novel Process for Fabricating Al/Steel Layered Composite and for Dissimilar Joining of Al to Steel, *Metall. Mater. Trans. A.* 42 (2011) 2850–2861. doi:[10.1007/s11661-011-0677-0](https://doi.org/10.1007/s11661-011-0677-0).
- [13] C. Leitão, I. Galvão, R.M. Leal, D.M. Rodrigues, Determination of local constitutive properties of aluminium friction stir welds using digital image correlation, *Mater. Des.* 33 (2012) 69–74. doi:<https://doi.org/10.1016/j.matdes.2011.07.009>.
- [14] C. Leitão, M.I. Costa, K. Khanijomdi, D.M. Rodrigues, Assessing strength and local plastic behaviour of welds by shear testing, *Mater. Des.* 51 (2013) 968–974. doi:<https://doi.org/10.1016/j.matdes.2013.04.100>.
- [15] D.G. Andrade, C. Leitão, D.M. Rodrigues, Influence of base material characteristics and process parameters on frictional heat generation during Friction Stir Spot Welding of steels, *J. Manuf. Process.* 43 (2019) 98–104. doi:<https://doi.org/10.1016/j.jmapro.2019.05.015>.
- [16] M. Chiumenti, M. Cervera, C. Agelet de Saracibar, N. Dialami, Numerical modeling of friction stir welding processes, *Comput. Methods Appl. Mech. Eng.* 254 (2013) 353–369. doi:[10.1016/j.cma.2012.09.013](https://doi.org/10.1016/j.cma.2012.09.013).
- [17] N. Dialami, M. Chiumenti, M. Cervera, C. Agelet de Saracibar, An apropos kinematic framework for the numerical modeling of friction stir welding, *Comput. Struct.* 117 (2013) 48–57. doi:<https://doi.org/10.1016/j.compstruc.2012.12.006>.
- [18] N. Dialami, M. Chiumenti, M. Cervera, A. Segatori, W. Osikowicz, Enhanced friction model for Friction Stir Welding (FSW) analysis: Simulation and experimental validation, *Int. J. Mech. Sci.* 133 (2017) 555–567.

## Appendix E

- doi:<https://doi.org/10.1016/j.ijmecsci.2017.09.022>.
- [19] N. Dialami, M. Cervera, M. Chiumenti, C. Agelet de Saracibar, A fast and accurate two-stage strategy to evaluate the effect of the pin tool profile on metal flow, torque and forces in friction stir welding, *Int. J. Mech. Sci.* 122 (2017) 215–227. doi:10.1016/j.ijmecsci.2016.12.016.
- [20] N. Dialami, M. Cervera, M. Chiumenti, Defect formation and material flow in Friction Stir Welding, *Eur. J. Mech. - A/Solids.* 80 (2020) 103912. doi:<https://doi.org/10.1016/j.euromechsol.2019.103912>.
- [21] T.J. Lienert, W.L. Stellwag Jr, B.B. Grimmitt, R.W. Warke, Friction stir welding studies on mild steel, *Weld. Journal-New York-*. 82 (2003) 1--S.
- [22] H. Fujii, L. Cui, N. Tsuji, M. Maeda, K. Nakata, K. Nogi, Friction stir welding of carbon steels, *Mater. Sci. Eng. A.* 429 (2006) 50–57. doi:10.1016/j.msea.2006.04.118.
- [23] S. Karami, H. Jafarian, A.R. Eivani, S. Kheirandish, Materials Science & Engineering A Engineering tensile properties by controlling welding parameters and microstructure in a mild steel processed by friction stir welding, *Mater. Sci. Eng. A.* 670 (2016) 68–74. doi:10.1016/j.msea.2016.06.008.
- [24] D.M. Sekban, S.M. Aktarer, H. Zhang, P. Xue, Z. Ma, G. Purcek, Microstructural and Mechanical Evolution of a Low Carbon Steel by Friction Stir Processing, *Metall. Mater. Trans. A.* 48 (2017) 3869–3879. doi:10.1007/s11661-017-4157-z.
- [25] H. Schmidt, J. Hattel, J. Wert, An analytical model for the heat generation in friction stir welding, *Model. Simul. Mater. Sci. Eng.* 12 (2003) 143–157. doi:10.1088/0965-0393/12/1/013.
- [26] AWS D8.1, Specification for automotive weld quality – resistance spot welding of steel, 2007.